Design and Development of Small Molecular Fluorescent Probes for Monitoring Cellular Microenvironment

by

ANAGHA THOMAS

10CC19A39010

A thesis submitted to the
Academy of Scientific & Innovative Research
for the award of the degree of
DOCTOR OF PHILOSOPHY
in
SCIENCE

Under the supervision of
Prof. A. AJAYAGHOSH (Supervisor)
and
Dr. JOSHY JOSEPH (Co-supervisor)

CSIR-National Institute for Interdisciplinary Science and Technology (CSIR-NIIST), Thiruvananthapuram – 695 019

Academy of Scientific and Innovative Research
AcSIR Headquarters, CSIR-HRDC campus
Sector 19, Kamla Nehru Nagar,
Ghaziabad, U. P. – 201 002, India

April 2025

The thesis is dedicated to

everyone who has brought

light and joy into my life

राष्ट्रीय अंतर्विषयी विज्ञान तथा प्रौद्योगिकी संस्थान
वैज्ञानिक तथा औद्योगिक अनुसंधान परिषद् | विज्ञान तथा प्रौद्योगिकी मंत्रालय, भारत सरकार
इंडस्ट्रियल इस्टेट पी.ओ., पाप्पनंकोड, तिरुवनंतपुरम, भारत-695 019
CSIR-NATIONAL INSTITUTE FOR INTERDISCIPLINARY SCIENCE AND TECHNOLOGY (CSIR-NIIST)
Council of Scientific & Industrial Research | Ministry of Science and Technology, Govt. of India
Industrial Estate P.O., Pappanamcode, Thiruvananthapuram, India-695 019

CERTIFICATE

This is to certify that the work incorporated in this Ph.D. thesis entitled, *"**Design and Development of Small Molecular Fluorescent Probes for Monitoring Cellular Microenvironment**"*, submitted by ***Ms. Anagha Thomas*** to the Academy of Scientific and Innovative Research (AcSIR) in fulfilment of the requirements for the award of the Degree of ***Doctor of Philosophy in Science***, embodies original research work carried out by the student. We further certify that this work has not been submitted to any other University or Institution in part or full for the award of any degree or diploma. Research materials obtained from other sources and used in this research work have been duly acknowledged in the thesis. Images, illustrations, figures, tables etc., used in the thesis from other sources, have also been duly cited and acknowledged.

28/04/25
Anagha Thomas

28.04.2025
Prof. A. Ajayaghosh
(Thesis Supervisor)

28/4/2025
Dr. Joshy Joseph
(Thesis Co-supervisor)

Tel : 91 471 2515226 | 2515234 | E-mail : director@niist.res.in | Website : http://niist.res.in

STATEMENTS OF ACADEMIC INTEGRITY

I Anagha Thomas, a Ph.D. student of the Academy of Scientific and Innovative Research (AcSIR) with Registration No. 10CC19A39010 hereby undertake that, the thesis entitled ***"Design and Development of Small Molecular Fluorescent Probes for Monitoring Cellular Microenvironment"*** has been prepared by me and that the document reports original work carried out by me and is free of any plagiarism in compliance with the UGC Regulations on *"Promotion of Academic Integrity and Prevention of Plagiarism in Higher Educational Institutions (2018)"* and the CSIR Guidelines for "*Ethics in Research and in Governance (2020)*".

April 28, 2025
Thiruvananthapuram

28/04/25
Anagha Thomas

It is hereby certified that the work done by the student, under my supervision, is plagiarism-free in accordance with the UGC Regulations on *"Promotion of Academic Integrity and Prevention of Plagiarism in Higher Educational Institutions (2018)"* and the CSIR Guidelines for "*Ethics in Research and in Governance (2020)*".

April 28, 2025
Thiruvananthapuram

28.04.2025
Prof. A. Ajayaghosh
(Thesis Supervisor)

28/4/2025
Dr. Joshy Joseph
(Thesis Co-supervisor)

ACKNOWLEDGEMENTS

I would like to express my deepest gratitude to Prof. A. Ajayaghosh, my thesis supervisor, for his invaluable guidance, unwavering support, and constant encouragement throughout this journey. I am also immensely grateful to Dr. Joshy Joseph, my co-supervisor, for his guidance, invaluable advice, and immense help throughout my Ph. D. tenure. I am thankful for the constant support and scientific knowledge he has shared with me throughout my research career, leading to the successful completion of this work.

I wish to extend my sincere thanks to Dr. C. Anandharamakrishnan, Director, CSIR-National Institute for Interdisciplinary Science and Technology, Thiruvananthapuram, for providing the necessary facilities to carry out this research.

My sincere thanks to

- *DAC members: Dr. C. Vijayakumar, Dr. Kaustabh Kumar Maiti, and Dr. Rajeev Sukumaran*
- *HODs (CSTD): Dr. U. S. Hareesh., Dr. K. V. Radhakrishnan, and Dr. P. Sujatha Devi*
- *AcSIR coordinators: Dr. P. Jayamurthy, Dr. V. Karunakaran, and Dr. C. H. Suresh*
- *Dr. K. N. Narayanan Unni, Dr. Biswapriya Deb, Dr. Jubi. John, Dr. V. K. Praveen, Dr. Sreejith Shankar and all scientists in CSTD Division*
- *Dr. Sarit S. Agasti and, Ms. Ritika Raghuvanshi, JNCASR, Bengaluru*
- *Dr. Anaga, Dr. Ropasree, Dr. Vishnupriya, Dr. Shamjith, Mr. Amarjith, Ms. Rumaisa, and Ms. Alisha*
- *Technical Support: Mr. Robert Philip, Mr. Kiran S. Jayakumar, Mr. Kiran Mohan, Mrs. Soumini, Mrs. Viji, Mr. Nidhin, Ms. Aswathy, Mr. Jerin, Mr. Merin, Mrs. Gayathri, Ms. Viji, Ms. Renju, and Ms. Soumaya*
- *Ms. Priyanka, Dr. Dipak, Ms. Anjali N., Dr. Vijayakumar, Ms. Lakshmi, Ms. Anjali, Mr. Sidhu*
- *Dr. Sreejith M., Dr. Rinu Elizabeth, Dr. Sajena K. S., Dr. Anjali B. R., Dr. Shibna Balakrishnan, Dr. Nishna N., Ms. Pavithra, Ms. Swathi, Mr. Arjun, Ms. Aswathi, Mr. Hrishi, Ms. Darshana, Ms. Brija, and former group members*
- *M.Sc. Project students: Mr. Adersh, Ms. Rojis, Ms. Anna, Ms. Meenu, and Ms. Niranjana*
- *Rani, Kavya, Navin, Riya, Mekha, Nayan, Lechu, Mani, Akshay, Aneesha, Ashita, Aswathi, Shanif, Sandesh, Dr. Anjali, Dr. Vibhu, Dr. Indu, Dr. Susanna, Dr. Sheba, Dr. Neethi, and all other present and former members of CSTD & friends at CSIR-NIIST*
- *Dr. Sumalakshmy and all my teachers for leading the way, and their encouragement at different stages of my academic career*
- *DST INSPIRE for fellowship*

I am profoundly grateful to Dr. Sandip Chakraborty for his unwavering support, guidance, and encouragement throughout this journey. His mentorship has been invaluable in shaping this thesis and in enriching my research experience.

I am deeply grateful to Appa, Amma, Unny, Joel, and his family for their unwavering love, care, and blessings. Their constant support has been a pillar of strength for me.

Thanks to the almighty.

Anagha Thomas

TABLE OF CONTENTS

LIST OF ABBREVIATIONS

A549 cells	Adenocarcinomic human alveolar basal epithelial cells
ACN	Acetonitrile
ACQ	Aggregation Caused Quenching
AD	Alzheimers
Ad	Adenosine
ADP	Adenosine diphosphate
AIE	Aggregation Induced Emission
Al	Aluminium
AMP	Adenosine monophosphate
Ar	Argon
ATP	Adenosine triphosphate
B&C	Brightness and contrast
Bodipy	Boron-dipyrromethane
bpy	2,2'-bipyridine
BSA	Bovine serum albumin
C	Carbon
cP	Centipoise
$CDCl_3$	Deuterated chloroform
CH_2Cl_2	Dichloromethane
CH_3CN	Acetonitrile
$CHCl_3$	Chloroform
CLSM	Confocal laser scanning microscopy
cm	Centimeter
CO_2	Carbon dioxide
ctDNA	Calf thymus deoxyribo nucleic acid
Cyt c	Cytochrome C
D-A-D	Donor-acceptor-donor
DAPI	4′,6-diamidino-2-phenylindole
DCM	Dichloromethane
DMEM	Dulbecco's Modified Eagle Medium
DMF	Dichloromethane
DMSO	Dimethyl sulfoxide

DNA	Deoxyribo nucleic acid
DPA	Dipicolylamine
dsDNA	Double-stranded deoxyribo nucleic acid
EB	Ethidium bromide
eq.	Equivalent
ET	Energy Transfer
EtOH	Ethanol
et al.	Et alia
EtOAc	Ethyl acetate
FRET	Förster Resonance Energy Transfer
FLIM	Fluorescence Lifetime Imaging
g	Gram
GFP	Green fluorescent protein
h	Hour
HeLa	Human cervical cancer cell line
HEPES	4-(2-hydroxyethyl)-1-piperazineethanesulfonic acid
H_2O	Water
HOMO	Highest occupied molecular orbital
HRMS	High resolution mass spectrometry
Hz	Hertz
IC	Internal Conversion
ICT	Intramolecular charge transfer
IR	Infrared
ISC	Inter System Crossing (ISC)
K_d	Dissociation constant
knr	Non radiative rate
kr	Radiative rate
LPS	Lipopolysaccharide
LUMO	Lowest Unoccupied Molecular Orbital
M	Molar
m	meter
MCF-7	Breast cancer cell line
MDA-MB-231	Breast cancer cell line
MeOH	Methanol

Mito	Mitochondria
min	Minute
mL	Millilitre
mM	Millimolar
MO	Molecular Orbitals
mol	Mole
MR	Merocyanine
MTT	3-(4, 5-dimethylthiazol-2-yl)-2,5diphenyltetrazolium bromide
N	Nitrogen
NaCl	Sodium chloride
Na_2CO_3	Sodium Carbonate
NIR	Near-Infra Red
NMR	Nuclear Magnetic Resonance
nm	Nanometer
ns	Nanosecond
NTR	Nitroreductase
O	Oxygen
PBS	Phosphate-Buffered Saline
PCC	Pearson's Correlation Coefficient
PD	Parkinsons disease
PET	Photo-induced Electron Transfer
RNS	Reactive nitrogen species
ROS	Reactive oxygen species
RA	Retinoic acid
rt	Room temperature
s	Second
S_0	Singlet ground state
S_1	Singlet excited state
SIM	Structured illumination microscopy
SOC	Spin-Orbit Coupling
SOQY	Singlet Oxygen Quantum Yield
SP	Spiropyran
ssDNA	Single-stranded deoxyribo nucleic acid
TBET	Through-bond energy transfer

TCSPC	Time-correlated single photon counting
TICT	Twisted intramolecular charge transfer
TPEN	(*N,N,N′,N′*-tetrakis(2-pyridinylmethyl)-1,2-ethanediamine
UV	Ultra Violet
UV-Vis	Ultra Violet-visible
Xe	Xenon
ε	Molar extinction coefficient
λ	Wavelength
λ_{em}	Wavelength of emission
λ_{ex}	Wavelength of excitation
$\Delta\lambda$	Change in wavelength
μL	Microliter
μM	Micromolar
τ	Excited state lifetime
Φ	Quantum yield
%	Percentage
°C	Degree Celsius

PREFACE

The cellular microenvironment maintains a complex and delicate balance within living systems, regulating various physiological processes and sustaining healthy development. Since disruption in this cellular homeostasis can lead to various diseases, real-time monitoring of biological species and microenvironments during physiological and pathological processes is essential for effective disease diagnosis and management. Small molecular fluorescent probes are powerful tools for real-time imaging of biological samples due to their easy synthesis, low cost, high spatial and temporal resolution, and ability to track the process with least disruption to normal cellular function. In the past few decades, there have been considerable efforts in developing fluorescent dyes and introducing diverse functional group modifications for specific sensing and imaging applications. Among the major core architectures used in fluorescence-based bioimaging, pyrylium and pyridinium derivatives are highly promising yet remain largely unexplored. Their facile synthesis, large Stokes shift, excellent chemical and photostability, good aqueous solubility, and low cytotoxicity make them highly advantageous for sensing and bioimaging applications. In this thesis, we have chosen pyrylium and pyridinium as the central fluorescent cores and modified the scaffold for different bioimaging applications such as metal ion sensing, viscosity monitoring, and understanding heat stroke mechanisms.

The thesis is organised into four chapters, of which Chapter 1 provides an overview and literature review of small molecular fluorescent probes, highlighting the design principles and underlying mechanisms for sensing various analytes. The use of pyrylium and pyridinium chromophores as fluorescent cores for bioimaging applications is discussed in detail. In Chapter 2A, we have developed a new, pentacyclic pyridinium-based probe, **PYD-PA**, having a pendant *N*,*N*-di(pyridin-2-ylmethyl)amine (DPA) for Zn^{2+} detection in the cellular environment. The pyridinium moiety, with its positive charge, also serves as an inherent mitochondria-targeting unit, while the DPA acts as the coordination site for Zn^{2+}. **PYD-PA** displayed a three-fold enhancement in fluorescence intensity upon Zn^{2+} binding with a 1:1 binding stoichiometry. Further, the probe showed selective response to Zn^{2+} over other biologically relevant metal ions with moderate binding affinity ($K_a = 6.29 \times 10^4\ M^{-1}$), good photostability, aqueous solubility, pH insensitivity and low cytotoxicity. Since high affinity Zn^{2+} imaging probes tend to saturate at lower concentrations, probes with modest affinity can be a useful tool for tracking the elevated Zn^{2+} levels (in the micromolar range), especially

during cellular processes like autophagy. The demonstration of bioimaging in SK-BR-3 breast cancer cell lines confirmed intracellular zinc ion sensing ability of the probe. The probe was successfully applied for real time monitoring of the fluctuation of intracellular free zinc ions during autophagy conditions, demonstrating its potential for cellular imaging of Zn^{2+}, at higher intracellular concentrations.

In **Chapter 2B**, we explored the differential binding properties of Zn^{2+} bound complex of PYD-PA, **PYD-PA-Zn^{2+}** towards nucleotides and DNA. In presence of adenosine and AMP, the probe showed negligible change in absorption and emission spectra indicating its poor binding affinity. On the other hand, the probe displayed significant enhancement in fluorescence intensity in presence of ADP and ATP, while the absorption spectra remained intact, suggesting phosphate assisted interactions between the probe and nucleotides. In the presence of ctDNA, the probe exhibited a hypochromic effect with a red shift in absorption maxima, and fluorescence enhancement with a blue shift in emission maxima, indicating selective binding affinity towards DNA. Extensive photophysical studies, including circular dichroism (CD) spectroscopy, thermal denaturation, and fluorescence lifetime measurements, revealed a phosphate assisted intercalative binding interaction. Notably, the probe displayed a significant enhancement in fluorescence lifetime upon interaction with ctDNA and double stranded DNA (dsDNA), compared to single stranded DNA (ssDNA). Thus a combination of fluorescence and fluorescence lifetime measurements can be utilized for the differential analysis of dsDNA, ssDNA, ADP, and ATP.

In **Chapter 3**, we synthesised three new active methylene appended rigid pentacyclic pyrylium derivatives, achieving a broad spectral range by varying the substitution at tetralone: **AM-PYR** (R= H, emitting blue), **AM-MPYR** (R= OCH_3, emitting green) and **AM-APYR** (R= NH_2, emitting red) and explored their photophysical properties. Since biocompatible molecules with a molecular rotor structure are effective for sensing viscosity, **AM-MPYR** was utilized to synthesize a series of new styryl-pyrylium derivatives, which can serve as fluorescence probes for monitoring the cellular microenvironment. Among these derivatives, styryl-pyrylium with hydroxyl functionality, **OH-MPYR** displayed a significant enhancement in fluorescence with increase in viscosity indicating the potential of this probe for monitoring intracellular viscosity. The probe exhibited highly selective response to viscosity changes, good water solubility, photostability, pH insensitivity, and low cytotoxicity. The demonstration of bioimaging in HeLa cell lines confirmed lysosome targeting ability of the probe. Furthermore, the

enhancement in fluorescence intensity of the probe in HeLa cells upon treatment with nystatin confirmed its ability to monitor the fluctuation of intracellular viscosity in real-time.

In **Chapter 4**, we developed a spiropyran-pyridinium conjugate, **SPI-PYD**, for the dual sensing of heat shock signalling molecules, HOCl and SO_2, in the cellular microenvironment. The pyridinium core with thiomethyl group act as recognition site for HOCl, while the UV activated open form of spiropyran acts as the recognition site for SO_2. Initially, the probe exhibited very weak fluorescence in both the green and red channels. However, in the presence of HOCl, the fluorescence intensity in the green channel increased due to the oxidation of the thiomethyl group by the analyte. Upon UV irradiation, spiropyran part of the probe undergo ring opening to form merocyanine, which absorbs in the range of 550 nm, aligning with the emission of the pyridinium component. This results in Förster Resonance Energy Transfer (FRET), leading to an increase in fluorescence intensity in the red channel and a corresponding decrease in fluorescence intensity in the green channel. Further, the presence of SO_2 resulted in decrease in fluorescence intensity in the red channel and a corresponding increase in fluorescence intensity in the green channel due to the disruption of double bond of merocyanin. The probe exhibited excellent mitochondria targeting ability, good aqueous solubility, and low cytotoxicity. The demonstration of bioimaging in SK-BR-3 breast cancer cell lines confirmed the intracellular ratiometric sensing ability of the probe towards HOCl and SO_2 ions. Due to oxidative and anti-oxidative properties of HOCl and SO_2 respectively, both are associated with the oxidative stress generated during heat stroke. Thus, we expect that the dynamic sensing of these two ions can provide deeper insights into the heat stroke process.

Small Molecular Fluorescent Probes for Monitoring Cellular Microenvironments: An Overview

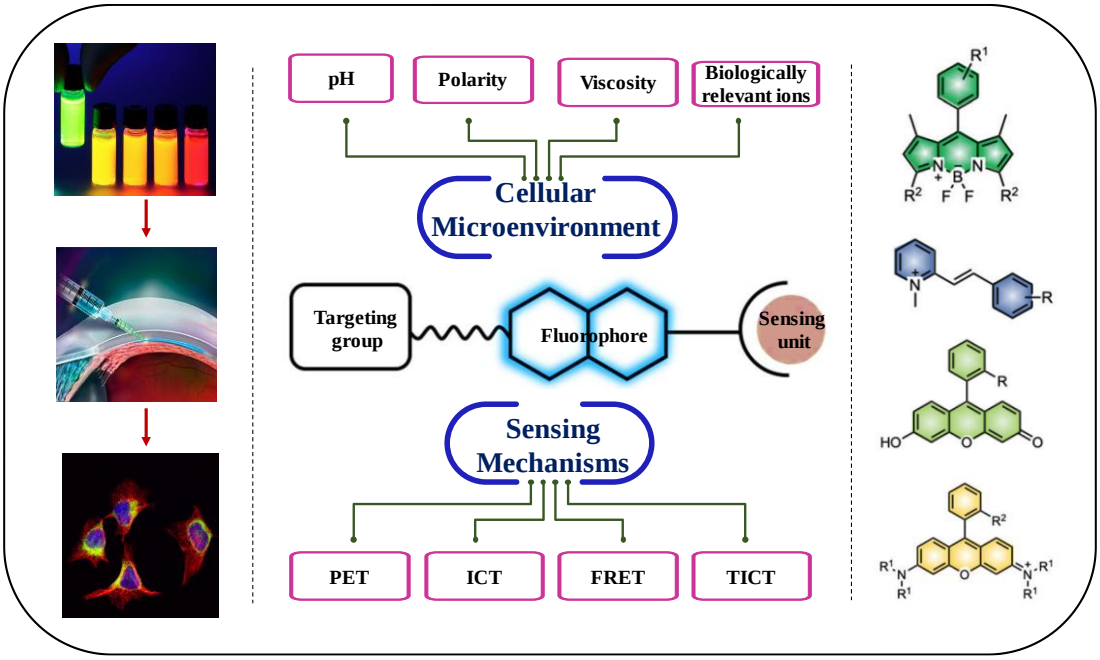

1.1. Abstract

The cellular microenvironment maintains a complex and delicate balance within living systems, regulating various physiological processes and sustaining healthy development. Disruptions to the cellular homeostasis are often associated with the onset and progression of various diseases. Therefore, real-time monitoring of biological species and microenvironments during physiological and pathological states is crucial for accurate disease diagnosis and effective management. Small molecular fluorescent probes have emerged as powerful tools for real-time monitoring of biological systems, owing to their facile synthesis, cost-effectiveness, high spatial and temporal resolution, and minimal interference with normal cellular functions. Over the past few decades, significant efforts have been directed towards the development of

fluorescent dyes having diverse functional groups to enhance specificity and sensitivity in sensing and imaging applications. Among the various core architectures used in fluorescence-based bioimaging, pyrylium and pyridinium derivatives stand out as highly promising, yet remain relatively underexplored. These chromophores offer several advantages, including ease of synthesis, large Stokes shifts, good aqueous solubility, and excellent chemical and photostability, making them particularly attractive for sensing and imaging applications. This introductory chapter provides an overview of recent advancements in small molecular fluorescent probes, with a focus on design strategies, sensing mechanisms, and the emerging role of pyrylium- and pyridinium-based chromophores in bioimaging and biosensing applications. In this thesis, we further explore the potential of the rigid pentacyclic chromophores in diverse applications such as metal ion sensing, viscosity mapping, and probing the molecular mechanisms underlying heat stroke.

1.2. Introduction

Cells are the fundamental building blocks of life, playing crucial roles in processes such as metabolism, growth, reproduction, and response to various stimuli.[1] Their complexity and functionality amaze the scientific community to inquire more into the secrets of life. Organelles require a well-regulated cellular microenvironment to maintain normal physiological functions. Abnormal microenvironments are often associated with organelle dysfunction and disease development. For example, cancer cells can be differentiated from normal cells by their low pH and increased viscosity.[2] Therefore, visualizing the microenvironmental parameters such as pH, polarity, viscosity, and concentration of biologically relevant species is extremely useful in understanding the underlying mechanisms of related diseases.

Early progress in understanding cellular chemistry has been achieved through the utilization of techniques such as high-performance liquid chromatography (HPLC)[3], mass spectrometry[4], and radioactive labeling.[5] Despite their efficacy, these methodologies are often

constrained by their time-consuming nature and inability to facilitate *in situ* monitoring of dynamic processes within living systems. Currently, fluorescence imaging has become a powerful tool for visualizing the cellular microenvironment, providing deeper insights into cellular and signalling events.[6] As a result, fluorescent probes are widely recognized as effective tools in biological applications such as cell imaging, cancer diagnosis and therapy, biosensors, drug discovery etc. They offer rapid response, specificity, real-time capability, and high reactivity in both *in vitro* and *in vivo* applications.[7] As research progresses, the development of new fluorescent probes continues to improve our ability to understand complex biological processes with greater precision and detail.

The discovery of fluorescence and its historical developments are described in early literatures.[8-10] Subsequently, fluorescence analysis underwent rapid advancements, leading to numerous breakthroughs in instrumentation with a broad spectrum of applications across various scientific domains. Owing to the advantages of non-invasive nature, exceptional sensitivity, precise spatial and temporal resolution, and suitability for *in situ* detection, fluorescence has become a state-of-the-art method in biological sciences.[11] Recent advancements in fluorescence microscopy and photonic technologies have facilitated the emergence of super-resolution imaging modalities, enabling precise visualization of subcellular structures and dynamic biological processes.

1.3. Fluorescence: An integral biosensing modality

Fluorescence is widely recognized as a leading technique in biosensing and bioimaging, enabling direct *in situ* analysis of biological samples, providing detailed biomolecular information with high spatial and temporal resolution. Since biological objects exhibit weak intrinsic fluorescence, the current fluorescence techniques rely strongly on fluorescent dyes which improve signal detection and visualization. Small molecular fluorescent probes are widely used for staining cells, monitoring specific bioanalytes, and tracking biomolecules of

interest. These synthetic fluorophores are often modified as fluorescent tags that can be attached to target molecules through chemical methods such as click chemistry or biological approaches such as self-labelling protein tags. The target molecules vary in size, ranging from small inorganic bioanalytes like calcium, iron, zinc and copper to intermediate-sized metabolites and lipids, and even larger macromolecules such as proteins, DNA, and RNA. In addition to their use in biological imaging, fluorescent probes have diverse applications, such as high-throughput screening, genome sequencing, activity-based protein profiling, cancer therapies etc.

1.4. Fluorescence imaging

When molecules in their ground state (S_0) absorb light energy, they become excited to a higher energy state (S_1*). Part of this energy can be dissipated through non-radiative pathways, bringing the molecule to a lower electronic state (S_1). The molecule then returns to its ground state (S_0), releasing a photon with lower energy. If this energy is emitted through a radiative pathway, the process is known as fluorescence, typically occurring within a few nanoseconds **(Figure 1.1A)**.

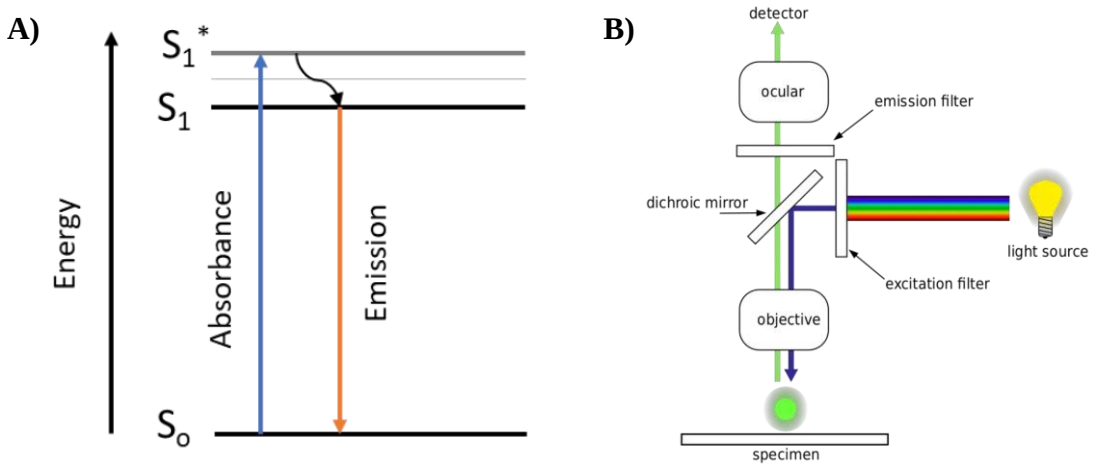

Figure 1.1. (A) Simplified Jablonski diagram representing absorption and emission; (B) Schematic representation of fluorescence microscope.

A fluorescence microscope is an essential tool for reliable bioimaging. The first step in visualizing a sample with a fluorescence microscope is to label it with fluorescent dyes. A

white light source is then directed onto an excitation filter, which isolates light of a specific wavelength capable of exciting the fluorescent molecules within the sample. This excitation light is reflected by a dichroic mirror and directed through the objective lens, ultimately illuminating the specimen. The sample absorbs the excitation light and emits fluorescent light, which passes through the emission filter and is guided to the detector by the objective lens **(Figure 1.1B)**. In an epifluorescence microscope, both the excitation of fluorophores and the detection of emitted fluorescence occur along the same optical pathway, passing through the objective lens. Traditional fluorescence microscopes illuminate the whole specimen, leading to a blurred background that reduces image resolution. This problem is effectively addressed by confocal laser scanning microscopy, which uses point-by-point illumination and a pinhole placed in an optically conjugate plane before the detector to remove out-of-focus light **(Figure 1.2)**. Additionally, it allows for the selection of specific excitation wavelengths and flexible collection wavelengths.

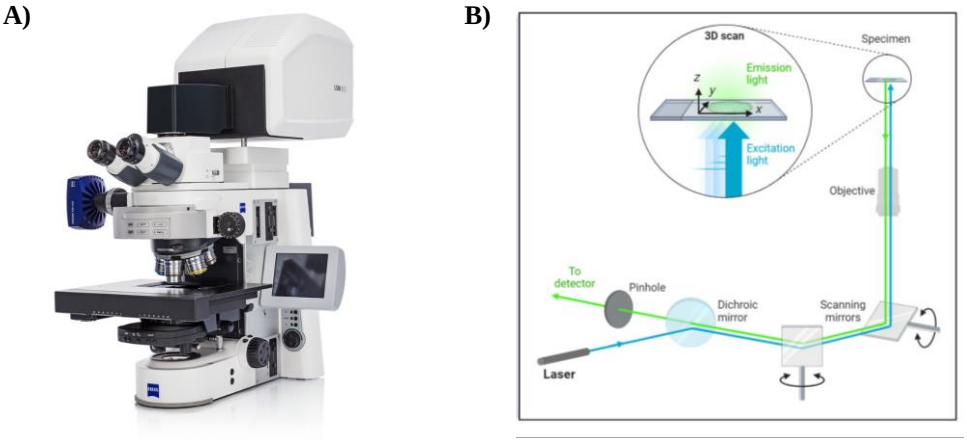

Figure 1.2. (A) Photograph and (B) schematic representation of confocal laser scanning microscope (Figure adapted from https://5.imimg.com and https://microbenotes.com).

1.5. Brief history of fluorescent probes

The first distinct small molecule fluorescent compound was quinine sulphate, an antimalarial drug discovered by Fredrick Herschel in 1845.[12] Later, in 1852, British scientist Sir George Stokes attributed this emission phenomenon as the absorption and subsequent re-

emission of light by quinine and coined the term 'fluorescence'.[13] However, fluorescent compounds gained significant attention only after the development of fluorimeter and fluorescence microscopy in the 1950's. Since that time, fluorophores have been widely used in bioanalytical methods for staining tissues and bacteria, leading to numerous discoveries of other organic dyes. During the early 1990's, Roger Tsien and his colleagues developed a range of fluorescent probes by modifying green fluorescent protein (GFP), resulting in a spectrum of colours and improved photophysical characteristics when compared to the original GFP.[14] In 2008, Tsien along with Osamu Shimomura and Martin Chalfie, were honored with the Nobel Prize in Chemistry for their groundbreaking work on GFP.[15] In 2014, the Nobel Prize in Chemistry was bestowed upon William E. Moerner, Eric Betzig, and Stefan Hell for their pioneering work in super-resolution fluorescence microscopy, a technique that allows imaging beyond the diffraction limits of traditional light microscopy.[16-19] Currently, synthetic fluorogenic probes are prevalent in most cellular biological experiments, highlighting their significance as diagnostic tools in clinical applications.

1.6. Sensing mechanisms of fluorescent probes

An optimal fluorescence sensing system delivers a consistent output response under experimental conditions in direct correlation with the analyte concentration. Interaction between the analyte and the receptor results in detectable changes in the fluorescence signal, either as enhancement, quenching, or a shift in fluorescence peaks. When coupled with imaging methods like confocal laser scanning microscopy (CLSM) and *in vivo* imaging systems, its capabilities extend to visualizing analytes in live cells, tissues, and entire organisms. Fluorescent molecular probes display changes in fluorescence intensity or emission wavelength through various sensing mechanisms which include intramolecular charge transfer (ICT), photoinduced electron transfer (PET), Forster resonance energy transfer (FRET), aggregation-induced emission (AIE), through-bond energy transfer (TBET), or combinations of dual/triple sensing mechanisms (DSM or TSM). [20]

Typically, ICT-based fluorescent probes are advantageous for their biocompatibility, stability, tunable spectra, and ease of processing.[21] TICT fluorescent probes typically display low fluorescence efficiency in solution, however exhibit significantly enhanced emission in certain environments. This sensitivity makes them highly effective for monitoring micro-environmental changes and molecular conformational dynamics.[22] PET fluorescent probes can exhibit fluorescence on or off states through interactions between a fluorophore and an electron acceptor, making them effective in quantitative and positional analysis of biomolecules.[23] AIE fluorescent probes show strong fluorescence in high concentrations or aggregated states, beneficial for biological imaging and biosensing due to their high sensitivity and low background signal.[24] Lastly, TBET fluorescent probes regulate fluorescence via through-bond energy transfer, useful for detecting molecular interactions and environmental changes within cells.[25] Since conventional sensing mechanisms, including intramolecular charge transfer (ICT), photoinduced electron transfer (PET), and fluorescence resonance energy transfer (FRET), are extensively used in the strategic design of fluorescent probes, we will discuss these mechanisms in detail.

1.6.1. Intramolecular charge transfer (ICT)

ICT-based fluorescent probes consist of three components, an electron donor (D), an electron acceptor (A) and π-conjugated linker. Upon interaction with the targeted analyte, the electron density within the recognition group undergoes modifications due to processes such as bond cleavage, substitution, or substrate coordination. These processes result in alterations in the energy gap between the HOMO and LUMO orbitals of the fluorophore leading to shift in fluorescence wavelength. A red shift occurs when the fluorophore's electron-withdrawing capability increases upon analyte binding, leading to higher electron cloud density and a reduced energy gap between the HOMO and LUMO orbitals, resulting in emission at a longer wavelength. Conversely, a blue shift occurs when the fluorophore's electron-donating capability increases upon analyte binding, leading to a shorter wavelength **(Figure 1.3)**.

Generally, presence of an analyte causes a reduction in the original fluorescence intensity and subsequent enhancement in a new fluorescence intensity. Thus, the ICT mechanism can be exploited to design ratiometric fluorescent probes for the selective detection of various analytes of interests.

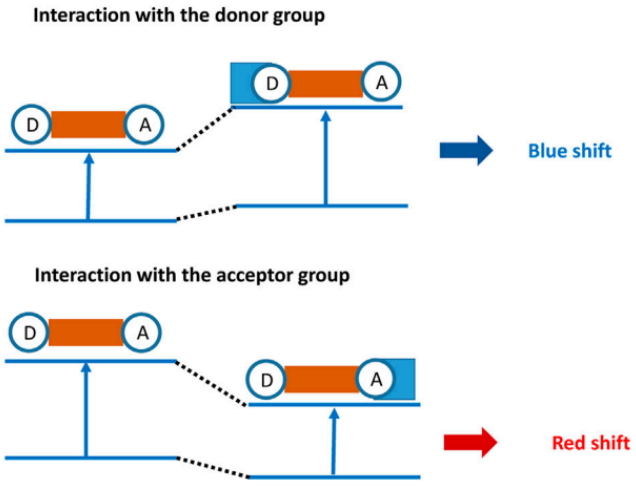

Figure 1.3. Principle of recognition for ICT-based fluorescent probes.

The use of ICT probes is prevalent in the detection of enzyme activity, particularly when conjugated with the benefits of near-infrared (NIR) fluorescence. Zhu and co-workers have developed an *in vivo* near-infrared probe to specifically target the enzyme β-galactosidase (**DCM-β-gal**), which serves as a biomarker for cell senescence and primary ovarian cancers **(Figure 1.4)**.[26] The probe, **DCM-βgal** displayed a broad absorption band at 440 nm from its intrinsic intramolecular charge transfer (ICT). In the presence of β-galactosidase (β-gal), the absorption peak of **DCM-βgal** at 440 nm decreases, accompanied by the emergence of a new peak around 535 nm, with a well-defined isosbestic point at 450 nm. This shift is attributed to the hydrolysis of **DCM-βgal** via C–O bond cleavage, releasing the electron-rich aglycone DCM-O^-, which emits in the NIR region and displays a distinct ratiometric fluorescent signal with a significant spectral shift. The emission spectrum intensity at 685 nm demonstrated a linear increase corresponding to the concentration of β-gal with a limit of detection (LOD) of 1.7×10^{-4} U mL^{-1}. Notably, the probe was effectively used for *in situ* and *in vivo* imaging of

β-gal activity in a mouse model of human colorectal tumors. It also enabled real-time visualization of intracellular endogenous β-gal distribution in living 293T cells with overexpression achieved through lacZ gene transfection. This research successfully captured β-gal activity in real-time within tumor sites for the first time, utilizing high-resolution 3D imaging. The NIR fluorescent probe offers a simple, sensitive, and biocompatible tool for detecting β-gal activity, advancing colorectal cancer diagnosis.

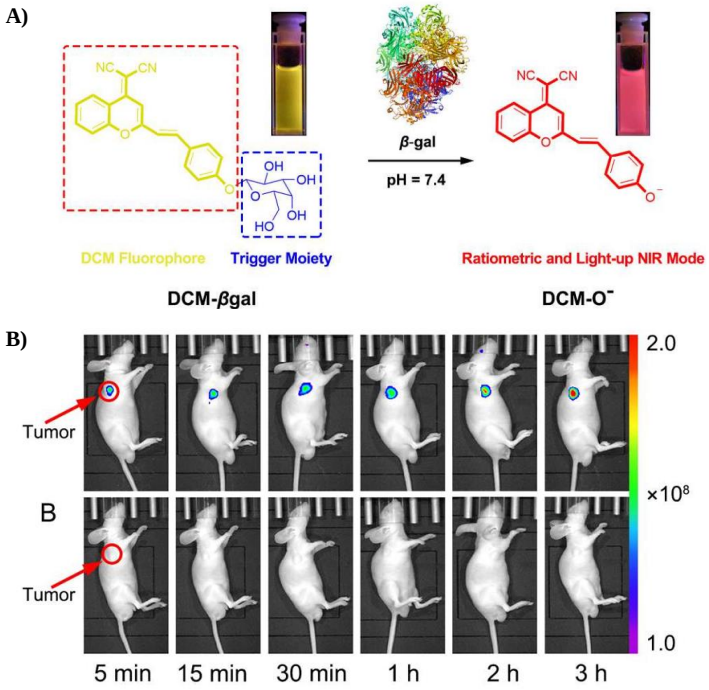

Figure 1.4. (A) Detection mechanism of β-galactosidase enzyme **by DCM-βGal.**; (B**)** *In vivo* visualization of β-galactosidase activity in nude mice with tumors (Figure adapted from reference 26).

The ratiometric fluorescent pH probe, 4-((1E,3E)-4-(benzo[d]thiazol-2-yl)buta-1,3-dienyl)-*N*,*N*-dimethylbenzenamine (**BTDB**), is reported to exhibit a large Stokes shift based on the ICT mechanism **(Figure 1.5)**.[27] **BTDB** consist of a cinnamaldehyde unit as electron donor and benzothiazole moiety as electron acceptor, connected through an ethylene bridge. The probe displayed a ratiometric response (F_{425nm}/F_{595nm}) to pH, effectively detecting pH changes in the range of 2.3 - 4.0, with a pKa of 2.34. This observation can be attributed to protonation, which notably reduced the electron acceptor capacity of the benzothiazole group, subsequently

affecting its interaction with the electron-donating cinnamaldehyde group in the D-A system. Furthermore, **BTDB** has been successfully applied in Hela cells and E. coli cells, demonstrating its use as a ratiometric fluorescent pH probe for visualizing pH variations within the physiological range with exceptional lysosomal localization capability.

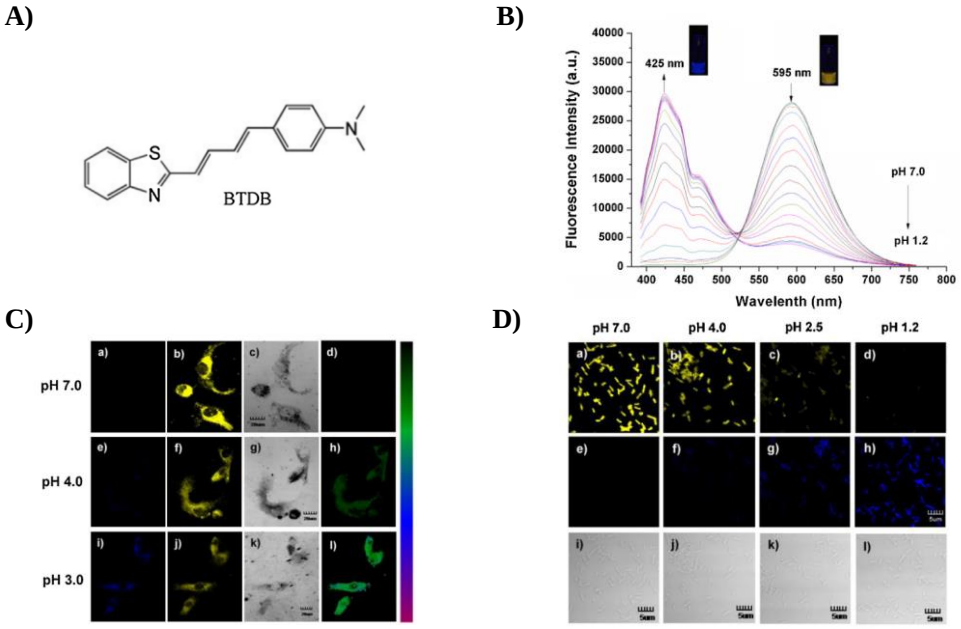

Figure 1.5. (A) Structure of the probe, **BTDB**; (B) Emission spectra of **BTDB** at varying pH (1.2-7); Fluorescence images of (C) HeLa and (D) E. coli cells incubated with **BTDB** (10 μM) at different pH (Figure adapted from reference 27).

In 2019, Tang et al. have developed a novel two-photon fluorescent probe, **TCE**, for the imaging of hydroxyl radical (•OH) with high specificity and sensitivity **(Figure 1.6)**.[28] The probe contains a coumarin 151 fluorophore, chosen for its favourable two-photon absorption, large Stokes shift, and ICT characteristics. A pyrazolone group was used to recognize hydroxyl radicals (•OH), where the electron-donating effect of the anilinic nitrogen is reduced, masking the ICT system. In presence of •OH, the probe undergoes one electron oxidation to yield **TCE-OH**, in which the carbonyl group is positioned away from the coumarin ring, restoring the push-pull electron effect of the coumarin ring, leading to enhanced fluorescence. Further, the probe was successfully used for *in situ* visualization of •OH in the mouse brain, revealing a direct correlation between increased •OH levels and the severity of depression phenotypes.

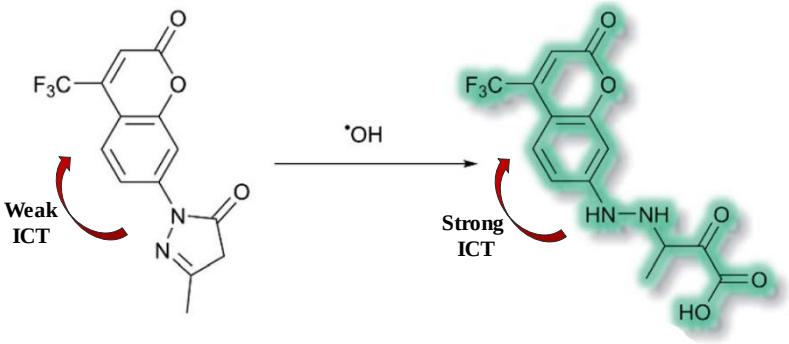

Figure 1.6. Sensing mechanism of **TCE** for •OH (Figure adapted from reference 28).

Qu and co-workers have synthesised a new "turn-on" fluorescent probe for detecting ClO^- by modifying 4′-hydroxybiphenyl-4-carbonitrile with *N*, *N*-dimethylthiocarbamate as a recognition site **(Figure 1.7)**.[29] Initially, the probe exhibited negligible fluorescence. However, upon the addition of ClO^-, the ICT process between the electron-donating hydroxyl group and the electron-withdrawing cyano group was restored, resulting in a significant increase in cyan fluorescence. The probe displayed 291-fold fluorescence enhancement with a significant Stokes shift (7519 cm^{-1}), fast response time (30 s), low limit of detection (72 nM), and wide pH operating range (6-8). Further, the probe has been effectively utilized to image exogenous ClO^- in living MCF-7 cells and endogenous ClO^- in living HeLa cells, demonstrating its specificity and efficiency for imaging applications. Additionally, the probe was successfully used to monitor fluctuations in ClO^- level in fluoxetine-induced liver injury using a mouse model.

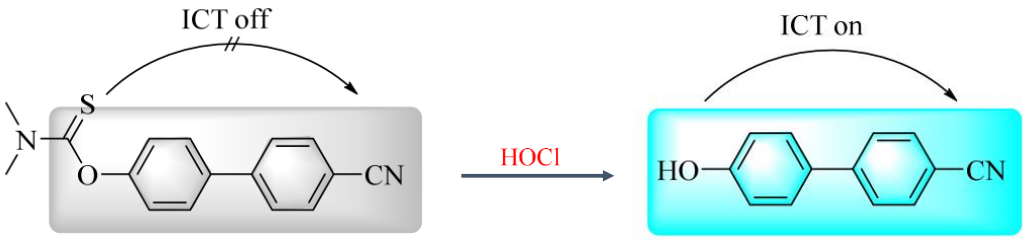

Figure 1.7. ICT-based sensing mechanism for the HClO sensor (Figure adapted from reference 29).

The limitations of ICT probes include reduced fluorescence due to aggregate-caused quenching (ACQ) and the dependence of their fluorescence properties on the solvent. However,

ICT probes are typically simple in design, enabling easy synthesis and well-defined sensing mechanisms through the formation of a donor-π-acceptor (D-π-A) system. Once a detection mechanism, such as "turn-on" fluorescence or ratiometric response, is established, the response units of ICT probes can be simply modified to detect other analytes. This flexibility makes ICT systems an effective platform for developing series of probes targeting wide range of analytes.

1.6.2. Photoinduced electron transfer (PET)

A typical PET system consists of multiple components, where a fluorophore (electron acceptor) is connected to a recognition group (electron donor) through a short spacer.[30] Here, the intramolecular electron transfer between the receptor and the fluorophore within the system are responsible for fluorescence quenching. Depending on the electron transfer direction, PET can be classified into two, a-PET and d-PET **(Figure 1.8)**.[31] In the a-PET process, electron transfer occurs from the receptor to the fluorophore because the receptor's highest occupied molecular orbital (HOMO) has a higher energy level than that of the fluorophore. Conversely, during the d-PET process, the excited fluorophore transfers electrons to the receptor's lowest unoccupied molecular orbital (LUMO), leading to fluorescence quenching. However, upon receptor-target interaction, this PET process is inhibited, allowing the probe to regain its fluorescence.

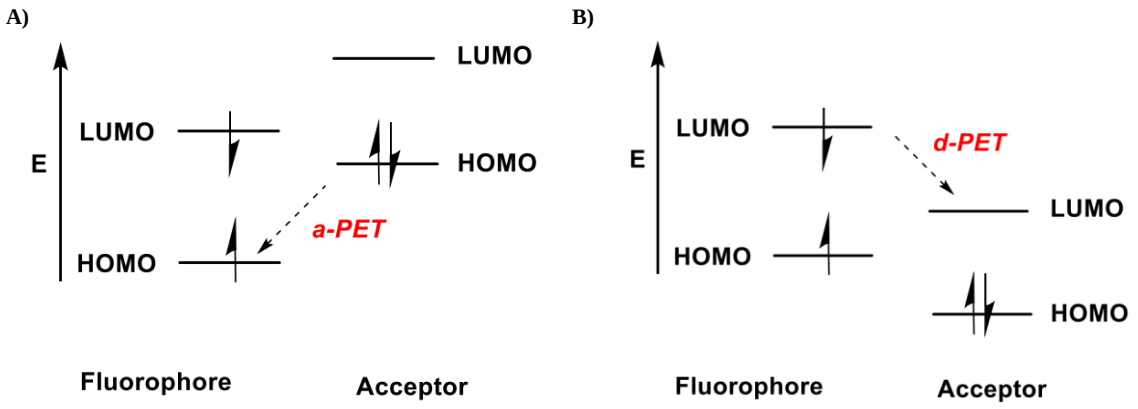

Figure 1.8. Frontier orbital energy diagrams of (A) a-PET and (B) d-PET mechanisms (Figure adapted from reference 31).

PET is a key design strategy for developing "off-on" or "on-off" fluorescent probes.[32-34] In this process, the recognition group interacts with the target analyte, resulting in either the inhibition of PET, which turns on the fluorescence ("off-on") or the initiation of PET, which turns off the fluorescence ("on-off"). The PET process is highly dependent on the chemical characteristics of the analyte of interest, as it influences the HOMO-LUMO energy levels of the recognition group. PET occurs due to electron transfer between the fluorophore and the recognition group, and the ability to gain or lose electrons is indicated by the oxidation/reduction potential. Therefore, PET-based fluorescent probes can be classified into four types based on the variations in the oxidation/reduction potential of the recognition unit during the detection process **(Figure 1.9)**.[23]

- Type 1: Upon binding to the target, the recognition group's oxidation potential increases, preventing the a-PET process. [35]
- Type 2: Upon binding to the target, the recognition group's oxidation potential decreases, preventing the d-PET process.[36]
- Type 3: The recognition group can be cleaved and a-PET is prohibited[37]
- Type 4: The recognition group can be cleaved and d-PET is prohibited[38]

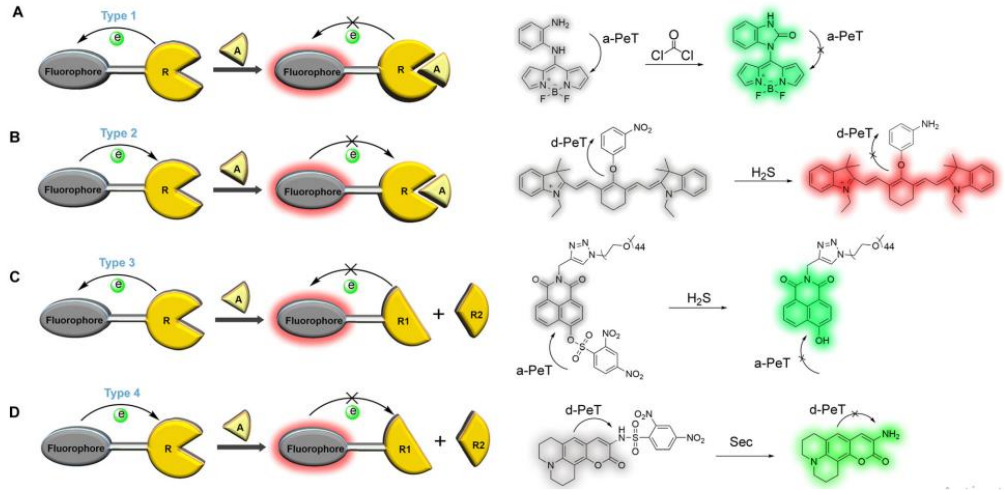

Figure 1.9. The four design types of PET based fluorescent probes; R: Recognition group, A: Analyte (Figure adapted from reference 23).

Typical PET probes are extensively used to detect metal ions, pH levels, and reactive small molecules, utilizing single atoms (O, S, N, Se, Te, etc.) as electron donors.[39-41] In 2005, Gao and co-workers developed a PET-based fluorescence sensor (**BDA**) for Zn^{2+} that utilizes

1,3,5,7-tetramethyl-boron dipyrromethene as the fluorophore and di(2-picolyl)amine as the coordination site for Zn^{2+}**(Figure 1.10A).**[40] Initially, the probe showed negligible fluorescence due to the quenching effect by photoinduced electron transfer (PET). However, upon the addition of Zn^{2+}, the quenching is interrupted by the binding of Zn^{2+} with the DPA moiety, leading to an increase in fluorescence intensity. This sensor functions effectively in aqueous solutions with lower pKa values, addressing the common issue of proton interference seen in PET-based probes **(Figure 1.10B)**. The excellent selectivity, nanomolar sensitivity, pH insensitivity, low toxicity, and cell permeability make the probe a promising candidate as a Zn^{2+} sensor for biological applications. Further, fluorescence microscopy imaging in TCA cells has demonstrated that the sensor can effectively monitor the changes in intracellular Zn^{2+} levels.

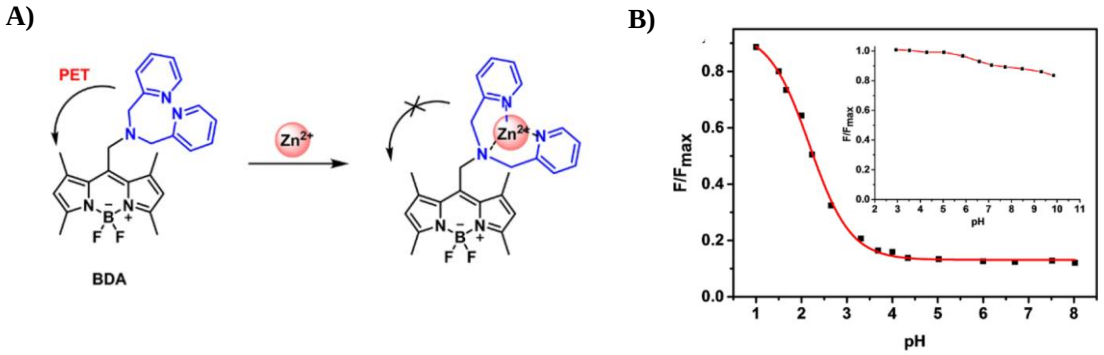

Figure 1.10. (A) Chemical structures and sensing mechanisms of **BDA** to Zn^{2+}; (B) The effect of pH on the fluorescence intensity of **BDA** (Figure adapted from reference 40).

The NIR fluorescent pH probe, **Tpy-Cy**, reported by Wang et al. exhibits high sensitivity within the pH range of 6.70-7.90 **(Figure 1.11).**[42] The probe contains tricarbocyanine (Cy), a near-infrared (NIR) fluorescent dye with large molar extinction coefficient, as the fluorophore, and 4'-(aminomethylphenyl)-2,2':6',2"-terpyridine (Tpy) as the recognition site. pH titration studies have shown that **Tpy-Cy** can accurately track small variations in physiological pH, with a pKa of approximately 7.10. The probe exhibits a rapid and linear response to slight pH changes within the range of 6.70 - 7.90, displaying a strong dependence on pH variations with good sensitivity, high photostability, and excellent cell

membrane permeability. Further, the probe was successfully used for *in situ* visualization of cellular pH in living HepG2 and HL-7702 cells with negligible background fluorescence.

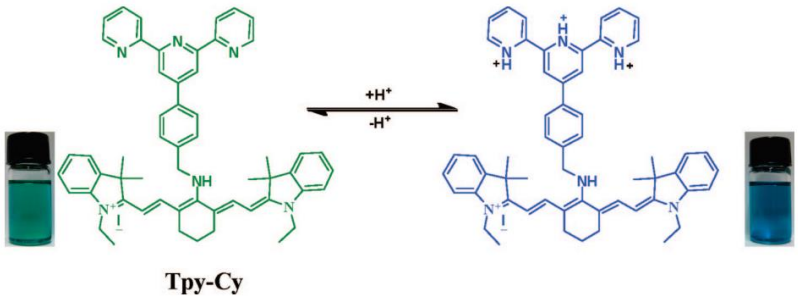

Figure 1.11. Chemical structures and sensing mechanisms of **Tpy-Cy** (Figure adapted from reference 42).

Kumar and co-workers have developed a lysosome targetable naphthalimide based fluorescent probe, **LyNC** which detects hydrogen peroxide (H_2O_2) utilizing PET mechanism **(Figure 1.12)**.[43] The probe contains 1,8-naphthalimide as the central fluorophore, catechol as the reactive site for H_2O_2, and a morpholine unit to target lysosomes. When excited at 450 nm in water at pH 7.4, the probe exhibited a very weak fluorescence emission attributed to the a-PET process from the catechol to the naphthalimide. However, upon exposure to H_2O_2, the catechol is oxidized to *o*-quinone, which inhibits the a-PET process and enhances fluorescence emission. Further, cell imaging experiments demonstrate that **LyNC** can function as a fluorescent probe for tracking dynamic changes in H_2O_2 levels in lysosomes, brain tissues, and living nematodes.

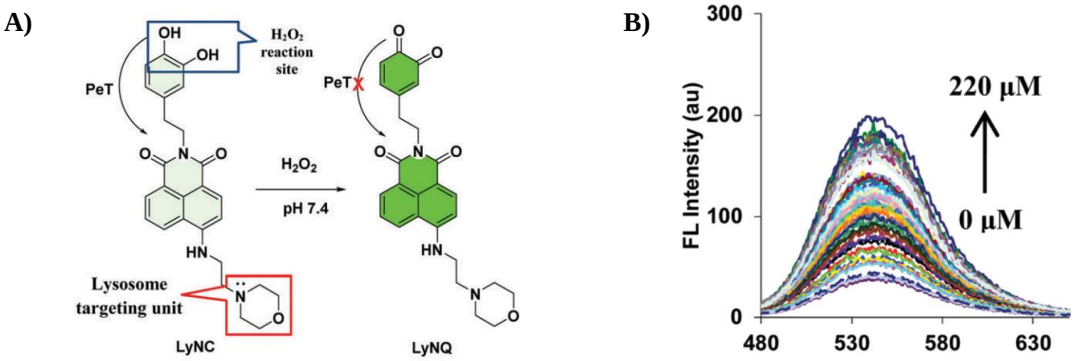

Figure 1.12. (A) Chemical structures and sensing mechanisms of **Ly-NC** and (B) Fluorescence spectra of **Ly-NC** (5.0 μM) upon increasing concentration of H_2O_2 (0-20 μM) in PBS buffer. (Figure adapted from reference 43).

A typical limitation of PET-based fluorescent probes is proton interference, where protonation of the recognition site of the analyte, suppresses the PET effect and increases the fluorescence intensity. To overcome this problem, designing PET probes with lower pKa values could be an effective approach that minimize the proton interference. Compared to sensors without fluorescence switches, PET-based probes provide superior signal-to-noise ratios, which are essential for effective fluorescence imaging in both *in vitro* and *in vivo*. Additionally, PET-based probes effectively reveal the localization, distribution, and conformational changes of target molecules, making them advantageous for cancer diagnosis and therapy.

1.6.3. Forster resonance energy transfer (FRET)

FRET is a non-radiative energy transfer process that occurs through long-range dipole-dipole interactions between a donor-acceptor pair.[44] Upon photoexcitation, the excited state energy of the donor is transferred to a dye acceptor in the ground state **(Figure 1.13)**.[45] When both the donor and acceptor are fluorophores, FRET is commonly known as "fluorescence resonance energy transfer."[46]

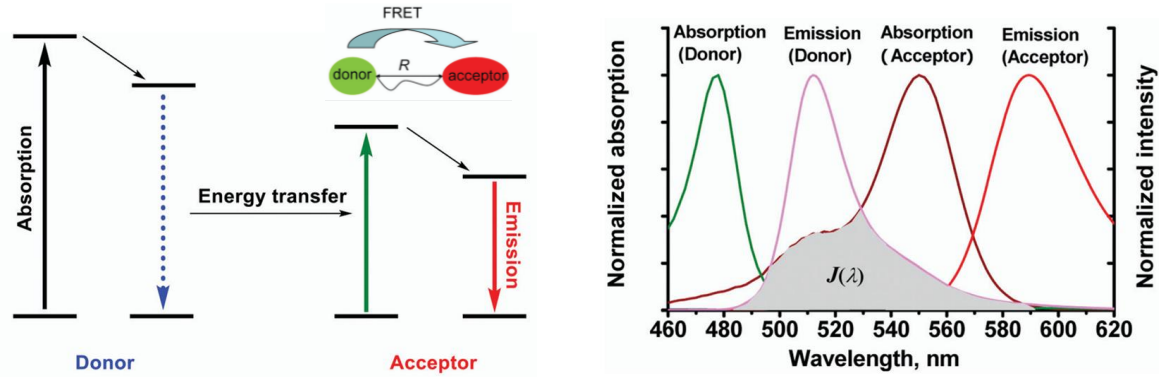

Figure 1.13. FRET mechanism, where R is the distance between donor-acceptor pair, and J(λ) is the spectral overlap between donor emission and acceptor absorption (Figure adapted from reference 45).

Designing small-molecule-based FRET ratiometric fluorescent probes requires an efficient FRET energy transfer platform, which includes an energy donor, a linker, and an energy acceptor with following prerequisites:

- The donor and acceptor should be placed in close proximity to each other (typically within 10-100 Å)
- The donor's emission spectrum must overlap with the acceptor's absorption spectrum
- The emission dipole moment of the donor, the absorption dipole moment of the acceptor, and the vector separating them must be favourably aligned with each other

Small molecular probes based on FRET are used as chemosensors and imaging agents in biological applications because of their fast cellular uptake, suitability for non-destructive imaging methods, capability for real time monitoring with minimal interference to the structure and function of key biomacromolecules, and adaptable structural properties. In 2008, Qian et al. have developed a FRET-based fluorescent probe for tracking Hg^{2+} **(Figure 1.14)**.[47] The probe was designed by covalently linking BODIPY and rhodamine as a FRET donor-acceptor pair. In the presence of Hg^{2+}, the thiosemicarbazide group in the probe undergoes cyclization to form a 1,3,4-oxadiazole, activating FRET. Initially, upon excitation at 488 nm, the probe exhibited an emission maximum at 514 nm, corresponding to the BODIPY chromophore. Upon addition of Hg^{2+}, a new absorption peak emerged at 560 nm, accompanied by a decrease in BODIPY fluorescence at 514 nm and a simultaneous increase in emission at 589 nm, indicating efficient FRET activation. The probe achieved a FRET efficiency of 99% and was successfully applied for the detection of Hg^{2+} in MCF-7 cancer cells via ratiometric fluorescence imaging.

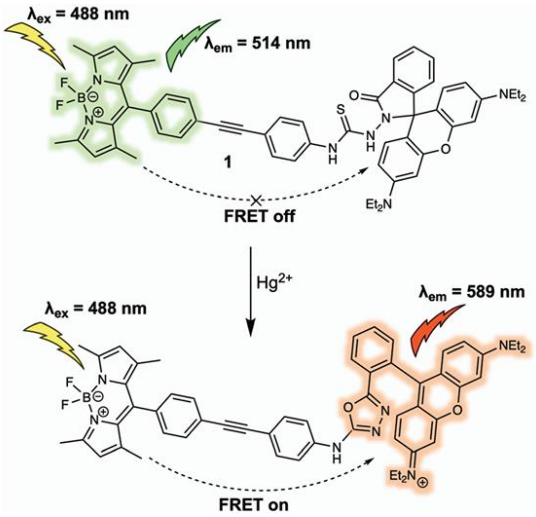

Figure 1.14. Hg^{2+} sensing mechanism of BODIPY-Rhodamine based fluorescent probe (Figure adapted from reference 47).

The FRET-based fluorescent probe, **FP-H_2O_2-NO**, reported by Lin and co-workers was effective for the simultaneous sensing of endogenous nitric oxide (NO) and hydrogen peroxide (H_2O_2) in live macrophage cells **(Figure 1.15)**.[48] The probe consists of a coumarin-rhodamine dyad functionalized with an H_2O_2 sensitive boronate moiety and an NO sensitive phenylenediamine group. In its initial state, the probe exhibits no detectable fluorescence upon excitation at either 400 nm or 550 nm. Upon exposure to NO and excitation at 550 nm, the probe exhibits strong fluorescence emission at 580 nm, while showing minimal emission under 400 nm excitation. However, sequential addition of H_2O_2 leads to a significant fluorescence signal at 580 nm upon 400 nm excitation, indicating the activation of FRET between the coumarin (donor) and rhodamine (acceptor) moieties. In contrast, exposure to H_2O_2 alone results in fluorescence at 460 nm under 400 nm excitation, with no detectable emission at 580 nm. Subsequent addition of NO under these conditions restores strong fluorescence at 580 nm upon 400 nm excitation, further confirming the FRET activation mechanism. This dual analyte sensing system functions in a logic gate like manner, responding to H_2O_2, NO, and H_2O_2/NO with distinct fluorescence signal patterns of blue-black-black, black-black-red, and black-red-red, respectively. Moreover, **FP-H_2O_2-NO** was demonstrated as a dual-responsive fluorescent probe capable of concurrently monitoring endogenous NO and H_2O_2 within live macrophage cells, enabling multicolor imaging for the first time.

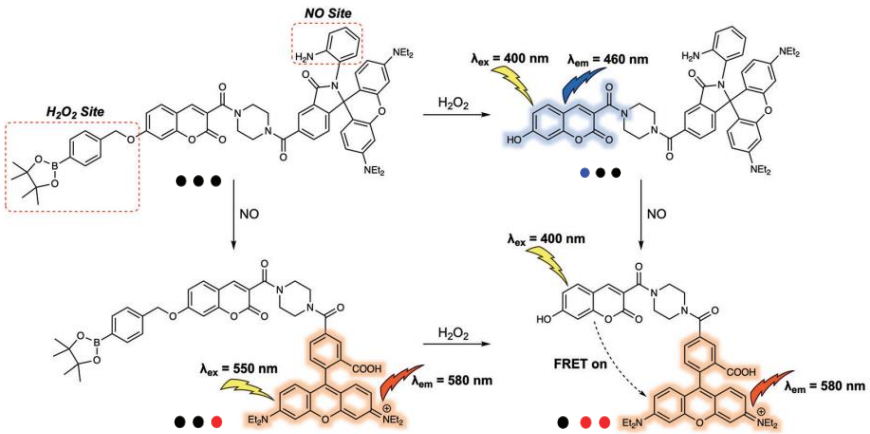

Figure 1.15. Chemical structure of the dual-responsive probe **FP-H_2O_2-NO** and its sensing mechanism for H_2O_2 and NO (Figure adapted from reference 48).

Ahn et al. have reported a FRET-based fluorescent probe for ratiometric detection of ATP within lysosomes of live cells **(Figure 1.16)**.[49] The probe consist of a rhodamine 6G derivative and BODIPY as the FRET donor-acceptor pair. Upon ATP binding, hydrogen bonding between the tetramine linker and ATP's phosphate groups induces the opening of the rhodamine lactam ring, resulting in FRET activation. Initially, the probe shows a fluorescence emission peak at 454 nm. After ATP interaction, a new emission peak appears at 557 nm. This response is pH-dependent, occurring specifically under acidic conditions, which makes the probe ideal for selective detection of lysosomal ATP in live cells. Additionally, the probe was successfully used for ratiometric fluorescence imaging of ATP levels in both live cells and the corpus callosum of a mouse brain.

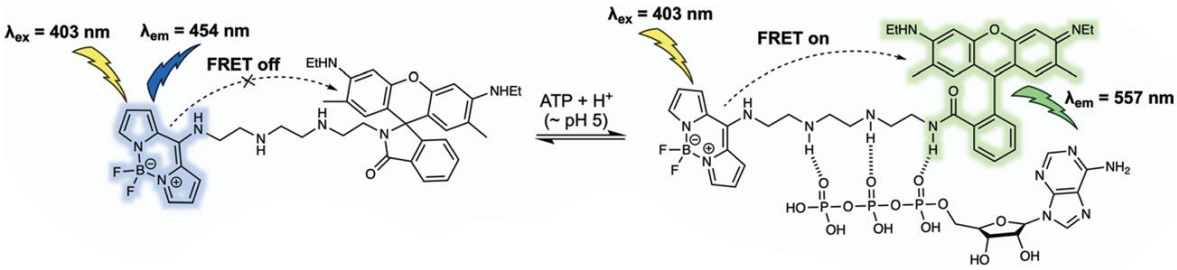

Figure 1.16. Rhodamine 6G-BODIPY based fluorescent probe for the detection of ATP (Figure adapted from reference 49).

Even though FRET imaging has the limitation of low signal-to-noise ratio, FRET-based fluorescent probes are widely utilized for real-time monitoring of cellular dynamics in living cells. These probes offer several advantages, including large Stokes shifts, ratiometric sensing, and dual/multi-analyte responsiveness. However, the effectiveness of FRET is highly influenced by the efficiency of energy transfer, which depends on the distance between donor and acceptor moieties. Therefore, adjusting the donor-acceptor distance and the spectral overlap integral are the two primary approaches for modulating energy transfer efficiency in an analyte-dependent manner. Moreover, integrating FRET with advanced fluorescence microscopy methods, like fluorescence lifetime imaging microscopy (FRET-FLIM), enables more sensitive and quantitative analysis.

1.6.4. Twisted intramolecular charge transfer (TICT)

Twisted Intramolecular Charge Transfer (TICT) probes have emerged as versatile tools in fluorescence based sensing and imaging due to their unique photophysical properties. The TICT mechanism involves the redistribution of electron density within a fluorophore upon excitation, leading to a twisted conformation that is often non-emissive. This dynamic behaviour allows TICT based probes to exhibit significant changes in fluorescence intensity, wavelength, or lifetime in response to environmental or chemical stimuli. By modulating the formation or inhibition of the TICT state through chemical reactions or physical constraints, these probes enable highly sensitive and selective detection of various analytes. Their tunable emission properties make them valuable in applications ranging from cellular imaging to real-time monitoring of biochemical processes.

In 2012, Li et al. have developed a new near-IR "turn-on" fluorescent sensor, **NDI-1** with high selectivity for Hg^{2+} ions based on twisted intramolecular charge transfer (TICT) mechanism **(Figure 1.17)**.[50] The probe consists of naphthalenedimide (NDI) as fluorophore, di-2-picolylamine (DPA) as the recognition site for Hg^{2+}, and an additional hexylamine unit as a strong electron donor for modulating the emission to the targeted NIR region. The probe exhibited negligible fluorescence in solution (the "off" state) due to the formation of a TICT state. However, upon binding of Hg^{2+} to the DPA moiety, the TICT process was suppressed, leading to a pronounced red fluorescence emission. Further demonstration of bioimaging in HeLa cells confirmed the intracellular Hg^{2+} sensing ability of the probe.

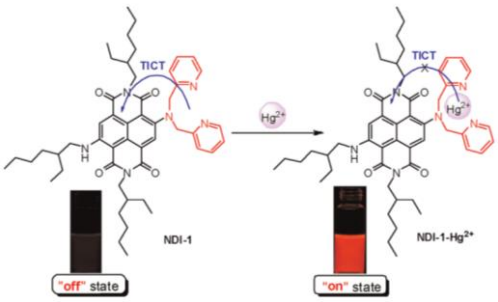

Figure 1.17. Structure of **NDI-1** and sensing mechanism for the detection of Hg^{2+} (Figure adapted from reference 50).

Meng and co-workers have developed a two-photon fluorescent probe, **DMPCA**, for monitoring bisulfite anion based on TICT mechanism.[51] Coumarin was chosen as the fluorophore with an *N*,*N*-dimethyl group [-$N(CH_3)_2$] serving as the TICT donor, formaldehyde EWG as the reaction site and a phenyl alkynyl group to enhance two-photon fluorescence performance. The aldehyde group in the probe can selectively react with bisulfite to form an aldehyde-hydrogen sulfite adduct, suppressing TICT formation and recovering the fluorescence **(Figure 1.18)**. Notably, **DMPCA** is the first TICT-based two-photon fluorescent probe for bisulfite detection. Additionally, the probe was effectively utilized for detecting bisulfite anions in living cells using two-photon excitation.

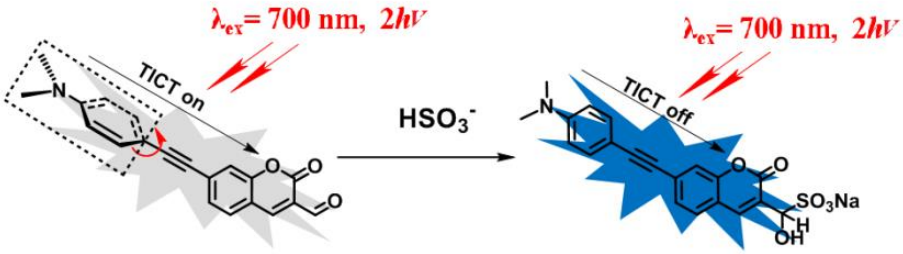

Figure 1.18. Structure of **DMPCA** and TICT mechanism for the determination of HSO_3^- (Figure adapted from reference 51).

TICT probes provide high sensitivity, selectivity, and low background fluorescence, making them ideal for detecting ions, pH changes, and viscosity monitoring. They are particularly useful in two-photon imaging for deep-tissue applications. However, their performance can be affected by environmental polarity, limited photo-stability, and low brightness. Despite these challenges, TICT probes are valuable tools for fluorescence-based sensing and imaging.

1.7. Rational design of fluorophores

Since the discovery of quinine, the first organic fluorophore, in 1845, extensive experimental and theoretical efforts have been focused on the fluorescence modulation of organic compounds. To accelerate rational and efficient probe development, each step in the fluorescence process can be modulated by organic synthetic procedures.[52] Firstly, the

absorption and emission spectra of a fluorophore can be tuned by introducing electronically diverse substituents to its fluorescent core. Secondly, the fluorophore's brightness can be regulated by managing photoinduced electron transfer (PET) and limiting the bond rotation. Finally, fluorescence output can be modified through inter chromophore FRET or PET mechanisms.

In general, a donor-π-acceptor moiety serves as the fundamental structural framework for fluorescent small organic compounds. Variations in the electronic structure of a donor-π-acceptor dye within the core fluorophore can lead to alterations in fluorescence. Also, enhanced "push-pull" effects in dyes, where excitation involves intramolecular charge transfer (ICT), result in a bathochromic shift in their UV-vis absorption and emission spectra. Moreover, expanding the π-conjugated network through the addition of appended methylene moieties or aromatic substituents results in a bathochromic shift and usually an improved extinction coefficient. Alteration of substituents can also contribute to improving quantum yield or water solubility of synthetic dyes. Furthermore, the challenges associated with the lipophilicity and poor water solubility of synthetic dyes caused by the planar structure of fused rings can be addressed by incorporating sulfonate or carboxyl groups.

Typical fluorescent probes used in biological research consist of three components: a sensing unit, a fluorophore, and an organelle targeting unit **(Figure 1.19)**.[53] The sensing unit can either be a reactive site, undergoing a chemical reaction with the analyte, or a receptor capable of selectively binding to the analyte. Ideally, the sensing unit is specific to the analyte of interest, and interaction with the analyte results in an alteration in the photophysical properties of the fluorophore. This can be fluorescence enhancement, quenching, or shift in fluorescence maximum. In addition, targeting units are incorporated to the probe to target specific organelle that host the analytes. For example, lysosome-targeting probes typically contain weakly basic, lipophilic amine groups such as morpholine or dimethylamino moieties;

positively charged lipophilic dyes are efficiently targeted to mitochondria; and planar aromatic cations with short hydrophobic chains are well-suited for nuclear localization.

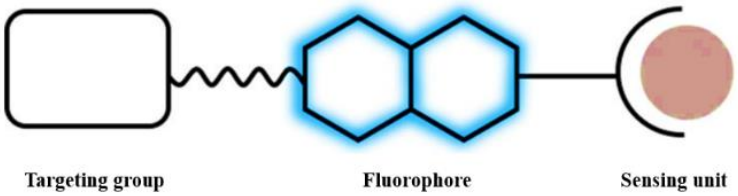

Figure 1.19. Typical design of small molecular probes for bioimaging. (Figure adapted from reference 53).

1.8. Development of novel fluorescent cores

Due to the low inherent fluorescence of biological entities, the current fluorescence techniques rely strongly on fluorescent dyes, especially, small molecule based probes due to their small size, ease of chemical modification, reliable reproducibility, and compatibility with biological systems.[54] Rhodamine[55], coumarin[56], fluorescein[57], anthocyanins[58], naphthalene amide[59], BODIPY[60] and quinoline[61] are some examples of extensively explored organic small molecule-based fluorescent dyes which find widespread application in various scientific domains such as sensing, enzyme analysis, and cellular imaging **(Figure 1.20)**. Each of these dyes exhibits distinct photophysical and physicochemical characteristics with its own merits and demerits. For example, coumarin's limited excitation and emission range may hinder its practical use in imaging applications, yet its exceptional photostability and large Stokes shift offer notable advantages.[62] Conversely, fluorescein's narrow Stokes shift and susceptibility to photobleaching may restrict its effectiveness as a contrast agent, but its high molar extinction coefficient and quantum yield values in aqueous environments make it a widely utilized fluorescent dye for imaging purposes.[63] Similarly, rhodamine's narrow stokes shift may result in autofluorescence, yet its derivatives are photostable and easily synthesized.[64] Also in the case of cyanine dyes, the near-infrared (NIR) emission properties make them attractive for *in vivo* imaging, despite their stability and quantum yield limitations.[65] Therefore, the design and development of fluorescent probes that exhibit desirable characteristics, including high

absorption coefficient, large stokes shift, high fluorescence quantum efficiency, extended absorption and emission wavelength, photostability, aqueous solubility, biocompatibility, targeting ability, and nontoxic nature are still challenging.

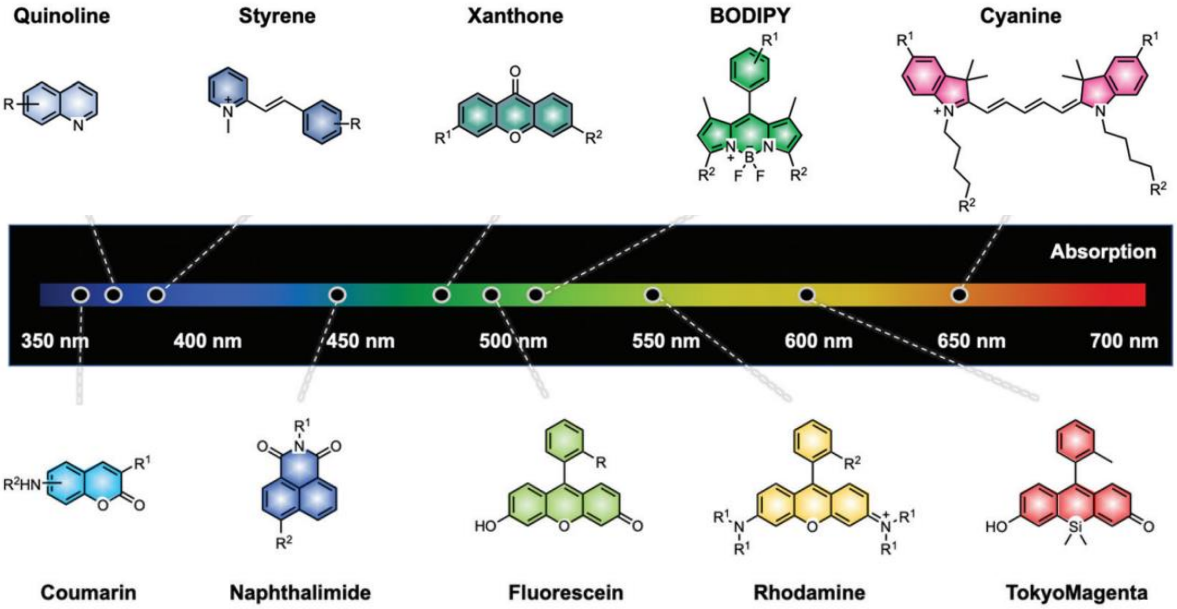

Figure 1.20. Common fluorescent dyes arranged in the increasing order of absorption values. R groups represent positions for suitable functional modifications.

For advancing the domain of fluorescence imaging techniques, there remains a significant demand for new fluorescent probes that integrate the strengths of the existing ones while allowing extensive functional group modifications to enable specific organelle targeting property and bioanalyte recognition. Such innovative core architectures could serve as the foundation for novel fluorescent probes with enhanced performance. Early progress in this field relied on the utilization of small molecule fluorophores like coumarin and fluorescein derivatives as pH sensors, operating on a simple protonation and deprotonation mechanism. However, as research progressed, more sophisticated design strategies based on photophysical mechanisms emerged, enhancing the accuracy and sensitivity in monitoring microenvironments within living systems. For instance, the development of viscosity-responsive probes based on twisted intramolecular charge transfer (TICT), polarity-responsive probes utilizing intramolecular charge transfer (ICT) between electron donor and acceptor pair,

metal ion sensing probes based on photoinduced electron transfer (PET) exemplify such advancements.

1.9. Small molecular fluorescent probes for cellular microenvironment

Organelle require a proper cellular microenvironment for their distinct biological functions. Alterations in this microenvironmental balance result in organelle damage, potentially leading to cellular dysfunction and the progression of various diseases. Essential physicochemical factors that are crucial in maintaining and regulating these biological processes include pH, viscosity, polarity, temperature, and the presence of biologically relevant ions. Viscosity is a key factor in diffusion-driven processes and plays a vital role in various biological functions. It affects the transport of nutrients and waste products, supports signal transduction, and governs biomacromolecular interactions at both the cellular and systemic levels.[66,67] Polarity, hydrophilicity and hydrophobicity, are crucial factors that influences numerous cellular processes, such as enzyme-catalyzed reactions, protein folding and maturation, protein activation, and the regulation of lipid composition.[68,69] pH is an essential factor for cell proliferation, apoptosis and endocytosis.[70] Temperature plays a critical role in regulating biological processes, with most cellular activities occurring efficiently within an optimal temperature range.[71] Also, metal ions and other biologically important species are essential for the proper functioning of cells by maintaining enzyme activity, energy production, cell signalling, nerve function, protein and DNA structure, defence mechanisms etc.[72] Therefore, monitoring these parameters in living cells is highly important for understanding both cellular physiology and pathology.

1.9.1. Viscosity sensitive fluorescent probes

Intracellular microenvironments exhibit considerable heterogeneity across different regions, with viscosity ranging from 1 - 2 cP in the aqueous cytoplasmic phase to over 100 cP within mitochondria.[73,74] Abnormal viscosity levels are associated with dysfunctions and the development of diseases. For example, abnormal accumulation of biological waste in lysosomes is pathogenic, leading to lysosomal storage diseases (LSDs), resulting "crowded storages" and elevated viscosity levels in lysosomes.[75] Similarly, elevated mitochondrial viscosity impairs electron transport chain activity, promotes cytochrome C release, and ultimately increases the risk of atherosclerosis (ALS) and malignant tumors. Additionally, the formation of dense pathological aggregates is strongly linked to neurodegenerative diseases, including Alzheimer's disease (AD) and Parkinson's disease (PD).[76] Therefore, accurately profiling biological viscosity is essential for understanding the pathophysiological roles of viscosity in these associated diseases.

In 2018, Lin et al. synthesized a new mitochondria-targeted two-photon fluorescent viscosity probe, **TM-V (Figure 1.21)**.[77] The probe is composed of two fluorophores integrated within a single molecule: a blue-emitting fluorophore that is insensitive to viscosity and a red-emitting fluorophore that exhibits strong responsiveness to viscosity changes. As the solution's viscosity increases, the red emission significantly intensifies, whereas the blue emission remains unaffected, enabling a ratiometric response with viscosity changes. Additionally, they demonstrated that excessive ROS production increases mitochondrial viscosity, through one-photon and two-photon fluorescence imaging. Furthermore, the **TM-V** probe effectively monitors mitochondrial viscosity and enables deep-tissue fluorescence imaging using two-photon microscopy.

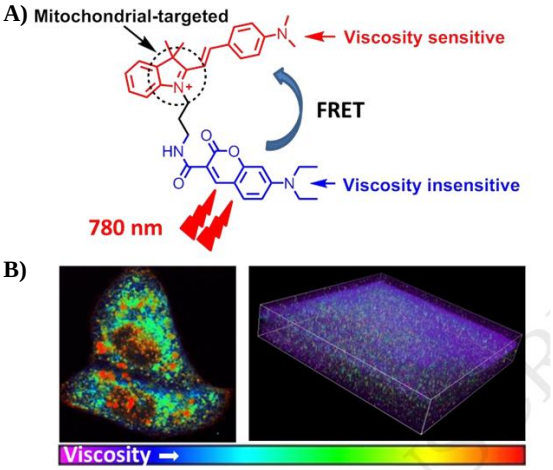

Figure 1.21. (A) The viscosity sensing mechanism of **TM-V** and (B) Two-photon fluorescence ratio images of viscosity in HeLa cells using the probe **TM-V** (10 μM) (Figure adapted from reference 77).

In 2020, Qian et al. have developed a red emissive lysosome-targeted viscosity probe based on BODIPY, **Lys-VBOD (Figure 1.22)**.[78] The probe consists of 8-hydroxyquinoline BODIPY as the fluorescent core and a morpholine group to target lysosome. The fluorescence intensity of the probe increases linearly as viscosity rises. In highly viscous solutions, the twisting of the double bond between the indole and BODIPY fluorophore is restricted, along with the rotation of the single bond connecting quinoline and BODIPY. This restriction reduces non-radiative decay pathways, leading to enhanced fluorescence intensity. Further, bioimaging in Bel-7402 cells confirmed the probe's ability for real-time monitoring of lysosomal viscosity changes in human hepatocellular cancer cell line.

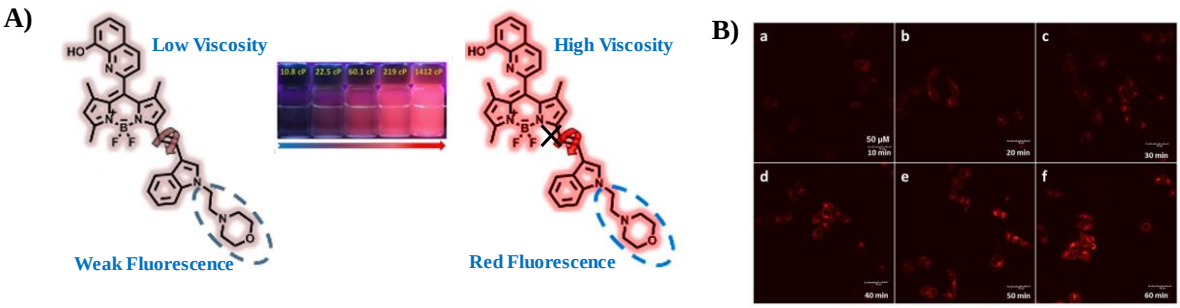

Figure 1.22. (A) The viscosity sensing mechanism and visible photograph of **Lys-VBOD** in high viscosity environment and (B) Live-cell imaging of Bel-7402 cells stained with **Lys-VBOD** (10 μM) and dexamethasone (20 μM) (Figure adapted from reference 78).

The meso-CF_3 BODIPY based fluorescent rotor reported by Yan et al. was utilized for cellular viscosity detection **(Figure 1.23)**.[79] The probe displayed weak fluorescence in low viscous solutions due to the free rotation of the meso-CF_3 group. However, increasing the viscosity, resulted in significant enhancement in fluorescence intensity due to the restricted rotation of the meso-CF_3 group. Furthermore, the probe effectively detects viscosity changes in living cells induced by lipopolysaccharide (LPS), specifically targeting the mitochondria, highlighting its potential as an AIE fluorescent "off-on" probe.

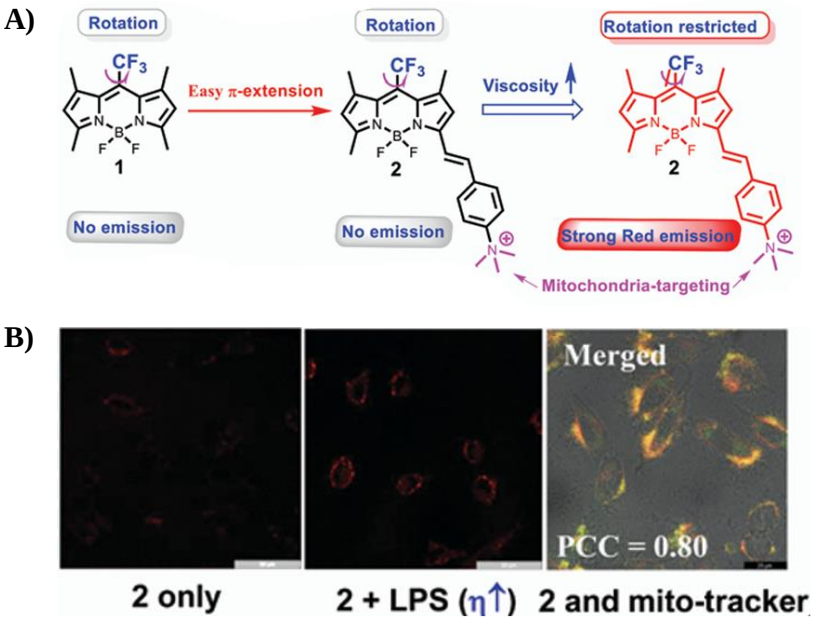

Figure 1.23. (A) The viscosity sensing mechanism of meso-CF_3 BODIPY based fluorescent probe and (B) Live cell images in SH-SY5Y cells the incubated with probe and LPS along with merged images showing co-localization with Mito-tracker (Figure adapted from reference 79).

Table 1.1. Selected examples of viscosity sensitive fluorescent probes.

Strucure of probe	Targeting component	Reference
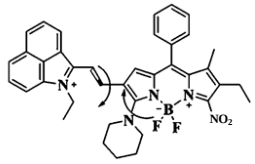	To track the variation of viscosity in diabetes-induced liver injury *in vivo.*	*Anal. Chem*. **2020**, 92, 4177-4181
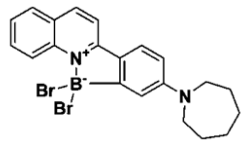	Monitoring lysosomal viscosity and sensing intracellular viscosity changes during oxidative stress.	*Dyes Pigm.* **2021**, 186, 108974
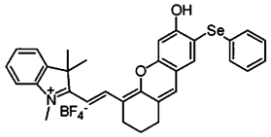	Lysosome-targeted probe for monitoring viscosity changes in living cells.	*J. Mater. Chem. B,* **2020**, 8, 8838-8844.
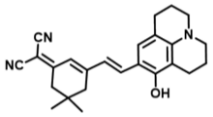	A fluorescent probe for monitoring viscosity changes in human blood and microplastic-induced variations in zebrafish.	*J. Mater. Chem. B,* **2020**, 8, 1310-1315
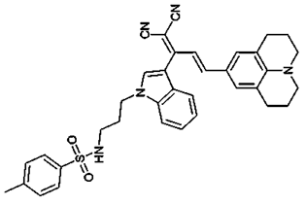	ER-targetable viscosity-sensitive fluorophore for tracking ER-phagy.	*Chem. Commun.*, **2023**,59, 1769-1772
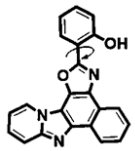	For monitoring intracellular viscosity and differentiating between malignant, differentiated, and apoptotic cancer cells.	*ACS Appl.BioMater.*, **2021**,4, 7532-7541
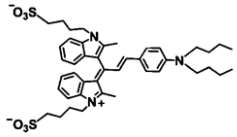	Monitoring viscosity of cell membranes.	*Chem. Commun.*, **2022**, 58, 12815
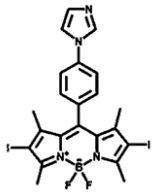	For detecting mitochondrial viscosity and acting as an effective photosensitizer for cancer therapy.	*Sensors and Actuators: B. Chemical.*, **2024**, 414 135911
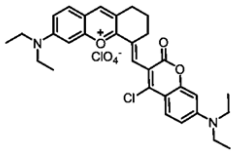	Mitochondria-targeted NIR probe for imaging viscosity in drug-treated cells and fatty liver mouse models.	*Anal.Chem.*,**2022**,94,5069−5074
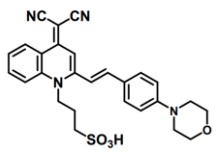	For monitoring lysosomal viscosity variations in living cells and differentiating cancer cells and normal cells.	*Chem. Commun*., **2023**, 59, 3570

1.9.2. Polarity sensitive fluorescent probes

Cell polarity is a crucial determinant of cellular state which greatly influences cellular events. Abnormal changes in polarity have been linked to cellular dysfunction and may act as a key marker for the onset of severe diseases. Currently, probes having donor-π-acceptor (D-π-A) design with push-pull electron systems are the most commonly utilized for biological polarity detection. In 2015, Xiong et al. reported the first mitochondrial polarity probe, **BOB (Figure 1.24)**.[80] The probe consists of coumarin as the donor, chosen for its high quantum yield and large extinction coefficient, with the benzothiazole group serving as the acceptor. The probe exhibits two absorption maxima at 426 nm and 561 nm, with corresponding emission peaks at 467 nm and 642 nm in methanol when excited at 405 nm. As the solution polarity decreased from 0.32 (water) to 0.013 (toluene), the fluorescence intensity of **BOB** at 467 nm showed a 24-fold enhancement, while the red emission at 645 nm exhibited only a minor fluorescence change, enabling a ratiometric response. Additionally, **BOB** exhibited high specificity for mitochondria, with a Pearson coefficient of 0.96, independent of the mitochondrial membrane potential. Moreover, ratiometric fluorescence imaging with **BOB** revealed that mitochondrial polarity in cancer cells is lower than in normal cells.

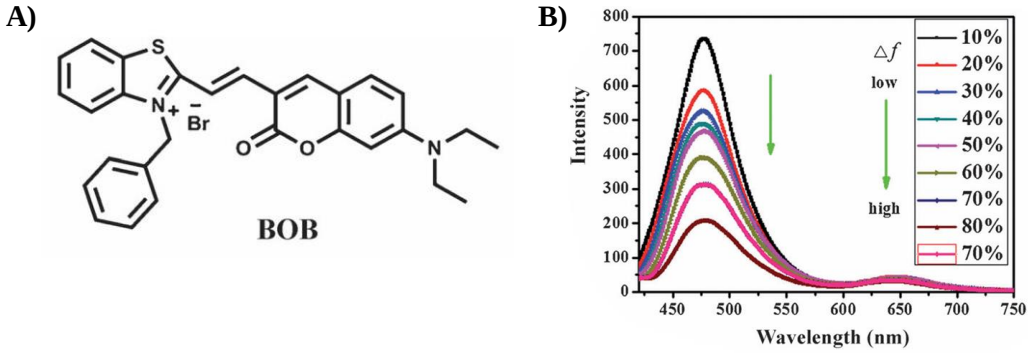

Figure 1.24. (A) Molecular structures of **BOB** and (B) Fluorescence spectra of **BOB** in water/1,4-dioxane solvent mixtures, with percentages indicating the water content (Figure adapted from reference 80).

Feng et al. have developed a polarity-sensitive cell membrane probe, **COP**, for detecting cancer cells **(Figure 1.25)**.[81] The probe comprises a coumarin unit as a polarity

sensitive dye, a pyridine salt unit for extended conjugation, and a quaternary ammonium salt unit to enhance water solubility and retention in the cell membrane. With decreasing polarity, the probe exhibited a gradual fluorescence enhancement, along with a blue shift from 679 - 610 nm. Notably, the probe exhibited strong cell membrane-targeting capability, with high selectivity for tumor cell membranes over normal ones, indicating that cancer cell membranes have lower polarity.

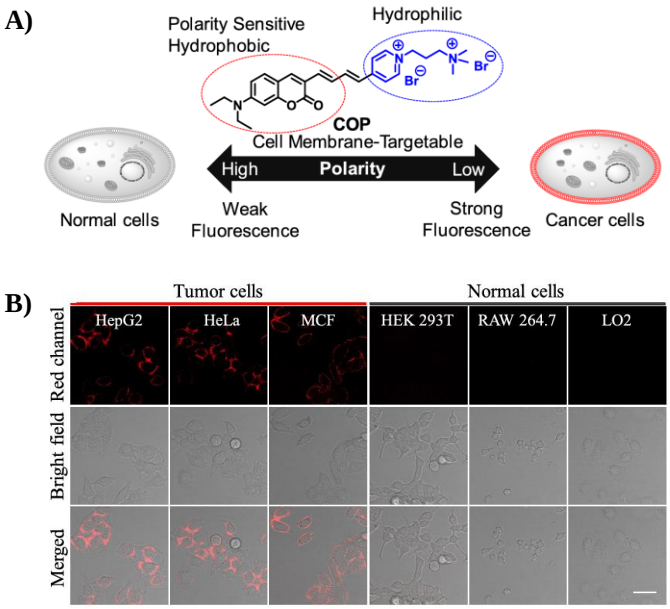

Figure 1.25. (A) Diagram showing the action of polarity-sensitive probe **COP** and (B) Fluorescence images of tumor and normal cells incubated with 10 μM **COP** (Figure adapted from reference 81).

In 2023, Yu et al. developed a dual-emissive polarity sensitive probe, **1P2N** based on pyrene-pyridinium cationic dyes **(Figure 1.26)**.[82] The pyrene unit functions as a blue-light-emitting fluorophore, enhancing the probe's overall lipophilicity. The pyridinium group serves as a strong electron acceptor, facilitating the formation of a push-pull electronic system and enhancing intramolecular charge transfer (ICT). The probe exhibits dual-emission properties under single-wavelength excitation and its fluorescence intensity ratio changes significantly with solvent polarity, enabling the detection of polarity variations in cells. Further, cell imaging experiments confirmed that the probe can effectively visualize polarity changes in the whole cytoplasm using ratiometric fluorescence imaging under various physiological conditions.

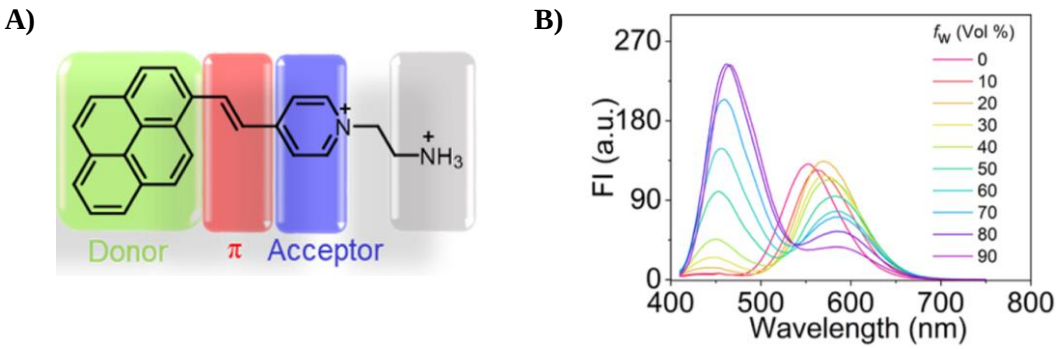

Figure 1.26. (A) Molecular structures of **1P2N** and (B) Emission spectra of **1P2N** in 1,4-dioxane/water mixtures with varying water percentage (Figure adapted from reference 82).

1.9.3. pH sensitive fluorescent probes

Maintaining hydrogen ion balance is crucial for cellular function, as it regulates pH levels in different cellular regions. Different organelles maintain distinct pH levels, with lysosomes having an acidic pH of 4.5-5.5, mitochondria exhibiting a more alkaline pH around 8.0, and the cytosol maintaining a pH of 6.8-7.4.[83] Since each organelle requires an optimal pH range for normal cellular activities, disruptions in pH balance are often linked to cellular dysfunction. For example, in healthy cells, the intracellular pH is typically around 7.2, while the extracellular environment has a slightly higher pH of approximately 7.4. However, in cancerous cells, the extracellular pH exceeds 7.4, whereas the intracellular pH ranges between 6.7 and 7.1. Therefore, it is essential to visualize pH levels within organelles.

In 2016, O'Shea and co-workers developed a novel lysosome targeted pH responsive probe **(Figure 1.27)**.[84] This probe features an Aza-BODIPY core with an ortho-nitrophenol group as the pH-sensitive unit. The electron-withdrawing effect of the *o*-nitro group facilitates phenolate ionization at pH 7.2, leading to fluorescence quenching due to a non-emissive intramolecular charge transfer (ICT) excited state. Under acidic conditions, protonation of the probe occurs, forming a neutral phenol species, which leads to a significant increase in NIR emission. The probe exhibits high selectivity for lysosomes and enables real-time imaging of key cellular processes, including endocytosis, lysosomal trafficking, and efflux, in both 3D and

4D. Furthermore, the PEG-conjugated probe was employed in a mouse model for NIR fluorescence imaging, demonstrating efficient accumulation in cancerous cells due to their acidic microenvironment.

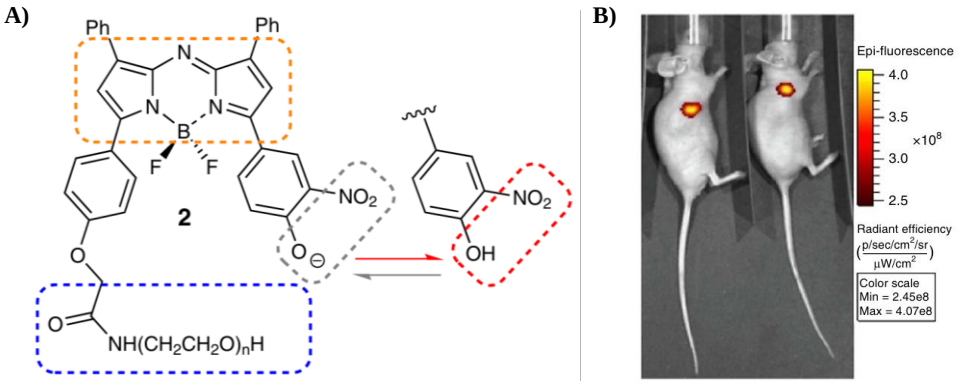

Figure 1.27. (A) Mechanism of pH detection by the aza-BODIPY-based probe and (B) NIR fluorescence imaging of MDA-MB-231-luc-D3H1 tumors in mice (Figure adapted from reference 84).

In 2022, Collot and co-workers developed a ratiometric pH probe, **Mem-pH**, based on chromenoquinoline core **(Figure 1.28)**.[85] The probe exhibited selective accumulation in the plasma membrane with a 10-fold increase in fluorescence intensity, enabling efficient pH sensing. **Mem-pH**, owing to its amphiphilic nature, forms non-emissive soluble aggregates through aggregation-caused quenching (ACQ). However, upon interacting with the lipophilic membrane, it de-aggregates and regains fluorescence. Moreover, **Mem-pH** effectively monitors vesicular acidification through ratiometric response and enables the assessment of vesicular pH, ranging from early endosomes (pH 5-6) to lysosomes (pH ≤4.6).

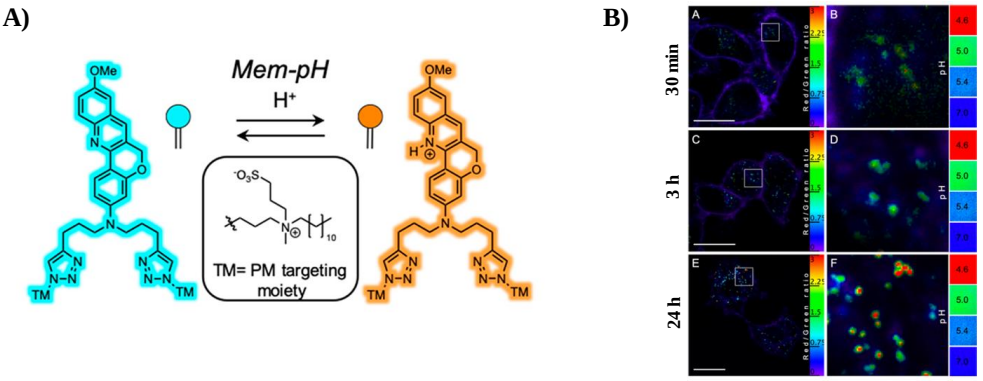

Figure 1.28. (A) pH-responsive mechanism of **Mem-pH** and (B) Ratiometric imaging of KB cells treated with **Mem-pH** at different pH (Figure adapted from reference 85).

Stacko et al. have synthesized a series of aminobenzocoumarin derivatives with various substituents **(Figure 1.29)**.[86] The detailed photophysical investigation of these derivatives revealed a pronounced pH-responsive fluorescence "turn-on" effect (up to 300-fold) in highly acidic environments. The probes remained non-fluorescent at pH 4-5, however exhibited a sharp fluorescence increase as the pH dropped to 1.5, with a pKa ranging from 1.7 - 2.6. This observation can be attributed to the inhibition of the photoinduced electron transfer effect by protonation of the electron donating amine group. Furthermore, they carried out cytotoxicity and co-localization experiments with best performed pH probe demonstrating their application in bioimaging of acidic lysosomes in live human cells.

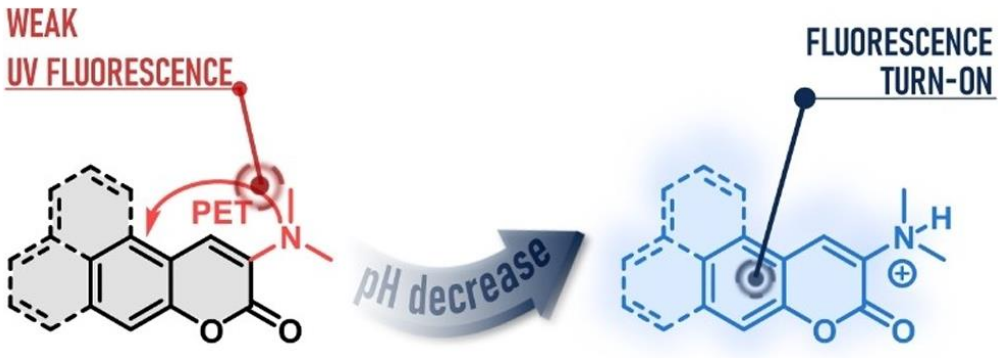

Figure 1.29. pH sensing mechanism of an aminobenzocoumarin derivative (Figure adapted from reference 86).

1.9.4. Temperature sensitive fluorescent probes

Temperature serves as a key indicator in various pathological conditions and physiological processes. Cellular metabolism responds to temperature fluctuations by modulating enzymatic activity, ensuring optimal function and efficient energy production. Therefore, visualizing temperature in living cells and tissues is essential for understanding the heat shock response. In recent decades, there has been increasing interest in developing analytical methods for measuring *in vivo* temperature, particularly using fluorescent probes known as “fluorescent thermometers.” These fluorescent thermometers enable real-time, targeted temperature monitoring of cellular microenvironment, offering valuable insights into biomolecular activities and cellular processes.

In 2014, Chang et al. have reported the first small molecular fluorescent thermometer, **ER-Thermo Yellow**, for selective targeting of the endoplasmic reticulum **(Figure 1.30)**.[87] Upon heating, the fluorescence intensity of **ER-Thermo Yellow** decreased, likely due to the increased rotational motion of the C8-phenyl group on the BODIPY scaffold at higher temperatures. This enhanced rotation promotes non-radiative decay and increases PET efficiency from the C8-phenyl group to the BODIPY core, resulting in reduced fluorescence. They further demonstrated that **ER-Thermo Yellow** can track heat production by regulating intracellular Ca^{2+} levels in HeLa cells.

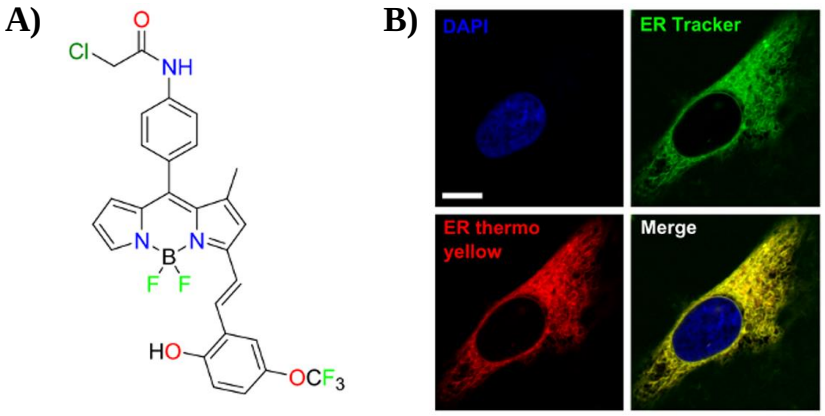

Figure 1.30. (A) Structure of **ER thermo yellow** and (B) Co-localization images of the probe with endoplasmic reticulum tracker green (Figure adapted from reference 87).

Bai et al. have developed a thermosensitive fluorogenic probe based on rhodamine B, **RhBIV (Figure 1.31)**.[88] Within the temperature range of 20-42 °C, the fluorescence of **RhBIV** decreases as temperature increases. At lower temperatures, **RhBIV** forms unstable ion pairs due to kinetic factors, resulting in strong fluorescence. As the temperature rises, these ion pairs break down, leading to the formation of **RhBV**, a thermodynamically controlled conjugated form, causing fluorescence quenching. Furthermore, the probe showed excellent accumulation in mitochondria, enabling temperature dependent response within the organelle. Additionally, *in vivo* experiments using a mouse model showed that the probe primarily accumulated in the liver, with minimal distribution in the kidneys and lymph nodes.

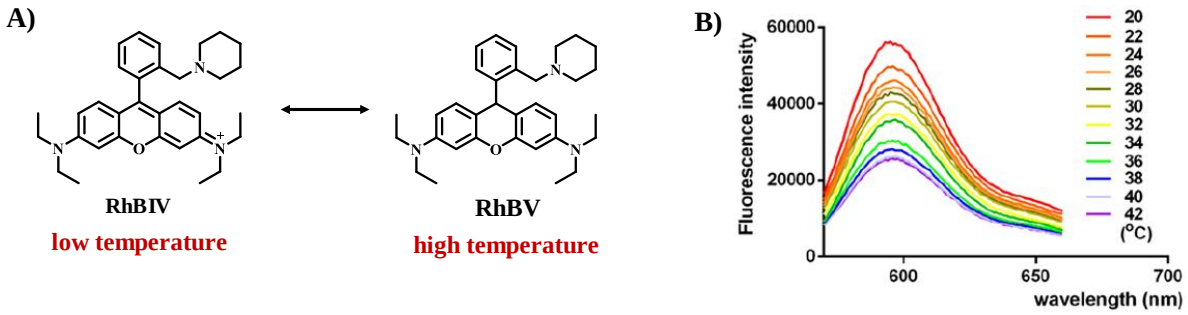

Figure 1.31. (A) Temperature sensing mechanism of **RhBIV** and (B) Fluorescence spectra of **RhBIV** at different temperatures (Figure adapted from reference 88).

In the same year, Xiao et al. developed **Mito-TEM**, a temperature-sensitive probe, by integrating a BODIPY-rhodamine fluorophore as a FRET pair and a formaldehyde group as a mitochondrial targeting unit **(Figure 1.32)**.[89] With increase in temperature, the fluorescence intensity of the BODIPY component remained unchanged, while the temperature sensitive FRET acceptor, rhodamine B, exhibited reduced fluorescence, resulting in a decreased intensity ratio I_{red}/I_{green}. Moreover, **Mito-TEM** was effectively utilized for visualizing mitochondrial temperature changes in live cells and zebrafish during various inflammatory processes.

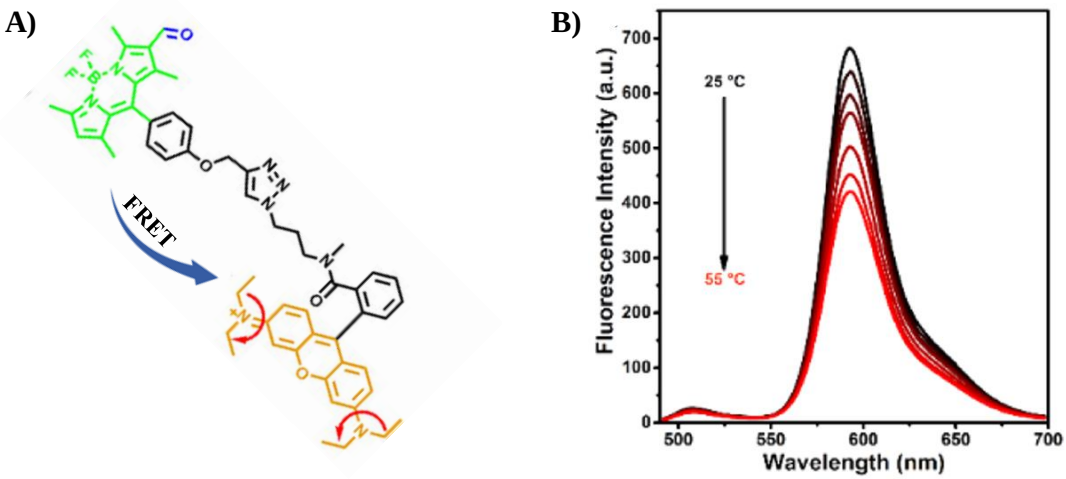

Figure 1.32. (A) Temperature sensing mechanism of **Mito-TEM** and (B) Fluorescence spectra of **Mito-TEM** with increasing temperature (Figure adapted from reference 89).

1.9.5. Fluorescent probes for metal ion sensing

Metal ions are essential components of biological systems, playing a crucial role in various biochemical processes, including material transport, energy conversion, signal

transmission, and metabolic regulation.[90,91] However, the imbalances of metal ions, whether deficiency or excess can lead to health complications.[92] Metal ions in biological systems are generally categorized into essential and non-essential. The essential metal ions include potassium (K), sodium (Na), calcium (Ca), magnesium (Mg), cobalt (Co), molybdenum (Mo), iron (Fe), copper (Cu), zinc (Zn), and manganese (Mn). Among these, K, Na, Ca, and Mg account for over 99% of the total metal content in the human body, while the other six are present in trace amounts. Both deficiency and excessive levels of these essential metal ions can result in serious health issues and toxicity. Therefore, monitoring metal ion levels in cells helps in understanding metabolic processes and facilitates disease diagnosis.

Zinc is an essential trace element that plays a crucial role in neurobiology. In 2007, Nagano et al. developed a ratiometric Zn^{2+} sensor, **ZnIC**, by incorporating iminocoumarin as the fluorophore and (ethylamino)dipicolylamine as the Zn^{2+} chelating unit **(Figure 1.33)**.[93] The probe exhibited an absorption maximum at 513 nm and an emission maximum at 543 nm. Upon addition of Zn^{2+}, the absorption peak of **ZnIC** shifts to 524 nm, while the fluorescence emission shifts to 558 nm, enabling ratiometric sensing of Zn^{2+} (F_{558}/F_{543}). This red shift in emission upon Zn^{2+} binding is attributed to the intramolecular charge transfer (ICT) mechanism. Additionally, the probe showed a highly selective response towards Zn^{2+} over other biologically relevant metal ions with minimal toxicity. The bioimaging of **ZnIC** in cultured cells and rat hippocampal slices further confirmed its ability for tracking neuronal zinc.

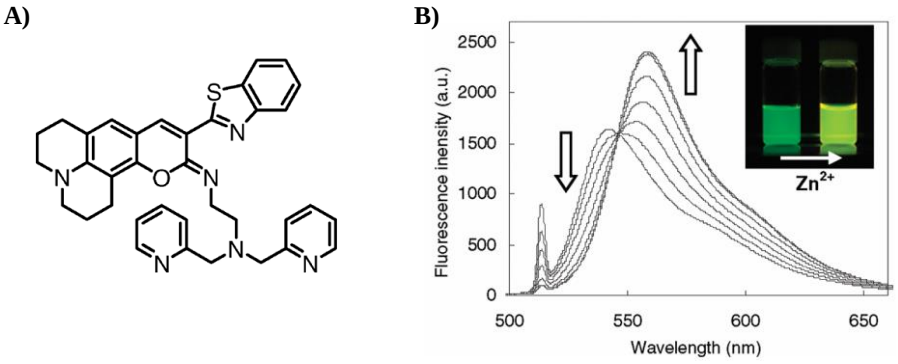

Figure 1.33. (A) Structure of **ZnIC** and (B) Changes in emission spectra **ZnIC** (5 μM) with increasing concentrations of Zn^{2+} (Figure adapted from reference 93).

Recently, Jiang et al. developed a salicylaldehyde-based Schiff base probe **SSD** for Zn ion detection **(Figure 1.34)**.[94] The probe exhibited high sensitivity toward Zn^{2+}, displaying a linear response over the concentration range of 0 - 5 μM with a detection limit of 9.1 nM. Additionally, the probe demonstrated excellent selectivity over other biologically relevant interfering ions with its good stability and pH insensitivity. Also, the probe is capable of detecting Zn^{2+} in various environments, including soil, food, and drinking water, and is compatible with smartphone detection platforms. Moreover, the probe exhibited low cytotoxicity and effectively detected both endogenous and exogenous Zn^{2+} in living cells, which was further utilized to study intracellular redox status.

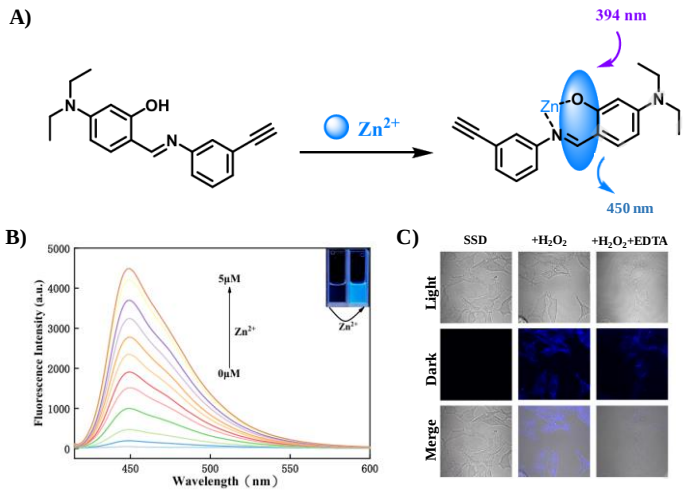

Figure 1.34. (A) Structure and sensing mechanism of **SSD**; (B) Changes in emission spectra of **SSD** (5 μM) with increasing concentrations of Zn^{2+};(C) Visualization of increased Zn^{2+} concentration during redox balance disruption in T24 cells (Figure adapted from reference 94).

Very recently, Qi et al. have developed two "turn-on" fluorescent probes, **Py-Ph** and **Py-Nap**, based on pyrene chromophore for Zn^{2+} sensing **(Figure 1.35)**.[95] In the presence of Zn^{2+}, the absorption maxima of **Py-Ph** and **Py-Nap** exhibited a blue-shift, accompanied by the appearance of a new absorption band and an isosbestic point, indicating the formation of a new species. Additionally, both probes displayed strong green fluorescence upon binding with Zn^{2+},

characterized by rapid response, high sensitivity and selectivity, low detection limits, good reversibility, and large Stokes shifts. Moreover, both probes were successfully applied for efficient fluorescence imaging of Zn^{2+} in HeLa cells and rat testis tissues.

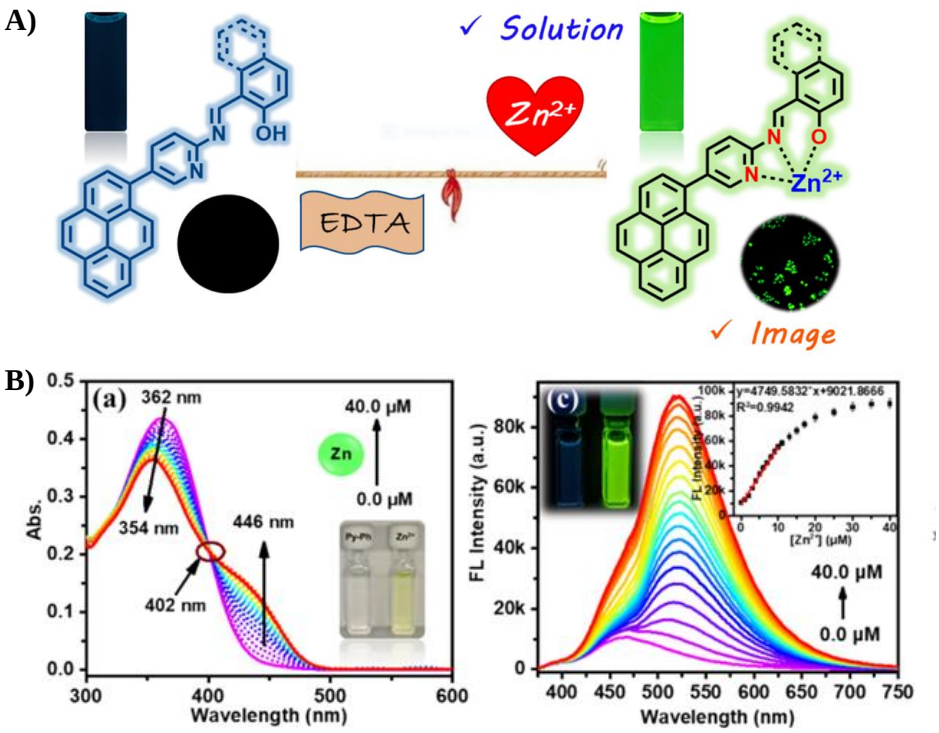

Figure 1.35. (A) Zn^{2+} sensing mechanism of **Py-Ph** and **Py-Nap**; (B) Changes in absorption and emission properties of **Py-Ph** (10 μM) with increasing concentrations of Zn^{2+} (Figure adapted from reference 95).

Table 1.2. Selected examples of Zn^{2+} sensitive fluorescent probes.

Strucure of probe	Targeting component	Reference
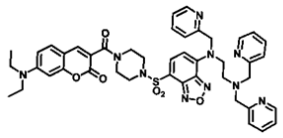	An ER-targeted ratiometric fluorescent probe for monitoring cisplatin induced Zn^{2+} fluctuations. LOD = 14 pM	*Chem. Sci*., **2020**, 11, 11037–11041
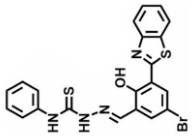	For ratiometric sensing of Zn^{2+} ions and live cell imaging. LOD = 37.7 nM	*Analyst*, **2021**, 146,4348-4356
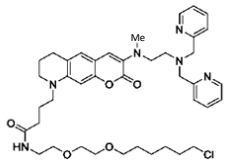	A "turn-on" fluorescent probe for detecting labile Zn^{2+} in various cellular compartments, such as the cytosol, nucleus, ER, and mitochondria. LOD = 0.16 nM	*ACS Sens.*, **2022**, 7, 748-757
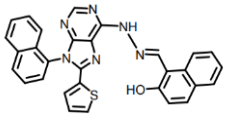	A "turn-on" fluorescent probe based on a biological purine derivative for detecting Zn^{2+}. LOD = 61.6 nM	*New J. Chem.*, **2020**,44, 15195-15201
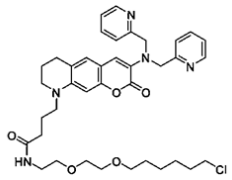	Quantitative imaging of labile Zn^{2+} in the golgi apparatus. LOD = 0.54 ± 0.05 μM	*Cell Chem. Biol*., **2020**, 27, 1521-1531
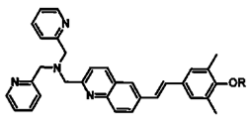	Two-photon fluorescent Zn^{2+} probe for ratiometric imaging and biosensing of Zn^{2+} in living cells and larval zebrafish. LOD = 2.94 ± 0.50 μM	*Biosensors and Bioelectronics*, **2020**, 148, 111666
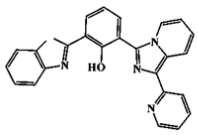	A "turn-on" fluorescence sensor for Zn^{2+} detection. LOD = 23.6 nM	*RSC Adv*., **2022**, 12, 27839-27845
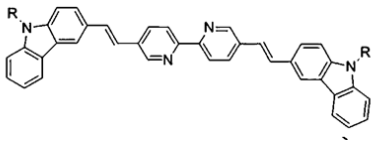	A ratiometric fluorescent probe with remarkable increase in two-photon absorption upon Zn^{2+} binding. LOD in micromolar range.	*Chem. Sci*., **2014**, 5, 3469-3474
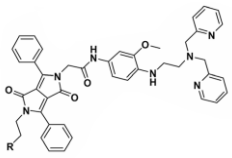	For the imaging of lysosomal Zn^{2+} and identification of prostate cancer in human tissue. LOD = 1.91 nM	*Chem. Sci*., **2019**,10, 5699-5704
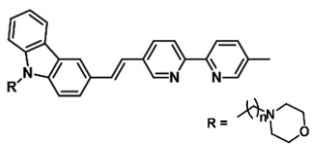	For monitoring lysosomal zinc ions in cancer cells. LOD = 369 nM (at pH 6)	*Chemistry Select*, **2018**, 3, 2416-2422

1.10. Evolution of pyrylium and pyridinium chromophore

Among the major core architectures used in fluorescence based bioimaging, pyrylium and pyridinium derivatives are extremely promising yet largely unexplored. Pyrylium salts are six-membered heteroaromatic compounds with a positive charge located on the oxygen. The oxygen atom in the pyrylium represents the most electronegative heteroatom found in an aromatic ring. Due to this remarkable electronic perturbation, pyryliums react quite differently than analogous benzene or pyridine compounds. Pyrylium salts usually do not undergo electrophilic aromatic substitution, however, they are capable of reacting readily with nucleophiles or undergoing one-electron reduction. In 1911, Baeyer reported the first pyrylium salt with perchlorate as the counter ion, however it remained underappreciated for approximately fifty years.[96]

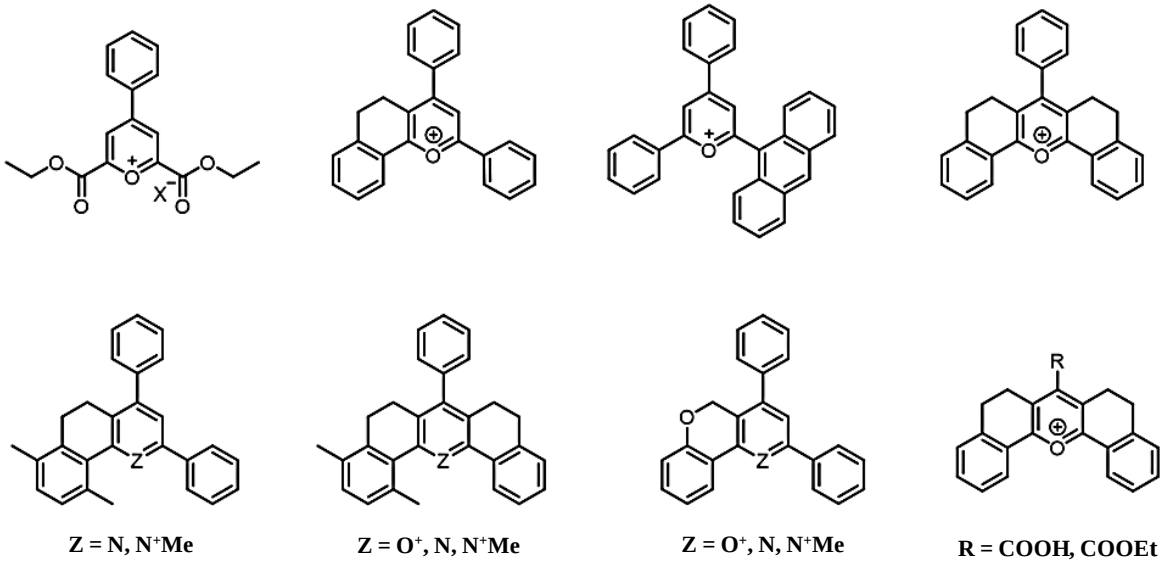

Figure 1.36. Structures of the pyrylium and pyridinium based compounds having different aromatic ring counts and functional groups.

Pyrylium and pyridinium cores were introduced by Katritzky and colleagues by synthesizing a series of sterically hindered salts with varying numbers of aromatic rings **(Figure 1.36)**.[97] They have utilized substituted α-tetralones and chalcones for condensation reaction with aromatic aldehydes in presence of an acid to yield heteroatomic polycyclic pyrylium derivatives. These pyrylium derivatives, upon reaction with primary and aromatic

amines, resulted in corresponding pyridinium derivatives. This strategy enabled the gram-scale synthesis of both pyrylium and pyridinium derivatives with high potential for scalability. In 2015, Aliaga et al. have reported a collection of pyrylium and pyridinium compounds and provided a comprehensive report on their photophysical properties **(Figure 1.37)**.[98] They observed that the emission intensity of these derivatives increased as the rigidity of the core structure was enhanced. Conjugating a radical species, TEMPO, with pyridinium fluorophores led to emission quenching, which was attributed to a spin-exchange process involving the nitroxyl radical. The molecule's original emission was restored when it reacted with TROLOX in acetonitrile, converting the nitroxyl radical into diamagnetic hydroxylamine, thereby eliminating any spin-exchange interactions. This fluorescence quenching process was observed using both fluorescence and EPR techniques.

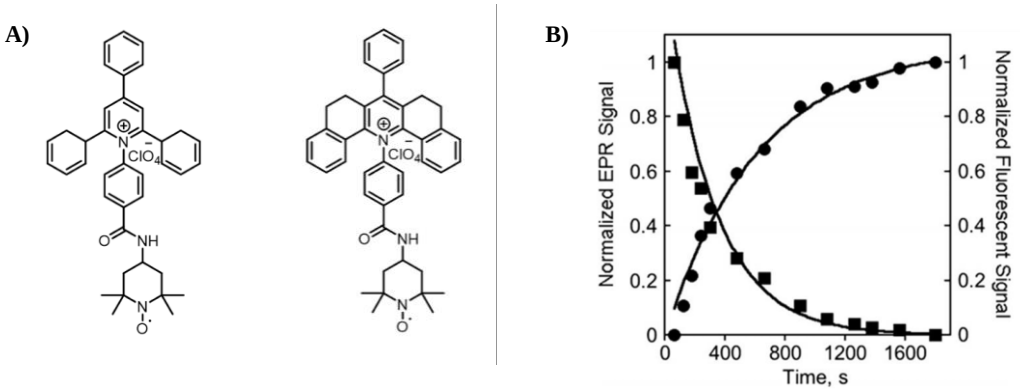

Figure 1.37. (A) Structures of flexible and rigid pyridinium molecules functionalized with TEMPO and (B) Time-dependent secondary plot of the probe's EPR and fluorescence signal intensities during radical quenching (Figure adapted from reference 98).

The "turn-on" sensor reported by Ge and co-workers is a nitric oxide sensor which utilizes pyrylium chromophore as the fluorophore **(Figure 1.38A)**.[99] The condensation reaction of 6-aminonaphthalen-1-ol derivatives with *N*-(2-amino-4-formylphenyl)acetamide is utilized for the synthesis of the probe. Upon addition of 1-hydroxy-2-oxo-3-(3-aminopropyl)-3-methyl-1-triazene (NOC13), a nitric oxide donor, the weak emission peak of the probe centered at 750 nm displayed a 35-fold enhancement in fluorescence intensity, with a corresponding

enhancement in fluorescence quantum yield from 0.015 - 0.13 **(Figure 1.38B)**. This increase in NIR emission intensity in presence of NO donor was attributed to inhibition of photoinduced electron transfer effect from donor to acceptor. Further, the probe exhibited long excitation and emission wavelength, good sensitivity and selectivity, and was effectively utilized for cellular imaging of nitric oxide in HeLa cells **(Figure 1.38C)**.

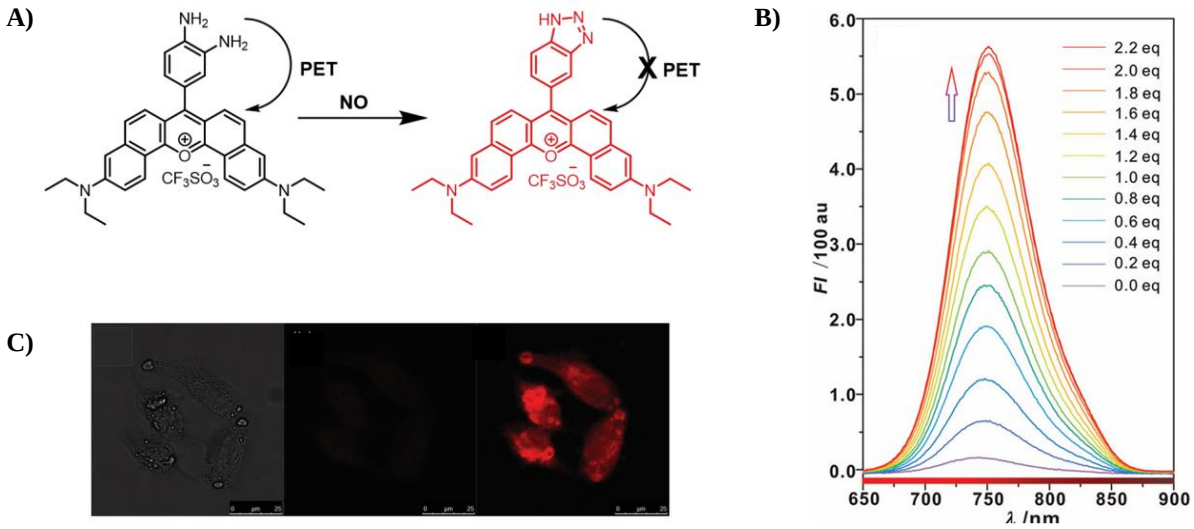

Figure 1.38. (A) Chemical structure and mechanism of action of the pyrylium based probe with NO; (B) Fluorescence spectra of the probe with increasing concentration of NOC13 and (C) Cell imaging studies with the probe in HeLa cells in the absence and presence of nitric oxide (Figure adapted from reference 99).

Yuan and co-workers have developed a single step acid-catalysed condensation method for synthesising a series of pyrylium derivatives and studied their photophysical properties **(Figure 1.39)**.[100] Detailed investigation of the photophysical properties demonstrated that enhancing structural rigidity increases chemical stability and improves emission properties. Also, modifying functional groups on both sides of the pyrylium ring resulted in changes in quantum yield values. Later, the same research group proposed a pyrylium based ratiometric fluorescent probe for detecting nitroreductase (NTR) in cancer cells. Upon exposure to nitroreductase, the initial yellow-red emission (λ_{em} = 575 nm) is shifted to the far-red region (λ_{em} = 650 nm).

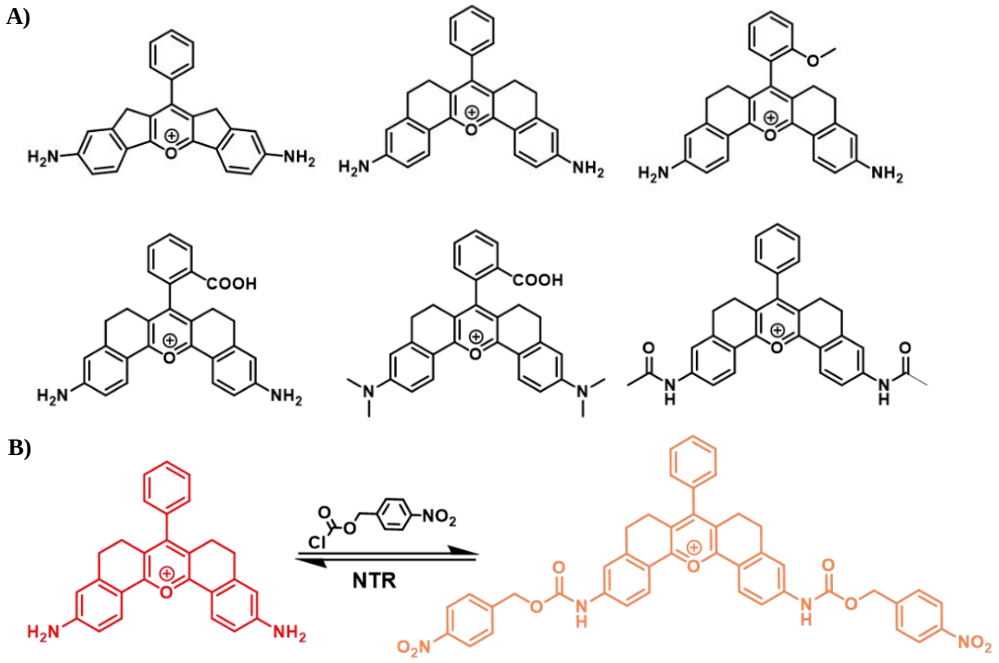

Figure 1.39. (A) Structure of different substituted rigid pyrylium derivatives and (B) Mechanism of action of the probe as an NTR sensor (Figure adapted from reference 100).

In 2020, Cornella et al. have synthesized a set of pyrylium and pyridinium derivatives with different functional groups, and utilised them for the radical C-N borylation of aromatic amines **(Figure 1.40)**.[101] They synthesized all the pyrylium derivatives in relatively large scale, which precipitated in pure form without requiring lengthy work-up or purification. Synthesising any fluorophore in its pure form at such large quantities is quite uncommon, which makes pyrylium and pyridinium derivatives particularly appealing for a broader range of applications.

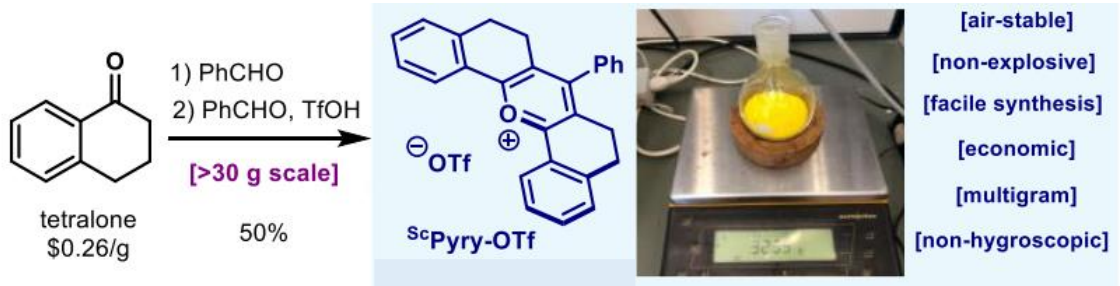

Figure 1.40. Scheme for the synthesis of the rigid pyrylium derivative, its daylight photograph (Figure adapted from reference 101).

Recently, Somappa and co-workers have developed pyrylium salts that can detect various amines through a rapid change in fluorescence color or intensity.[102] Pyrylium salts were synthesized through the reaction of naphthalenyl chalcone with phenyl acetylenes. When exposed to various classes of amines (primary, secondary, tertiary) in both solution and vapour forms, pyrylium salts undergo fluorescence quenching due to the formation of pyridinium analogue, which displays a distinct fluorescence behaviour with significantly reduced intensity **(Figure 1.41A)**. Further, they have utilized these probes as sensors to indicate spoilage in fish, meat, or cheese by detecting biogenic amines released from spoiled food **(Figure 1.41B)**.

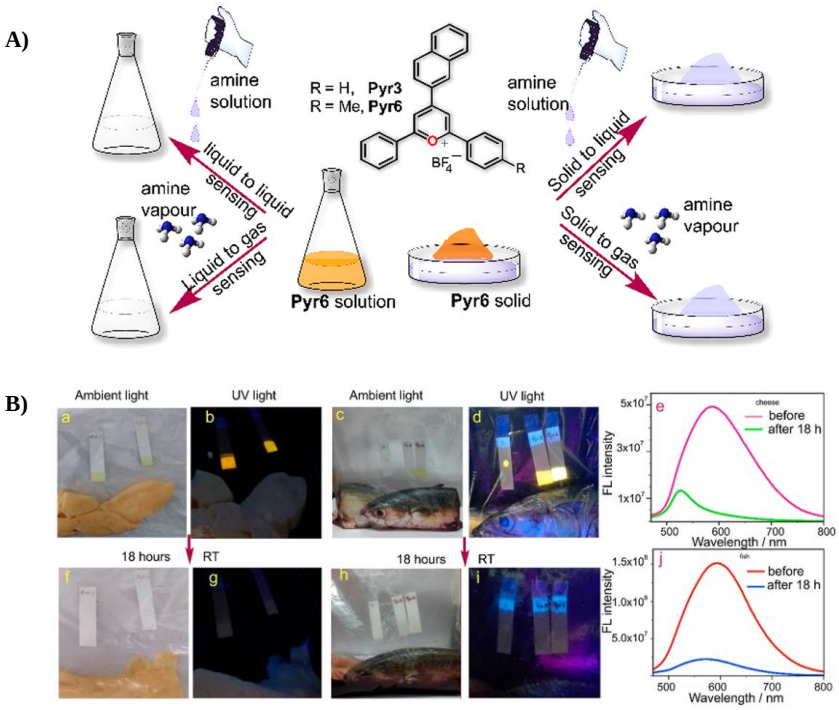

Figure 1.41. (A) Structures of pyrylium compounds exhibiting multiphase responsiveness toward amine and (B) Detection of biogenic amines using pyrylium compounds and their application as indicators of food spoilage (Figure adapted from reference 102).

Ajayaghosh and coworkers have reported the synthesis of a rigid pentacyclic pyrylium probe, **PS-OMe**, in one step utilizing modified Vilsmeier-Haack reaction **(Figure 1.42A)**.[103] It consists of a donor-acceptor-donor (D-A-D) system with the highly electron-deficient pyrylium ring serving as an effective acceptor, while the two anisole rings attached at the 2 and 6 positions of the pyrylium ring function as strong electron donors. Additionally, the six-

membered bridges significantly contribute to increasing the structural rigidity, thereby enhancing fluorescence quantum efficiency. The novel fluorophore exhibited outstanding photophysical characteristics, such as photostability, high molar absorptivity, and substantial Stokes shifts. Further, **PS-OMe** is demethylated to form a "turn-on" pH sensor **PS-OH** and utilized for tracking pH imbalances during apoptosis **(Figure 1.42B)**.

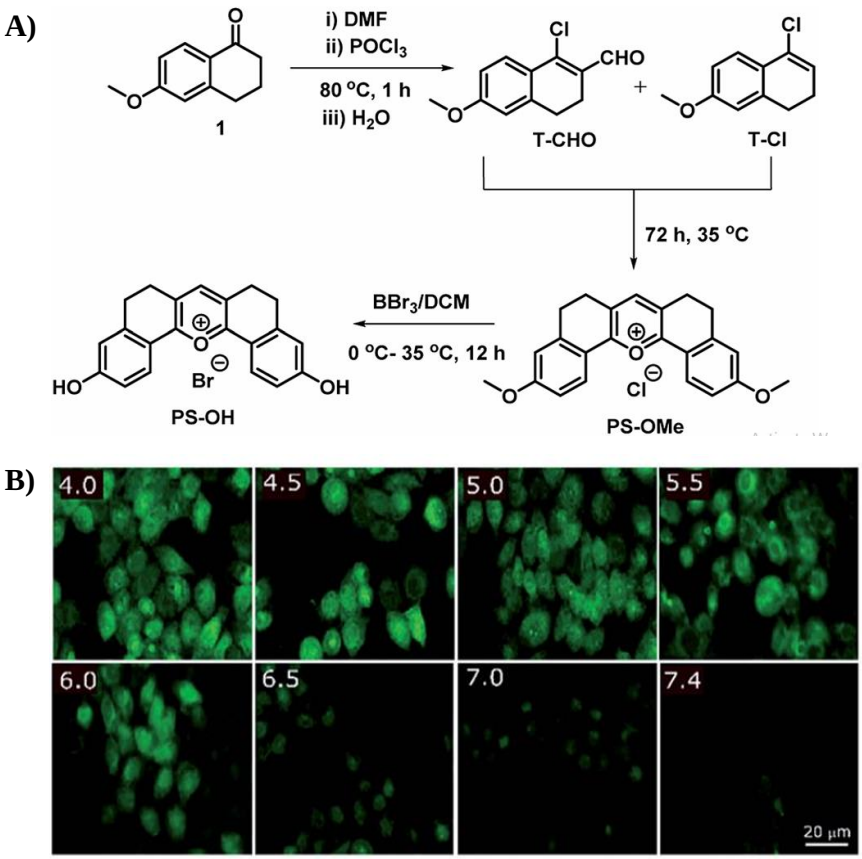

Figure 1.42. (A) Synthesis of **PS-OH** via modified Vilsmeier-Haack reaction followed by BBr_3-mediated demethylation and (B) Fluorescence imaging of A549 cells treated with **PS-OH** (20 μM) and nigericin at different pH (Figure adapted from reference 103).

Recently, our group reported a pyridinium based fluorescent molecule, **PM-ER-OH**, as a multichannel imaging probe for monitoring pH changes in the endoplasmic reticulum during heat shock **(Figure 1.43A)**.[104] The probe exhibited absorption maxima at 420 nm and 490 nm, with a near-isosbestic point at 450 nm, indicating an operational equilibrium between the protonated and deprotonated species **(Figure 1.43B)**. When excited at the first absorption

maximum (λ_{ex} = 420 nm), the emission at 566 nm gradually decreased as the pH increased, with no detectable signal at 660 nm, indicating a "turn-off" response at 566 nm **(Figure 1.43D)**. Similarly, excitation at the second absorption maximum (λ_{ex} = 490 nm) resulted in a steady increase in emission at 660 nm, with minimal emission at 566 nm, confirming a "turn-on" response at 660 nm over the same pH range **(Figure 1.43E)**. Further, excitation at the isosbestic wavelength (λ_{ex} = 450 nm) resulted in a decrease in emission maximum at 566 nm and an increase in emission maximum at 660 nm as the pH increased from 4 to 10, indicating a ratiometric fluorescence response **(Figure 1.43C)**. Thus, by changing the excitation wavelength, we could modulate the fluorescence signal in "turn-on", "turn-off", and single excitation ratiometric modes, making the fluorophore a multichannel probe for *in vitro* pH monitoring in the endoplasmic reticulum during heat shock.

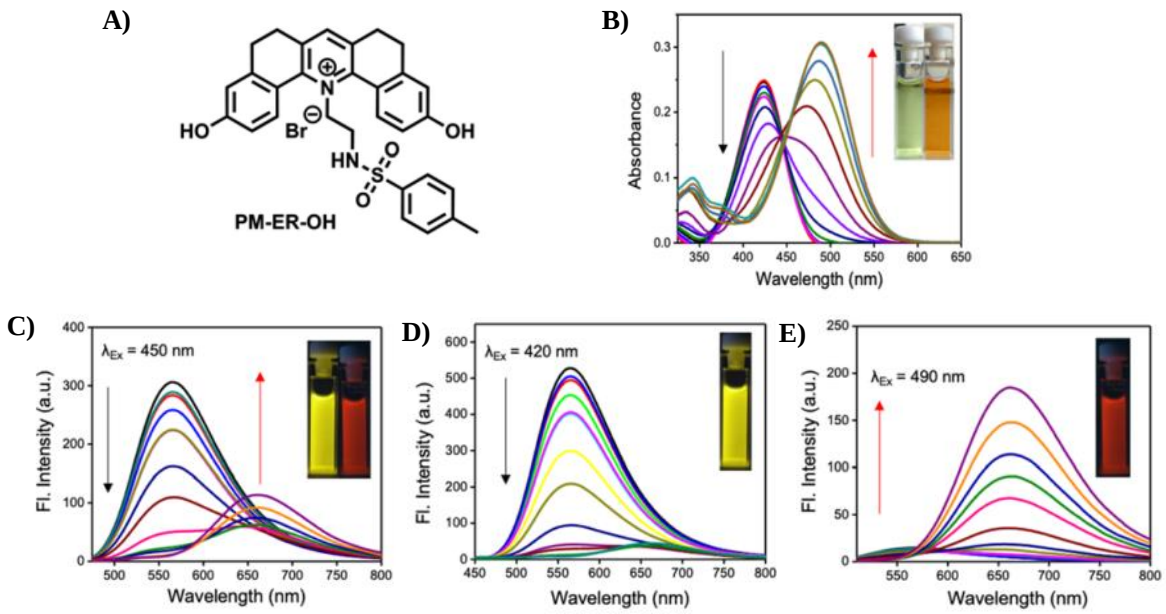

Figure 1.43. (A) Structure of **PM-ER-OH**; (B) Absorption spectrum; (C)-(E) Fluorescence spectra of **PM-ER-OH** (10 μM) in PBS from pH 4 to 10 (Figure adapted from reference 104).

The discussions above highlight the importance of small molecule based fluorescent probes in sensing and imaging applications. Advancements in the construction of small molecular probes, optimization of their optical properties, sensitivity, operational range, and in-depth understanding of response mechanisms have allowed chemists to design probes with

enhanced utility and promising applications. The application of these probes in subcellular imaging has facilitated the development of effective protocols for diagnosis and therapy, contributing to progress in the healthcare field. Additionally, the well-established synthetic approaches for creating rigid pyrylium and pyridinium salts, combined with their favourable photophysical properties, biocompatibility, and remarkable physicochemical stability, suggest a promising new fluorescent core architecture with significant potential for functional group modification and bioimaging applications.

1.11. Objectives and methodologies for the present investigation

The design and development of new fluorescent probes with improved efficacy and selectivity is a viable alternative for achieving a better understanding of cellular homeostasis. In this thesis, we have chosen pyrylium and pyridinium as the central fluorescent cores and modified the scaffold for different bioimaging applications. Major objectives of the present thesis include:

- Design and development of a new, pentacyclic pyridinium based probe, **PYD-PA**, having a pendant *N*,*N*-di(pyridin-2-ylmethyl)amine (DPA) for zinc ion detection in cellular environment. (Chapter 2A)
- Investigation of differential interactions of the Zn^{2+}-bound pyridinium-based probe, **PYD-PA-Zn^{2+}**, with nucleotides, single-stranded DNA, and double-stranded DNA through fluorescence and lifetime analysis. (Chapter 2B)
- Synthesis of a series of styryl-pyrylium derivatives, exploration of their photophysical characteristics, and investigation of the viscosity sensitivity and imaging potential of the hydroxyl-appended derivative, **OH-MPYR**. (Chapter 3)
- Development of a pyridinium spiropyran complex for dual sensing of heat shock signalling molecules HOCl and SO_2. (Chapter 4)

The Pyrylium compounds used in the thesis were synthesized through cyclisation reaction of 6-R-tetralone (R= H, OMe, NH_2) with corresponding aromatic and aliphatic aldehydes. The pyrylium chromophore can easily convert into pyridinium by simple reaction with aliphatic amines. Ancillary ligands were selected to design the newly synthesized probes for a specific purpose. All the intermediates and final products were purified through column chromatography and characterized using ^{1}H NMR, ^{13}C NMR, and HRMS Analysis. Detailed photophysical properties of the probes were investigated using UV-Vis absorption, fluorescence spectroscopy, and excited-state dynamics by using TCSPC. Sensitivity and selectivity toward the target analyte, detection limit, pH responsiveness, photostability, cytotoxicity, and co-localization ability were evaluated, followed by their respective bioimaging applications. The bioimaging experiments were carried out using established protocols in cancer cells (SK-BR-3 and HeLa) to ensure reliable and reproducible results.

We successfully synthesized and characterized several pyrylium and pyridinium derivatives, explored their optical properties, and utilized for sensing and imaging applications. Large Stokes shift exhibited by these fluorescent sensors simplifies the use of filter sets and helps to minimize autofluorescence and background noise, which are key requirements for effective imaging applications. Through their unique design, these fluorescent probes demonstrate high selectivity towards specific analytes, excellent co-localization, good aqueous solubility, and reduced toxicity, making them well-suited for monitoring the cellular microenvironment. Overall, we have explored the photophysics and biosensing properties of a series of new pyrylium and pyridinium derivatives and utilized these probes to investigate key cellular events, including autophagy, viscosity changes, and heat shock, demonstrating how dynamic changes in specific analytes can be monitored to track these processes.

1.12. References

(1) Xu, W.; Zeng, Z.; Jiang, J. H.; Chang, Y. T.; Yuan, L. Discerning the chemistry in individual organelles with small-molecule fluorescent probes. *Angew. Chem. Int. Ed.* **2016**, *55*, 13658-13699.

(2) Song, Y.; Zhang, H.; Wang, X.; Geng, X.; Sun, Y.; Liu, J.; Li, Z. One stone, three birds: pH triggered transformation of aminopyronine and iminopyronine based lysosome targeting viscosity probe for cancer visualization. *Analytical Chemistry* **2020**, *93*, 1786-1791.

(3) Ozturk, S. S.; Thrift, J. C.; Blackie, J. D.; Naveh, D. Real-time monitoring of protein secretion in mammalian cell fermentation: Measurement of monoclonal antibodies using a computer-controlled HPLC system (BioCad/RPM). *Biotechnol. Bioeng.* **1995**, *48*, 201-206.

(4) Mao, S.; Li, W.; Zhang, Q.; Zhang, W.; Huang, Q.; Lin, J.-M. Cell analysis on chip-mass spectrometry. *TrAC, Trends Anal. Chem.* **2018**, *107*, 43-59.

(5) Gawne, P. J.; Man, F.; Blower, P. J.; Tm de Rosales, R. Direct cell radiolabeling for in vivo cell tracking with PET and SPECT imaging. *Chem. Rev.* **2022**, *122*, 10266-10318.

(6) Swift, L. H.; Colarusso, P.: Fluorescence microscopy: A field guide for biologists. In *Fluorescent Microscopy*; Springer, 2022; pp 3-39.

(7) Danylchuk, D. I.; Jouard, P.-H.; Klymchenko, A. S. Targeted solvatochromic fluorescent probes for imaging lipid order in organelles under oxidative and mechanical stress. *Journal of the American Chemical Society* **2021**, *143*, 912-924.

(8) Yin, J.; Huang, L.; Wu, L.; Li, J.; James, T. D.; Lin, W. Small molecule based fluorescent chemosensors for imaging the microenvironment within specific cellular regions. *Chemical Society Reviews* **2021**, *50*, 12098-12150.

(9) Strehmel, B.; Strehmel, V.; Malpert, J. J. Molecular Fluorescence 2nd. *Markono Print Media, Singapore* **2013**.

(10) Valeur, B.; Berberan-Santos, M. N. A brief history of fluorescence and phosphorescence before the emergence of quantum theory. *J. Chem. Educ.* **2011**, *88*, 731-738.

(11) Chan, J.; Dodani, S. C.; Chang, C. J. Reaction-based small-molecule fluorescent probes for chemoselective bioimaging. *Nature chemistry* **2012**, *4*, 973-984.

(12) Herschel, J. F. W. IV.'Αμόρφωτα, no. I.—on a case of superficial colour presented by a homogeneous liquid internally colourless. *Philosophical Transactions of the Royal Society of London* **1845**, 143-145.

(13) Stokes, G. G. XXX. On the change of refrangibility of light. *Philosophical transactions of the Royal Society of London* **1852**, 463-562.

(14) Heim, R.; Cubitt, A. B.; Tsien, R. Y. Improved green fluorescence. *Nature* **1995**, *373*, 663-664.

(15) Chalfie, M.; Tu, Y.; Euskirchen, G.; Ward, W. W.; Prasher, D. C. Green fluorescent protein as a marker for gene expression. *Science* **1994**, *263*, 802-805.

(16) Betzig, E.; Chichester, R. J. Single molecules observed by near-field scanning optical microscopy. *Science* **1993**, *262*, 1422-1425.

(17) Hell, S. W. Toward fluorescence nanoscopy. *Nat. Biotechnol.* **2003**, *21*, 1347-1355.

(18) Moerner, W. E. Nobel Lecture: Single-molecule spectroscopy, imaging, and photocontrol: Foundations for super-resolution microscopy. *Reviews of Modern Physics* **2015**, *87*.

(19) Lippincott-Schwartz, J. Profile of Eric Betzig, Stefan Hell, and WE Moerner, 2014 Nobel Laureates in Chemistry. *Proceedings of the National Academy of Sciences* **2015**, *112*, 2630-2632.

(20) Fang, H.; Chen, Y.; Jiang, Z.; He, W.; Guo, Z. Fluorescent probes for biological species and microenvironments: from rational design to bioimaging applications. *Accounts of Chemical Research* **2023**, *56*, 258-269.

(21) Jana, A.; Baruah, M.; Munan, S.; Samanta, A. ICT based water-soluble fluorescent probe for discriminating mono and dicarbonyl species and analysis in foods. *Chemical Communications* **2021**, *57*, 6380-6383.

(22) Wang, C.; Chi, W.; Qiao, Q.; Tan, D.; Xu, Z.; Liu, X. Twisted intramolecular charge transfer (TICT) and twists beyond TICT: from mechanisms to rational designs of bright and sensitive fluorophores. *Chemical Society Reviews* **2021**, *50*, 12656-12678.

(23) Niu, H.; Liu, J.; O'Connor, H. M.; Gunnlaugsson, T.; James, T. D.; Zhang, H. Photoinduced electron transfer (PeT) based fluorescent probes for cellular imaging and disease therapy. *Chemical Society Reviews* **2023**, *52*, 2322-2357.

(24) Ding, D.; Li, K.; Liu, B.; Tang, B. Z. Bioprobes based on AIE fluorogens. *Accounts of chemical research* **2013**, *46*, 2441-2453.

(25) Cao, D.; Zhu, L.; Liu, Z.; Lin, W. Through bond energy transfer (TBET)-based fluorescent chemosensors. *Journal of Photochemistry and Photobiology C: Photochemistry Reviews* **2020**, *44*, 100371.

(26) Gu, K.; Xu, Y.; Li, H.; Guo, Z.; Zhu, S.; Zhu, S.; Shi, P.; James, T. D.; Tian, H.; Zhu, W.-H. Real-time tracking and in vivo visualization of β-galactosidase activity in colorectal tumor with a ratiometric near-infrared fluorescent probe. *Journal of the American Chemical Society* **2016**, *138*, 5334-5340.

(27) Zhang, W.-J.; Fan, L.; Li, Z.-B.; Ou, T.; Zhai, H.-J.; Yang, J.; Dong, C.; Shuang, S.-M. Thiazole-based ratiometric fluorescence pH probe with large Stokes shift for intracellular imaging. *Sensors and Actuators B: Chemical* **2016**, *233*, 566-573.

(28) Wang, X.; Li, P.; Ding, Q.; Wu, C.; Zhang, W.; Tang, B. Illuminating the function of the hydroxyl radical in the brains of mice with depression phenotypes by two-photon fluorescence imaging. *Angewandte Chemie International Edition* **2019**, *58*, 4674-4678.

(29) Zheng, Y.; Wu, S.; Bing, Y.; Li, H.; Liu, X.; Li, W.; Zou, X.; Qu, Z. A simple ICT-based fluorescent probe for HOCl and bioimaging applications. *Biosensors* **2023**, *13*, 744.

(30) De Silva, A. P.; Moody, T. S.; Wright, G. D. Fluorescent PET (Photoinduced Electron Transfer) sensors as potent analytical tools. *Analyst* **2009**, *134*, 2385-2393.

(31) Sun, W.; Li, M.; Fan, J.; Peng, X. Activity-based sensing and theranostic probes based on photoinduced electron transfer. *Accounts of Chemical Research* **2019**, *52*, 2818-2831.

(32) Liu, J.; Sun, Y.-Q.; Huo, Y.; Zhang, H.; Wang, L.; Zhang, P.; Song, D.; Shi, Y.; Guo, W. Simultaneous fluorescence sensing of Cys and GSH from different emission channels. *Journal of the American Chemical Society* **2014**, *136*, 574-577.

(33) Singha, S.; Kim, D.; Seo, H.; Cho, S. W.; Ahn, K. H. Fluorescence sensing systems for gold and silver species. *Chemical Society Reviews* **2015**, *44*, 4367-4399.

(34) Matsumoto, T.; Urano, Y.; Shoda, T.; Kojima, H.; Nagano, T. A thiol-reactive fluorescence probe based on donor-excited photoinduced electron transfer: key role of ortho substitution. *Organic letters* **2007**, *9*, 3375-3377.

(35) Xia, H.-C.; Xu, X.-H.; Song, Q.-H. BODIPY-based fluorescent sensor for the recognization of phosgene in solutions and in gas phase. *Analytical chemistry* **2017**, *89*, 4192-4197.

(36) Wang, R.; Yu, F.; Chen, L.; Chen, H.; Wang, L.; Zhang, W. A highly selective turn-on near-infrared fluorescent probe for hydrogen sulfide detection and imaging in living cells. *Chemical communications* **2012**, *48*, 11757-11759.

(37) Xiao, P.; Liu, J.; Wang, Z.; Tao, F.; Yang, L.; Yuan, G.; Sun, W.; Zhang, X. A color turn-on fluorescent probe for real-time detection of hydrogen sulfide and identification of food spoilage. *Chemical Communications* **2021**, *57*, 5012-5015.

(38) Sun, Q.; Yang, S.-H.; Wu, L.; Dong, Q.-J.; Yang, W.-C.; Yang, G.-F. Detection of intracellular selenol-containing molecules using a fluorescent probe with near-zero background signal. *Analytical chemistry* **2016**, *88*, 6084-6091.

(39) Zhang, W.; Li, P.; Yang, F.; Hu, X.; Sun, C.; Zhang, W.; Chen, D.; Tang, B. Dynamic and reversible fluorescence imaging of superoxide anion fluctuations in live cells and in vivo. *Journal of the American Chemical Society* **2013**, *135*, 14956-14959.

(40) Wu, Y.; Peng, X.; Guo, B.; Fan, J.; Zhang, Z.; Wang, J.; Cui, A.; Gao, Y. Boron dipyrromethene fluorophore based fluorescence sensor for the selective imaging of Zn (II) in living cells. *Organic & biomolecular chemistry* **2005**, *3*, 1387-1392.

(41) Lee, M. H.; Park, N.; Yi, C.; Han, J. H.; Hong, J. H.; Kim, K. P.; Kang, D. H.; Sessler, J. L.; Kang, C.; Kim, J. S. Mitochondria-immobilized pH-sensitive off–on fluorescent probe. *Journal of the American Chemical Society* **2014**, *136*, 14136-14142.

(42) Tang, B.; Yu, F.; Li, P.; Tong, L.; Duan, X.; Xie, T.; Wang, X. A near-infrared neutral pH fluorescent probe for monitoring minor pH changes: imaging in living HepG2 and HL-7702 cells. *Journal of the American Chemical Society* **2009**, *131*, 3016-3023.

(43) Reja, S. I.; Gupta, M.; Gupta, N.; Bhalla, V.; Ohri, P.; Kaur, G.; Kumar, M. A lysosome targetable fluorescent probe for endogenous imaging of hydrogen peroxide in living cells. *Chemical communications* **2017**, *53*, 3701-3704.

(44) Förster, T.: Mechanisms of energy transfer. In *Comprehensive biochemistry*; Elsevier, 1967; Vol. 22; pp 61-80.

(45) Sapsford, K. E.; Berti, L.; Medintz, I. L. Materials for fluorescence resonance energy transfer analysis: beyond traditional donor–acceptor combinations. *Angewandte Chemie International Edition* **2006**, *45*, 4562-4589.

(46) Wu, L.; Huang, C.; Emery, B. P.; Sedgwick, A. C.; Bull, S. D.; He, X.-P.; Tian, H.; Yoon, J.; Sessler, J. L.; James, T. D. Förster resonance energy transfer (FRET)-based small-molecule sensors and imaging agents. *Chemical Society Reviews* **2020**, *49*, 5110-5139.

(47) Zhang, X.; Xiao, Y.; Qian, X. A ratiometric fluorescent probe based on FRET for imaging Hg^{2+} ions in living cells. *Angewandte Chemie* **2008**, *120*, 8145-8149.

(48) Yuan, L.; Lin, W.; Xie, Y.; Chen, B.; Zhu, S. Single fluorescent probe responds to H2O2, NO, and H_2O_2/NO with three different sets of fluorescence signals. *Journal of the American Chemical Society* **2012**, *134*, 1305-1315.

(49) Jun, Y. W.; Wang, T.; Hwang, S.; Kim, D.; Ma, D.; Kim, K. H.; Kim, S.; Jung, J.; Ahn, K. H. A Ratiometric Two-Photon Fluorescent Probe for Tracking Lysosomal ATP: Direct In Cellulo Observation of Lysosomal Membrane Fusion Processes. *Angewandte Chemie* **2018**, *130*, 10299-10304.

(50) Li, Q.; Peng, M.; Li, H.; Zhong, C.; Zhang, L.; Cheng, X.; Peng, X.; Wang, Q.; Qin, J.; Li, Z. A new "turn-on" naphthalenedimide-based chemosensor for mercury ions with high selectivity: successful utilization of the mechanism of twisted intramolecular charge transfer, near-IR fluorescence, and cell images. *Organic letters* **2012**, *14*, 2094-2097.

(51) Yu, S.; Yang, X.; Shao, Z.; Feng, Y.; Xi, X.; Shao, R.; Guo, Q.; Meng, X. A TICT based two-photon fluorescent probe for bisulfite anion and its application in living cells. *Sensors and Actuators B: Chemical* **2016**, *235*, 362-369.

(52) Jun, J. V.; Chenoweth, D. M.; Petersson, E. J. Rational design of small molecule fluorescent probes for biological applications. *Organic & biomolecular chemistry* **2020**, *18*, 5747-5763.

(53) Trinh, N.; Jolliffe, K. A.; New, E. J. Dual-functionalisation of fluorophores for the preparation of targeted and selective probes. *Angewandte Chemie International Edition* **2020**, *59*, 20290-20301.

(54) Fu, Y.; Finney, N. S. Small-molecule fluorescent probes and their design. *RSC advances* **2018**, *8*, 29051-29061.

(55) Grimm, J. B.; Tkachuk, A. N.; Patel, R.; Hennigan, S. T.; Gutu, A.; Dong, P.; Gandin, V.; Osowski, A. M.; Holland, K. L.; Liu, Z. J. Optimized red-absorbing dyes for imaging and sensing. *J. Am. Chem. Soc.* **2023**, *145*, 23000-23013.

(56) Han, J.; Yang, S.; Wang, B.; Song, X. Tackling the selectivity dilemma of benzopyrylium–coumarin dyes in fluorescence sensing of HClO and SO2. *Analytical Chemistry* **2021**, *93*, 5194-5200.

(57) Verma, V. P.; Singh, A. P.; Shrivastava, R. Recent advancement in development of fluorescein based molecular probes for analytes sensing. *J. Mol. Struct.* **2023**, 136549.

(58) Tang, B.; He, Y.; Liu, J.; Zhang, J.; Li, J.; Zhou, J.; Ye, Y.; Wang, J.; Wang, X. Kinetic investigation into pH-dependent color of anthocyanin and its sensing performance. *Dyes and Pigments* **2019**, *170*, 107643.

(59) Kumari, R.; Sunil, D.; Ningthoujam, R. S. Naphthalimides in fluorescent imaging of tumor hypoxia–An up-to-date review. *Bioorg. Chem.* **2019**, *88*, 102979.

(60) Kowada, T.; Maeda, H.; Kikuchi, K. BODIPY-based probes for the fluorescence imaging of biomolecules in living cells. *Chem. Soc. Rev.* **2015**, *44*, 4953-4972.

(61) Jun, J. V.; Petersson, E. J.; Chenoweth, D. M. Rational design and facile synthesis of a highly tunable quinoline-based fluorescent small-molecule scaffold for live cell imaging. *J. Am. Chem. Soc.* **2018**, *140*, 9486-9493.

(62) Das, S.; Indurthi, H. K.; Saha, P.; Sharma, D. K. Coumarin-based fluorescent probes for the detection of ions, biomolecules and biochemical species responsible for diseases. *Dyes and Pigments* **2024**, 112257.

(63) Verma, V. P.; Singh, A. P.; Shrivastava, R. Recent advancement in development of fluorescein based molecular probes for analytes sensing. *Journal of Molecular Structure* **2024**, *1295*, 136549.

(64) Zeng, S.; Liu, X.; Kafuti, Y. S.; Kim, H.; Wang, J.; Peng, X.; Li, H.; Yoon, J. Fluorescent dyes based on rhodamine derivatives for bioimaging and therapeutics: recent progress, challenges, and prospects. *Chemical Society Reviews* **2023**, *52*, 5607-5651.

(65) Sun, W.; Guo, S.; Hu, C.; Fan, J.; Peng, X. Recent development of chemosensors based on cyanine platforms. *Chemical reviews* **2016**, *116*, 7768-7817.

(66) Minton, A. P. The influence of macromolecular crowding and macromolecular confinement on biochemical reactions in physiological media. *Journal of biological chemistry* **2001**, *276*, 10577-10580.

(67) Dix, J. A.; Verkman, A. S. Crowding effects on diffusion in solutions and cells. *Annu. Rev. Biophys.* **2008**, *37*, 247-263.

(68) Simons, K.; Toomre, D. Lipid rafts and signal transduction. *Nature reviews Molecular cell biology* **2000**, *1*, 31-39.

(69) Berns, M. W.; Krasieva, T.; Sun, C.-H.; Dvornikov, A.; Rentzepis, P. M. A polarity dependent fluorescence "switch" in live cells. *Journal of Photochemistry and Photobiology B: Biology* **2004**, *75*, 51-56.

(70) Pérez-Sala, D.; Collado-Escobar, D.; Mollinedo, F. Intracellular Alkalinization Suppresses Lovastatin-induced Apoptosis in HL-60 Cells through the Inactivation of a pH-dependent Endonuclease (∗). *Journal of Biological Chemistry* **1995**, *270*, 6235-6242.

(71) Pinney, M. M.; Mokhtari, D. A.; Akiva, E.; Yabukarski, F.; Sanchez, D. M.; Liang, R.; Doukov, T.; Martinez, T. J.; Babbitt, P. C.; Herschlag, D. Parallel molecular mechanisms for enzyme temperature adaptation. *Science* **2021**, *371*, eaay2784.

(72) Divya, K. P.; Sreejith, S.; Ashokkumar, P.; Yuzhan, K.; Peng, Q.; Maji, S. K.; Tong, Y.; Yu, H.; Zhao, Y.; Ramamurthy, P. A ratiometric fluorescent molecular probe with enhanced two-photon response upon Zn^{2+} binding for in vitro and in vivo bioimaging. *Chemical Science* **2014**, *5*, 3469-3474.

(73) Luby-Phelps, K. Cytoarchitecture and physical properties of cytoplasm: volume, viscosity, diffusion, intracellular surface area. *International review of cytology* **1999**, *192*, 189-221.

(74) Su, D.; Teoh, C. L.; Wang, L.; Liu, X.; Chang, Y.-T. Motion-induced change in emission (MICE) for developing fluorescent probes. *Chemical Society Reviews* **2017**, *46*, 4833-4844.

(75) Platt, F. M.; d'Azzo, A.; Davidson, B. L.; Neufeld, E. F.; Tifft, C. J. Lysosomal storage diseases. *Nature reviews Disease primers* **2018**, *4*, 27.

(76) Zheng, A.; Liu, H.; Gao, X.; Xu, K.; Tang, B. A mitochondrial-targeting near-infrared fluorescent probe for revealing the effects of hydrogen peroxide and heavy metal ions on viscosity. *Analytical Chemistry* **2021**, *93*, 9244-9249.

(77) Ren, M.; Zhou, K.; Wang, L.; Liu, K.; Lin, W. Construction of a ratiometric two-photon fluorescent probe to monitor the changes of mitochondrial viscosity. *Sensors and Actuators B: Chemical* **2018**, *262*, 452-459.

(78) Shen, B.; Wang, L. F.; Zhi, X.; Qian, Y. Construction of a red emission BODIPY-based probe for tracing lysosomal viscosity changes in culture cells. *Sensors and Actuators B: Chemical* **2020**, *304*, 127271.

(79) Shi, W.-J.; Yang, J.; Wei, Y.-F.; Li, X.-T.; Yan, X.-H.; Wang, Y.; Leng, H.; Zheng, L.; Yan, J.-w. Novel cationic meso-CF_3 BODIPY-based AIE fluorescent rotors for imaging viscosity in mitochondria. *Chemical Communications* **2022**, *58*, 1930-1933.

(80) Jiang, N.; Fan, J.; Xu, F.; Peng, X.; Mu, H.; Wang, J.; Xiong, X. Ratiometric fluorescence imaging of cellular polarity: decrease in mitochondrial polarity in cancer cells. *Angewandte Chemie International Edition* **2015**, *54*, 2510-2514.

(81) Li, Q.; Hong, J.; Feng, S.; Gong, S.; Feng, G. Polarity-sensitive cell membrane probe reveals lower polarity of tumor cell membrane and its application for tumor diagnosis. *Analytical Chemistry* **2022**, *94*, 11089-11095.

(82) Liu, Y.; Zhou, S.; Jin, W.; Niu, J.; Wang, K.-N.; Liu, Z.; Yu, X. Engineering hydrophilic/hydrophobic moieties of ratiometric fluorescence probe to visualize whole cytoplasmic polarity. *Chemical Engineering Journal* **2023**, *459*, 141651.

(83) Casey, J. R.; Grinstein, S.; Orlowski, J. Sensors and regulators of intracellular pH. *Nature reviews Molecular cell biology* **2010**, *11*, 50-61.

(84) Grossi, M.; Morgunova, M.; Cheung, S.; Scholz, D.; Conroy, E.; Terrile, M.; Panarella, A.; Simpson, J. C.; Gallagher, W. M.; O'Shea, D. F. Lysosome triggered near-infrared fluorescence imaging of cellular trafficking processes in real time. *Nature communications* **2016**, *7*, 10855.

(85) Michelis, S.; Danglot, L.; Vauchelles, R.; Klymchenko, A. S.; Collot, M. Imaging and measuring vesicular acidification with a plasma membrane-targeted ratiometric pH probe. *Analytical Chemistry* **2022**, *94*, 5996-6003.

(86) Schniererová, K.; Janeková, H.; Joniak, J.; Putala, M.; Štacko, P.; Stankovičová, H. pH-Responsive Aminobenzocoumarins as Fluorescent Probes for Biological Acidity. *Chemistry–A European Journal* **2024**, *30*, e202400111.

(87) Arai, S.; Lee, S.-C.; Zhai, D.; Suzuki, M.; Chang, Y. T. A molecular fluorescent probe for targeted visualization of temperature at the endoplasmic reticulum. *Scientific reports* **2014**, *4*, 6701.

(88) Shen, F.; Yang, W.; Cui, J.; Hou, Y.; Bai, G. Small-molecule fluorogenic probe for the detection of mitochondrial temperature in vivo. *Analytical Chemistry* **2021**, *93*, 13417-13420.

(89) Huang, Z.; Li, N.; Zhang, X.; Xiao, Y. Mitochondria-anchored molecular thermometer quantitatively monitoring cellular inflammations. *Analytical Chemistry* **2021**, *93*, 5081-5088.

(90) Shi, Y.; Zhang, W.; Xue, Y.; Zhang, J. Fluorescent sensors for detecting and imaging metal ions in biological systems: recent advances and future perspectives. *Chemosensors* **2023**, *11*, 226.

(91) Zheng, X.; Cheng, W.; Ji, C.; Zhang, J.; Yin, M. Detection of metal ions in biological systems: A review. *Reviews in Analytical Chemistry* **2020**, *39*, 231-246.

(92) Carter, K. P.; Young, A. M.; Palmer, A. E. Fluorescent sensors for measuring metal ions in living systems. *Chemical reviews* **2014**, *114*, 4564-4601.

(93) Komatsu, K.; Urano, Y.; Kojima, H.; Nagano, T. Development of an iminocoumarin-based zinc sensor suitable for ratiometric fluorescence imaging of neuronal zinc. *Journal of the American Chemical Society* **2007**, *129*, 13447-13454.

(94) Zhang, D.; Zhu, Z.; Ma, X.; Jiang, Y. Preparation and Application of Multipurpose Zn2+ Sensor Based Salicylaldehyde. *Available at SSRN 5113886*.

(95) Yu, J.; Jiang, T.; Lin, Z.; Yu, H.; Wang, S.; Qi, Y. Two novel pyrene-based Schiff base fluorescent probes for the turn-on detection of Zn2+ and their application in bioimaging. *Microchemical Journal* **2025**, *209*, 112715.

(96) Baeyer, A.; Piccard, J. Untersuchungen über das Dimethylpyron. *Justus Liebigs Annalen der Chemie* **1911**, *384*, 208-224.

(97) Katritzky, A. R.; Thind, S. S. The synthesis and reactions of sterically constrained pyrylium and pyridinium salts. *Journal of the Chemical Society, Perkin Transactions 1* **1980**, 1895-1900.

(98) Aliaga, C.; Celis, F.; Lühr, S.; Oñate, R. TEMPO-attached pre-fluorescent probes based on pyridinium fluorophores. *Journal of fluorescence* **2015**, *25*, 979-983.

(99) Liu, W.; Fan, C.; Sun, R.; Xu, Y.-J.; Ge, J.-F. Near-infrared emission of dibenzoxanthenium and its application in the design of nitric oxide probes. *Organic & Biomolecular Chemistry* **2015**, *13*, 4532-4538.

(100) Wen, S. Y.; Zhang, W.; Ren, T. B.; Zhang, Q. L.; Liu, Y. P.; Shi, L.; Hu, R.; Zhang, X. B.; Yuan, L. Donor and ring-fusing engineering for far-red to near-infrared triphenylpyrylium fluorophores with enhanced fluorescence performance for sensing and imaging. *Chemistry–A European Journal* **2019**, *25*, 6973-6979.

(101) Ma, Y.; Pang, Y.; Chabbra, S.; Reijerse, E. J.; Schnegg, A.; Niski, J.; Leutzsch, M.; Cornella, J. Radical C− N borylation of aromatic amines enabled by a pyrylium reagent. *Chemistry–A European Journal* **2020**, *26*, 3738-3743.

(102) Basavaraja, D.; Dey, D.; Varsha, T. L.; Salfeena, C. T. F.; Panda, M. K.; Somappa, S. B. Rapid visual detection of amines by pyrylium salts for food spoilage taggant. *ACS Appl. Bio Mater* **2020**, *3*, 772-778.

(103) Chakraborty, S.; Joseph, M. M.; Varughese, S.; Ghosh, S.; Maiti, K. K.; Samanta, A.; Ajayaghosh, A. A new pentacyclic pyrylium fluorescent probe that responds to pH imbalance during apoptosis. *Chemical Science* **2020**, *11*, 12695-12700.

(104) Chakraborty, S.; Bindra, A. K.; Thomas, A.; Zhao, Y.; Ajayaghosh, A. pH-Assisted Multichannel Heat Shock Monitoring in Endoplasmic Reticulum with a Pyridinium Fluorophore. *Chemical Science* **2024**.

A Pyridinium Fluorophore for the Detection of Zinc Ions under Autophagy Conditions

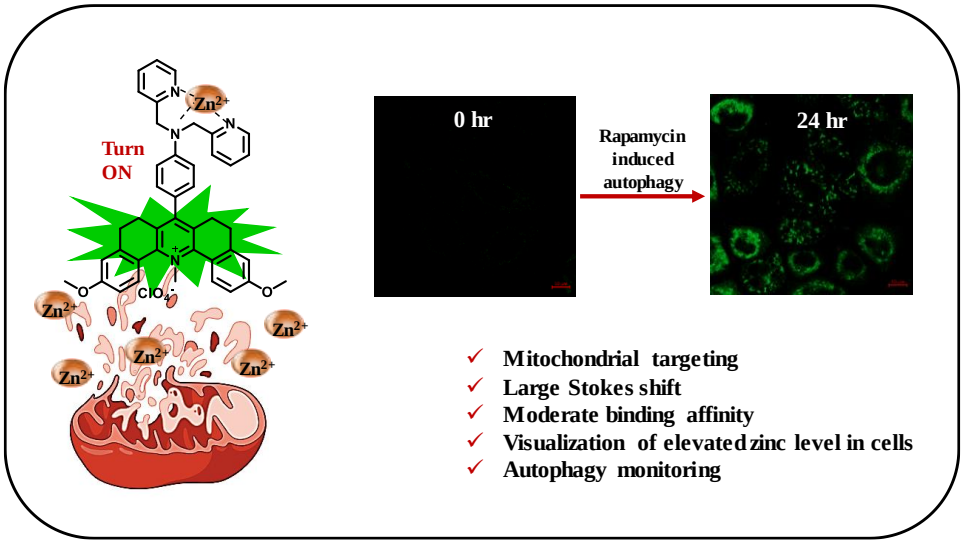

2A.1. Abstract

Small molecular fluorescent probes for sensing and imaging various analytes and biological specimens are of great importance in clinical diagnostics, therapy, and disease management. Zinc is an essential trace element crucial for numerous physiological functions. Altered zinc ion levels are associated with conditions such as neurodegenerative diseases, ADHD, diabetes, hypertension, etc. Since the cellular concentration of free Zn^{2+} varies from nanomolar to micromolar range during cellular processes and the high affinity Zn^{2+} imaging probes tend to saturate at lower concentrations of free Zn^{2+}, fluorescence based probes with moderate binding affinity are desirable for tracking higher zinc ion concentrations in the cells. Herein, we report a new, pentacyclic pyridinium based probe, ***PYD-PA,*** *having a pendant N,N-di(pyridin-2-*

*ylmethyl)amine (DPA) for Zn^{2+} detection in the cellular environment. The probe has a donor-acceptor design with DPA as the donor and pyridinium as the acceptor. The pyridinium core, with its positive charge, also serves as a mitochondria targeting unit and enhances aqueous solubility, whereas the pendent DPA acts as the coordination site for Zn^{2+}. **PYD-PA** initially exhibited a quenched green fluorescence due to photoinduced electron transfer (PET.) Zn^{2+} binding resulted in the inhibition of PET process leading to threefold enhancement in fluorescence intensity. Further, the probe showed a selective response to Zn^{2+} over other biologically relevant metal ions with a moderate binding affinity (K_a = 6.29 ×10^4 M^{-1}), 1:1 binding stoichiometry, good photostability, pH insensitivity, and low cytotoxicity. The demonstration of bioimaging in SK-BR-3 breast cancer cell lines confirmed the intracellular Zn ion sensing ability of the probe. Additionally, the probe was successfully applied for real-time monitoring of the fluctuation of intracellular free zinc ions during autophagy conditions, demonstrating its potential for cellular imaging of Zn^{2+} at higher intracellular concentrations.*

2A.2. Introduction

Mitochondria is the powerhouse of a cell, which plays a crucial role in maintaining cellular health.[1, 2] Mitochondrial dysfunction is closely associated with various disease conditions such as cancer, cardiovascular diseases, and neurological disorders.[3] As a protective mechanism, cells undergo a process called mitophagy, which prevents the accumulation of dysfunctional mitochondria.[4] Several techniques have been used to understand this process which include western blot, fluorescence microscopy, transmission electron microscopy, and flow cytometry. Most of these techniques rely on the measurement of LC3-II proteins expressed on the autophagosomes.[5] Although these methods have achieved some success in monitoring the autophagy process, they are tedious and time consuming, expensive, and have difficulty in visualizing autophagosomes. In this context, small molecular fluorescent probes can be promising

alternatives due to their easy synthesis, low cost, high spatial and temporal resolution, and ability to track the process with least disruption to normal cellular function.[6]

Several small molecular fluorescent probes have already been developed to track autophagy process by monitoring the changes in pH, polarity, viscosity, Reactive Oxygen Species (ROS), and Reactive Nitrogen Species (RNS) levels in cells.[7-11] Even though there are several reports on the close correlation between intracellular Zn^{2+} concentration and autophagy process, there have been very few attempts to develop a Zn^{2+} sensor to monitor the autophagy process.[12, 13] Zn^{2+} is a biologically relevant transition metal ion that plays a crucial role in cell homeostasis, neurological functions, insulin secretion, immune function, signal transduction, and apoptosis.[14-16] Therefore, zinc probes have been used for different applications such as prostate cancer identification, apoptosis monitoring, controlled photodynamic therapy, etc.[17-20]

Hwang et al. have reported the activation of autophagy by tamoxifen-induced accumulation of labile zinc ions in autophagosomes and lysosomes in MCF-7 cells.[21] Further, Lee et al. have found an increase of zinc ions in autophagic vacuoles, including autolysosomes, as a pre-requisite for lysosomal membrane permeabilization and cell death in cultured brain cells.[12] This increase in Zn^{2+} level can be attributed to its release under oxidative conditions from zinc-binding proteins such as metallothioneins. Investigating the role of Zn^{2+} in autophagy in human hepatoma cells VL-17A, Yoo et al. have demonstrated that Zn^{2+} depletion significantly suppressed autophagy, whereas Zn^{2+} addition to the medium stimulated autophagy.[22] There is a report on the role of Zn^{2+} as a positive regulator of autophagy by Kim and co-workers, showing that the zinc ionophore PCI-5002 radiosensitizes lung cancer cells by inducing autophagic cell death.[23]

In 2021, Diao and coworkers developed a "turn on" Zn^{2+} fluorescent probe and utilized it to monitor mitophagy **(Figure 2A.1A** and **B)**.[24] The probe showed a 2.0-fold increase in green

fluorescence intensity of the mitophagic cells when compared to that of non-autophagic cells, confirming the rise in the average labile Zn^{2+} levels. Additionally, using Structured Illumination Microscopy (SIM) imaging, they observed an increase in labile Zn^{2+} within both the mitochondria and ER during carbonyl cyanide 3-chlorophenylhydrazone (CCCP)-induced mitophagy in HeLa cells **(Figure 2A.1C** and **D)**. Notably, the levels of labile Zn^{2+} varied between the mitochondria and ER, with autophagosomes and autolysosomes displaying the most significant release of labile Zn^{2+}. This elevated labile Zn^{2+} in autophagosomes and autolysosomes may result from the degradation of Zn^{2+}-containing proteins, similar to the release observed during tamoxifen-induced autophagy in MCF-7 cells. These findings suggest a strong link between autophagy and intracellular Zn^{2+} levels, emphasizing the need for further real-time studies.

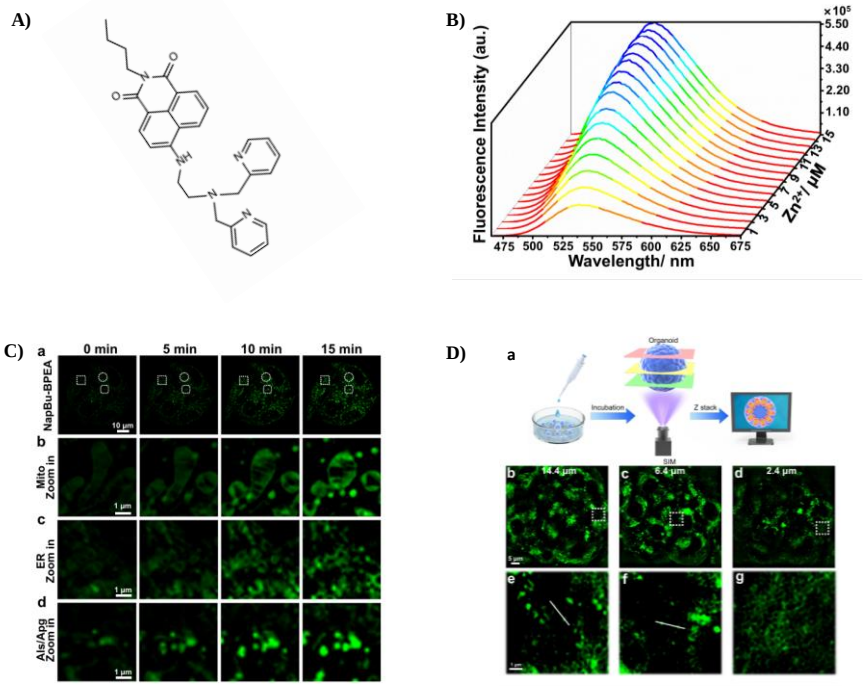

Figure 2A.1. (A) Structure of the Zn^{2+} probe; (B) Changes in emission spectra of the probe upon Zn^{2+} binding; (C)Time-lapse SIM images of HeLa cells stained by NapBu-BPEA recorded upon incubation with 20 μM CCCP; and zoom-in images of regions of interest marked with squares (b, mitochondria), circles (c, ERs), and rounded squares (d, autophagosomes/autolysosomes); (D) SIM imaging of organoids treated with CCCP for 24 h, a: Schematic diagram of Z-stack SIM

imaging for organoid, b-d: SIM images of organoids recorded at different imaging depths, e-g: enlarged images for the regions of interest showed in the frames in b-d (Figure adapted from reference 24).

Zinc is the second most abundant transition metal ion in the human body, with intracellular zinc ion concentrations maintained in the range from 100 μM to 500 μM.[25-27] However, 99% of intracellular zinc is in the protein bound form and the concentration of labile zinc is minimal, estimated between 10^{-9} M to 10^{-12} M.[28] Numerous fluorescent probes, with detection limits in the picomolar to nanomolar range, have been developed for intracellular zinc sensing.[29-34] The affinity of a probe towards the analyte is a crucial parameter in sensing applications. For example, a low affinity probe may not respond to a low zinc ion concentration, while a high affinity probe could easily become saturated at a high zinc ion concentration.[35] During processes such as autophagy, intracellular zinc ion concentrations can rise to the micromolar range due to the release of zinc ions from zinc-bound proteins like metallothioneins under oxidative stress. In this context, using a high-affinity probe with a detection limit in the nanomolar or lower range may result in saturation of fluorescent signals even with a small increase in Zn^{2+} levels. Therefore, an imaging probe with modest affinity would be more suitable for tracking elevated Zn^{2+} levels (in the micromolar range), especially during cellular processes like autophagy.

Although numerous reported studies have a close correlation between Zn^{2+} and autophagy, only a few attempts have been made to develop Zn^{2+} sensors for monitoring autophagy. To address this issue, we designed a mitochondria targeting, pyridinium-based fluorescence imaging probe with a pendant *N*,*N*-di(pyridin-2-ylmethyl)amine (DPA) group to track elevated Zn^{2+} levels in the cellular environment during autophagy (**PYD-PA**). The probe, **PYD-PA** has a donor-acceptor (D-A) design with a rigid pentacyclic pyridinium based acceptor core and a pendant *N*,*N*-di(pyridin-2-ylmethyl)amine (DPA) donor. The pyridinium moiety, with its positive charge, serves also as an

inherent mitochondria-targeting unit,[36] while the DPA acts as the coordination site for Zn^{2+}.[37] **PYD-PA** in buffered aqueous solutions shows a quenched, green fluorescence due to the efficient, photoinduced electron transfer from the DPA to the pyridinium chromophore. As per the design, Zn^{2+} binding to the DPA receptor will perturb the PET process, resulting in an enhancement of the fluorescence emission from the probe **(Figure 2A.2)**. We have chosen DPA as the receptor to achieve moderate binding affinity, ensuring that the probe remains non-fluorescent under normal sub-nanomolar cellular Zn^{2+} levels. However, it acts as a fluorescence "Turn-on" sensor, specifically tracking elevated Zn^{2+} levels in cells through fluorescence enhancement upon binding. The following sections will outline the general synthetic strategy and the application of this new imaging agent for monitoring Zn^{2+} levels in the cellular environment.

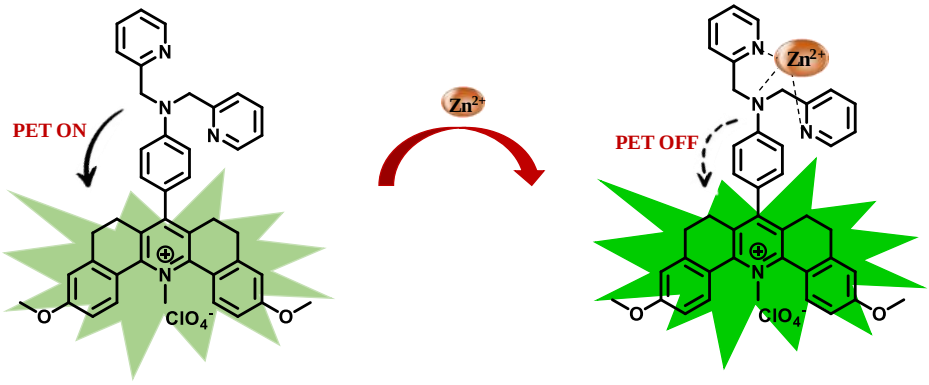

Figure 2A.2. Design strategy of the probe, **PYD-PA**.

2A.3. Results and Discussion

2A.3.1 Synthesis and characterisation of PYD-PA

The synthesis of the probe, **PYD-PA** has been achieved by cyclization reaction of 4-(bis(pyridin-2-ylmethyl)amino)benzaldehyde with 6-methoxytetralone followed by methylamine reaction for converting pyrylium to pyridinium fluorophore (**Scheme 2A.1**).[38] All the intermediates and final products were characterized by ^{1}H NMR, ^{13}C NMR, and HRMS, details of which are provided in the experimental section.

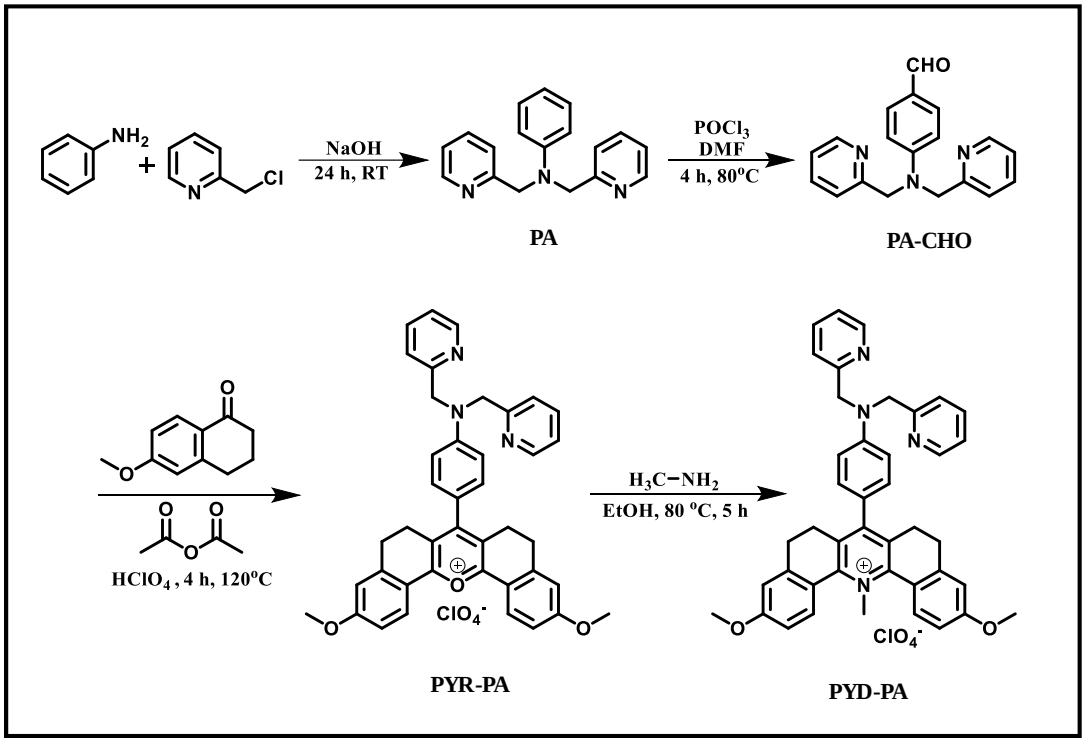

Scheme 2A.1. Scheme for the synthesis of **PYD-PA**.

2A.3.2. Photophysical studies of PYD-PA

PYD-PA in HEPES buffer displayed an absorption maximum at 402 nm and a fluorescence maximum at 542 nm, with a significant Stokes shift of 6425 cm^{-1} **(Figure 2A.3A)**. A Contour map of the three-dimensional fluorescence spectra at different excitation wavelengths is depicted in **Figure 2A.3B**, which confirms that fluorescence intensity approaches its maximum when the irradiation wavelength is at 400 nm. Further, absorption and emission spectra of the probe was recorded in different solvents, including water, ACN, chloroform, DMSO, methanol, THF and toluene. All the stock solutions (10 mM) were prepared in DMSO and diluted using different solvents, as required. The probe, **PYD-PA**, exhibited absorption (λ_{abs}) and emission (λ_{em}) maxima at 401 nm and at 542 nm, respectively, with a significant Stokes shift of 6487 cm^{-1} in water. In other solvents, such as acetonitrile, chloroform, DMSO, methanol, THF and toluene, **PYD-PA** displayed a slight bathochromic shift in the absorption maximum while the emission

maximum did not shift significantly, indicating its non-solvatochromic behavior **(Figure 2A.4 & Table 2A.1)**.

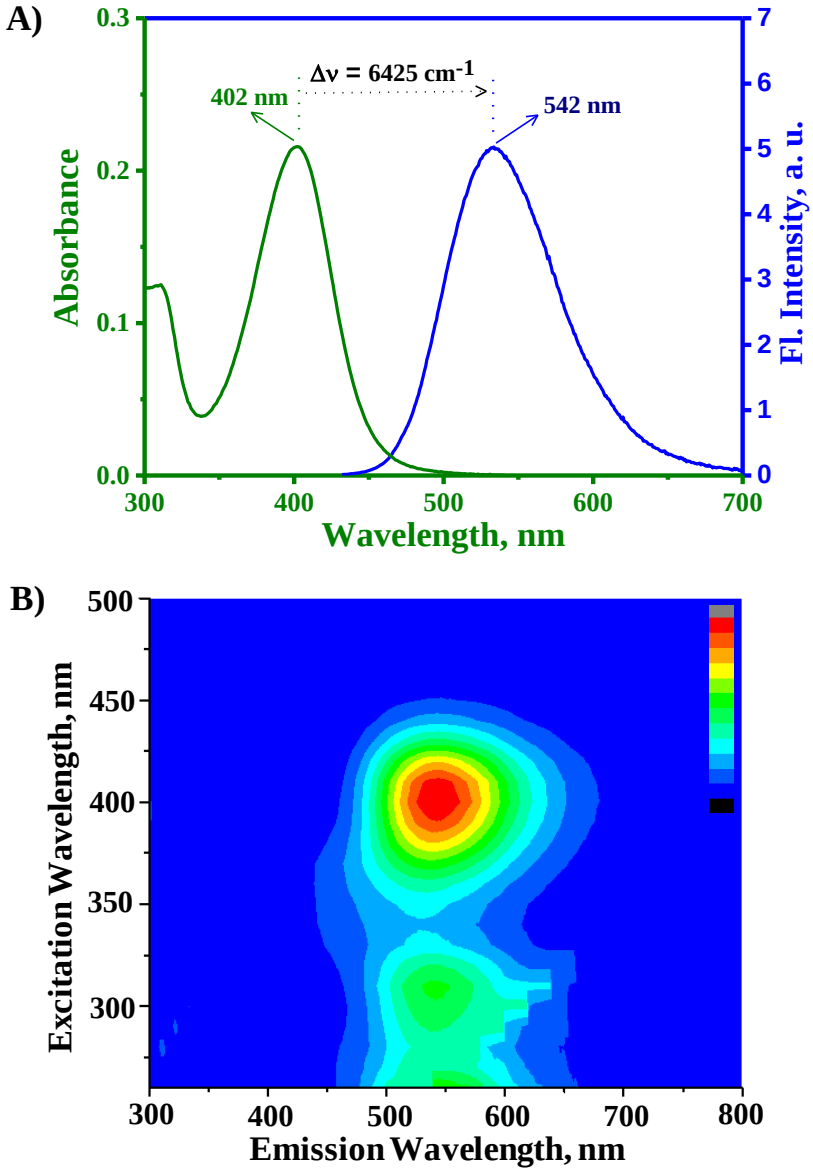

Figure 2A.3. (A) Absorption and emission spectra of **PYD-PA** (10 μM) in HEPES buffer (0.1 M, pH = 7.4) and (B) Contour map of the three-dimensional fluorescence excitation-emission spectra.

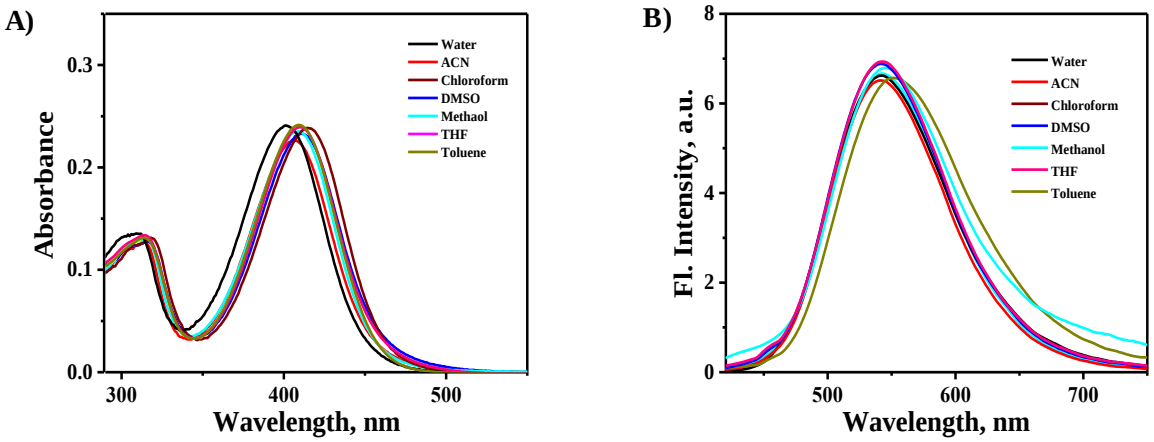

Figure 2A.4. Solvent dependent (A) absorption and (B) emission of **PYD-PA** (10 μM)

Table 2A.1. The solvent dependent absorption and emission details of **PYD-PA**.

Solvent	Ab. max (nm)	Em. max (nm)	Stokes Shift (cm^{-1})
Toluene	409	553	6367
Chloroform	414	545	5806
Acetonitrile	406	542	6180
DMSO	410	542	5940
Water	401	542	6487
Methanol	408	543	6094
THF	410	542	5940

2A.3.3. Aqueous solubility of PYD-PA

Many organic fluorophores have limited water solubility, which limits their use in biological applications. Aggregation of fluorophores may result in fluorescence quenching and uneven intracellular distribution, leading to inconsistent signal and data errors in cellular imaging. The positively charged pyridinium core enables **PYD-PA** to dissolve effectively in polar organic

solvents and buffers. The concentration-dependent absorption spectra of **PYD-PA** were recorded in 0.1M aqueous HEPES buffer at pH 7.4 **(Figure 2A.5A)**. The absorption intensity at 402 nm increased linearly with concentration, with a molar extinction coefficient of 22,840 $M^{-1}cm^{-1}$ **(Figure 2A.5B)**, confirming good aqueous solubility and the absence of any aggregated state in the aqueous medium.

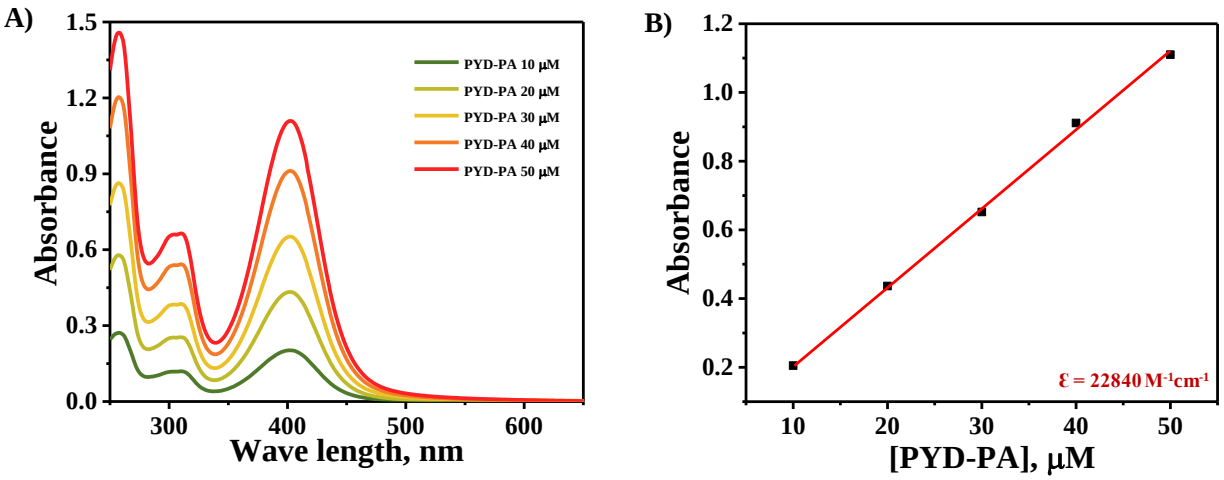

Figure 2A.5. (A) Absorption spectra of **PYD-PA** at different concentrations (10-50 µM) in HEPES buffer (0.1 M, pH = 7.4) and (B) The secondary plot of absorbance maximum (λ_{max} = 402 nm) vs. concentration of **PYD-PA**.

2A.3.4. pH Response of PYD-PA

To investigate the pH sensitivity of the probe, fluorescence spectra of **PYD-PA** were recorded in different pH (4 - 9) HEPES buffer solutions. The probe, **PYD-PA** displayed negligible changes in emission intensity at the physiological pH range of 5 - 8, indicating minimal impact of acidity on its photophysical properties. On the other hand, at pH 4, the probe displayed a significant enhancement in fluorescence emission intensity due to protonation of the DPA amine which further attests to the possible PET fluorescence quenching of the probe **(Figure 2A.6)**. However, at the physiological pH range, **PYD-PA** remains unprotonated and hence, the pH response at lower pH conditions will not interfere with the cellular metal-probe interactions.

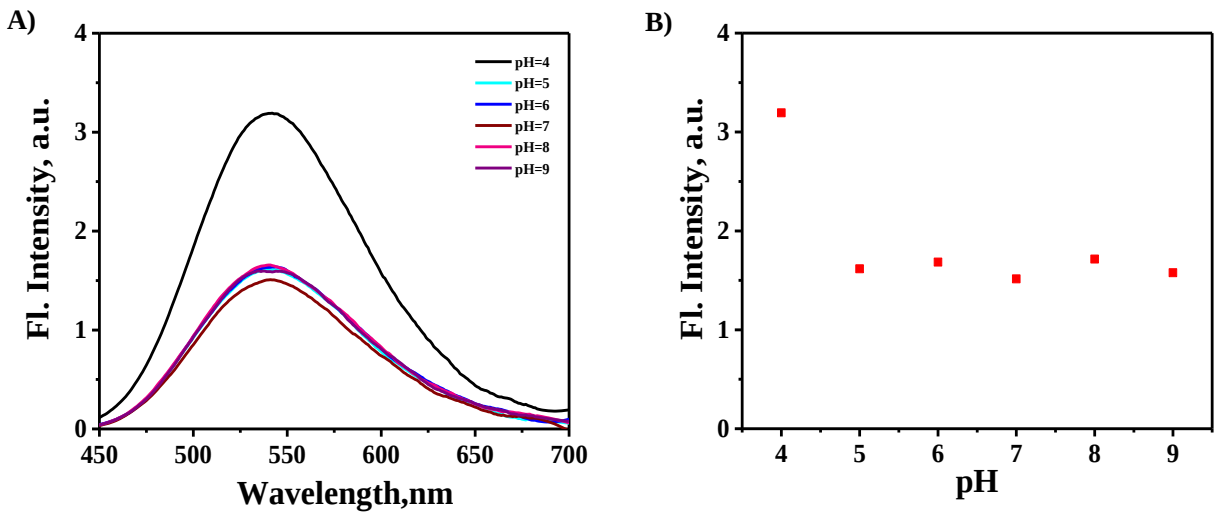

Figure 2A.6. (A) Emission spectra of **PYD-PA** (10 µM) in HEPES buffer (0.1 M) of different pH ranging from pH 4 to 9 (λ_{ex} = 400 nm); (B) The secondary plot of fluorescence intensity at emission maximum of **PYD-PA** at different pH.

2A.3.5. Photostability of PYD-PA

To investigate the photobleaching effect of the probe, photostability studies of **PYD-PA** were conducted in HEPES buffer (0.1 M, pH 7.4) under a 200 W mercury lamp on an Oriel optical bench. The sample was positioned 50 cm from the light source and exposed for 60 minutes using a 400 nm long-pass filter, and the stability was compared with Coumarin 153 and Rhodamine B. Upon irradiation, the probe exhibited stable emission profiles with time, indicating the excellent photostability of the probe. The secondary plot of fluorescence intensity versus time for **PYD-PA** confirmed minimal photobleaching of the probe when compared to Coumarin 153 and Rhodamine B **(Figure 2A.7)**.

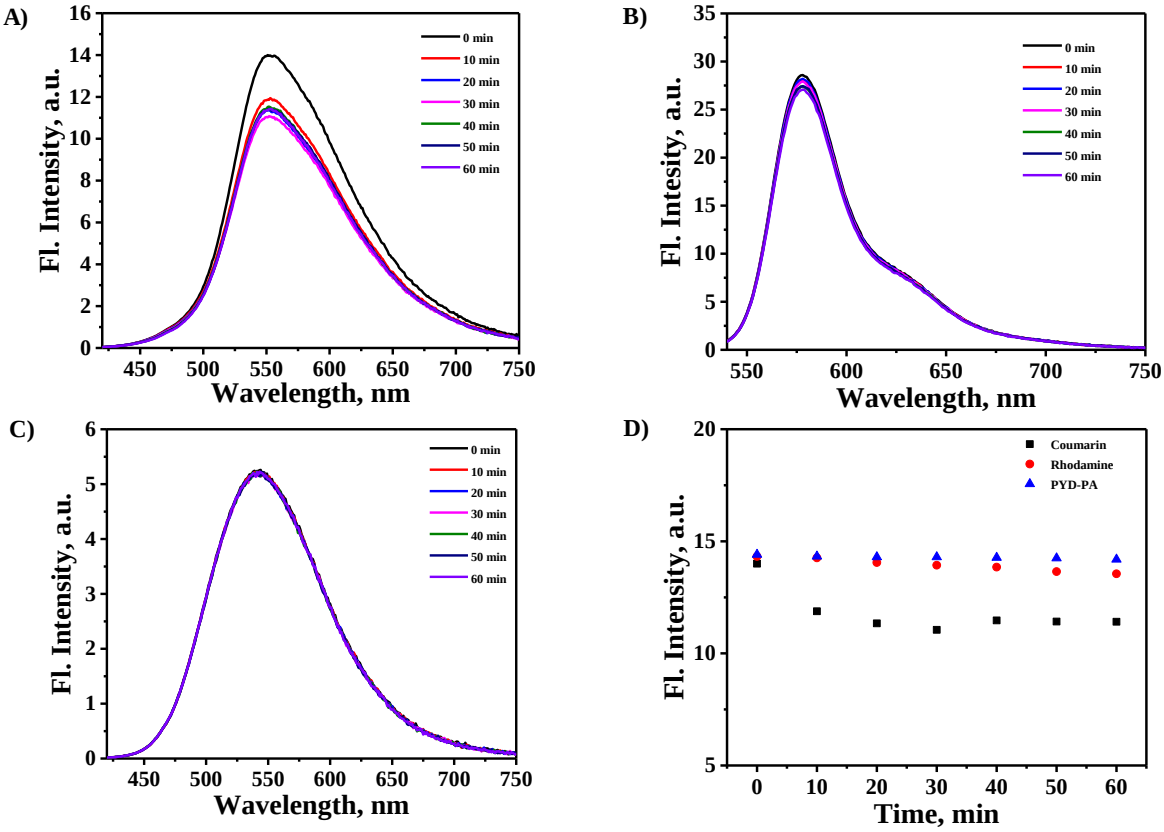

Figure 2A.7. Emission of (A) Coumarin 153; (B) Rhodamine B; (C) PYD-PA and (D) The secondary plot of fluorescence intensity for (A)-(C) at the emission maximum with time.

2A.3.6. Zn^{2+} sensing studies of PYD-PA

The changes in the absorption and emission properties of **PYD-PA** in presence of Zn^{2+} were evaluated by titrating a buffered solution of **PYD-PA** against 0-100 µM Zinc chloride. Absorption spectra in the presence of Zn^{2+} did not show significant changes, indicating that the Zn^{2+} binding to the DPA unit has negligible effect on the chromophore ground state properties **(Figure 2A.8A)**. On the other hand, the fluorescence emission of **PYD-PA** with a maximum at 542 nm showed a gradual enhancement with added Zn^{2+} **(Figure 2A.8B** and **C)**, without any shift in the emission maximum. This enhancement in emission could be attributed to the disruption of PET from the di-2-picolylamine moiety to pyridinium fluorophore due to the binding of Zn^{2+}.

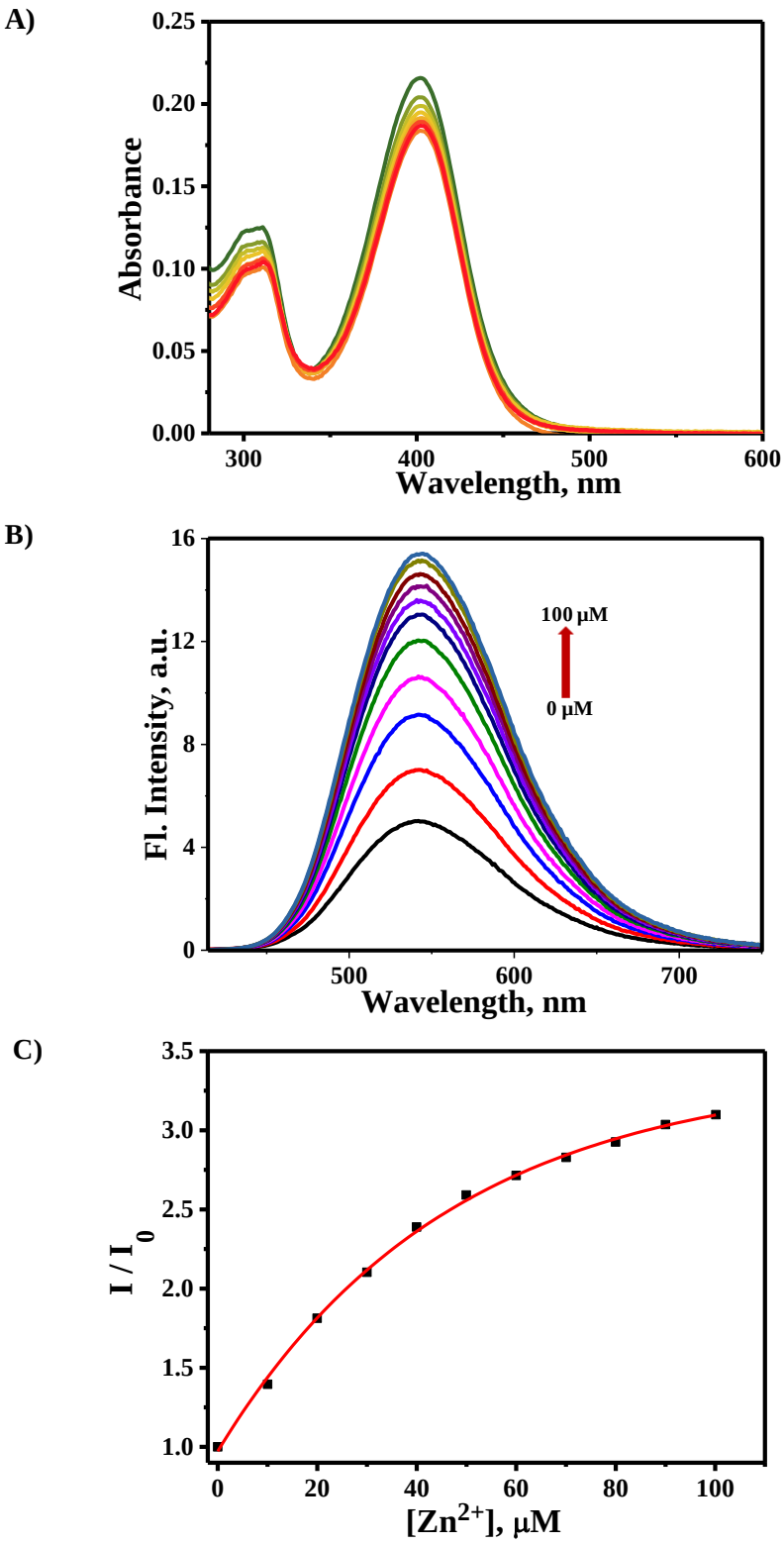

Figure 2A.8. Changes in the (A) absorption and (B) fluorescence spectrum of **PYD-PA** (10 µ M) against varying concentrations of Zn^{2+} (0-100 µM) in HEPES buffer (0.1 M, pH = 7.4); (C) corresponding changes in the ratio of integrated, fluorescence area.

2A.3.7. Quantum yield measurements

Quantum yield (QY) measurements of the probe **PYD-PA** before and after addition of Zn^{2+} were carried out in standard absorption and emission spectrometers using the following equation,

$$\Phi_f^i = \frac{F^i f_s n_i^2}{F^s f_i n_s^2} \Phi_f^s \qquad \text{Equation (2A.1)}$$

where Φ^i_f and Φ^s_f are the photoluminescence QY of the sample and that of the standard, F^i and F^s are the integrated intensities (areas) of sample and standard emission spectra, f_x is the optical density at the excitation wavelength, n_i and n_s are the refractive indices of the sample and reference solution, respectively.[39] Coumarin 153 in ethanol with quantum yield 0.38 was used as standard.[40] The relative quantum yield values in HEPES buffer are found to be 0.44% for the probe alone and 1.1% after addition of Zn^{2+}, indicating a moderate (2.5 times) enhancement of the fluorescence emission in presence of Zn^{2+}.

2A.3.8. Job's plot and binding constant

The binding mode of probe **PYD-PA** and Zn^{2+} was investigated using Job's method of continuous variation by controlling the total concentration of the probe and Zn^{2+} at 50 μM in HEPES buffer **(Figure 2A.9A)**. The maximum emission intensity reached at a mole fraction of 0.5, indicating that the binding stoichiometry between the probe **PYD-PA** and Zn^{2+} was 1:1. The apparent association constant (K_a) of **PYD-PA-Zn^{2+}** complex was determined by the Benesi-Hildebrand Equation,

$$\frac{1}{(I - I_0)} = \frac{1}{\{K_a \times (I_{max} - I_0) \times [Zn^{2+}]\}} + \frac{1}{(I_{max} - I_0)} \qquad \text{Equation (2A.2)}$$

where, I is the fluorescence intensity at 542 nm at any given Zn^{2+} concentration, I_0 is the fluorescence intensity at 540 nm in the absence of Zn^{2+}, and I_{max} is the maximum fluorescence intensity at 542 nm in the presence of Zn^{2+} in solution. The association constant K_a was evaluated graphically by plotting $1/(I - I_0)$ against $1/[Zn^{2+}]$. Data were linearly fitted and the K_a value was calculated to be 6.3×10^4 M^{-1} from the slope and intercept of the line **(Figure 2A.9B)**.

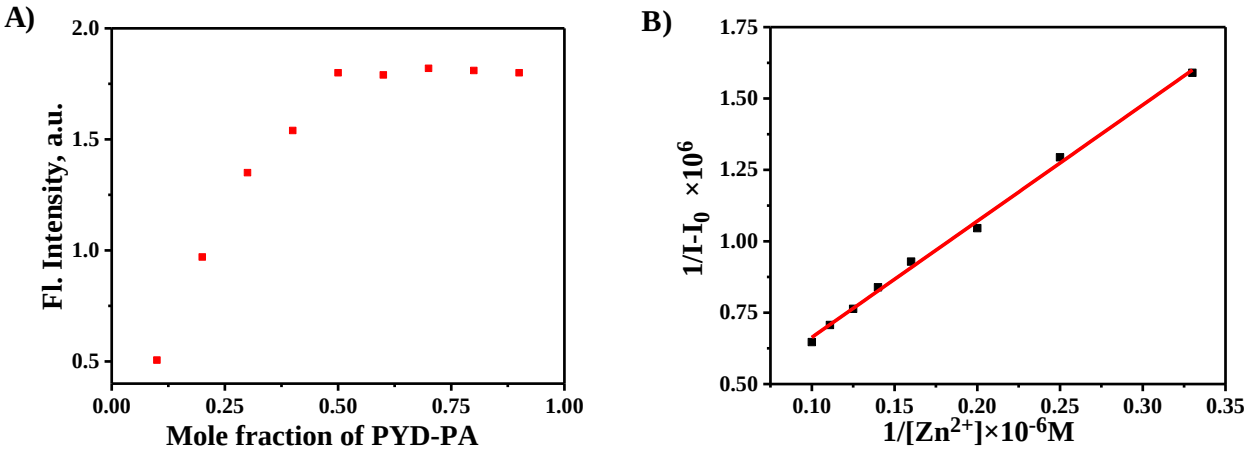

Figure 2A.9. (A) Job's plot for the determination of the stoichiometry of **PYD-PA** and Zn^{2+} in HEPES buffer (0.1 M, pH=7.4), the total concentration was 50 µM and (B) The Benesi–Hildebrand plot of $1/(I-I_0)$ vs. $1/[Zn^{2+}]$.

2A.3.9. Detection limit

The detection limit for the binding of Zn^{2+} was calculated based on the fluorescence titration curve of **PYD-PA** (1 µM) in the presence of Zn^{2+} (0-10 µM). The fluorescence intensity of **PYD-PA** and the standard deviation of the blank measurement were carried out for three times. The detection limit was calculated with the following equation:

$$\text{Detection limit} = 3\sigma/k \qquad \text{Equation (2A.3)}$$

where, σ is the standard deviation of the blank measurement, and k is the slope between the fluorescence intensity and Zn^{2+} concentrations. The limit of detection (LOD) was calculated to be 0.60 µM **(Figure 2A.10)**, indicating the probe's moderate affinity for Zn^{2+}. Since high affinity

probes easily get saturated even with a small change in zinc ion concentrations, probes with moderate binding affinity are extremely useful for monitoring elevated Zn^{2+} concentrations during processes like autophagy.

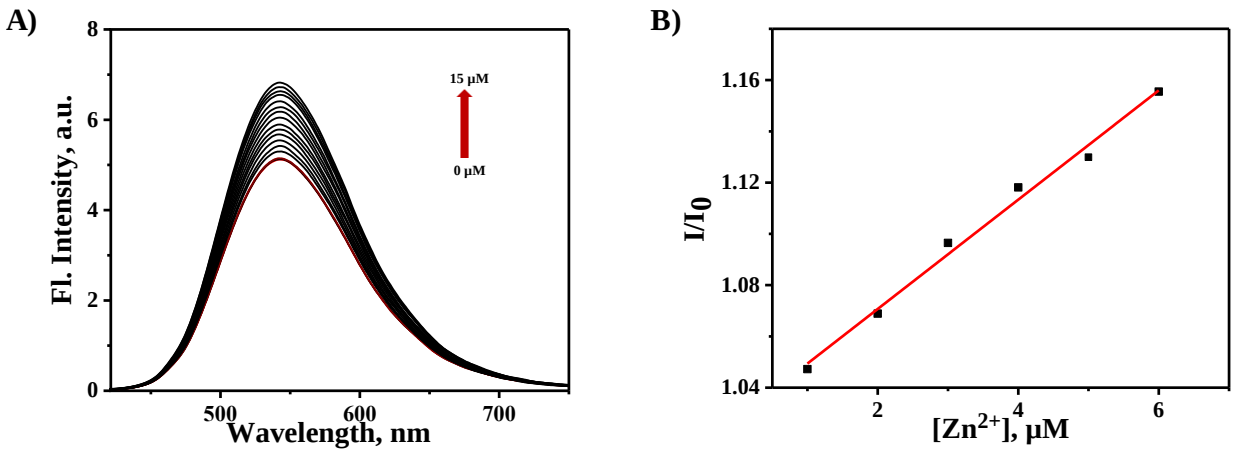

Figure 2A.10. (A) Fluorescence spectra of **PYD-PA** (1 μM) upon the titration of Zn^{2+} (0-15μM) in HEPES buffer (0.1 M, pH = 7.4). (B) Fluorescence ratio (I/I_0) changes as a function of Zn^{2+} concentration (0-6 μM). Excitation wavelength was 400 nm.

2A.3.10. Selectivity studies

The selective binding of the probe, **PYD-PA** towards Zn^{2+} was investigated by monitoring the changes in the fluorescence response of the probe in the presence of various biologically relevant metal ions; [**PYD-PA**]: [metal ion] = 1:10 **(Figure 2A.11)**. The probe displayed negligible fluorescence changes in presence of biologically relevant and competing cations such as Na^+, K^+, Ag^+, Mg^{2+}, Fe^{2+}, Fe^{3+}, Mg^{2+}, Mn^{2+}, Pb^{2+} and Co^{2+}. Among other toxic metal cations in the same group, the presence of Cd^{2+} and Hg^{2+} caused a slight fluorescence enhancement of the probe. However, this will not interfere with cellular imaging of Zn^{2+} due to the negligible concentrations of these cations in cells.[41, 42] To study the influence of other metal ions on Zn^{2+} binding with the probe **PYD-PA**, competitive experiments were performed with different metal ions (100 μM) in the presence of Zn^{2+} (100 μM) **(Figure 2A.12** to **14)**. Addition of Zn^{2+} in presence of these metal

ions resulted in an enhancement of fluorescence, confirming the competitive binding of Zn^{2+} even in the presence of these metal ions. On the other hand, addition of Cu^{2+} resulted in a significant quenching of the fluorescence. Further addition of Zn^{2+} to this solution showed negligible fluorescence changes, revealing comparatively stronger interactions of Cu^{2+} with the DPA receptor moiety.[43]

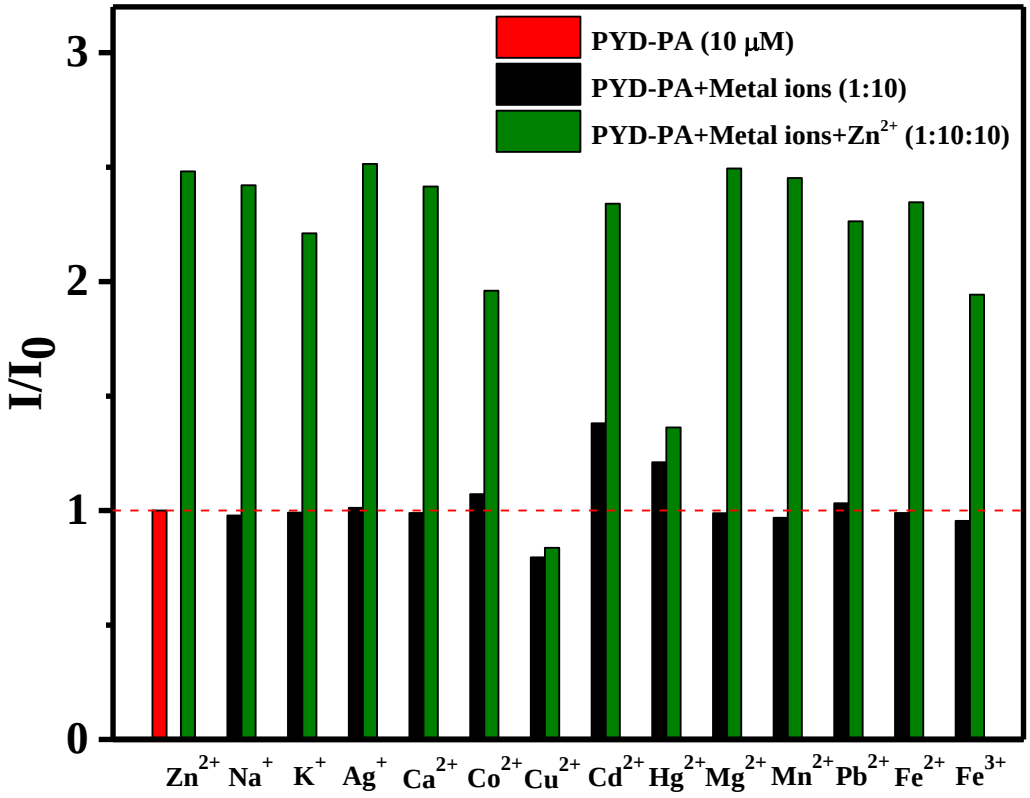

Figure 2A.11. Fluorescence response of **PYD-PA** (10 μM) at 542 nm (the red bar portion), with 100 μM of other metal ions (the black bar portion) and to the mixture of other metal ions (100 μM) with 100 μM of Zn^{2+} (the green bar portion).

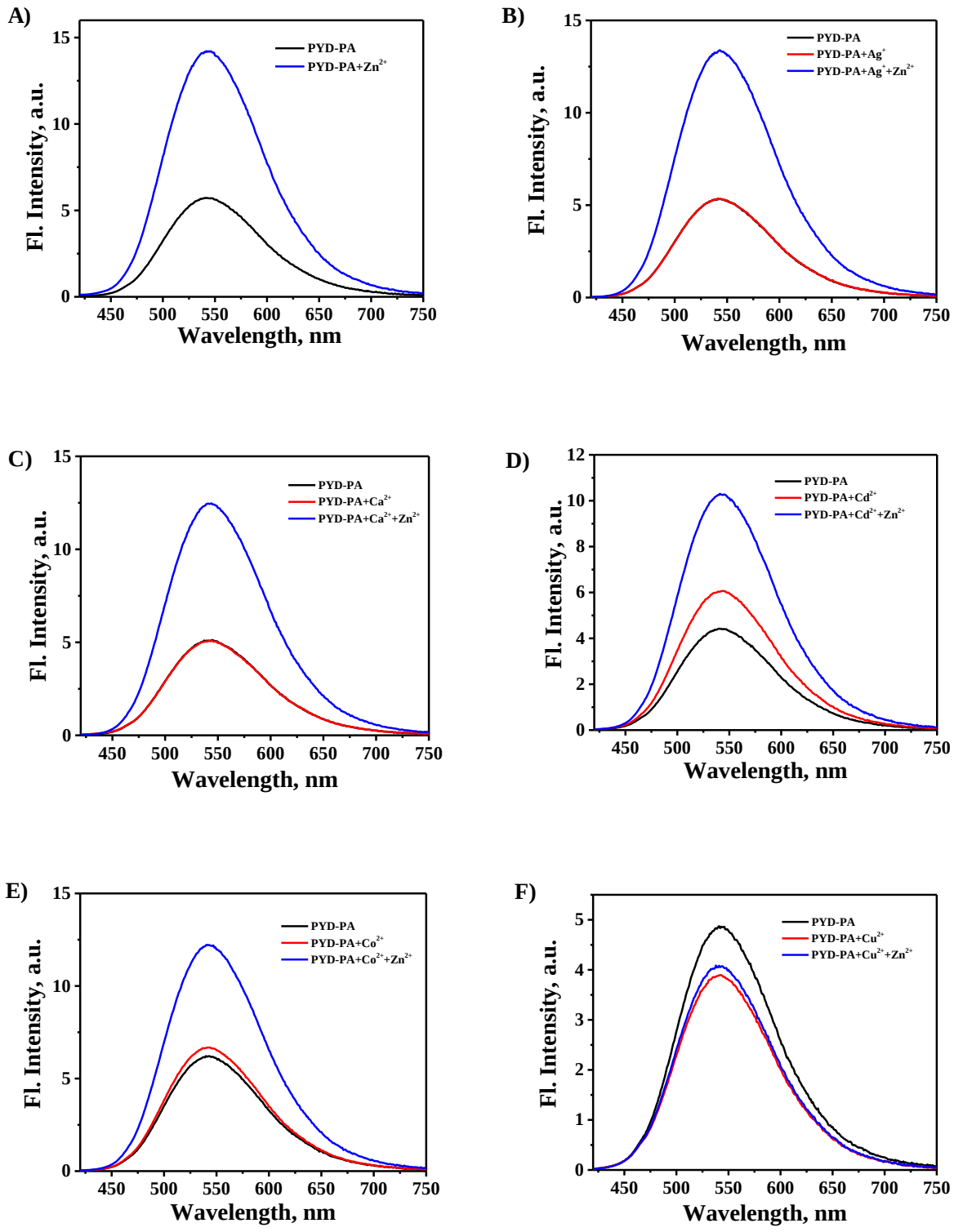

Figure 2A.12. Fluorescence response of the probe **PYD-PA** (10 μM) to other metal ions (100 μM) in HEPES buffer (0.1 M, pH = 7.4) A) Zn^{2+}; B) Ag^{+}; C) Ca^{2+}; D) Cd^{2+}; E) Co^{2+}; F) Cu^{2+}.

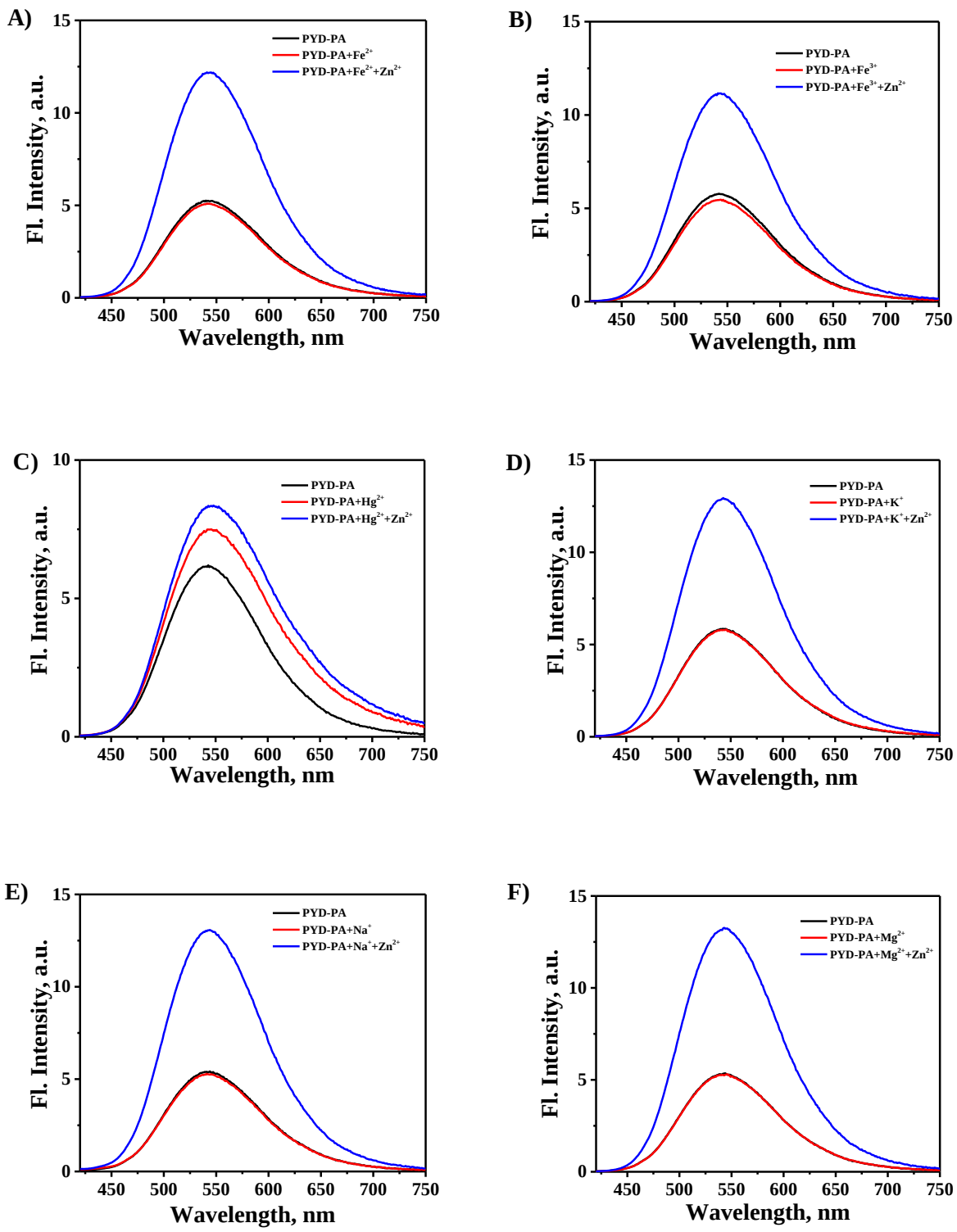

Figure 2A.13. Fluorescence response of the probe **PYD-PA** (10 μM) to other metal ions (100 μM) in HEPES buffer (0.1 M, pH = 7.4) A) Fe^{2+}; B) Fe^{3+}; C) Hg^{2+}; D) K^{+}; E) Na^{+}; F) Mg^{2+}.

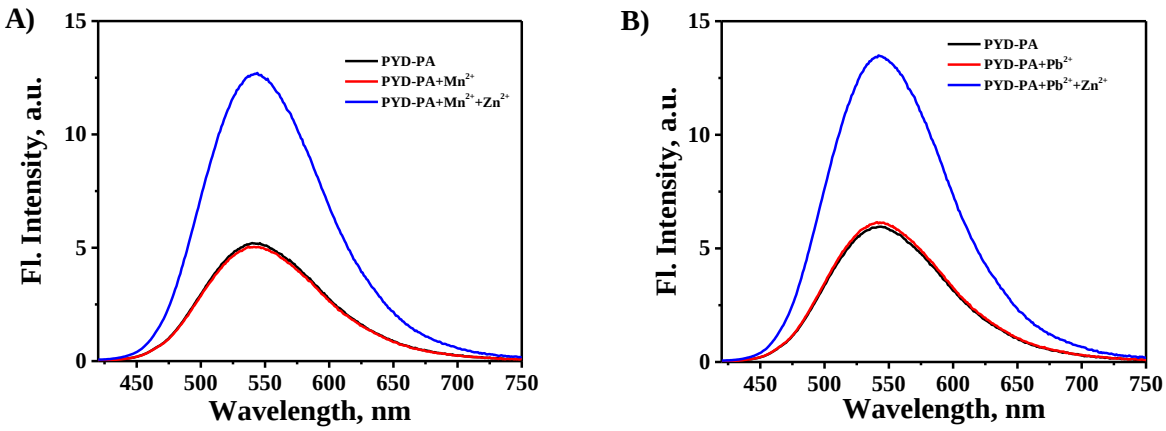

Figure 2A.14. Fluorescence response of the probe **PYD-PA** (10 μM) to other metal ions (100 μM) in HEPES buffer (0.1 M, pH = 7.4) A) Mn^{2+} and B) Pb^{2+}.

2A.3.11. ^{1}H-NMR titration experiment

In order to confirm the site of Zn^{2+} coordination, ^{1}H-NMR measurements of **PYD-PA** and its corresponding 1:1 Zn^{2+} complex were performed in acetonitrile **(Figure 2A.15)**. After the addition of Zn^{2+}, the ^{1}H NMR signals of the protons on carbon adjacent to the N atom (marked n), exhibited a downfield shift from 8.57 to 9.12 ppm, indicating significant deshielding upon Zn^{2+} coordination. Similarly, all the aromatic protons of the DPA units (marked l, k, j) and the two protons in the benzene ring near to the imino N atom (marked f) showed downfield shifts from 7.74 to 8.11, 7.35 to 7.65, 7.25 to 7.63 and 6.88 to 7.13, respectively. However, the protons of pyridinium core and the aliphatic protons remain unaffected in the presence of Zn^{2+}. These results indicate that the imino N atom and the two pyridine N atoms are involved in Zn^{2+} coordination in the Zn-complex.[44]

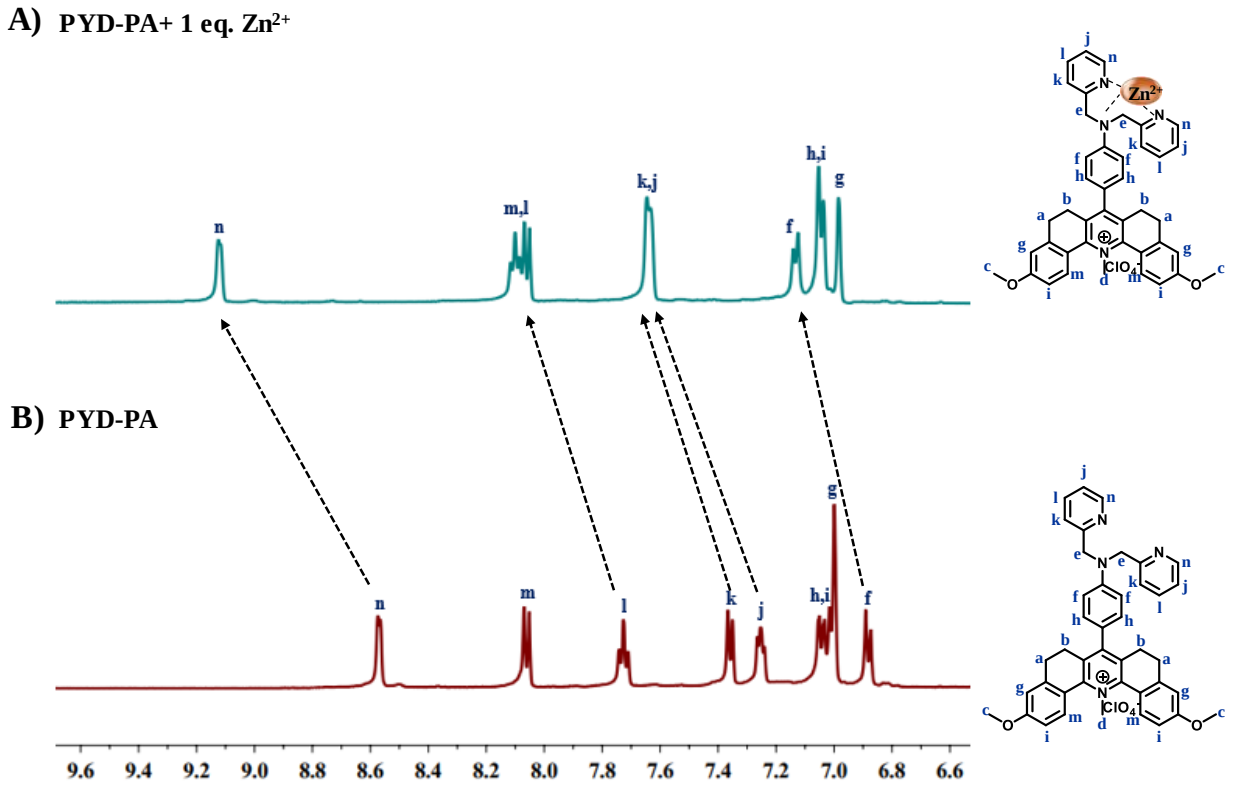

Figure 2A.15. ^{1}H-NMR (in 500 MHz) spectra of (A) **PYD-PA** in the presence of 1 equivalent of Zn^{2+} and (B) **PYD-PA** before the addition of Zn^{2+}.

2A.3.12. Cytotoxicity of PYD-PA

Cytotoxicity of the probe is a major concern in the development of cellular imaging probes, which detrimentally affect various bioassays.[45] The cytotoxicity of **PYD-PA** was evaluated on SK-BR-3, breast cancer cell lines using MTT assay, at different concentrations of the probe (500 nM - 50 μM). The probe exhibited a proliferation of cells above 90% and minimal toxicity up to 50 μM concentration, confirming its non-toxic nature under the experimental conditions **(Figure 2A.16)**. We are using 1 μM concentration of **PYD-PA** for bioimaging experiments.

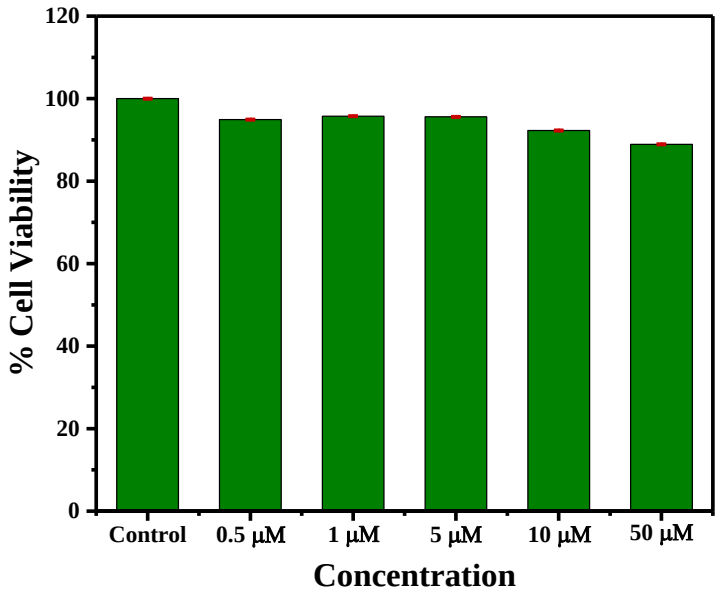

Figure 2A.16. Cytotoxicity study of **PYD-PA** (500 nM - 50 μM) in SK-BR-3 cell line using standard MTT assays.

2A.3.13. Co-localization studies of PYD-PA

Positively charged pyridinium dyes are known to exhibit selective accumulation in the mitochondria.[36, 46] Our Zn^{2+} probe design facilitates the mitochondria targeted cellular accumulation of the pyridinium derivatives in monitoring elevated Zn^{2+} concentration during autophagy. To confirm the selective accumulation of the **PYD-PA** in mitochondria, the co-localization ability of the probe was evaluated in SK-BR-3 cells through confocal microscopy imaging, utilizing co-staining assays **(Figure 2A.17)**. Cells pretreated with $ZnCl_2$ were subsequently co-stained with **PYD-PA** (1 μM) along with Mito-tracker red (100 nM), Lyso-tracker red (100 nM), and Hoechst 33342 (1 μM), a nucleus staining dye. The fluorescence of **PYD-PA** from the green channel overlays well with that of the Mito-tracker red, which was obtained from the red channel with a Pearson's Correlation Coefficient[47] of ~0.95, indicating an excellent co-localization within the mitochondria. Further, **PYD-PA** displayed relatively small co-localization with Lyso-tracker and negligible co-localization with Hoechst 33342.

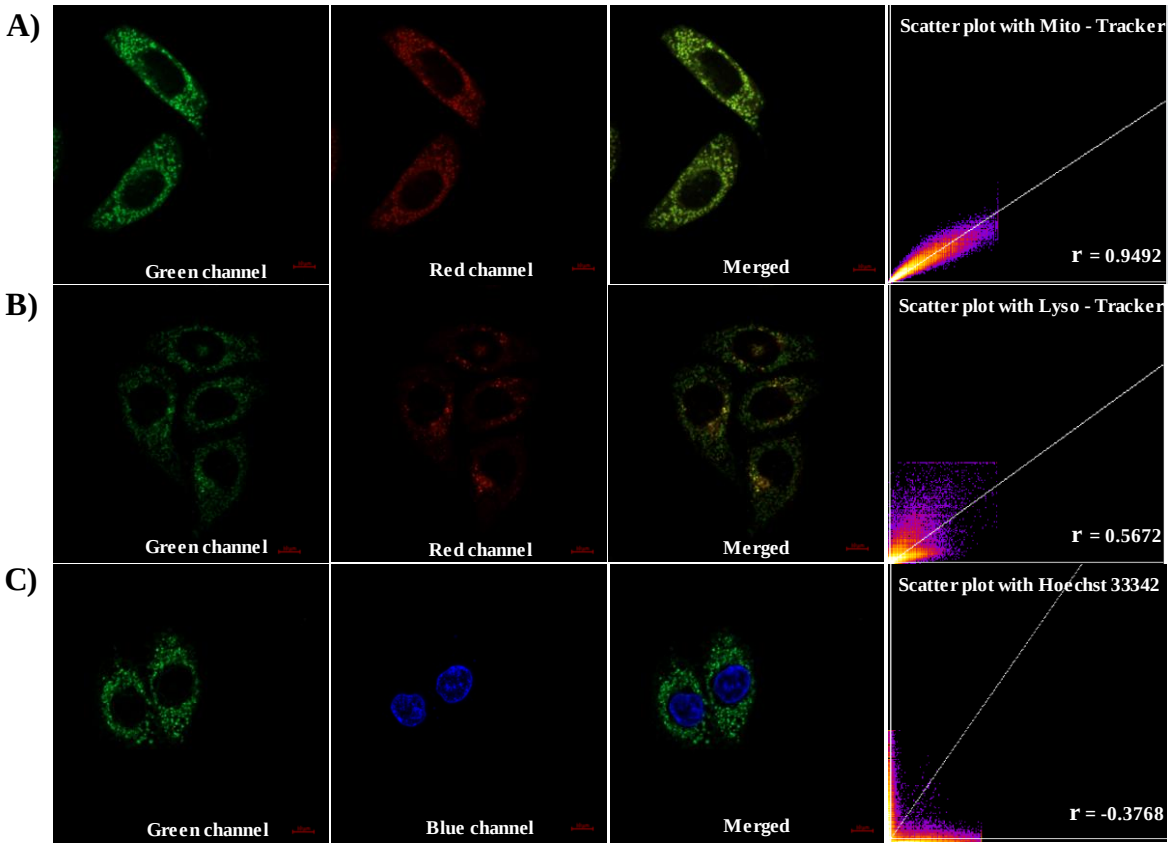

Figure 2A.17. Confocal laser scanning microscopy images and scatter plots for intracellular localization of **PYD-PA** (1 μM) in SK-BR-3 cells imaged after counter-staining with (A) Mito-tracker (100 nM), (B) Lyso-tracker (100 nM) and (C) Hoechst 33342 (1 μM). The co-localization was estimated using Pearson's Correlation Coefficient (r). Scale bar 10 μm.

2A.3.14. Zn^{2+} sensing in cells under oxidative stress

To confirm the intracellular zinc sensing ability of the probe, SK-BR-3 cells were pretreated with $ZnCl_2$ and incubated with **PYD-PA**. Confocal microscopy images of cells incubated with the probe in $ZnCl_2$-pretreated cells displayed a considerable enhancement in emission intensity in the green channel compared to non-treated cells, confirming the ability of the probe to monitor exogenous Zn^{2+} **(Figure 2A.18A** to **C)**. Further, the probe, **PYD-PA** was used to monitor the release of Zn^{2+} during oxidative stress induced by H_2O_2. During oxidative stress within cells, a rapid influx of hydrogen peroxide takes place, which causes the oxidation of cysteine

residues in the Zn-bound metallothioneins and the subsequent release of Zn^{2+}.[48] SK-BR-3 cells incubated with **PYD-PA** showed negligible, initial fluorescence **(Figure 2A.18D)**. Subsequent treatment of these cells with H_2O_2 to induce oxidative stress resulted in a significant increase in fluorescence intensity, signaling the release of free Zn^{2+} **(Figure 2A.18F)**. Pre-treatment of the cells with a competitive Zn^{2+} chelator, *N,N,N',N'*-tetrakis(2-pyridylmethyl)-ethylenediamine (TPEN), showed reduced cellular fluorescence **(Figure 2A.18E)**, which confirms the role of free Zn^{2+} in the enhancement of fluorescence. Thus, these experiments demonstrate that the probe **PYD-PA** can efficiently monitor the elevated, intracellular Zn^{2+} levels during cellular events such as oxidative stress.

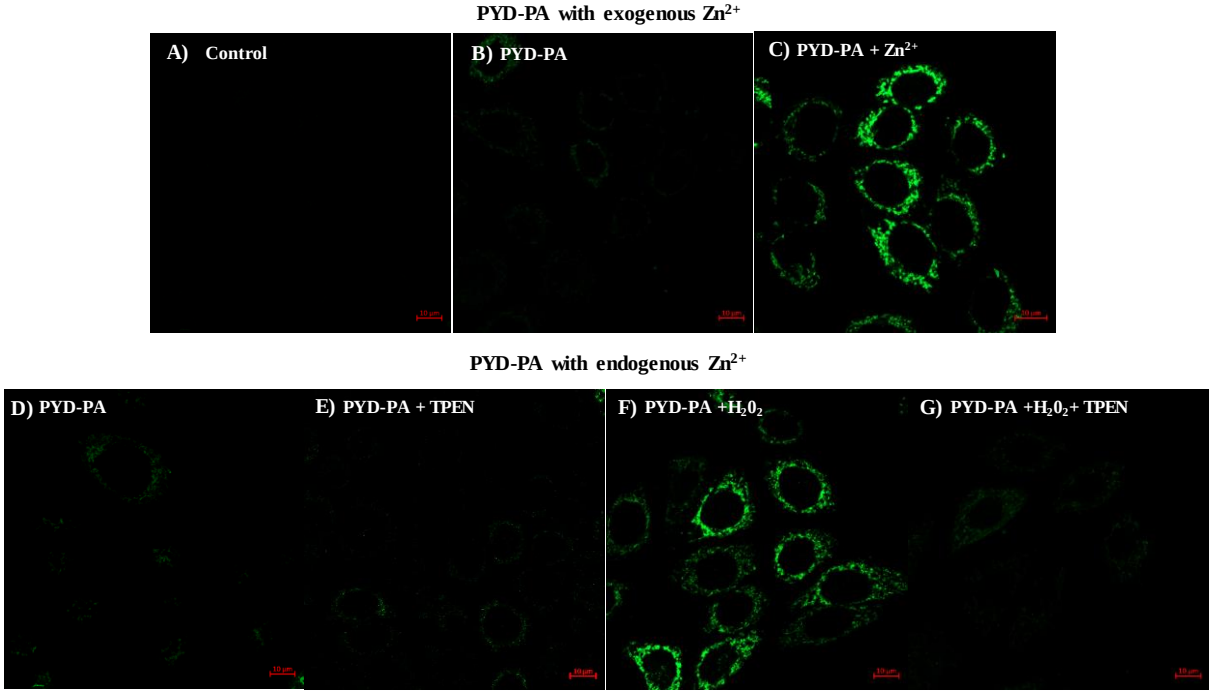

Figure 2A.18. Confocal microscopy images of **PYD-PA** in SK-BR-3 cells, with exogenous Zn^{2+}; (A) Control; (B) treated with **PYD-PA** (1 μM); (C) pretreated with $ZnCl_2$ (10 μM) followed by **PYD-PA** (1 μM) and with endogenous Zn^{2+} generators and chelators; (D) treated with **PYD-PA** (1 μM); (E) pretreated with TPEN (20 μM) followed by **PYD-PA** (1 μM); (F) pretreated with H_2O_2 (50 μM) followed by **PYD-PA** (1 μM) and (G) pretreated with TPEN (20 μM) and H_2O_2 (50 μM) followed by **PYD-PA** (1 μM). Scale bar 10 μm.

2A.3.15. Zn^{2+} sensing in cells under autophagy conditions

Autophagy is a cellular degradative process in which cells remove dysfunctional components and recycle their constituents. During autophagy, the cellular microenvironments, including pH, viscosity, and polarity will change and these changes can be used to monitor the autophagy process.[49] Along with these microenvironmental fluctuations, elevated Zn^{2+} levels in the cells can also be an indication of autophagy. Since Rapamycin is a generally used chemical for inducing autophagy in cells during biological experiments,[50, 51] SK-BR-3 cells were incubated with Rapamycin as an autophagy model. Confocal fluorescence microscopy imaging of SK-BR-3 cells treated with the probe, **PYD-PA,** without Rapamycin incubation did not show green fluorescence, while the fluorescence in the cells with Rapamycin exposure (10 μM) confirmed the autophagy induction. With time, the probe displayed considerable fluorescence increment in the green channel, indicating an upregulation of mitochondrial Zn^{2+} concentration during autophagy **(Figure 2A.19)**. For a longer time period of 24 h, the fluorescence increment was even higher. This is a clear indication that Zn^{2+} is a positive regulator of autophagy, and there is an increase in Zn^{2+} concentration associated with the process.

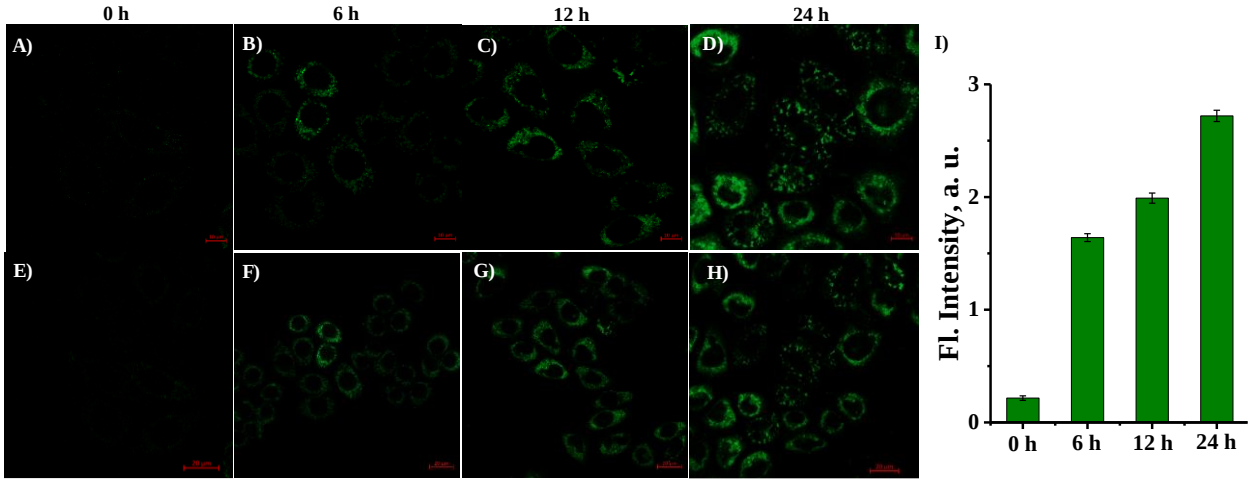

Figure 2A.19. Confocal microscopy images of **PYD-PA** in SK-BR-3 cells pretreated with Rapamycin (10 μM) for (A) & (E) 0 h; (B) & (F) 6 h; (C) & (G) 12 h; (D) & (H) 24 h at two

different maginifications; (I) A plot of the fluorescence intensity with time during autophagy. Scale bar is 10 μm for A-D and 20 μm for E-H.

2A.4. Conclusion

In conclusion, the pentacyclic pyridinium-based fluorophore, **PYD-PA,** presented here is a novel "turn-on" fluorescent probe for the selective detection of Zn^{2+}. Upon Zn^{2+} binding, the probe displayed a three-fold increase in fluorescence intensity, demonstrating remarkable selectivity in the presence of other biologically relevant metal ions. Moreover, the probe showed excellent water solubility, photostability, pH insensitivity, and low cytotoxicity, making it highly suitable for cellular imaging applications. With a moderate binding affinity for Zn^{2+} ($K_a = 6.29 \times 10^4\ M^{-1}$) and its ability to target mitochondria, the probe is effective in detecting elevated Zn^{2+} levels, particularly within mitochondria. Bioimaging experiments conducted in SK-BR-3 breast cancer cells confirmed the ability of the probe to efficiently monitor dynamic changes in intracellular Zn^{2+} levels. Furthermore, the probe was successfully utilized for real-time monitoring of intracellular free zinc ion fluctuations during autophagy.

2A.5. Experimental Section

2A.5.1. Materials and methods

The starting materials and reagents utilized in this study were procured from commercial suppliers (Sigma Aldrich and TCI chemicals) and used without further purification. Moisture-sensitive reactions were carried out under an argon atmosphere using dried solvents obtained from Sigma-Aldrich and Merck chemical suppliers. Thin layer chromatography (TLC) was conducted on aluminum plates coated with silica gel obtained from Merck. Silica gel of mesh size 100-200 was used for column chromatography. ^{1}H NMR (500 MHz) and ^{13}C NMR (125 MHz) analyses were conducted using a Bruker Avance DPX Spectrometer, with TMS as the internal standard. High-resolution mass spectra (HRMS) were acquired using the Thermo Scientific Q Exactive Hybrid Quadrupole-Orbitrap Electrospray Ionization Mass Spectrometer (ESI-MS). UV-Vis absorption spectra were obtained utilizing a Shimadzu UV−Vis Spectrophotometer (UV-2600), while emission spectra were recorded using a SPEX Fluorolog Spectrofluorimeter. The photostability of **PYD-PA** was investigated by recording emission spectra of a freshly prepared 10 μM solution in HEPES buffer with and without light irradiation using an Oriel optical bench model 11200 equipped with a 200 W mercury lamp and a 400 nm long-pass filter at regular time intervals. The pH-dependent behavior of **PYD-PA** was examined by recording emission spectra of its 10 μM solution in HEPES buffer across a pH range from 4 - 9. *In vitro* studies were conducted using the SK-BR-3 breast cancer cell line (obtained from ATCC), and images were captured using a Zeiss LSM 980 confocal inverted microscope, equipped with Airyscan 2 detector, using 63x, 1.4 N.A. oil immersion objective under ambient conditions. A 488 nm laser at 5% power was used for imaging in the green channel.

2A.5.1.1. Cell culture

SK-BR-3 breast cancer cell lines were maintained in DMEM supplemented with 10% Fetal Bovine Serum (FBS), 1% antibiotic antimycotic mix in a humidified 5% CO_2 atmosphere at 37°C. When confluent, the cells grown in 25 cm^2 culture flasks were trypsinized with Trypsin-EDTA mix. The cells were seeded in 8-well chamber slide for confocal fluorescent microscope analysis.

2A.5.1.2. Cytotoxicity

The growth inhibition capacity of the probe **PYD-PA** was evaluated on SK-BR-3 cell lines by 3-(4, 5-dimethylthiazol-2-yl)-2,5diphenyltetrazolium bromide (MTT) assay as previously reported. Cell suspensions of 5×10^3 cells/well (100 µL) were seeded in a 96-well plate, and 100 µL of PYD-PA at various concentrations (10-50 µM) was added in triplicate. The plates were then incubated for 24 h in a CO_2 incubator. After incubation, MTT dissolved in DMEM (0.5 g/L) was added to each well and kept at 37 ºC in a CO_2 incubator for 2-4 h, 100 µL of DMSO was added to each well and the ability of the cells to reduce this substrate to the blue formazan product was determined colorimetrically (570 nm) after 20 min using a microplate reader (TecanInfinite 200PRO, Mannedorf, Switzerland).

Proliferation [%] = $A_{sample} / A_{control} \times 100$

Inhibition [%] = 100 - % Proliferation

2A.5.1.3. Subcellular co-localization imaging

For confocal microscopy imaging, the culture medium was removed and the cells were washed with phosphate buffered saline (PBS, pH 7.4) twice. For labeling of lysosomes and mitochondria, SK-BR-3 cells were pretreated with $ZnCl_2$ followed by Lyso-tracker red (100 nM) and Mito-tracker red (100 nM) in PBS (pH 7.4), 30 min prior to imaging and for nuclear staining, cells were treated with Hoechst 33342 (1 µM) in PBS, 20 min prior to imaging. The cells were

then co-stained with 1 μM **PYD-PA** for 10 min, and imaging experiments were performed in a Zeiss confocal laser scanning microscope, and images were processed in Zen blue software.

2A.5.1.4. Zn^{2+} generation and chelation studies

The efficiency and sensitivity of the probe **PYD-PA** towards varying concentration of intracellular Zn^{2+} were evaluated using intracellular zinc generators and chelators. SK-BR-3 cells were seeded in 8-well plate and upon attaining 60% confluency, treated with $ZnCl_2$ (10 μM) as exogenous Zn^{2+}, *N,N,N′,N′*-Tetrakis(2-pyridylmethyl) ethylenediamine (TPEN, 20 μM), a membrane permeable metal ion chelator, for 20 min in different wells. Similarly, cells were incubated with hydrogen peroxide (H_2O_2, 50 μM) for 30 min, which is a strong oxidant and an endogenous zinc generator. Further, cells after treatment with H_2O_2 (50 μM) for 30 min, were subjected to TPEN exposure (20 μM) for 20 min. After the respective treatments, cells were incubated with the probe, **PYD-PA** (1 μM) for 10 min and washed two times. The images were acquired in Zeiss confocal laser scanning microscope and the images were processed in Zen blue software.

2A.5.1.5. Zn^{2+} sensing in autophagy conditions

To evaluate the effect of Zn^{2+} in autophagy condition, SK-BR-3 cells were pretreated with Rapamycin, an autophagy inducer. Cells were seeded in 8-well plate and upon attaining 70% confluency, it was treated with 10 μM Rapamycin and incubated for different time periods (6 h, 12 h, 24 h) following which, cells were incubated with **PYD-PA** (1 μM) for 10 minutes. Images were acquired in Zeiss confocal laser scanning microscope and processed in Zen blue software.

2A.5.2. Synthesis and characterization

2A.5.2.1. Synthesis of **PA**

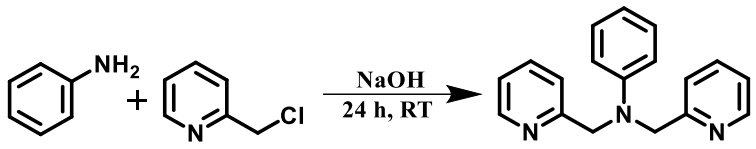

To a solution of 2-chloromethylpyridine (1.524 g, 12 mmol) in H_2O (0.5 mL), aniline (0.558 g, 6 mmol), 5 N NaOH (3 mL) and hexadecyltrimethylammoniumchloride (20 mg) were added under argon atmosphere. The mixture was stirred vigorously for 24 h at room temperature. The mixture was extracted with dichloromethane, washed with H_2O and dried over Na_2SO_4. After evaporation of solvent, the desired product was obtained as beige solid after purification by column chromatography over silica using 60% ethyl acetate/dichloromethane (Yield 40%).

^{1}HNMR ($CDCl_3$, 500 MHz) δ (ppm): 4.83 (s, 4H), 6.73 (m, 3H), 7.16 (m, 4H), 7.27 (d, J = 5Hz, 2H), 7.64 (t, J =10 Hz, 2H), 8.60 (d, J = 5Hz, 2H).

^{13}CNMR ($CDCl_3$, 125 MHz): 57.2, 112.5, 117.2, 120.8, 122.0, 129.3, 136.8, 148.1, 149.7, 158.8.
HRMS: calculated = 275.1422, found = 276.1502

2A.5.2.2. Synthesis of **PA-CHO**

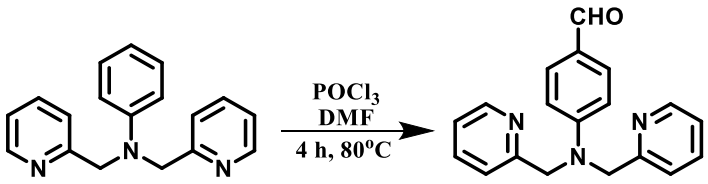

$POCl_3$ (1.56 mL, 17 mmol) was added into ice bath cooled DMF solution (2 mL, 26 mmol) in portions and the solution was then stirred for 30 minutes in chilled condition. **PA** (0.6 g, 2.18 mmol) in 1mL DMF was added in portions to the above solution. The mixture was heated for 4 h

at 80 ^{o}C, cooled to room temperature and then poured into H_2O. It was neutralized to pH 7-8 with K_2CO_3 solution with stirring. Mixture was extracted with CH_2Cl_2 and dried over anhydrous Na_2SO_4 (Yield: 92%).

^{1}H NMR (500 MHz, $CDCl_3$), δ (ppm): 4.91 (s, 4H), 6.79 (d, J = 10 Hz, 2H), 7.21–7.22 (m, 4H), 7.66–7.70 (m, 4H), 8.61 (d, J = 5Hz, 2H), 9.73 (s, 1H).

^{13}CNMR ($CDCl_3$, 125 MHz): 57.1, 112.0, 120.7, 122.5, 126.5, 132.1, 137.0, 149.9, 153.1, 157.2, 190.3.

HRMS calculated = 303.1472, found = 304.1454.

2A.5.2.3. Synthesis of **PYR-PA**

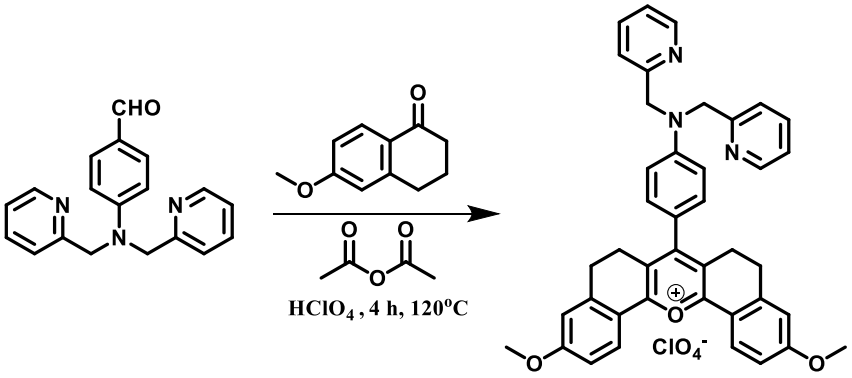

To a solution of **PA-CHO** (0.2 g, 0.6 mmol) in toluene 6-methoxy tetralone (0.23 g, 1.3 mmol) and acetic anhydride (0.12 mL) were added and the mixture was refluxed at 130 ^{o}C for 2 h. Then perchloric acid (0.1 mL) was added drop wise and the reaction was kept for 4 h under the same conditions. After completion of reaction, toluene was decanted and the precipitate formed was washed with diethyl ether. The product was purified using silica column using 5% methanol/chloroform (Yield 65%).

^{1}H NMR (500 MHz, $CDCl_3$) δ (ppm): 2.8 (m, 4H), 2.9(m, 4H), 3.86 (s, 6H), 4.96 (s, 4H),6.83 (d, J = 10Hz, 2H), 6.92 (s, 2H), 7.04 (d, J = 10Hz, 2H), 7.15 (d, J = 10Hz, 2H), 7.32(m, 2H), 7.41 (d, J = 10Hz, 2H), 7.81 (m, 2H), 8.15 (d, J = 10Hz, 2H), 8.53 (d, J = 10Hz,2H).

^{13}CNMR (Acetone- d_6, 125MHz): 25.1, 27.2, 29.9, 56.4, 114.4, 114.9, 119.5, 121.9, 127.3, 127.4, 128.7, 130.4, 130.5, 144.7, 163.8, 165.6.

HRMS: calculated = 618.2751, found = 618.2774.

2A.5.2.4. Synthesis of **PYD-PA**

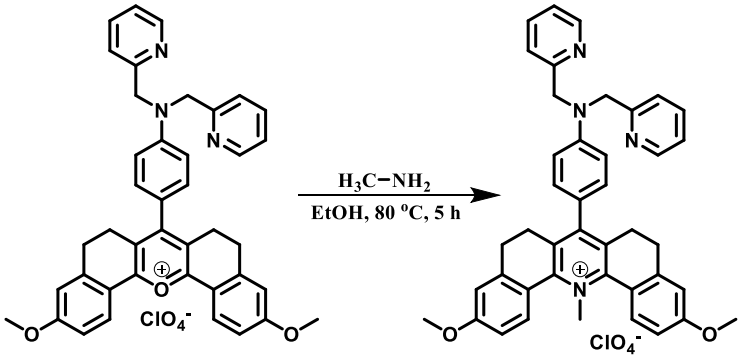

To a solution of **PYR-PA** (0.1 g, 0.16 mmol) in ethanol (3 mL) methyl amine (0.2 mL) was added and the reaction was kept at 80 °C for 5 h in a pressure tube. After completion of the reaction, the product formed was purified through silica column using 5% methanol/chloroform (Yield 19%).

^{1}H NMR (500 MHz, $CDCl_3$) δ(ppm): 2.53 (m, 4H), 2.71 (m, 4H), 3.83 (s, 6H), 4.43 (s,3H), 4.83 (s, 4H), 6.78 (m, 4H), 6.94 (d, J = 5Hz, 2H), 7.05 (d, J = 5Hz, 2H), 7.16 (m, 2H), 7.25 (d, J = 10Hz, 2H), 7.63 (d, J = 10Hz, 2H), 8.31 (d, J = 5Hz, 2H), 8.56 (d, J = 5Hz, 2H).

^{13}CNMR (CDCl3, 125MHz): 21.7, 25.7, 27.6, 28.3, 28.7, 30.9, 52.5, 54.7, 56.2, 111.7, 113.2, 119.5, 119.9, 121.4, 128.1, 131.4, 134.3, 136.0, 143.1, 148.8, 151.2, 157.1, 161.6.

HRMS: calculated = 631.3068, found = 631.3102.

2A.5.3. Spectral Data

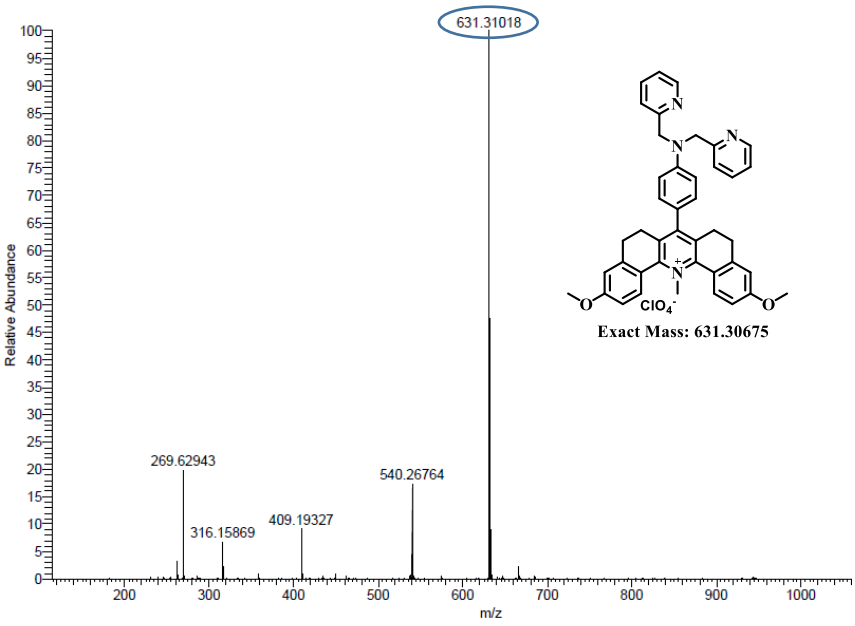

Figure 2A.20. HRMS spectrum of **PYD-PA**.

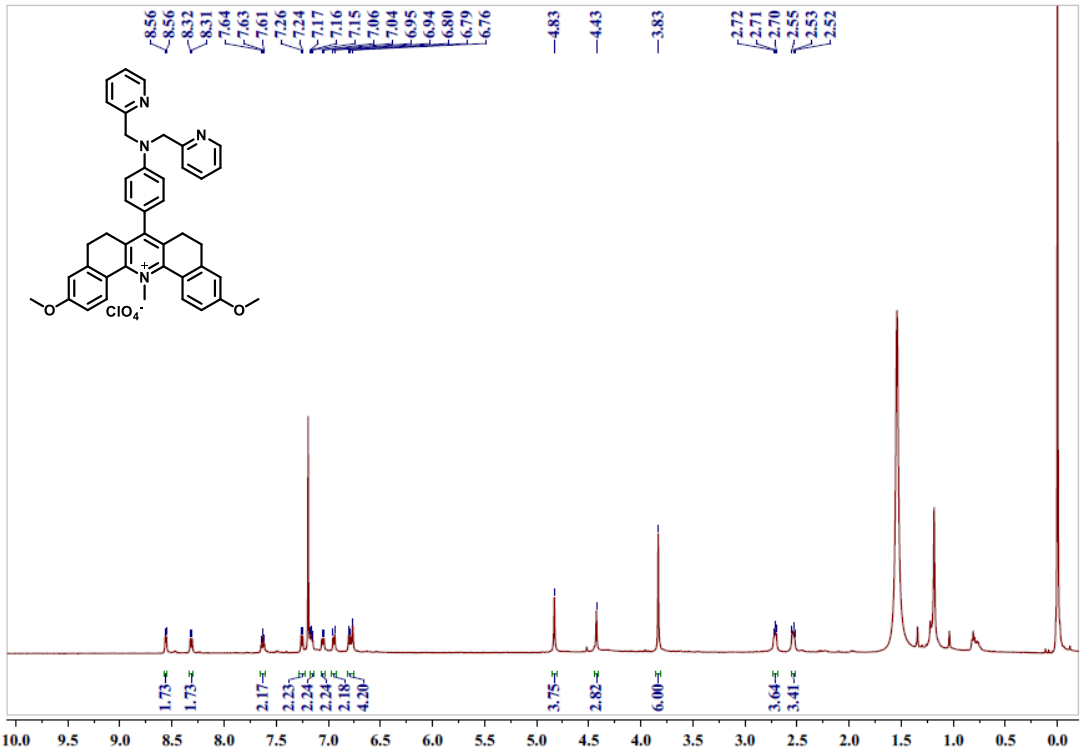

Figure 2A.21. ^{1}H NMR spectrum of **PYD-PA**.

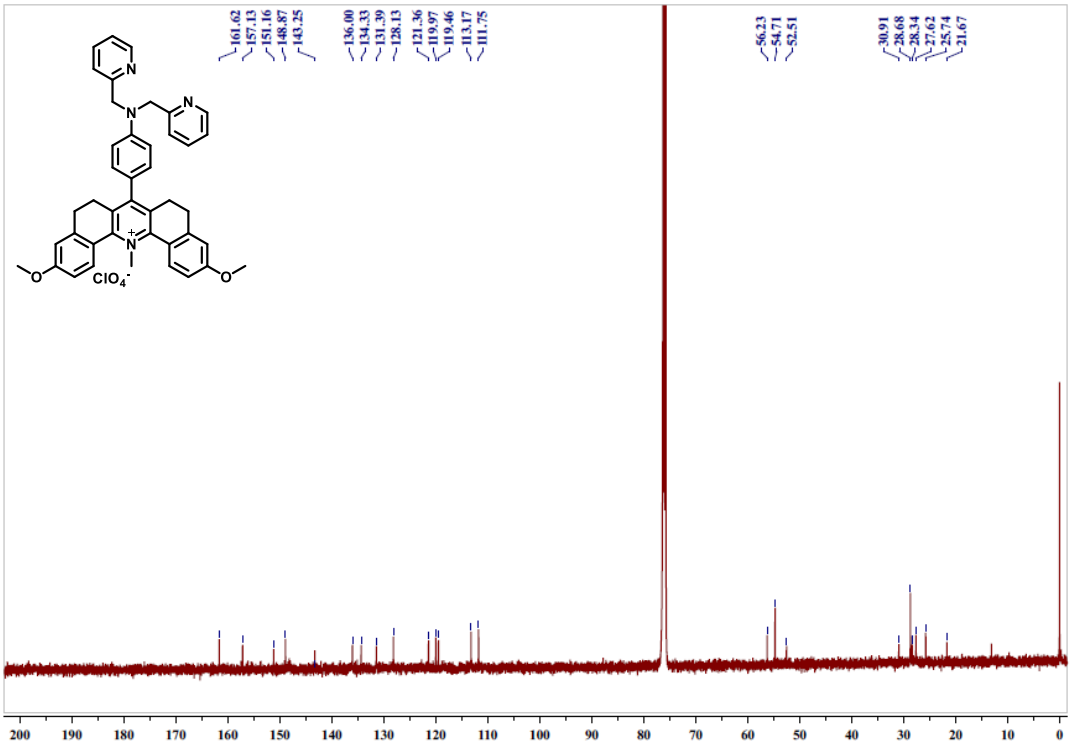

Figure 2A.22. ^{13}C NMR spectrum of **PYD-PA**.

2A.6. References

1. Javadov, S.; Kuznetsov, A. V., Mitochondria: the cell powerhouse and nexus of stress. *Frontiers in Physiology* **2013,** *4*, 61695.

2. McBride, H. M.; Neuspiel, M.; Wasiak, S., Mitochondria: more than just a powerhouse. *Current biology* **2006,** *16* (14), R551-R560.

3. Xie, D.; Ma, W.; Wang, C.; Zhang, W.; Ding, Z., Mitochondria-targeted fluorescent probe for imaging viscosity in hepatic ischemia–reperfusion injury cell model. *Chem. Commun.* **2023,** *59* (8), 1030-1033.

4. Ding, W.-X.; Yin, X.-M., Mitophagy: mechanisms, pathophysiological roles, and analysis. *Biol. Chem.* **2012,** *393* (7), 547-564.

5. Chen, Z.; Li, J.; Chen, X.; Cao, J.; Zhang, J.; Min, Q.; Zhu, J.-J., Single gold@ silver nanoprobes for real-time tracing the entire autophagy process at single-cell level. *J. Am. Chem. Soc.* **2015,** *137* (5), 1903-1908.

6. Chan, J.; Dodani, S. C.; Chang, C. J., Reaction-based small-molecule fluorescent probes for chemoselective bioimaging. *Nat. Chem.* **2012,** *4* (12), 973-984.

7. Liu, Y.; Zhang, D.; Qu, Y.; Tang, F.; Wang, H.; Ding, A.; Li, L., Advances in Small-Molecule Fluorescent pH Probes for Monitoring Mitophagy. *Chem. Biomed. Imaging* **2024,** *2*, 81–97

8. Li, X.; Li, X.; Ma, H., A near-infrared fluorescent probe reveals decreased mitochondrial polarity during mitophagy. *Chem. Sci.* **2020,** *11* (6), 1617-1622.

9. Su, S.; Chai, L.; An, Q.; Hu, W.; Wang, L.; Li, X.; Zhang, H.; Li, C., Tracking autophagy process with a TBET and AIE-based ratiometric two-photon viscosity probe. *Anal. Chem.* **2022,** *94* (43), 15146-15154.

10. Gu, K.; Xu, Y.; Li, H.; Guo, Z.; Zhu, S.; Zhu, S.; Shi, P.; James, T. D.; Tian, H.; Zhu, W.-H., Real-time tracking and in vivo visualization of β-galactosidase activity in colorectal tumor with a ratiometric near-infrared fluorescent probe. *Journal of the American Chemical Society* **2016,** *138* (16), 5334-5340.

11. Feng, J.; Chen, X.; Shen, J., Reactive nitrogen species as therapeutic targets for autophagy: implication for ischemic stroke. *Expert Opin. Ther. Targets* **2017,** *21* (3), 305-317.

12. Lee, S.-J.; Koh, J.-Y., Roles of zinc and metallothionein-3 in oxidative stress-induced lysosomal dysfunction, cell death, and autophagy in neurons and astrocytes. *Mol. Brain* **2010,** *3*, 1-9.

13. Liuzzi, J. P.; Pazos, R., Interplay between autophagy and zinc. *J. Trace Elem. Med. Biol.* **2020,** *62*, 126636.

14. Mao, Z.; Hu, L.; Dong, X.; Zhong, C.; Liu, B.-F.; Liu, Z., Highly sensitive quinoline-based two-photon fluorescent probe for monitoring intracellular free zinc ions. *Anal. Chem.* **2014,** *86* (13), 6548-6554.

15. Santhakumar, H.; Nair, R. V.; Philips, D. S.; Shenoy, S. J.; Thekkuveettil, A.; Ajayaghosh, A.; Jayasree, R. S., Real time imaging and dynamics of hippocampal Zn^{2+} under epileptic condition using a ratiometric fluorescent probe. *Sci. Rep.* **2018,** *8* (1), 9069.

16. Divya, K. P.; Sreejith, S.; Ashokkumar, P.; Yuzhan, K.; Peng, Q.; Maji, S. K.; Tong, Y.; Yu, H.; Zhao, Y.; Ramamurthy, P., A ratiometric fluorescent molecular probe with enhanced two-photon response upon Zn^{2+} binding for in vitro and in vivo bioimaging. *Chemical Science* **2014,** *5* (9), 3469-3474.

17. Du, C.; Fu, S.; Wang, X.; Sedgwick, A. C.; Zhen, W.; Li, M.; Li, X.; Zhou, J.; Wang, Z.; Wang, H., Diketopyrrolopyrrole-based fluorescence probes for the imaging of lysosomal Zn^{2+} and identification of prostate cancer in human tissue. *Chem. Sci.* **2019,** *10* (22), 5699-5704.

18. Kwong, J. M. K.; Hoang, C.; Dukes, R. T.; Yee, R. W.; Gray, B. D.; Pak, K. Y.; Caprioli, J., Bis (Zinc-Dipicolylamine), Zn-DPA, a new marker for apoptosis. *Investig. Ophthalmol. Vis. Sci.* **2014,** *55* (8), 4913-4921.

19. Xia, H.-C.; Xu, X.-H.; Song, Q.-H., BODIPY-based fluorescent sensor for the recognization of phosgene in solutions and in gas phase. *Analytical chemistry* **2017,** *89* (7), 4192-4197.

20. Divya, K. P.; Sreejith, S.; Balakrishna, B.; Jayamurthy, P.; Anees, P.; Ajayaghosh, A., A Zn^{2+}-specific fluorescent molecular probe for the selective detection of endogenous cyanide in biorelevant samples. *Chem. Commun.* **2010,** *46* (33), 6069-6071.

21. Hwang, J. J.; Kim, H. N.; Kim, J.; Cho, D.-H.; Kim, M. J.; Kim, Y.-S.; Kim, Y.; Park, S.-J.; Koh, J.-Y., Zinc (II) ion mediates tamoxifen-induced autophagy and cell death in MCF-7 breast cancer cell line. *BioMetals* **2010,** *23*, 997-1013.

22. Liuzzi, J. P.; Yoo, C., Role of zinc in the regulation of autophagy during ethanol exposure in human hepatoma cells. *Biol. Trace Elem. Res.* **2013,** *156*, 350-356.

23. Kim, K. W.; Speirs, C. K.; Jung, D. K.; Lu, B., The zinc ionophore PCI-5002 radiosensitizes non-small cell lung cancer cells by enhancing autophagic cell death. *J. Thorac. Oncol.* **2011,** *6* (9), 1542-1552.

24. Fang, H.; Geng, S.; Hao, M.; Chen, Q.; Liu, M.; Liu, C.; Tian, Z.; Wang, C.; Takebe, T.; Guan, J.-L., Simultaneous Zn^{2+} tracking in multiple organelles using super-resolution morphology-correlated organelle identification in living cells. *Nat. Commun.* **2021,** *12* (1), 109.

25. Carol, P.; Sreejith, S.; Ajayaghosh, A., Ratiometric and Near-Infrared Molecular Probes for the Detection and Imaging of Zinc Ions. *Chem. Asian J.* **2007,** *2* (3), 338-348.

26. Thambiayya, K.; Kaynar, A. M.; Croix, C. M. S.; Pitt, B. R., Functional role of intracellular labile zinc in pulmonary endothelium. *Pulm. Circ.* **2012,** *2* (4), 443-451.

27. Sreejith, S.; Divya, K. P.; Ajayaghosh, A., Detection of zinc ions under aqueous conditions using chirality assisted solid-state fluorescence of a bipyridyl based fluorophore. *Chem. Commun.* **2008,** (25), 2903-2905.

28. Bafaro, E.; Liu, Y.; Xu, Y.; Dempski, R. E., The emerging role of zinc transporters in cellular homeostasis and cancer. *Signal Transduct. Target. Ther.* **2017,** *2* (1), 1-12.

29. Aich, K.; Goswami, S.; Das, S.; Mukhopadhyay, C. D., A new ICT and CHEF based visible light excitable fluorescent probe easily detects in vivo Zn^{2+}. *RSC Adv.* **2015,** *5* (39), 31189-31194.

30. Jayaraj, A.; Gayathri, M. S.; Sivaraman, G., A highly potential acyclic Schiff base fluorescent turn on sensor for Zn^{2+} ions and colorimetric chemosensor for Zn^{2+}, Cu^{2+} and Co^{2+} ions and its applicability in live cell imaging. *J. Photochem. Photobiol. B* **2022,** *226*, 112371.

31. Wang, Y.; Xia, C.; Han, Z.; Jiao, Y.; Yao, X.; Lun, Z.; Fu, S.; Zhang, H.; Hou, P.; Ning, D., Aminoantipyrine based efficient chemosensor for Zn (II) ions and its effectiveness in live cell imaging. *J. Photochem. Photobiol. B* **2019,** *199*, 111602.

32. Zhang, X.; Jin, G.; Chen, Z.; Wu, Y.; Li, Q.; Liu, P.; Xi, G., An efficient turn-on fluorescence chemosensor system for Zn (II) ions detection and imaging in mitochondria. *J. Photochem. Photobiol. B* **2022,** *234*, 112485.

33. Wang, P.; Wu, J., A highly sensitive turn-on fluorescent chemosensor for recognition of Zn (II) ions and its application in live cells imaging. *J. Photochem. Photobiol., A* **2020,** *386*, 112111.

34. Philips, D. S.; Sreejith, S.; He, T.; Menon, N. V.; Anees, P.; Mathew, J.; Sajikumar, S.; Kang, Y.; Stuparu, M. C.; Sun, H., A Three-Photon Active Organic Fluorophore for Deep Tissue Ratiometric Imaging of Intracellular Divalent Zinc. *Chem. Asian J.* **2016,** *11* (10), 1523-1527.

35. Saleem, M.; Lee, K. H., Optical sensor: a promising strategy for environmental and biomedical monitoring of ionic species. *RSC Adv.* **2015,** *5* (88), 72150-72287.

36. Huang, Y.; Li, M.; Zan, Q.; Wang, R.; Shuang, S.; Dong, C., Mitochondria-Targeting Multifunctional Fluorescent Probe toward Polarity, Viscosity, and $ONOO^-$ and Cell Imaging. *Anal. Chem.* **2023,** *95* (27), 10155-10162.

37. Sumalekshmy, S.; Henary, M. M.; Siegel, N.; Lawson, P. V.; Wu, Y.; Schmidt, K.; Brédas, J.-L.; Perry, J. W.; Fahrni, C. J., Design of emission ratiometric metal-ion sensors with enhanced two-photon cross section and brightness. *J. Am. Chem. Soc.* **2007,** *129* (39), 11888-11889.

38. Chakraborty, S.; Joseph, M. M.; Varughese, S.; Ghosh, S.; Maiti, K. K.; Samanta, A.; Ajayaghosh, A., A new pentacyclic pyrylium fluorescent probe that responds to pH imbalance during apoptosis. *Chemical Science* **2020,** *11* (47), 12695-12700.

39. Brouwer, A. M., Standards for photoluminescence quantum yield measurements in solution (IUPAC Technical Report). *Pure and Applied Chemistry* **2011,** *83* (12), 2213-2228.

40. Jones, G.; Jackson, W. R.; Choi, C. Y.; Bergmark, W. R., Solvent effects on emission yield and lifetime for coumarin laser dyes. Requirements for a rotatory decay mechanism. *The Journal of Physical Chemistry* **1985,** *89* (2), 294-300.

41. Sudheesh, K. V.; Joseph, M. M.; Philips, D. S.; Samanta, A.; Kumar Maiti, K.; Ajayaghosh, A., pH-Controlled Nanoparticles Formation and Tracking of Lysosomal Zinc Ions in Cancer Cells by Fluorescent Carbazole–Bipyridine Conjugates. *ChemistrySelect* **2018,** *3* (8), 2416-2422.

42. Liu, H.-M.; Venkatesan, P.; Wu, S.-P., A sensitive and selective fluorescent sensor for Zinc (II) and its application to living cell imaging. *Sens. Actuators B: Chem.* **2014,** *203*, 719-725.

43. Gomes, L. J.; Carrilho, J. P.; Pereira, P. M.; Moro, A. J., A Near InfraRed Emissive Chemosensor for Zn^{2+} and Phosphate Derivatives Based on a Di-(2-picolyl) amine-styrylflavylium Push-Pull Fluorophore. *Sensors* **2023,** *23* (1), 471.

44. Xue, L.; Wang, H.-H.; Wang, X.-J.; Jiang, H., Modulating affinities of di-2-picolylamine (DPA)-substituted quinoline sensors for zinc ions by varying pendant ligands. *Inorg. Chem.* **2008,** *47* (10), 4310-4318.

45. Tian, M.; Ma, Y.; Lin, W., Fluorescent probes for the visualization of cell viability. *Acc. Chem. Res.* **2019,** *52* (8), 2147-2157.

46. Jiao, S.; Dong, X.; Zhao, W., Meso pyridinium BODIPY-based long wavelength infrared mitochondria-targeting fluorescent probe with high photostability. *Anal. Methods* **2023,** *15* (26), 3149-3155.

47. Cohen, I.; Huang, Y.; Chen, J.; Benesty, J.; Benesty, J.; Chen, J.; Huang, Y.; Cohen, I., Pearson correlation coefficient. *Noise reduction in speech processing* **2009**, 1-4.

48. McCord, M. C.; Aizenman, E., The role of intracellular zinc release in aging, oxidative stress, and Alzheimer's disease. *Front. aging neurosci.* **2014,** *6*, 77.

49. Li, X.; Liang, X.; Yin, J.; Lin, W., Organic fluorescent probes for monitoring autophagy in living cells. *Chem. Soc. Rev.* **2021,** *50* (1), 102-119.

50. Iwashita, H.; Sakurai, H. T.; Nagahora, N.; Ishiyama, M.; Shioji, K.; Sasamoto, K.; Okuma, K.; Shimizu, S.; Ueno, Y., Small fluorescent molecules for monitoring autophagic flux. *FEBS Lett.* **2018,** *592* (4), 559-567.

51. Hu, F.; Cai, X.; Manghnani, P. N.; Wu, W.; Liu, B., Multicolor monitoring of cellular organelles by single wavelength excitation to visualize the mitophagy process. *Chem. Sci.* **2018,** *9* (10), 2756-2761.

Differential Binding Interactions of a Pyridinium Dye Integrated Dipicolylamine-Zn^{2+} Complex with Nucleotides and Nucleic Acids

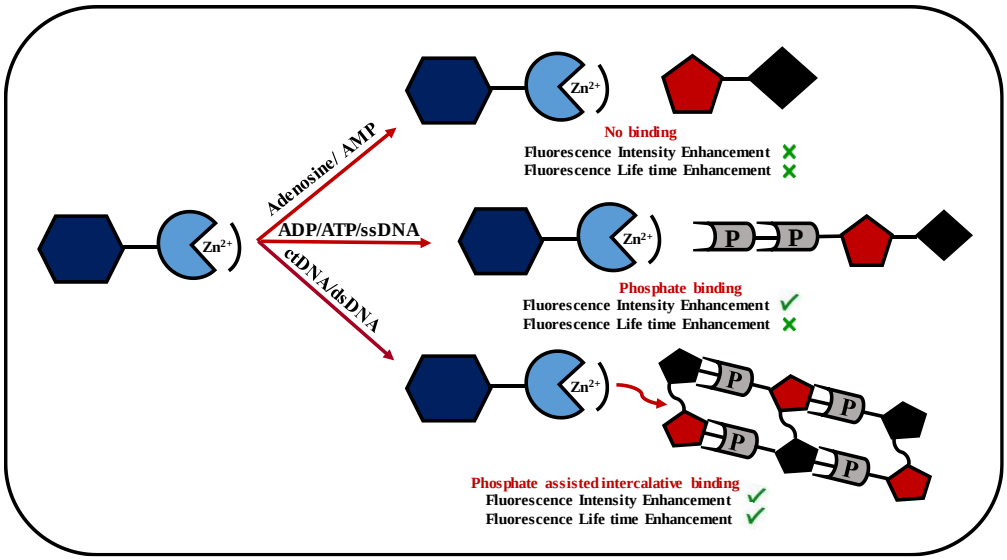

2B.1. Abstract

Developing small molecular fluorescent probes for targeting helical DNA plays a vital role in diagnostics, oncology, drug delivery, and forensic science. Among the various DNA-binding mechanisms, intercalation, where planar aromatic moieties insert between DNA bases, is particularly significant in differentiating and stabilizing various DNA secondary structures. While traditional intercalators such as ethidium bromide are effective, their associated toxicity necessitates the development of safer alternatives. Zn^{2+}- dipicolylamine complexes known for their strong affinity for phosphate groups, have proven to be valuable probes for targeting phosphate-containing biomolecules. In this Chapter, we explore the binding interactions of a pyridinium dye attached dipicolylamine zinc ion complex, ***PYD-PA-Zn^{2+}*** *(described in Chapter 2A) with various nucleotides and DNA. The probe,* ***PYD-PA-Zn^{2+}*** *exhibited differential binding*

interactions with adenosine, ATP, ADP, AMP and DNA. Notably, it showed minimal changes in both absorption and emission spectra in the presence of adenosine and AMP, indicating a poor binding affinity. In contrast, significant fluorescence enhancement was observed in the presence of ADP and ATP, while the absorption spectra remained unchanged, suggesting phosphate-assisted interactions between the probe and nucleotides. In contrast, with ctDNA, the absorption spectra of the probe exhibited a gradual decrease in absorbance (~37% hypochromicity) along with a red shift in the absorption maximum from 402 - 419 nm. The emission spectra, however, revealed a significant enhancement in fluorescence intensity with a blue shift in the emission maximum, resembling the behaviour of ethidium bromide when binding to DNA. To gain further insights into the binding interactions, we conducted extensive photophysical studies, including circular dichroism (CD) spectroscopy, thermal denaturation, and fluorescence lifetime measurements. Changes in the CD signal of DNA, along with an induced CD signal in the 355 - 485 nm range upon increasing ***PYD-PA-Zn***$^{2+}$ *concentration, suggest an intercalative binding interaction. Additionally, thermal denaturation studies revealed a 10 °C increase in the melting temperature of dsDNA in the presence of* ***PYD-PA-Zn***$^{2+}$*, indicating stabilization via intercalation. Notably, the probe exhibited a significant enhancement of the fluorescence lifetime when bound to ctDNA and double-stranded DNA (dsDNA) when compared to single-stranded DNA (ssDNA), ATP, and ADP. Thus, the probe turned out to be a powerful tool for differentiating different nucleotides and nucleic acids.*

2B.2. Introduction

Development of small molecular fluorescent probes, targeting various DNA secondary structures is an important area of research due to their broad applications in infectious disease diagnosis, oncology, targeted drug delivery, and forensic DNA fingerprinting.[1-4] Non-covalent mechanisms through which the probes bind to DNA include intercalation, insertion, groove binding, and discrete phosphate coordination.[5] Among these interactions, intercalation, where intercalating agents insert between the planar bases of DNA, plays an important role.[6]

Intercalating agents are essential tools in molecular biology, with many having clinical utility in cancer therapy, antimicrobial treatment, and molecular diagnostics.[7] Therefore, the development of new small molecules to explore DNA interactions remains a high priority in modern medicinal chemistry.[8]

In general, planar, polycyclic aromatic molecules efficiently intercalate between DNA base pairs through π-stacking interactions. Additionally, because DNA is a polyanion, the presence of cationic groups alongside aromatic groups enhances small molecule-DNA interactions.[9] Groove binding, where small molecules bind to the minor or major grooves of DNA through non-covalent interactions with the edges of base pairs also can augment the intercalative interactions.[10] Based on these principles, numerous dyes have been developed and successfully applied in DNA detection, fluorescence imaging techniques, and real-time polymerase chain reaction (PCR).[11-13] The commonly used positively charged small heterocyclic compounds in this category include phenanthridine derivatives and cyanine fluorescent dyes.[14, 15] One of the most extensively studied and widely used phenanthridine derivatives is 3,8-diamino-5-ethyl-6-phenylphenanthridinium, commonly known as ethidium bromide (EB), which has long been considered as the gold standard fluorescent marker for DNA and RNA. However, due to their toxicity and mutagenic effects, there is a growing demand for alternative fluorescent light-up probes that can selectively bind to DNA.[16]

Another class of effective intercalators comprises metal complexes, in which a planar aromatic ligand facilitates intercalation, while the metal center enhances binding through electrostatic interactions or secondary coordination. Typical metallo-intercalators include ruthenium bipyridine $[Ru(bpy)_2(dppz)]^{2+}$, ruthenium phenanthroline $[Ru(phen)_2(dppz)]^{2+}$, rhodium phenanthrenequinone diimine $[Rh(phi)_2(bpy')]^{3+}$, and platinum phenanthroline $[Pt(phen)Py_2]^{2+}$ complexes, and are well studied **(Figure 2B.1)**.[17-20] The fluorescence of these DNA intercalators can be either quenched or enhanced, depending on their chromophore

structure and electrostatic interactions with DNA. Fluorescence enhancement may result from increased rigidity, inhibition of solvent-induced quenching, or disruption of photoinduced electron transfer (PET). In contrast, fluorescence quenching can occur due to excited-state electron transfer (ET), photoinduced charge transfer (PCT), or Förster resonance energy transfer (FRET).[21] For example, the classic DNA intercalating ruthenium complex $[Ru(bpy)_2(dppz)]^{2+}$ exhibits a "light-switch" effect, remaining non-emissive in water, however becoming highly fluorescent upon DNA binding, due to the restricted motion of the dppz ligand within the DNA-binding environment.[22]

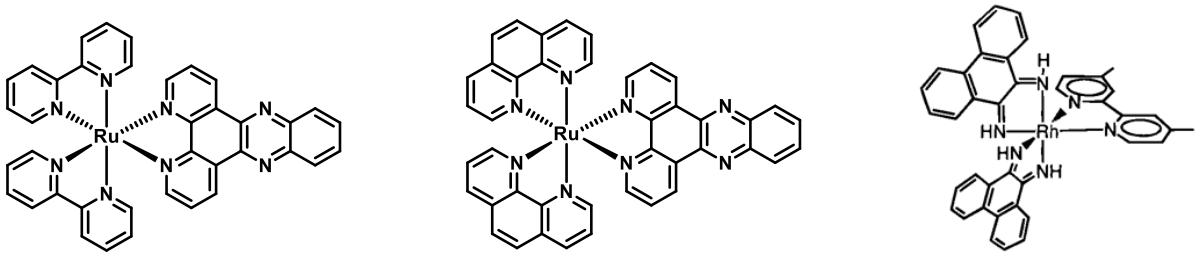

$[Ru(bpy)_2(dppz)]^{2+}$ **$[Ru(phen)_2(dppz)]^{2+}$** **$[Rh(phi)_2(bpy')]^{3+}$**

Figure 2B.1. Representative examples of metallo-intercalators.

Zn(II)-dipicolylamine [Zn(II)-DPA] receptors are known for their selective binding towards phosphate derivatives. In 2016, Tian et al. have synthesised two mononuclear Zn(II) complexes based on DPA ligand ($[ZnLX_2]_2CH_3OH$; X = Br for **1**, Cl for **2**) and investigated their interactions with ctDNA, pBR322 plasmid DNA, and Bovine serum albumin (BSA), utilizing different physicochemical techniques **(Figure 2B.2)**.[23] Upon addition of ctDNA to the Zn(II) complexes, a decrease in absorption intensity (hypochromism of 36.1% for **1** and 41.7% for **2**) accompanied by notable red shifts (10 nm for **1** and 9 nm for **2**), was observed. Additionally, fluorescence quenching of EB bound to ctDNA by the complexes, along with changes in the CD spectrum of DNA, confirmed that the observed interactions resulted from partial intercalation between the complexes and ctDNA. Furthermore, the anticancer and apoptosis-inducing activities of the complexes were also investigated.

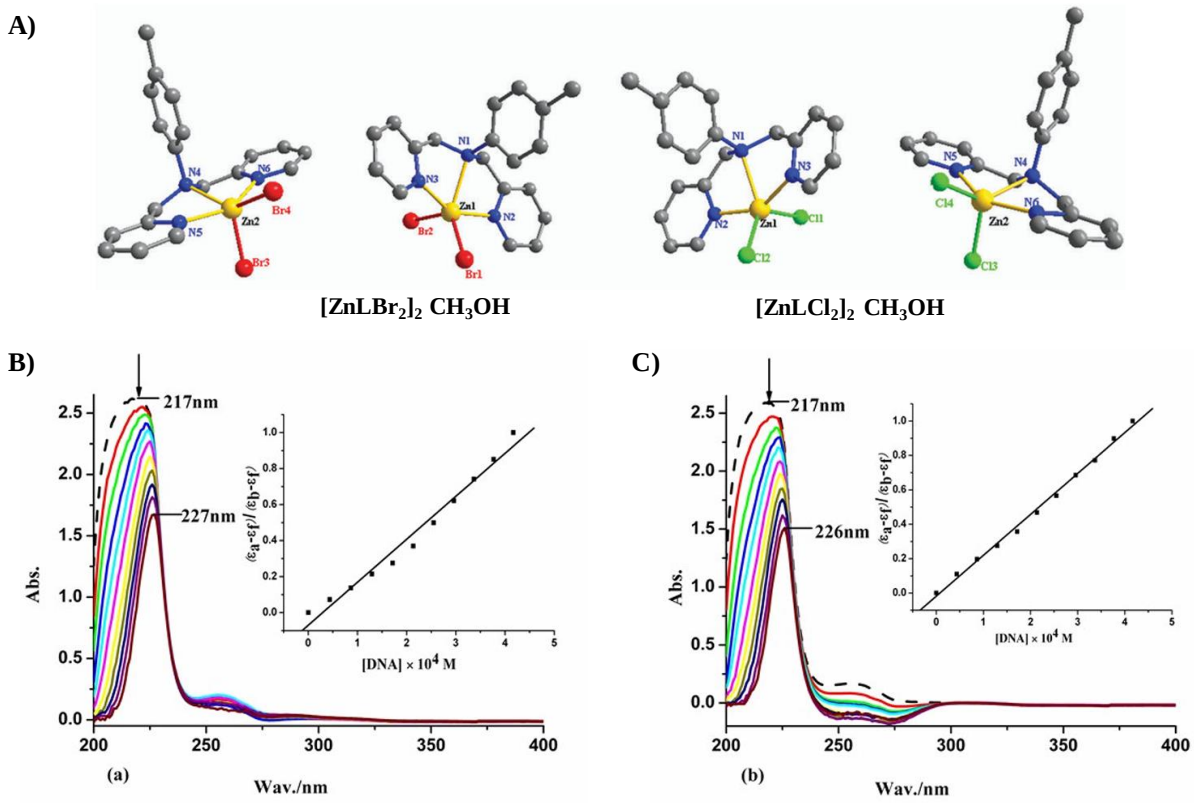

Figure 2B.2. (A) Ball-and-stick representation of the crystal structures of **1** and **2**. Hydrogen atoms and dissociative small molecules are omitted for clarity; (B) Absorption spectra of complexes **1** and **2** (1.96 μM) in the absence (dashed line) and presence (solid line) of increasing amounts of ctDNA (44, 87, 129, 172, 214, 255, 296, 337, 377 and 417 μM) in 5 mM Tris HCl/50 mM NaCl buffer (pH = 7.2) (Figure adapted from reference 23).

In the year 2021, Wang et al. have developed a dipicolylamino-functionalized styryl-carbazole derivative (**YCJ**) and its Zn(II) complex (**YCJ-Zn(II)**), and compared their binding interactions with G-quadruplex (G4) DNA **(Figure 2B.3)**.[24] Comprehensive analysis revealed that the YCJ-Zn(II) complex possesses markedly stronger binding affinity and enhanced spectral response towards G4 DNA, primarily due to the presence of a Zn(II)-DPA unit. This unit lowers the electron density of the carbazole core, which in turn promotes more effective π–π stacking interactions with G4 DNA. Moreover, the incorporation of the Zn-DPA moiety imparts excellent cell permeability and enables effective labelling of endogenous DNA, making it well-suited for tracking nuclear activities.

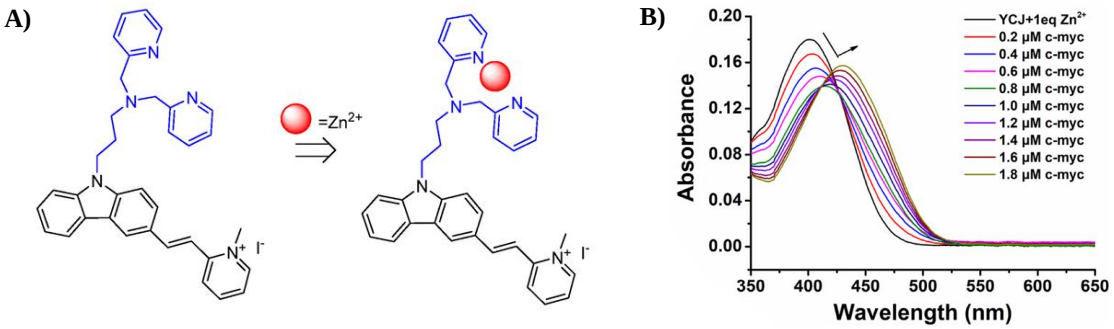

Figure 2B.3. (A) Molecular structures of **YCJ** and its Zn(II) complex; (B) UV-Vis spectra for titrations of G4 DNA stepwise to **YCJ-Zn(II)** complex (5 μM) in 10 mM Tris-HCl buffer, 60 mM KCl, pH 7.4 (Figure adapted from reference 24).

An azulene-based fluorescent chemosensor for nucleotides namely **AzuFluor**, is reported to be selective for ADP over other phosphorylated states of adenosine **(Figure 2B.4**).[25] The probe contains two Zn-DPA receptor motifs connected to a central azulene core through a π-conjugated linker at *para* (**1.2Zn**) or *meso* (**2.2Zn**) position. The receptor motifs can exhibit different selectivity profiles for various phosphate analytes, with **1.2Zn** displaying a distinct selectivity for ADP over ATP. The selectivity for ADP arises from the precise positioning of the Zn(II)-DPA receptor motifs. The nucleobase-fluorophore-nucleobase π-stacked arrangement explains the relatively weak response to PPi and ATP.

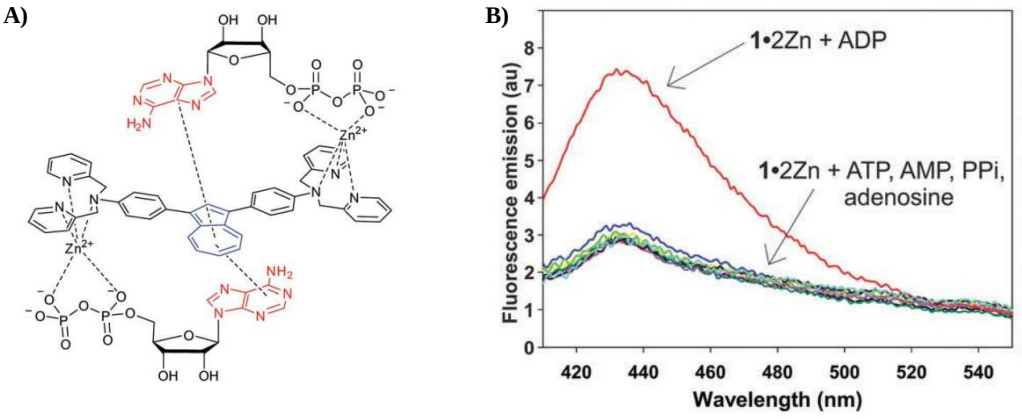

Figure 2B.4. (A) The proposed sensing mechanism of **1.2Zn** towards ADP; (B) Fluorescence emission spectra for **1.2Zn** (100 μM), in the presence of Na_2HPO_4, $Na_4P_2O_7$, AMP sodium salt, ADP sodium salt, ATP sodium salt and adenosine (all 1 mM). Spectra were recorded after 30 min and the fluorescence intensities were measured with λ_{exc} = 380 nm. (Figure adapted from reference 25).

Moro and colleagues have reported a Zn^{2+}- chemosensor based on styrylflavylium dye having a di-(2-picolyl)amine (DPA) moiety. They observed a fluorescence enhancement of this Zn^{2+} coordinated complex upon binding with ATP and ADP (**Figure 2B.5**).[26] The probe exhibited strong selectivity for adenosine 5′-triphosphate (ATP) and adenosine 5′-diphosphate (ADP), showing fluorescence enhancements of 2.1-fold and 3.0-fold, respectively. Fluorescence titration experiments indicated a 1:1 binding stoichiometry with both ATP and ADP, revealing a stronger affinity for ADP. The calculated association constants were 6.3×10^7 M^{-1} for ADP and 1.5×10^6 M^{-1} for ATP.

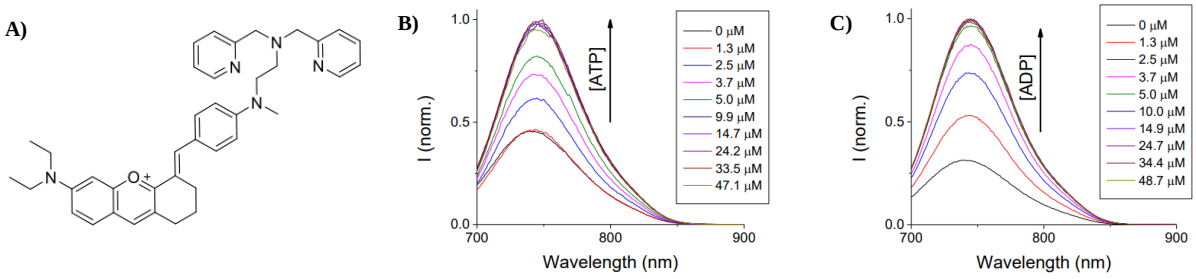

Figure 2B.5. (A) Structure of the styrylflavylium dye with DPA moiety; (B) and (C) Emission spectra of the probe with increasing concentration of ATP and ADP (λ_{exc} = 680 nm) (Figure adapted from reference 26).

As demonstrated in these examples, the selectivity of small molecular sensors with Zn(II)-DPA receptor motifs towards different phosphate derivatives can vary significantly depending on the fluorophore, scaffold, and the spatial arrangement of the Zn-DPA recognition units. In Chapter 2A, we discussed the Zn^{2+} binding of **PYD-PA** derivative, which showed enhanced fluorescence upon Zn^{2+} binding, and its application in imaging of elevated intracellular zinc levels during autophagy. We hypothesised that the **PYD-PA-Zn^{2+}**, with its Zn-DPA moiety and polycyclic aromatic pyridinium chromophore, could effectively bind to nucleotides and DNA strands through various interactions. In this Chapter, we studied the differential binding properties of **PYD-PA-Zn^{2+}** towards nucleotides and DNA.

2B.3. Results and Discussion

2B.3.1. Design, synthesis and characterisation of PYD-PA-Zn^{2+}

Ligands capable of interacting with DNA through multiple binding modes are particularly useful for the development of high-affinity probes targeting nucleic acids. Initial electrostatic interactions of cationic small molecules with DNA backbone can facilitate further binding through intercalation and/or covalent/non-covalent interactions with the phosphate backbone and DNA grooves.[27] Our probe design consists of a pentacyclic pyridinium chromophore appended with a Zn(II)-DPA complex (**Figure 2B.6)**. The positively charged Zn(II) complex can interact with the negatively charged phosphate backbone, facilitating its intercalation into the DNA. The Zn(II)-DPA moiety can bind to the phosphate groups of nucleotides and nucleic acids, while the planar aromatic pyridinium chromophore interacts with DNA base pairs through π-stacking interactions. These combined interactions may result in changes to the optoelectronic properties, which can be utilized for the differential analysis of nucleotides and nucleic acid structures.

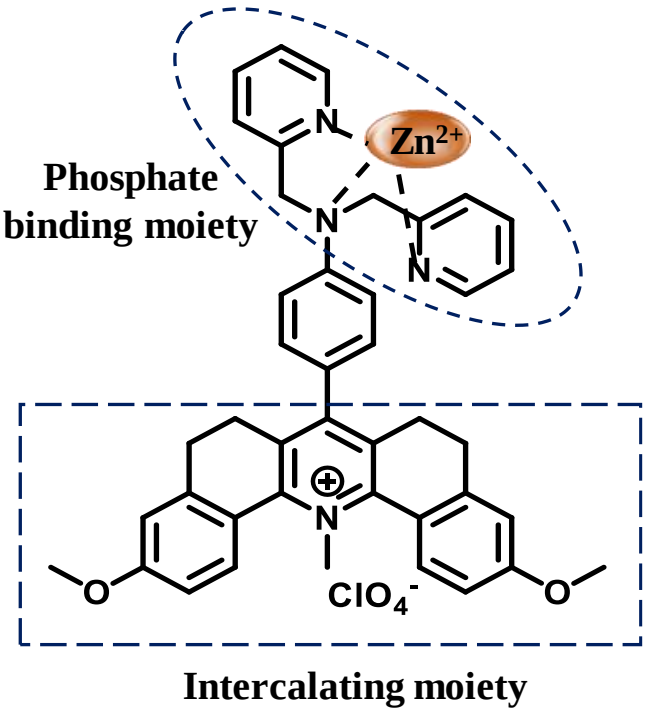

Figure 2B.6. Design of the **PYD-PA-Zn^{2+}** probe.

Synthesis of the **PYD-PA** is reported in chapter 2A. Further, its Zn^{2+} bound complex, **PYD-PA-Zn^{2+}** was prepared by chelating **PYD-PA** with Zinc chloride (**Scheme 2B.1**) in buffered aqueous solutions (100 mM HEPES buffer at pH 7.4). The **PYD-PA-Zn^{2+}** complex formation was characterized by ^{1}H NMR, details of which are provided in the experimental section.

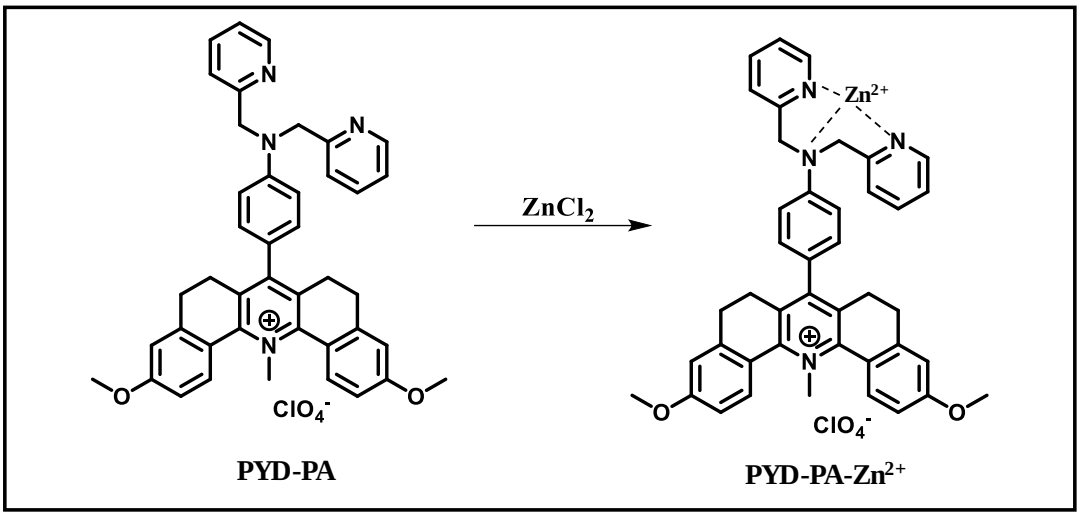

Scheme 2B.1. Scheme for the synthesis of **PYD-PA-Zn^{2+}**.

2B.3.2. Photophysical studies of PYD-PA-Zn^{2+} with different phosphate derivatives

To investigate the binding properties of the **PYD-PA-Zn^{2+}** as a molecular probe, UV-Vis absorption and fluorescence spectra were recorded in the presence of adenosine, AMP, ADP, ATP, and ctDNA. In presence of adenosine and AMP, the probe showed negligible change in absorption and emission spectra indicating its poor binding affinity (**Figure 2B.7 and Figure 2B.8**). In contrast, the probe exhibited a significant enhancement in fluorescence intensity in the presence of ADP and ATP, while the absorption spectra remained unchanged, indicating phosphate-assisted interactions between the probe and these nucleotides (**Figure 2B.9 and Figure 2B.10**). Compared to ADP and ATP, the probe showed an even greater increase in fluorescence intensity, along with shifts in both absorption and emission maxima, specifically with ctDNA (**Figure 2B.11**). For instance, the absorption spectra in the presence of ctDNA showed a 12 nm red shift along with significant hypochromicity. Similarly, the

fluorescence intensity showed a 1.7-fold enhancement in the presence of ctDNA. These spectral changes in absorption and emission wavelengths indicate intercalative binding interactions in addition to phosphate-assisted interactions. To gain further insight into these binding interactions, we investigated the binding of the **PYD-PA-Zn^{2+}** probe with various nucleic acid structures.

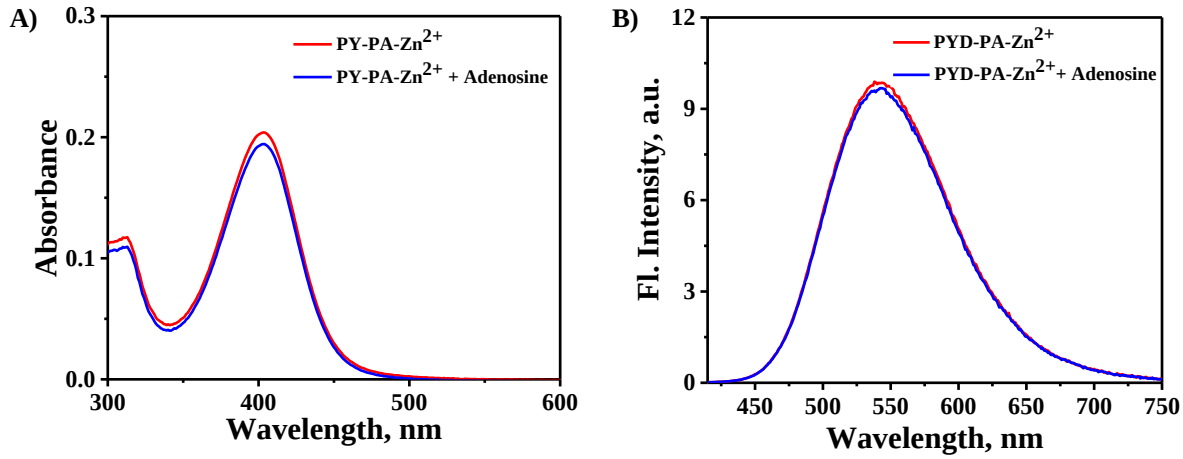

Figure 2B.7. (A) Absorption and (B) emission spectra of **PYD-PA-Zn^{2+}** (10 μM) in presence of adenosine (100 μM) in 0.1 M HEPES buffer (pH = 7.4).

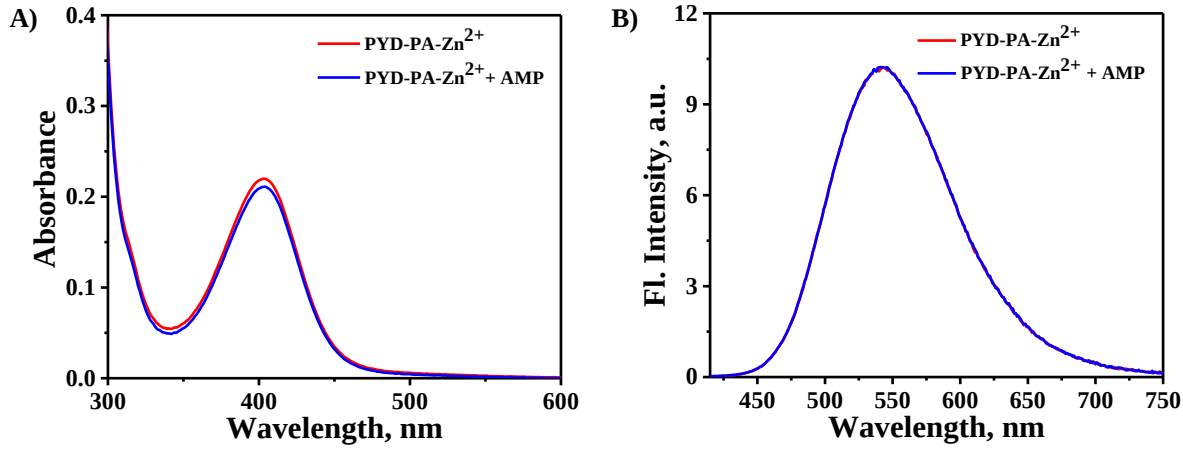

Figure 2B.8. (A) Absorption and (B) emission spectra of **PYD-PA-Zn^{2+}** (10 μM) in presence of AMP (100 μM) in 0.1 M HEPES buffer (pH = 7.4).

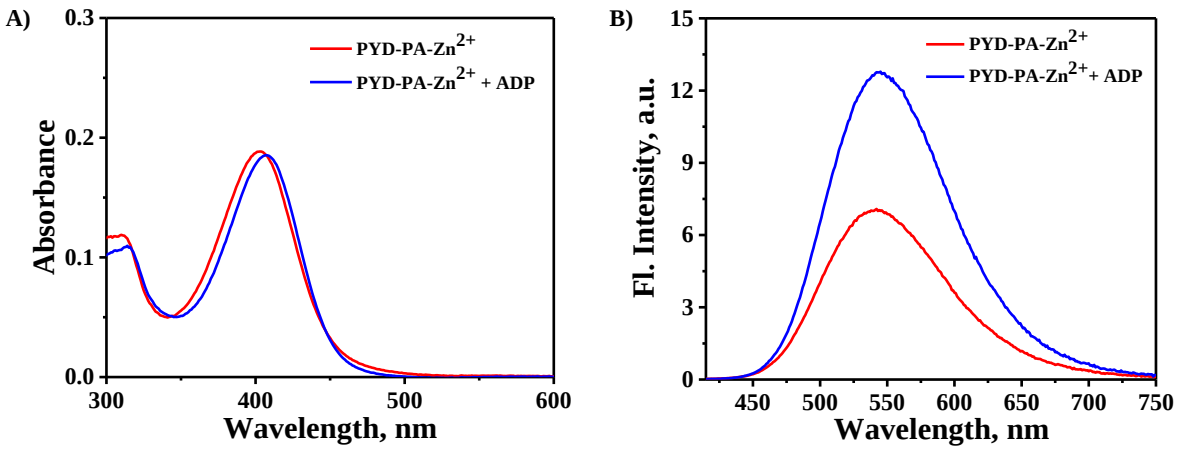

Figure 2B.9. (A) Absorption and (B) emission spectra of **PYD-PA-Zn^{2+}** (10 μM) in presence of ADP (100 μM) in 0.1 M HEPES buffer (pH = 7.4).

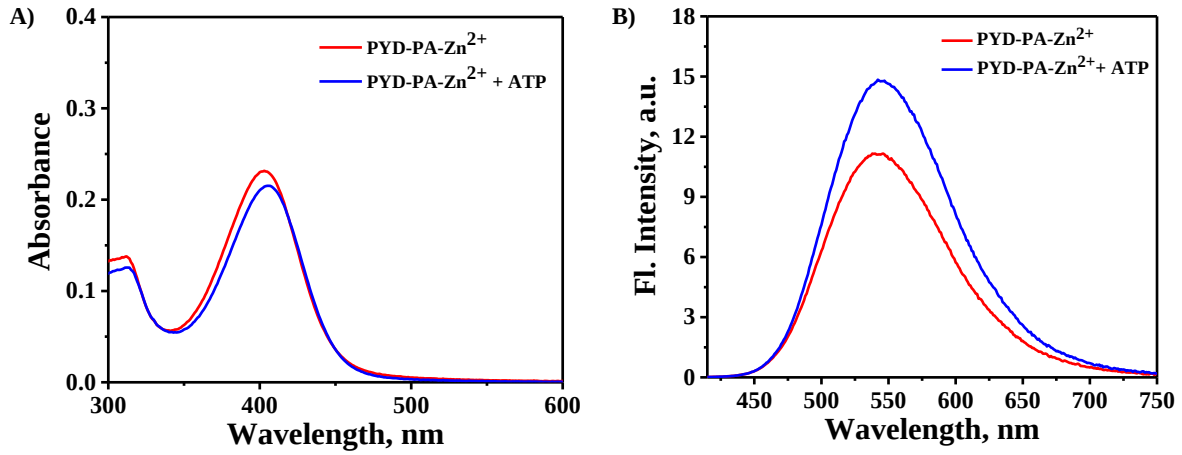

Figure 2B.10. (A) (A) Absorption and (B) emission spectra of **PYD-PA-Zn^{2+}** (10 μM) in presence of ATP (100 μM) in 0.1 M HEPES buffer (pH = 7.4).

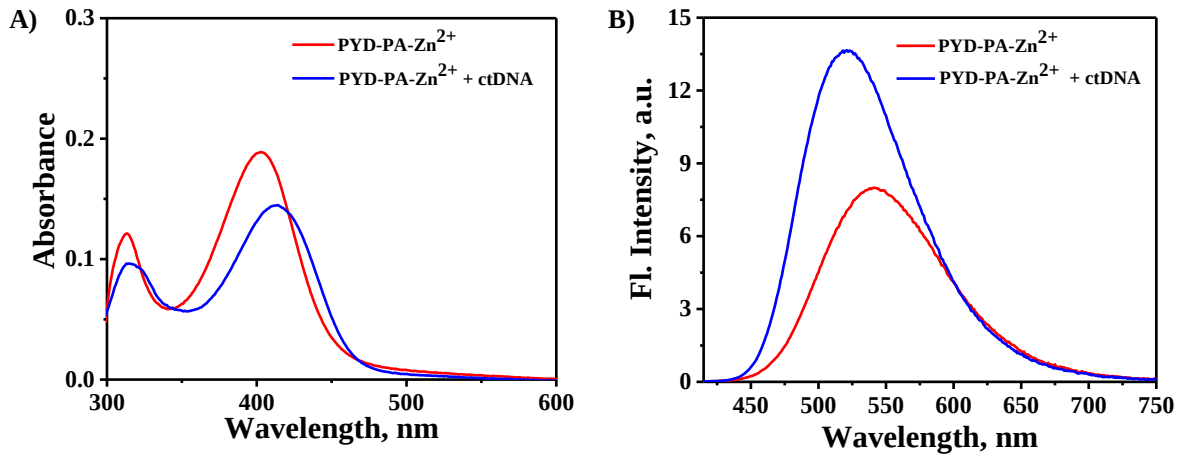

Figure 2B.11. (A) Absorption and (B) emission spectra of **PYD-PA-Zn^{2+}** (10 μM) in presence of ctDNA (100 μM) in 0.1 M HEPES buffer (pH = 7.4).

2B.3.3. UV-Visible absorption and fluorescence emission studies with DNA

To gain a better understanding of the binding interactions, the changes in the absorption and emission properties of **PYD-PA-Zn^{2+}** in the presence of ctDNA were further evaluated by titrating a buffered solution of **PYD-PA-Zn^{2+}** against 0 - 100 µM ctDNA. In 100 mM HEPES buffer (pH 7.4), **PYD-PA-Zn^{2+}** displayed an absorption maximum at 402 nm and a fluorescence maximum at 542 nm. Upon the addition of ctDNA, the absorbance of **PYD-PA-Zn^{2+}** showed a gradual decrease with red shift in the absorption maximum from 402 - 419 nm (**Figure 2B.12.A**). This hypochromic effect along with a red-shift in the absorption maximum, is commonly observed when ligands bind to DNA through intercalation.[28] A significant hypochromic effect and red shift of 17 nm displayed by the probe suggests that intercalation is the preferred binding mode. However, it is also possible that electrostatic interactions occur simultaneously between the negatively charged DNA phosphate backbone and the cationic regions of the probe.

Further, the fluorescence emission of **PYD-PA-Zn^{2+}** is evaluated in the absence and presence of varying amounts of ctDNA (**Figure 2B.12.B** and **Figure 2B.13.A**). The results showed a gradual enhancement in emission intensities of the probe with increasing concentrations of ctDNA, accompanied by a distinct blue shift in wavelength, resembling the classical model of ethidium bromide (EB) intercalating into DNA.[29] An increase in emission intensity upon binding to DNA is often considered as a strong indication of intercalation between DNA base pairs,[30] and therefore, these measurements further support a possible intercalative binding mode. Additionally, the intrinsic binding affinity of the probe for ctDNA was evaluated utilizing double reciprocal equation,[31] and the binding constant (K_b) was determined to be 1.4×10^4 M^{-1}, indicating a strong interaction with nucleic acids (**Figure 2B.13.B**).

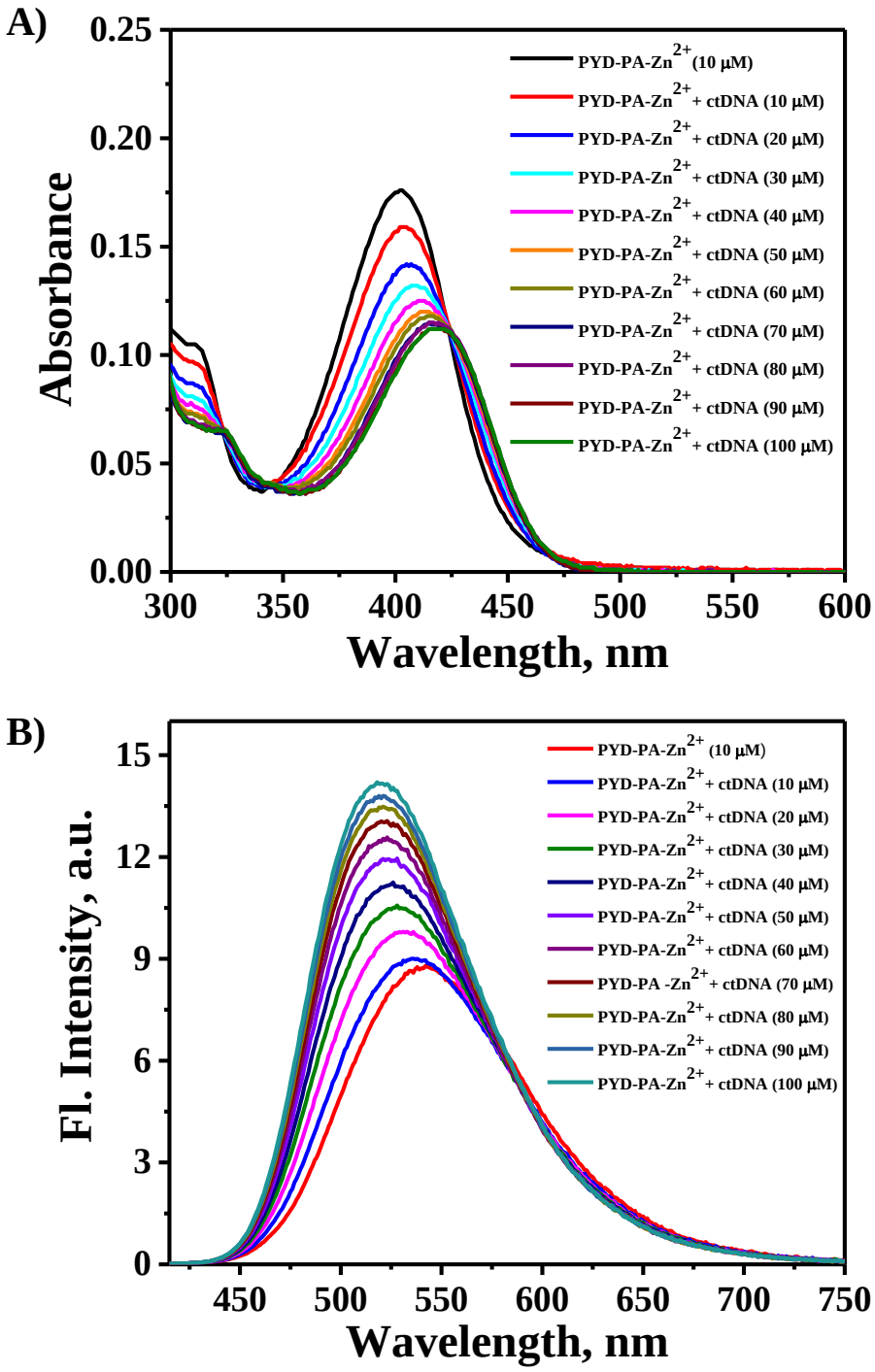

Figure 2B.12. Changes in (A) absorption and (B) emission spectra of **PYD-PA-Zn^{2+}** (10 μM) against varying concentrations of ctDNA (0-100 μM) in 0.1 M HEPES buffer (pH = 7.4); λ_{ex} = 400 nm.

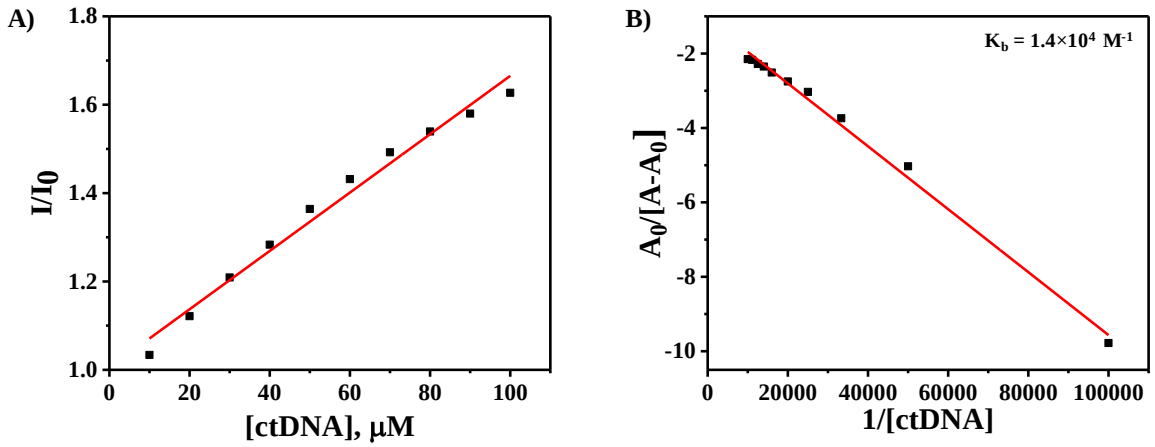

Figure 2B.13. (A) Changes in the ratio of fluorescence intensity of **PYD-PA-Zn^{2+}** with increasing concentration of ctDNA and (B) Plot of 1/[ctDNA] v/s $A_0/[A-A_0]$ for binding constant calculation.

Encouraged by the specific absorption and fluorescence changes observed with ctDNA, we explored the interaction of **PYD-PA-Zn^{2+}** with ssDNA and dsDNA (**Figure 2B.14** and **Figure 2B.15**). The absorption spectra of the probe exhibited a similar trend in both cases, showing a gradual decrease in absorbance accompanied by a red shift from 402 - 414 nm. The hypochromic shift observed in both cases are indicative of possible π-stacking interactions of the pyridinium chromophore with nucleic acid bases. In contrast, the emission spectra of **PYD-PA-Zn^{2+}** exhibited distinct behaviour in the presence of single- and double-stranded DNA. A slight fluorescence quenching (<15%) was observed with ssDNA, while the presence of dsDNA resulted in a gradual and significant enhancement in fluorescence intensity (~2 fold) accompanied by a blue shift in the emission maximum from 542 - 522 nm. Notably, the interaction with ssDNA did not produce any shift in the fluorescence maximum of the pyridinium probe. This difference can be attributed to the intercalative binding of the probe with dsDNA, which induces greater rigidity in the chromophore when compared to the less-rigid π-stacking interactions with the nucleobases of ssDNA. Intercalation involves the insertion of planar aromatic molecules, such as the pyridinium chromophore, between the stacked base pairs of dsDNA. This process stabilizes the DNA-probe complex by restricting the molecular flexibility of the chromophore, which is reflected in the enhanced fluorescence

and blue-shifted emission. In contrast, ssDNA lacks the well-defined, stacked helical structure of dsDNA, making intercalation physically unfeasible. As a result, the interactions between the probe and ssDNA are likely limited to surface-level π-stacking, which does not significantly alter the rigidity or optoelectronic properties of the chromophore. This observation explains the lack of a fluorescence shift and the relatively minor fluorescence quenching observed with ssDNA.

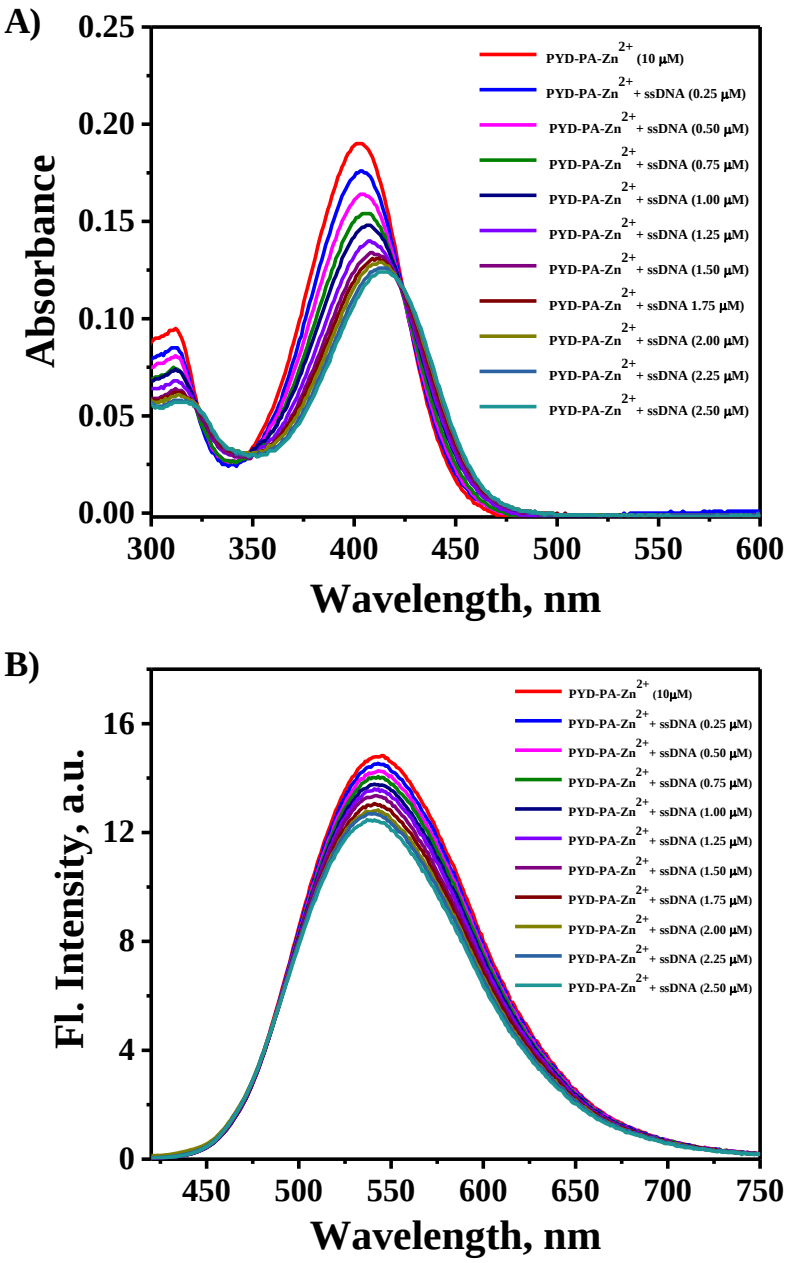

Figure 2B.14. Changes in (A) absorption and (B) emission spectra of **PYD-PA-Zn^{2+}** (10 μM) against varying concentrations of ssDNA (0-2.5 μM) in 0.1 M HEPES buffer (pH = 7.4); λ_{ex} = 400 nm.

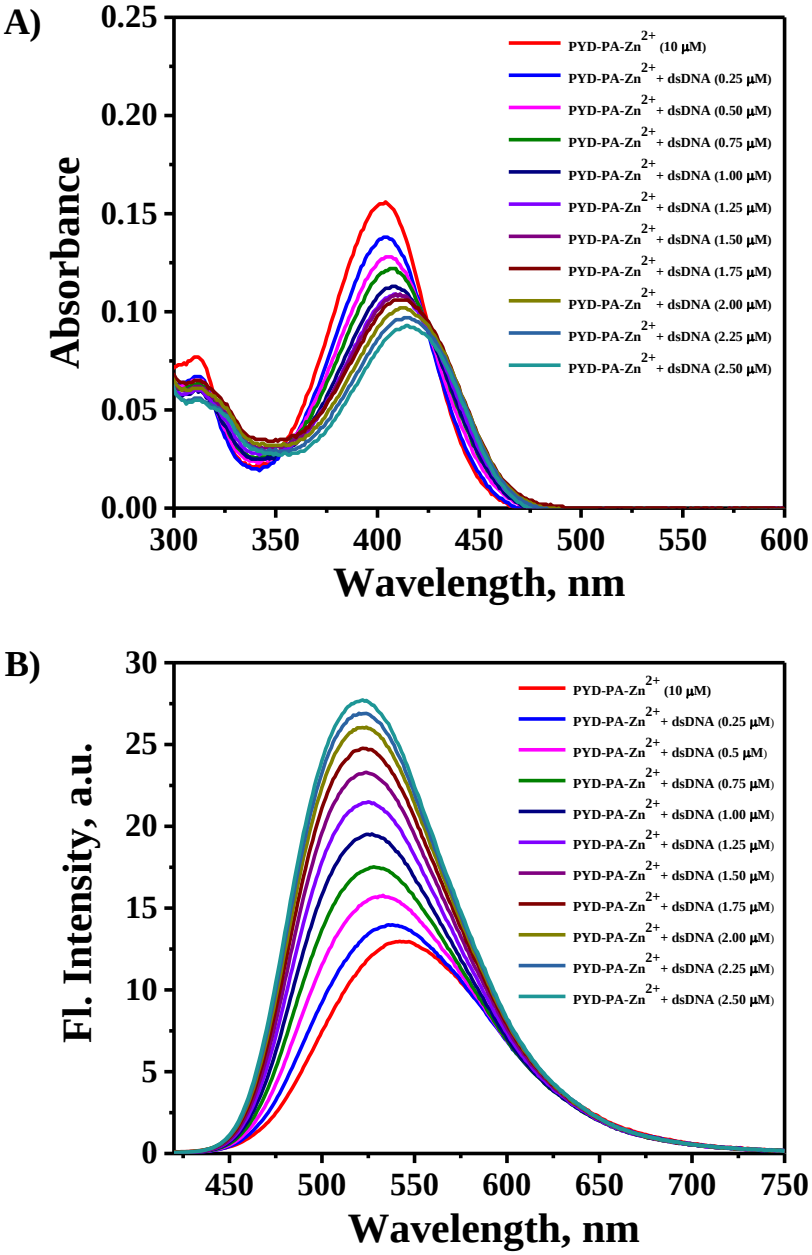

Figure 2B.15. Changes in (A) absorption and (B) emission spectra of **PYD-PA-Zn^{2+}** (10 μM) against varying concentrations of dsDNA (0-2.5 μM) in 0.1 M HEPES buffer (pH = 7.4); λ_{ex} = 400 nm.

2B.3.4. Circular dichroism spectroscopy studies

Circular dichroism (CD) spectroscopy is a powerful technique for observing conformational changes in DNA induced by small molecules.[32] By analysing the alterations in the CD signal of DNA and the induced circular dichroism (ICD) of probes, we can understand the binding mode and interaction mechanism. To explore these possibilities, CD spectrum of

ctDNA was recorded with varying concentrations of the **PYD-PA-Zn^{2+}** probe (**Figure 2B.16**). The CD spectrum of ctDNA showed a positive band around 277 nm, corresponding to the base stacking and a negative band near 245 nm, due to the helicity, indicating a typical B-form DNA structure. Generally, base-stacking and helicity bands remain unaffected by simple groove binding or electrostatic interactions. However, intercalation alters the intensities of these bands, either decreasing or increasing them due to the local disruption of the base stacking and partial unwinding of the helix at the sites of intercalation.[33] Upon addition of **PYD-PA-Zn^{2+}**, the CD spectrum of the ctDNA showed significant changes in both the positive and negative bands, suggesting an intercalative binding mode. Additionally, the ICD spectral bands in the range of 355 - 485 nm, corresponding to the pyridinium chromophore, further confirmed the ordered binding of the probe to dsDNA through intercalation.

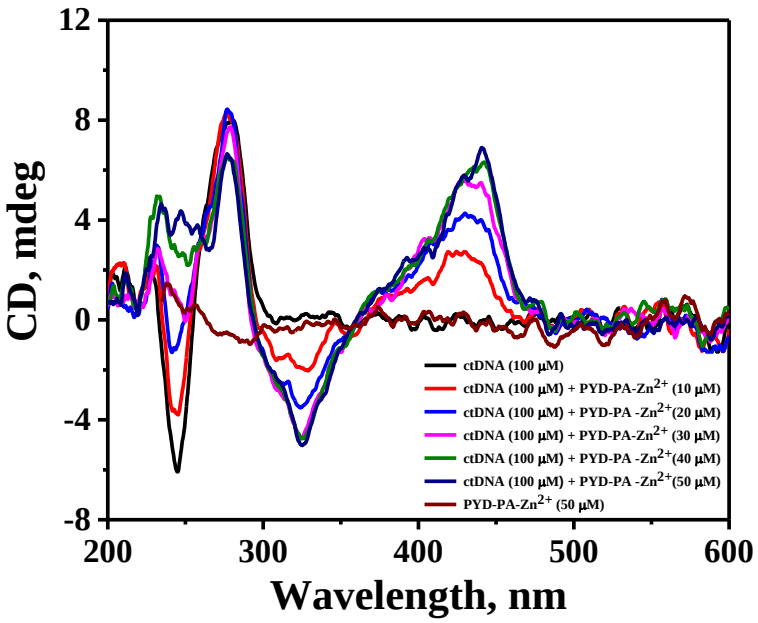

Figure 2B.16. (A) Changes in the CD spectra of ctDNA (100 μM) upon gradual addition of **PYD-PA-Zn^{2+}**(0-50 μM) in 0.1 M HEPES buffer (pH = 7.4).

To investigate the differential binding interactions of the probe with ssDNA and dsDNA, changes in their CD spectra were examined with increasing the concentration of **PYD-PA-Zn^{2+}** (0-50 μM). The CD signal of ssDNA remained largely unchanged in the presence of the probe, suggesting the absence of an intercalative binding mode (**Figure 2B.17.A**).

Furthermore, the interaction of the probe with ssDNA did not produce any ICD signal, indicating the absence of an ordered arrangement of the probe with ssDNA. In contrast, the CD spectrum of dsDNA exhibited changes in both the positive and negative bands upon probe addition, indicating an intercalative binding interaction (**Figure 2B.17.B**). Further, the induced CD signal in the 355 - 485 nm range, corresponding to the pyridinium chromophore, confirms the intercalative binding of the probe with dsDNA.

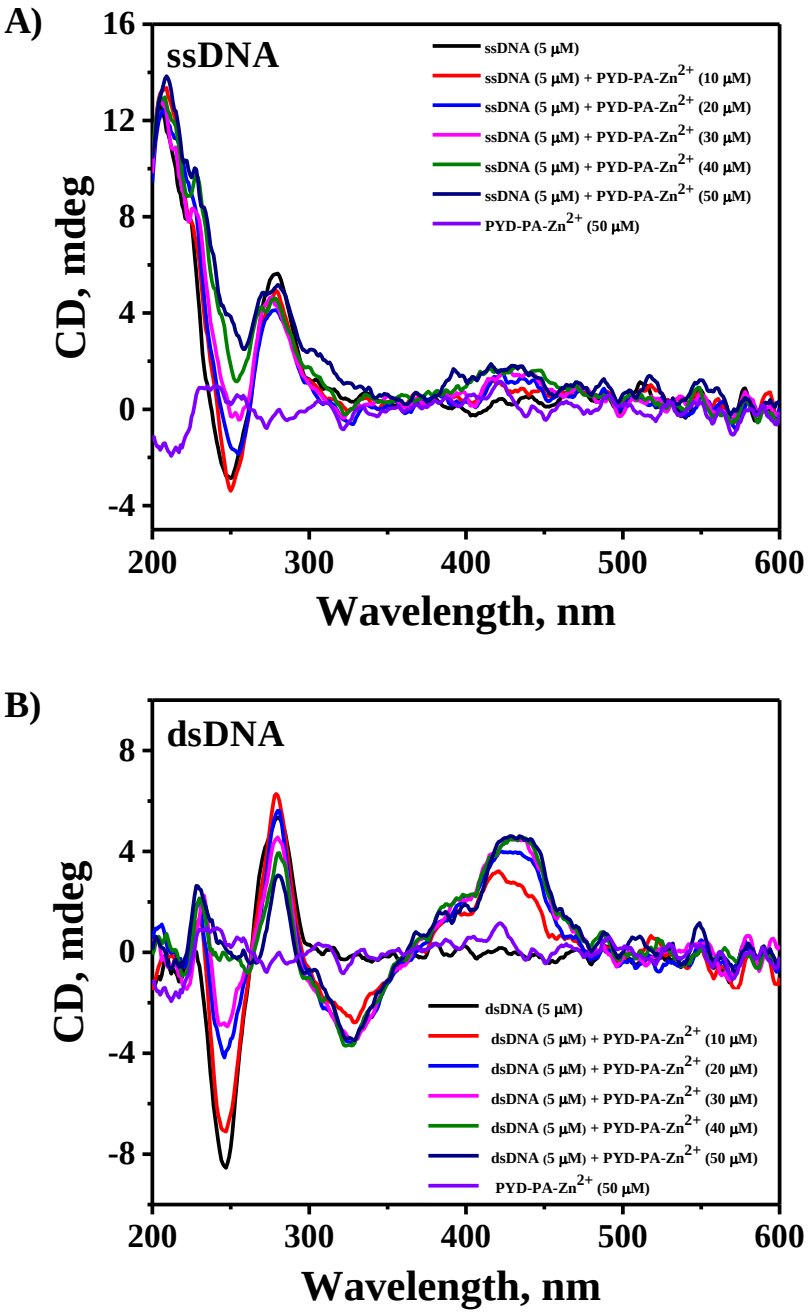

Figure 2B.17. Changes in the CD spectra of (A) ssDNA (5 μM) and (B) dsDNA(5 μM) upon gradual addition of **PYD-PA-Zn^{2+}**(0-50 μM) in 0.1 M HEPES buffer (pH = 7.4).

2B.3.5. Thermal denaturation studies

Thermal denaturation studies were conducted to assess the probe's ability to stabilize double-stranded DNA. The melting temperature (Tm) of DNA, which reflects the transition from double-stranded to single-stranded form, increases when small molecules intercalate into the double helix due to additional π-stacking interactions with the base pairs, stabilizing the duplex. Given that ctDNA has a melting temperature above 70 °C,[34] we synthesized a 20-mer dsDNA strand with a lower Tm for use in thermal denaturation experiments. Initially, the Tm of the dsDNA was 46 °C, however after the addition of **PYD-PA-Zn^{2+}**, it increased to 56 °C (**Figure 2B.18.A** and **B**). This 10 °C increase in Tm indicates the stabilizing effect of chromophore intercalation and supports the proposed binding mode.

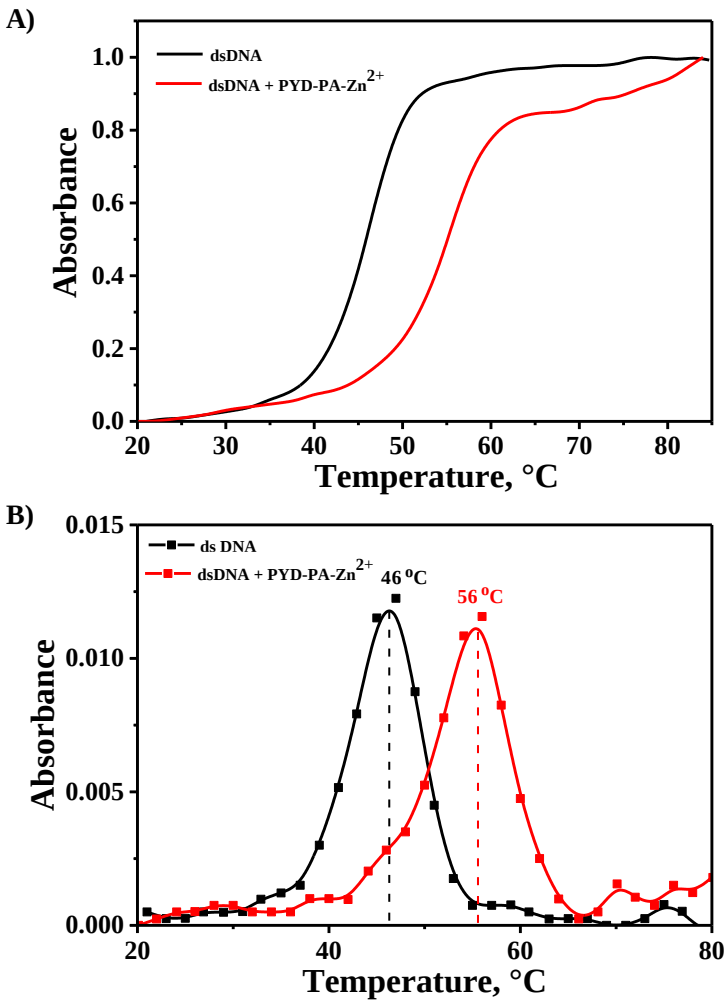

Figure 2B.18. (A) Melting curves of dsDNA (2 μM) in the absence and presence of **PYD-PA-Zn^{2+}** (50 μM) in 0.1 M HEPES buffer (pH = 7.4) and (B) the corresponding first derivative plots.

2B.3.6. Fluorescence lifetime studies

To gain deeper insights into the excited state dynamics, the fluorescence intensity decay profiles of the probe, **PYD-PA-Zn^{2+}** were investigated in the presence of ADP, ATP, ctDNA, ssDNA and dsDNA in 0.1 M HEPES buffer (pH = 7.4) using picosecond time-correlated single photon counting techniques (**Figure 2B.19A and Table 2B.1**). **PYD-PA-Zn^{2+}** showed a biexponential, singlet excited state decay with lifetimes of 0.99 ns (56%) and 4.16 ns (44%), with an average lifetime of 1.48 ns. In the presence of ADP, the fluorescence lifetimes were 1.17 ns (64%) and 3.62 ns (36%), resulting in an average lifetime of 1.55 ns. Similarly, with ATP, the biexponential lifetimes were 1.18 ns (58%) and 3.99 ns (42%), with an average lifetime of 1.68 ns. Based on UV-Vis absorption and fluorescence data, we deduce that the probe **PYD-PA-Zn^{2+}** bind to ATP and ADP via interactions with the phosphate group, which cause only minor changes in fluorescence lifetimes.

However, in the presence of ctDNA, the fluorescence lifetimes were 1.37 ns (21%) and 5.08 ns (79%), with an average lifetime of 3.26 ns, indicating a significant enhancement in fluorescence lifetime. Additionally, we examined the fluorescence decay profiles of **PYD-PA-Zn^{2+}** in the presence of saturating concentrations of ssDNA and dsDNA (**Figure 2B.19B and Table 2B.1**). With ssDNA, the lifetimes were 1.24 ns (15%) and 4.42 ns (85%), giving an average lifetime of 3.18 ns. In contrast, a much greater enhancement in fluorescence lifetime was observed with dsDNA, showing lifetimes of 1.74 ns (12%) and 5.87 ns (88%), with an average lifetime of 4.55 ns. The apparent enhancement in the fluorescence lifetimes observed for ctDNA and dsDNA, compared to ADP, ATP and ssDNA confirms the intercalative binding of the probe with ctDNA and dsDNA, where intercalation immobilizes the dye, reducing its dynamic fluctuations and possible quenching interactions. The observed longer lifetime of the intercalated probe can be utilized for distinguishing ssDNA and dsDNA through fluorescence lifetime imaging.

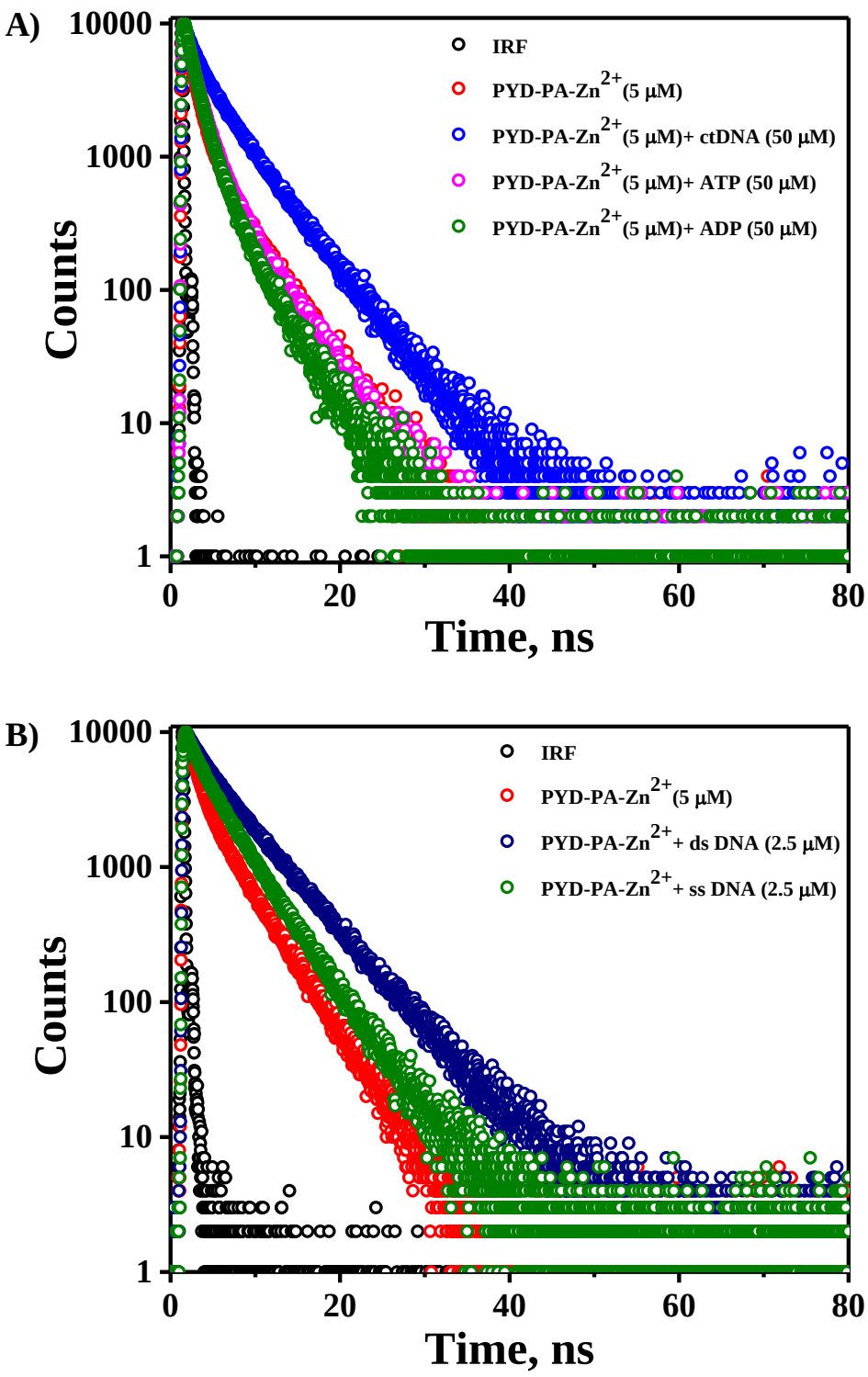

Figure 2B.19. Fluorescence decay profile of **PYD-PA-Zn^{2+}** (5 μM) in the presence of saturating concentrations of (A) ADP, ATP and ctDNA (50 μM); (B) ssDNA and dsDNA (2.5 μM).

Table 2B.1. Fluorescence lifetime data of **PYD-PA-Zn^{2+}** in the presence of saturating concentrations of ADP, ATP, ctDNA, ssDNA and dsDNA.

Compound	Lifetime (ns)		
	τ_1 (%)	τ_2 (%)	τ_{av}
PYDPA-Zn^{2+}	**0.99 (56)**	**4.16 (44)**	**1.48**
PYDPA-Zn^{2+}+ ctDNA	**1.37 (21)**	**5.08 (79)**	**3.26**
PYDPA-Zn^{2+}+ ATP	**1.18 (58)**	**3.99 (42)**	**1.68**
PYDPA-Zn^{2+}+ ADP	**1.17 (64)**	**3.62 (36)**	**1.55**
PYDPA-Zn^{2+}+ ssDNA	**1.24 (15)**	**4.42 (85)**	**3.18**
PYDPA-Zn^{2+}+ dsDNA	**1.74 (12)**	**5.87 (88)**	**4.55**

DNA light-up probes often interact with nucleotides, making it challenging to differentiate between nucleotides and DNA. However, the probe **PYD-PA-Zn^{2+}** effectively distinguishes between nucleotides and nucleic acids by combining fluorescence intensity and lifetime measurements. The probe showed increased fluorescence intensity with ATP and ADP, while the fluorescence lifetime remained largely unchanged. In contrast, the presence of DNA led to significant increases in both fluorescence intensity and lifetime, attributed to phosphate-assisted intercalation. These interactions involve both the pyridinium chromophore and the Zn^{2+}-DPA moiety, whereas interactions with ATP and ADP are primarily driven by the Zn^{2+}-DPA moiety alone. Thus, **PYD-PA-Zn^{2+}** serves as an effective tool for the differential analysis of nucleotides and DNA.

2B.4. Conclusions

In summary, we have developed a zinc(II)-dipicolylamine based pyridinium probe, **PYD-PA-Zn^{2+}**, and studied their binding interactions with nucleotides and DNA. The probe exhibited negligible changes in both absorption and emission spectra in the presence of adenosine and AMP, indicating weak binding affinity. However, notable fluorescence

enhancement was observed with ADP and ATP, while the absorption spectra remained unaffected. On the other hand, in the presence of ctDNA and dsDNA, the probe showed a decrease in absorbance with a red shift in the absorption maximum from 402 - 419 nm. Additionally, the emission spectra displayed a significant enhancement in fluorescence intensity accompanied by a blue shift in emission maxima, resembling the ethidium bromide interaction with DNA. Further photophysical studies, including CD spectroscopy and thermal denaturation analysis, confirmed that the probe binds to ctDNA and dsDNA via an intercalative mode, while its interactions with ADP, ATP, and ssDNA are primarily phosphate-assisted. Additionally, we observed a significant enhancement in the fluorescent lifetime of the probe in the presence of ctDNA and dsDNA when compared to ssDNA, ADP, and ATP, enabling differential analysis of these nucleic acids and nucleotides by combining fluorescence intensity and lifetime measurements. These promising findings could pave way for further molecular and mechanistic studies aimed at developing novel metal-based drugs with specific DNA-binding capabilities.

2B.5. Experimental Section

2B.5.1. Materials and Methods

All chemical reagents and solvents used in this study were procured from commercial suppliers (Sigma Aldrich and TCI chemicals) and used without further purification. ctDNA and 20-mer ssDNA were purchased from Sigma Aldrich. Stock solutions of calf thymus DNA (ctDNA) was prepared by dissolving commercially available white fibrous ctDNA in de-ionised Milli Q water. The concentration of ctDNA was determined by measuring its absorption intensity at 260 nm with a known molar absorption coefficient value of 6600 M^{-1} cm^{-1}. The dsDNA used in this study was prepared by hybridizing complementary 20-mer ssDNA strands (Strand 1: CGTCACGTAAATCGGTTAAC, Strand 2: GTTAACCGATTTAC GTGACG) through annealing in Milli Q water containing 10 mM PBS and 2 mM NaCl. ^{1}H NMR (500 MHz) analyses were conducted using a Bruker Avance DPX spectrometer, with TMS as the internal standard.

2B.5.1.1. UV-Vis absorption and fluorescence spectra

UV-Vis absorption spectra were recorded using a Shimadzu UV-Vis spectrophotometer (UV-2600) and fluoresce spectra were recorded using a SPEX Fluorolog spectrofluorimeter. The titration studies were performed by keeping the probe concentration constant (10 μM) while varying the analyte concentrations (adenosine, AMP, ADP, ATP, ctDNA, ssDNA, dsDNA) at room temperature. Absorption spectra were recorded from 300 to 600 nm, and changes in absorbance were monitored. Fluorescence spectra were recorded over 420 to 750 nm range with an excitation wavelength of 400 nm. The titration processes were repeated until binding saturation was achieved.

2B.5.1.2. Circular dichroism spectra

Circular dichroism studies were performed using JASCO J-810 spectropolarimeter equipped with Peltier controlled thermostatic cell holder. CD spectra were recorded by keeping the DNA concentration constant (ctDNA-100 µM, ssDNA-5 µM and dsDNA-5 µM) while varying the compound concentrations (10 - 50 µM). The spectra were recorded over a range of 200 - 600 nm. Titrations were repeated until no spectral changes were detected in the 200 - 500 nm region for at least three consecutive measurements.

2B.5.1.3. DNA thermal denaturation

Thermal denaturation experiments were carried out on a Shimadzu UV-Vis spectrophotometer (UV-2600) equipped with a high performance temperature controller. The dsDNA (2 µM) was denatured by increasing the temperature from 20 - 90 ^{o}C at a speed of 1 ^{o}C/min in the presence and absence of the probe (50 µM), while the corresponding absorbance was monitored at 260 nm. The melting temperature (Tm) was determined from the first derivative plot of the melting curves.

2B.5.1.4. Fluorescence lifetime studies

The fluorescence lifetime measurements were done using picosecond single photon counting system (Horiba, DeltaFlex) employing 378 nm laser as excitation source and picosecond photon detection module (PPD-850) as the detector. The absorbance of the probe was adjusted to 0.1 for lifetime measurements, and saturated concentrations of analytes were added. The fluorescence decay profile was deconvoluted using EzTime software and fitted with multi-exponential decay of chi-square value 1 ± 0.1.

2B.5.2. Synthesis and characterization

Synthesis of **PYD-PA-Zn^{2+}**: PYD-PA in HEPES buffer was treated with $ZnCl_2$ solution (10 equivalent) to yield **PYD-PA-Zn^{2+}**. The complex formation is confirmed from the chemical shift of the aromatic protons in the NMR spectrum.

^{1}H NMR (500 MHz, CD_3CN) δ(ppm): 2.41 (m, 4H), 2.73 (m, 4H), 3.90 (s, 6H), 4.27 (s,3H), 4.86 (s, 4H), 6.98 (s, 2H), 7.04 (d, J = 5 Hz, 4H), 7.13 (d, J = 10 Hz, 2H), 7.64 (d, J = 10 Hz, 4H), 8.09 (m, 4H), 9.12 (d, J =5Hz, 2H).

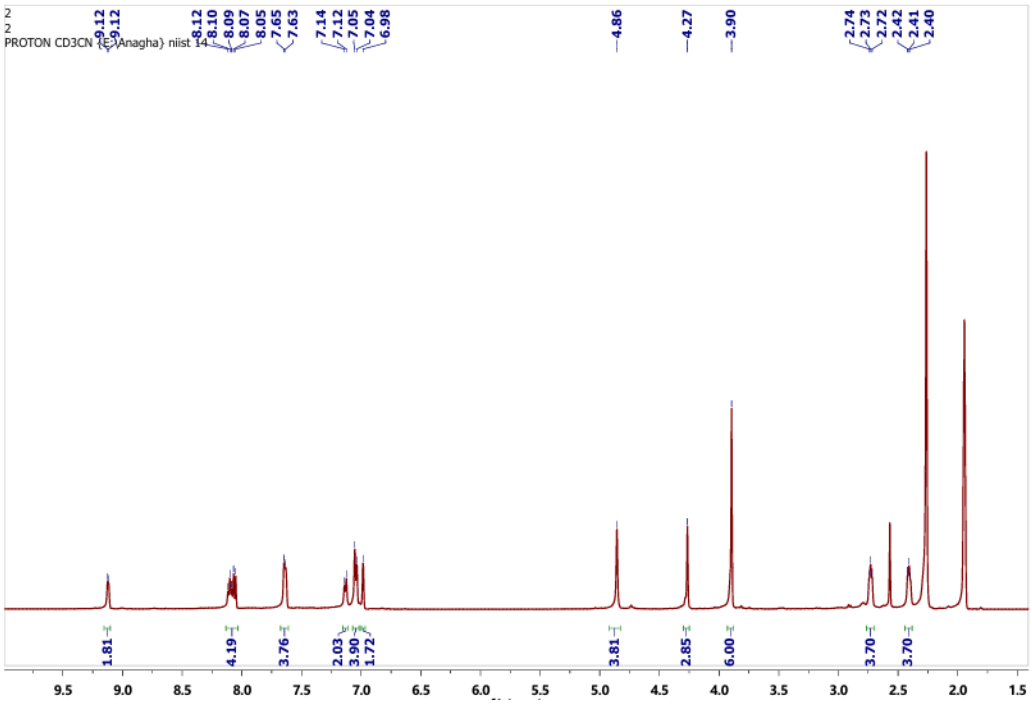

Figure 2B.20. ^{1}H NMR spectrum of **PYD-PA-Zn^{2+}**

2B.6. References

1. de Stigter, Y.; van der Veer, H. J.; Rosier, B. J. H. M.; Merkx, M., Bioluminescent Intercalating Dyes for Ratiometric Nucleic Acid Detection. *ACS Chemical Biology* **2024**.

2. Roewer, L., DNA fingerprinting in forensics: past, present, future. *Investigative genetics* **2013,** *4*, 1-10.

3. Yu, A. C.-H.; Vatcher, G.; Yue, X.; Dong, Y.; Li, M. H.; Tam, P. H. K.; Tsang, P. Y. L.; Wong, A. K. Y.; Hui, M. H. K.; Yang, B., Nucleic acid-based diagnostics for infectious diseases in public health affairs. *Frontiers of medicine* **2012,** *6* (2), 173-186.

4. Sohel, M. M. H., Circulating microRNAs as biomarkers in cancer diagnosis. *Life sciences* **2020,** *248*, 117473.

5. Kellett, A.; Molphy, Z.; Slator, C.; McKee, V.; Farrell, N. P., Molecular methods for assessment of non-covalent metallodrug–DNA interactions. *Chemical Society Reviews* **2019,** *48* (4), 971-988.

6. Goftar, M. K.; Kor, N. M.; Kor, Z. M., DNA intercalators and using them as anticancer drugs. *Int. J. Adv. Biol. Biomed. Res* **2014,** *2* (3), 811-822.

7. Brana, M. F.; Cacho, M.; Gradillas, A.; Pascual-Teresa, B. d.; Ramos, A., Intercalators as anticancer drugs. *Current pharmaceutical design* **2001,** *7* (17), 1745-1780.

8. Denny, W. A., DNA-intercalating ligands as anti-cancer drugs: prospects for future design. *Anti-cancer drug design* **1989,** *4* (4), 241-263.

9. Zhao, C.; Zhang, Y.; Wang, X.; Cao, J., Development of BODIPY-based fluorescent DNA intercalating probes. *Journal of Photochemistry and Photobiology A: Chemistry* **2013,** *264*, 41-47.

10. Rehman, S. U.; Sarwar, T.; Husain, M. A.; Ishqi, H. M.; Tabish, M., Studying non-covalent drug–DNA interactions. *Archives of biochemistry and biophysics* **2015,** *576*, 49-60.

11. Cosa, G.; Focsaneanu, K. S.; McLean, J. R. N.; McNamee, J. P.; Scaiano, J. C., Photophysical Properties of Fluorescent DNA-dyes Bound to Single-and Double-stranded DNA in Aqueous Buffered Solution¶. *Photochemistry and photobiology* **2001,** *73* (6), 585-599.

12. Zhang, J.; Song, S.; Zhang, L.; Wang, L.; Wu, H.; Pan, D.; Fan, C., Sequence-specific detection of femtomolar DNA via a chronocoulometric DNA sensor (CDS): effects of nanoparticle-mediated amplification and nanoscale control of DNA assembly at electrodes. *Journal of the American Chemical Society* **2006,** *128* (26), 8575-8580.

13. Gao, Y.; Qiao, G.; Zhuo, L.; Li, N.; Liu, Y.; Tang, B., A tumor mRNA-mediated bi-photosensitizer molecular beacon as an efficient imaging and photosensitizing agent. *Chemical communications* **2011,** *47* (18), 5316-5318.

14. Biver, T.; De Biasi, A.; Secco, F.; Venturini, M.; Yarmoluk, S., Cyanine dyes as intercalating agents: kinetic and thermodynamic studies on the DNA/Cyan40 and DNA/CCyan2 systems. *Biophysical journal* **2005,** *89* (1), 374-383.

15. Tumir, L.-M.; Stojković, M. R.; Piantanida, I., Come-back of phenanthridine and phenanthridinium derivatives in the 21st century. *Beilstein journal of organic chemistry* **2014,** *10* (1), 2930-2954.

16. Ferguson, L. R.; Denny, W. A., Genotoxicity of non-covalent interactions: DNA intercalators. *Mutation Research/Fundamental and Molecular Mechanisms of Mutagenesis* **2007,** *623* (1-2), 14-23.

17. Hartshorn, R. M.; Barton, J. K., Novel dipyridophenazine complexes of ruthenium (II): exploring luminescent reporters of DNA. *J. Am. Chem. Soc.* **1992,** *114* (15), 5919-5925.

18. Shao, F.; Elias, B.; Lu, W.; Barton, J. K., Synthesis and characterization of iridium (III) cyclometalated complexes with oligonucleotides: insights into redox reactions with DNA. *Inorg. Chem.* **2007,** *46* (24), 10187-10199.

19. Cusumano, M.; Di Pietro, M. L.; Giannetto, A., DNA interaction of platinum (II) complexes with 1, 10-phenanthroline and extended phenanthrolines. *Inorg. Chem.* **2006,** *45* (1), 230-235.

20. Li, G.; Sun, L.; Ji, L.; Chao, H., Ruthenium (II) complexes with dppz: from molecular photoswitch to biological applications. *Dalton Transactions* **2016,** *45* (34), 13261-13276.

21. Genereux, J. C.; Barton, J. K., Mechanisms for DNA charge transport. *Chemical reviews* **2010,** *110* (3), 1642-1662.

22. Jia, F.; Wang, S.; Man, Y.; Kumar, P.; Liu, B., Recent Developments in the Interactions of Classic Intercalated Ruthenium Compounds:[Ru (bpy) 2dppz] 2+ and [Ru (phen) 2dppz] 2+ with a DNA Molecule. *Molecules* **2019,** *24* (4), 769.

23. Zhang, Y.-P.; Ma, Z.-Y.; Gao, C.-Y.; Qiao, X.; Tian, J.-L.; Gu, W.; Liu, X.; Xu, J.-Y.; Zhao, J.-Z.; Yan, S.-P., Two dpa-based zinc (ii) complexes as potential anticancer agents: nuclease activity, cytotoxicity and apoptosis studies. *New Journal of Chemistry* **2016,** *40* (9), 7513-7521.

24. Yu, Q.-Q.; Lang, X.-X.; Gao, J.-J.; Li, H.-Y.; Bai, Y.-T.; Wang, H.-J.; Wang, M.-Q., Zn (II)-DPA Coordinative fluorescent probe for enhancing G4 DNA binding. *Dyes and Pigments* **2021,** *195*, 109707.

25. López-Alled, C. M.; Park, S. J.; Lee, D. J.; Murfin, L. C.; Kociok-Köhn, G.; Hann, J. L.; Wenk, J.; James, T. D.; Kim, H. M.; Lewis, S. E., Azulene-based fluorescent chemosensor for adenosine diphosphate. *Chemical Communications* **2021,** *57* (81), 10608-10611.

26. Gomes, L. J.; Carrilho, J. P.; Pereira, P. M.; Moro, A. J., A Near InfraRed Emissive Chemosensor for Zn2+ and Phosphate Derivatives Based on a Di-(2-picolyl) amine-styrylflavylium Push-Pull Fluorophore. *Sensors* **2023,** *23* (1), 471.

27. Kumar, N.; Kaushal, R.; Awasthi, P., Non-covalent binding studies of transition metal complexes with DNA: A review. *Journal of Molecular Structure* **2023,** *1288*, 135751.

28. Gu, Z.; Li, Y.; Ma, S.; Li, S.; Zhou, G.; Ding, S.; Zhang, J.; Wang, S.; Zhou, C., Synthesis, cytotoxic evaluation and DNA binding study of 9-fluoro-6 H-indolo [2, 3-b] quinoxaline derivatives. *RSC advances* **2017,** *7* (66), 41869-41879.

29. Chib, R.; Raut, S.; Sabnis, S.; Gryczynski, Z.; Gryczynski, I., Associated anisotropy decays of ethidium bromide interacting with DNA. *Biophysical Journal* **2014,** *106* (2), 67a.

30. Palchaudhuri, R.; Hergenrother, P. J., DNA as a target for anticancer compounds: methods to determine the mode of binding and the mechanism of action. *Current opinion in biotechnology* **2007,** *18* (6), 497-503.

31. Hajian, R.; Guan Huat, T., Spectrophotometric Studies on the Thermodynamics of the ds-DNA Interaction with Irinotecan for a Better Understanding of Anticancer Drug-DNA Interactions. *Journal of Spectroscopy* **2013,** *2013* (1), 380352.

32. Ivanov, V.; Minchenkova, L. E.; Schyolkina, A. K.; Poletayev, A. I., Different conformations of double-stranded nucleic acid in solution as revealed by circular dichroism. *Biopolymers: Original Research on Biomolecules* **1973,** *12* (1), 89-110.

33. Yuan, J.; Song, J.-Y.; Yang, H.-H.; Lan, H.-R.; Xing, A.-P.; Li, K.-H.; Zeng, D.; Zhang, Z.-Q.; Feng, S.-Y., Synthesis, cytotoxicity and DNA binding of novel Ni (II), Co (II) and Zn (II) complexes bearing pyrimidinyl hydrazone ligand. *Journal of Molecular Structure* **2023,** *1276*, 134724.

34. Cuartas, V.; Aragón-Muriel, A.; Liscano, Y.; Polo-Cerón, D.; del Pilar Crespo-Ortiz, M.; Quiroga, J.; Abonia, R.; Insuasty, B., Anticancer activity of pyrimidodiazepines based on 2-chloro-4-anilinoquinazoline: Synthesis, DNA binding and molecular docking. *RSC advances* **2021,** *11* (38), 23310-23329.

Design and Development of Viscosity-Sensitive, Pyrylium Fluorophores for Cellular Microenvironment Imaging

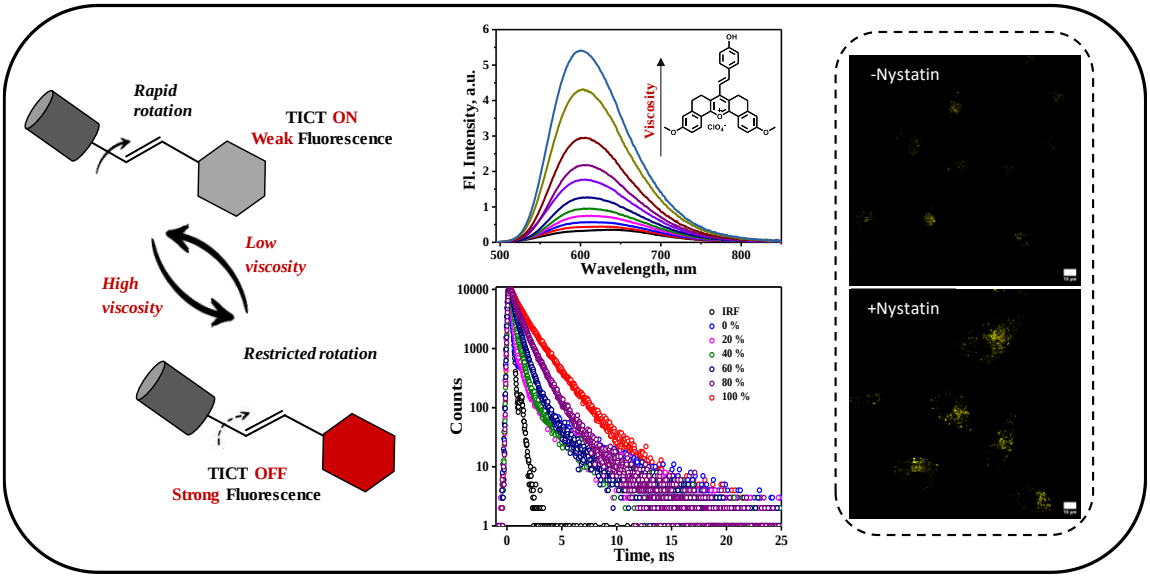

3.1. Abstract

Viscosity is a fundamental physical parameter that influences the intracellular microenvironment when cells undergo pathogenic changes. Intracellular viscosity is regarded as a key biomarker for diseases such as diabetes, atherosclerosis, and cancer, as these conditions can alter the protein interactions within cell membranes. It varies across cell types and organelles, typically ranging from 1 cP to 100's of cP (60-110 cP in HeLa cell mitochondria and 50-90 cP in MCF-7 cell lysosomes). In recent years, molecular rotors have emerged as effective probes for imaging viscosity in living cells through fluorescence intensity and/or lifetime-based responses. Herein, we report the synthesis of three rigid pyrylium derivatives functionalized with a reactive methyl group, achieving a broad spectral range by varying the substituents on both sides of a tetralone moiety, ***AM-PYR*** *(R= H) having blue*

emission, ***AM-MPYR*** *(R= OCH_3) having green emission, and* ***AM-APYR*** *(R= NH_2) with red emission. Further,* ***AM-MPYR*** *was used to synthesize a series of styryl-pyrylium derivatives incorporating different donor and acceptor groups. Among these derivatives, styryl-pyrylium with hydroxyl functionality (****OH-MPYR****) displayed a significant enhancement in fluorescence with increase in viscosity, indicating the potential of this probe for monitoring intracellular environment. The* ***OH-MPYR*** *probe exhibited a highly selective "turn-on" response to changes in viscosity, with an 18-fold enhancement in fluorescence intensity (λ_{max} = 602 nm) and an 8-fold enhancement in fluorescence lifetime as viscosity increased from 1.1 cP to 684 cP. Additionally, the probe showed good water solubility, photostability, and low cytotoxicity, making it suitable for monitoring intracellular viscosity. Bioimaging in HeLa cell lines confirmed the specific accumulation of the probe in lysosomes, with a co-localization coefficient of 0.84. Furthermore, the enhanced fluorescence intensity of the probe in HeLa cells pre-treated with Nystatin, which is known to increase cellular viscosity, confirmed its ability to monitor the fluctuation of intracellular viscosity in real time.*

3.2. Introduction

The cellular microenvironment plays a vital role in normal physiological activities of cells and its abnormal changes will lead to a variety of diseases.[1] Viscosity, polarity, temperature and pH are the important parameters that influences the intracellular microenvironment.[2] Among these cellular microenvironment related parameters, viscosity has recently attracted significant attention owing to its important role in many biological processes such as metabolism, signal transduction, electron transport, and apoptosis.[3] Also, abnormal viscosity levels are often associated with various diseases such as tumor growth[4], cardiovascular disease[5], diabetes,[6, 7] and Alzheimer's disease.[8, 9] Therefore, it is necessary to develop effective tools for tracking the intracellular viscosity changes which helps in disease prevention and clinical diagnosis.

Currently, the capillary viscometer, rotating viscometer, falling ball viscometer, and damping vibration viscometer are the common instruments used for measuring viscosity.[10] However, for measuring the intracellular microenvironment viscosity, these viscometers have practical disadvantages. Researchers have recently reported the use of techniques, such as fluorescence imaging, nuclear magnetic resonance, and electron paramagnetic resonance, to measure microscopic viscosity.[11-13] Fluorescence imaging technique has emerged as an effective tool because of its high sensitivity, non-invasiveness, and superior temporal and spatial resolution.[14] Even though there are many reports on viscosity sensitive fluorescent probes, it is challenging to obtain fluorescent probes with long emission wavelengths, large Stokes shifts, good biocompatibility, photostability, and more importantly specific targeting ability.[15]

The intracellular viscosity varies greatly in different organelles, such as lysosomes, mitochondria, nuclei, Golgi apparatus, and endoplasmic reticulum.[16] Therefore, it is necessary to develop specific organelle targeting viscosity sensors. Lysosomes play a crucial role in numerous physiological processes, such as protein degradation, secretion, migration, signaling, apoptosis, and autophagy.[17, 18] Also, lysosomes are one of the most desirable targets for cancer treatment and detection because of their involvement in the onset, progression, and resistance of cancer.[19] Additionally, in lysosomal dysfunction, particularly lysosomal storage diseases caused by deficiencies in specific lysosomal enzymes, macromolecular substances fail to break down and instead accumulate within lysosomes.[20] These changes lead to fluctuations in lysosomal viscosity, which vary with the amount and density of accumulated macromolecules. The functionality of lysosomes is closely associated with their viscosity and therefore it is crucial to design probes that can track lysosomal viscosity.[21]

In 2013, Xiao's group developed the first lysosome targeting viscosity probe, **Lyso-V**, based on a BODIPY molecular rotor and a morpholine unit for lysosomal localization.[22] The

rotor unit exhibits sensitivity to viscosity due to the free rotation around the single bond linking the BODIPY core to the phenyl group. Using fluorescence lifetime imaging, they demonstrated the capability to quantify real-time variations in lysosomal viscosity in live cells. Additionally, they reported the lysosomal viscosity data for MCF-7 cells for the first time and studied its variations in the presence of two common lysosome-stimulating drugs **(Figure 3.1A-B)**. In 2016, Manoj Kumar and coworkers synthesized a BODIPY based molecular rotor, **Probe 1**, which has been utilized to distinguish cancer, normal, and apoptotic cells on the basis of intracellular viscosity changes in living cells.[23] The probe consists of two phenyl rings as rotating units at the *meso*-position of the BODIPY core, which enhances excited state deactivation via a non-radiative pathway, making the rotor more sensitive to its environment. Additionally, the introduction of an amino group on the phenyl ring increases the rotor's sensitivity to low viscosity, providing an optimal donor-π-acceptor (D-π-A) system. Also, they have practically applied this probe for real-time quantification of intracellular viscosity changes during apoptosis pathways in live cells **(Figure 3.1C-D)**.

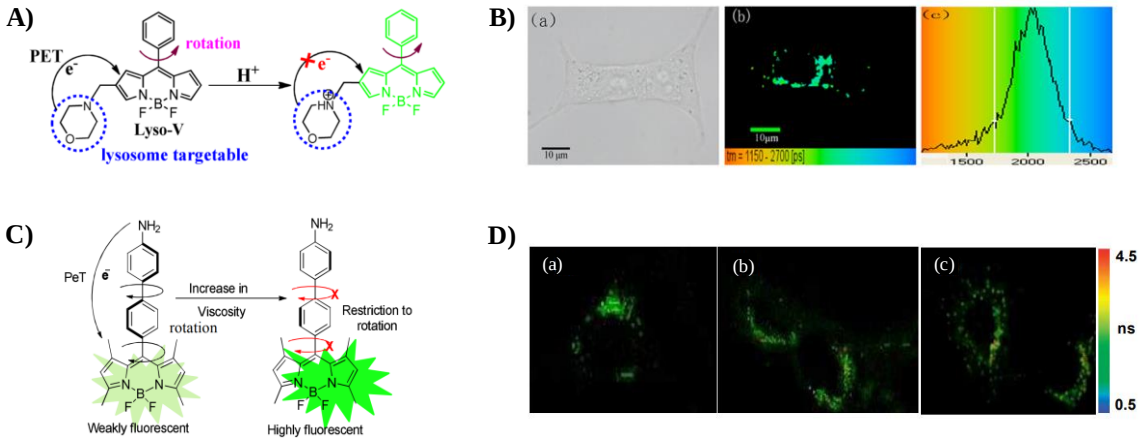

Figure 3.1. (A) Structure of the probe, **Lyso-V**; (B) FLIM investigation of an MCF-7 cell stained with **Lyso-V** (5 μM); (C) Structure of the **Probe 1** and (D) FLIM of C6 cells: (a) treated only with the probe (5 μM); (b) treated with retinoic acid (RA) and then incubated with the probe and (c) treated with camptothecin and then incubated with the probe (Figure adapted from reference 22 and 23).

In 2021, Li *et al.* reported a dual responsive lysosome targeting fluorescent probe for pH and viscosity, based on the transformation of amino and imino forms of pyronine and the twisted intramolecular charge shuttle sensing mechanism.[24] In neutral and basic conditions, the probe undergoes deprotonation of the amino group, resulting in absorption and fluorescence changes. Under acidic conditions, the probe exists in aminopyronine form, exhibiting minimal fluorescence in low-viscosity environments due to the efficient twisted intramolecular charge shuttle (TICS) mechanism. In contrast, high-viscosity environments suppress TICS, leading to strong fluorescence. Further, the probe was used for effectively distinguishing cancer cells and tumors from normal cells and tissues by exploiting the lower pH and elevated viscosity characteristics of cancer cell lysosomes **(Figure 3.2)**.

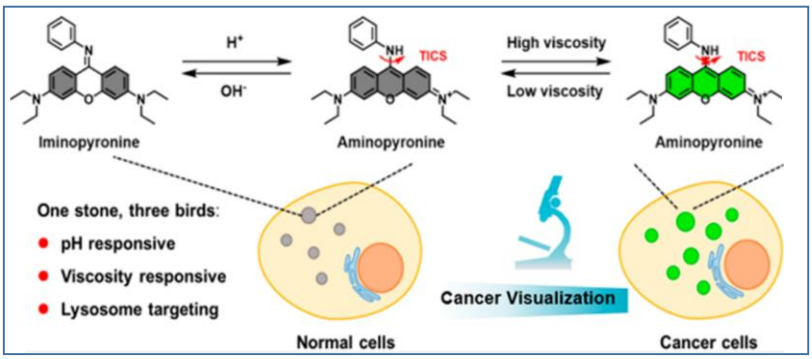

Figure 3.2. Molecular structure of the pyronine probe and the proposed pH and viscosity sensing mechanism (Figure adapted from reference 24).

In 2023, Liu and co-workers developed a viscosity responsive far-red fluorescent probe based on cinnamaldehyde and rhodamine, **Cin-Rho**. The probe exhibited higher accumulation in lipid droplets, good biocompatibility, good photostability and a large Stokes shift.[25] **Cin-Rho** is capable of detecting viscosity variations in live cells, zebrafish, and inflammatory mice. Furthermore, *ex-vivo* fluorescence imaging experiments confirmed enhanced fluorescence in tumor tissues, incubated with the probe, verifying higher viscosity of the tumor tissues than that of the normal muscle tissues **(Figure 3.3A-B)**. All these reports suggest that the viscosity variations in different organelles are associated with abnormalities in cellular microenvironment especially in the case of diseases like cancer.

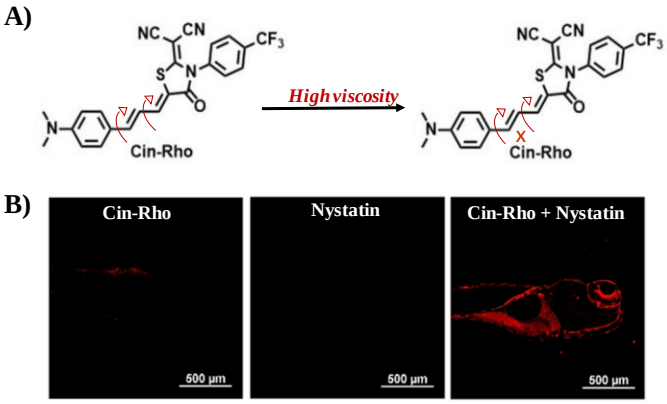

Figure 3.3. (A) Molecular structure of the probe **Cin-Rho** and (B) Confocal fluorescence images of zebra fish treated with **Cin-Rho** (10 µM) and Nystatin (10 µM) (Figure adapted from reference 25).

Active methylene compounds are of great importance in synthetic chemistry due to their structural diversity and unique reactivity.[26] The versatility of these classes of compounds is well demonstrated by their numerous applications in fundamental reactions such as Michael conjugate additions, aldol reactions, tandem processes, and in the synthesis of many natural and synthetic compounds.[27] Therefore, incorporating an active methylene group into a chromophore can be advantageous for its structural modifications and thereby enabling the fine-tuning of its properties. Pyrylium dyes comprise a well-characterized family of compounds with a large variety of applications in different fields.[28-30] Ease of synthesis and purification, high emission quantum yields, large stokes shift and low cytotoxicity make them desirable for bioimaging applications.[31, 32]

Here, we report the one-pot, single-step synthesis of three rigid pentacyclic pyrylium derivatives, each containing a reactive methyl group. The absorption of these compounds lies in the visible region and varies based on the substitution pattern. The one-pot synthesis of the pyrylium chromophore with the reactive methyl group is highly significant in this study, as there are no previous reports of incorporating reactive methyl group to pyrylium fluorophore in a single step with high yield. Further, a series of styryl-pyrylium derivatives with various functional groups were synthesized, and their photophysical properties were investigated in the

search for a potential viscosity sensor with a pronounced fluorescence response. Among the synthesized derivatives, the hydroxyl-functionalized styryl-pyrylium derivative, **OH-MPYR** exhibited an 18-fold enhancement in fluorescence intensity and 8-fold enhancement in fluorescence lifetime with increasing viscosity (1.1cP to 684 cP), indicating its potential for monitoring intracellular viscosity. Further, bioimaging experiments in HeLa cells confirmed the inherent lysosome targeting ability of the probe with a co-localization coefficient of 0.84. Additionally, the probe exhibited good aqueous solubility, excellent photostability, and minimal cytotoxicity making it well suited for bioimaging applications. Furthermore, enhanced fluorescence intensity of the probe in HeLa cells pre-treated with Nystatin, which is known to increase cellular viscosity, confirmed its ability to monitor intracellular viscosity changes in real time.

3.3. Results and Discussion

3.3.1. Design, synthesis and characterisation

Twisted intramolecular charge transfer (TICT) probes with an electron donor-π-acceptor (D-π-A) design are highly useful in monitoring the changes in the microenvironment, such as variations in viscosity, polarity, and intermolecular interactions, particularly within a cellular milieu.[33, 34] Molecular rotors with TICT characteristics, exhibit distinct photophysical behaviour due to conformational changes in the excited state. The rates of radiative and non-radiative processes in these probes are sensitive to the microenvironment, leading to perturbations in fluorescence quantum yields and lifetimes.[35] For example, efficient intra-molecular rotation enhances non-radiative decay processes, resulting in fluorescence quenching, while restricted rotation leads to fluorescence enhancement **(Figure 3.4A)**.

Small-molecule based TICT probes, whose fluorescence is sensitive to changes in viscosity, have emerged as promising viscosity sensors. In more viscous environments, the twisting mechanism responsible for increased non-radiative rates is inhibited, leading to enhanced fluorescence. However, most of the reported probes have limitations, including low

sensitivity, short emission wavelengths, and high background fluorescence.[36] Therefore, the design and development of new systems with easy synthesis, high sensitivity and minimal background fluorescence are necessary to overcome these limitations. Our D-π-A fluorophore design features a rigid pentacyclic pyrylium chromophore appended with a styryl moiety (**Figure 3.4B)**, with various substituent groups to modulate the photophysical properties.

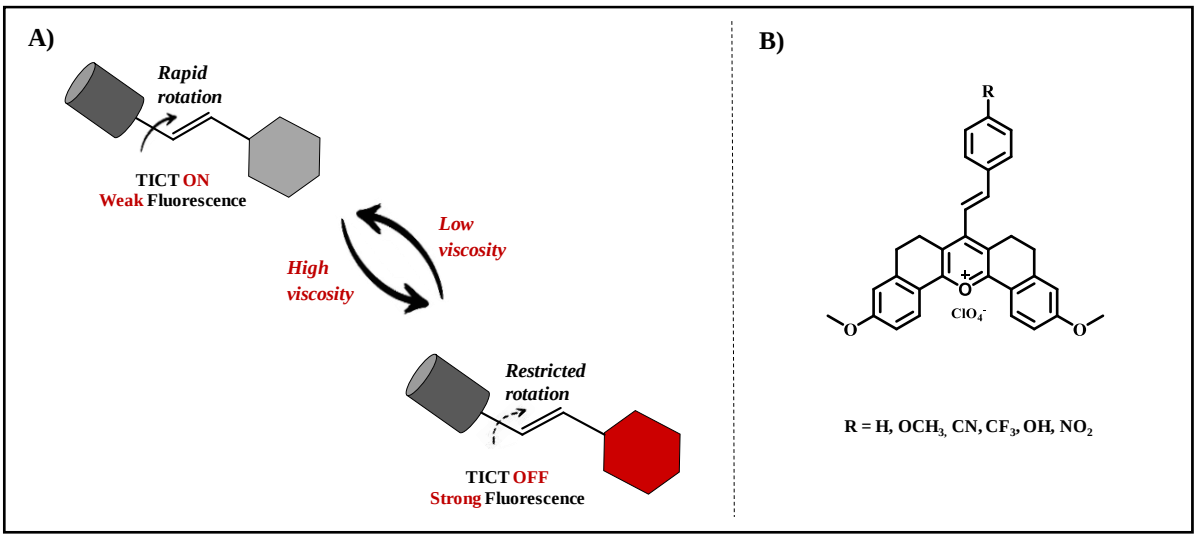

Figure 3.4. (A) Mechanism of action of TICT based viscosity sensors and (B) design of styryl-pyrylium derivatives.

The cyclisation of tetralone with aromatic aldehydes is a well-established reaction that yields rigid pyrylium derivatives with attached aromatic rings.[37] In a similar approach, we explored the use of aliphatic aldehydes in place of aromatic aldehydes and found the reaction to be feasible. The cyclization of tetralone derivatives with acetaldehyde enables the synthesis of rigid pyrylium cores containing a reactive methyl group. This one pot, single step process offers good yields, with significant potential for functional group modifications. Utilizing this process, we synthesized three new pyrylium derivatives by varying the substitution at the tetralone moiety: **AM-PYR** (R = H), **AM-MPYR** (R = OCH_3), and **AM-APYR** (R = NH_2) as per **Scheme 3.1A**.

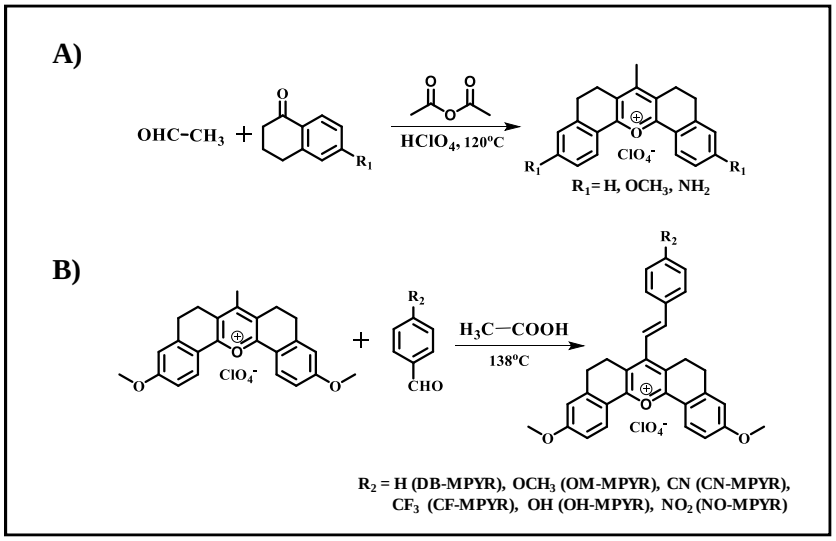

Scheme 3.1. Scheme for the synthesis of (A) pyrylium and (B) styryl-pyrylium derivatives.

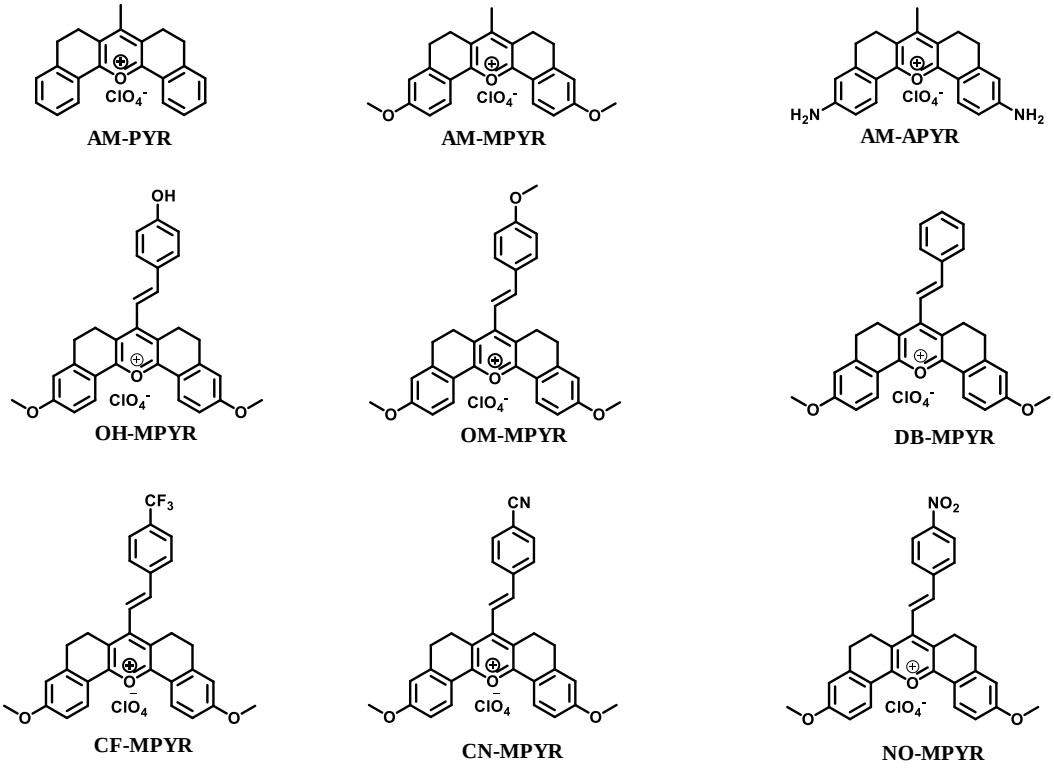

Figure 3.5. Structures of the synthesised pyrylium and styryl-pyrylium derivatives.

With an objective of synthesising a molecular rotor system, **AM-MPYR** is treated with differently substituted *para*-benzaldehydes in acetic acid at 138 °C for 24 h to yield the corresponding styryl-pyrylium derivatives as in **Scheme 3.1B**.[29] We obtained the products in moderate yields ranging from 40 - 55%. To generalize this synthetic method, we reacted **AM-MPYR** with 1-pyrenecarboxaldehyde and 9-anthracenecarboxaldehyde, and successfully

obtained the styryl-pyrylium derivatives with the respective fluorophores. Thus, we have synthesised three rigid pyrylium derivatives, six styryl-pyrylium derivatives with different benzaldehyde substituents, and two derivatives with appended pyrene and anthracene **(Figure 3.5)**. All the intermediates and final products were characterized by ^{1}HNMR, ^{13}C NMR and HRMS.

3.3.2. Photophysical properties

We investigated the absorption and emission characteristics of the three rigid pentacyclic pyrylium derivatives appended with methyl group in phosphate buffer (pH=7.4). The probes, **AM-PYR**, **AM-MPYR** and **AM-APYR** exhibited absorption maxima at 428 nm, 472 nm, and 522 nm, respectively, with corresponding emission maxima at 479, 538, and 627 nm **(Figure 3.6A-C** and **Figure 3.7A)**. Altering the substitution on both sides of the rigid pyrylium ring from -H to -OCH_3 and -NH_2, resulted in a red shift of both the absorption and emission maxima, achieving a wide spectral range: **AM-PYR** emitting blue, **AM-MPYR** emitting green and **AM-APYR** emitting red. This can be attributed to a reduction in the HOMO-LUMO energy gap at ground states as donor strength increases.[38, 39] The corresponding Stokes shift values were calculated as 2488, 2599, and 3205 cm^{-1} for **AM-PYR**, **AM-MPYR**, and **AM-APYR**, respectively. The photophysical properties of these derivatives, including molar extinction coefficients, relative quantum yields, brightness, and lifetimes, are summarized in **Table 3.1**. Among the compounds, **AM-MPYR** exhibits the highest quantum yield of 96%, followed by **AM-PYR** (54%) and **AM-APYR** (22%). The fluorescence lifetime values are <200 ps for **AM-PYR**, 379 ps for **AM-APYR**, and 4.74 ns for **AM-MPYR (Figure 3.7B)**. The brightness values, calculated from the molar extinction coefficient and quantum yield, are 1,410 $M^{-1}cm^{-1}$ for **AM-PYR**, 10,850 $M^{-1}cm^{-1}$ for **AM-MPYR** and 4,550 $M^{-1}cm^{-1}$ for **AM-APYR**. By modifying the substitution on tetralone, we successfully tuned the emission properties of the pyrylium core from blue to red, making these probes suitable for various applications.

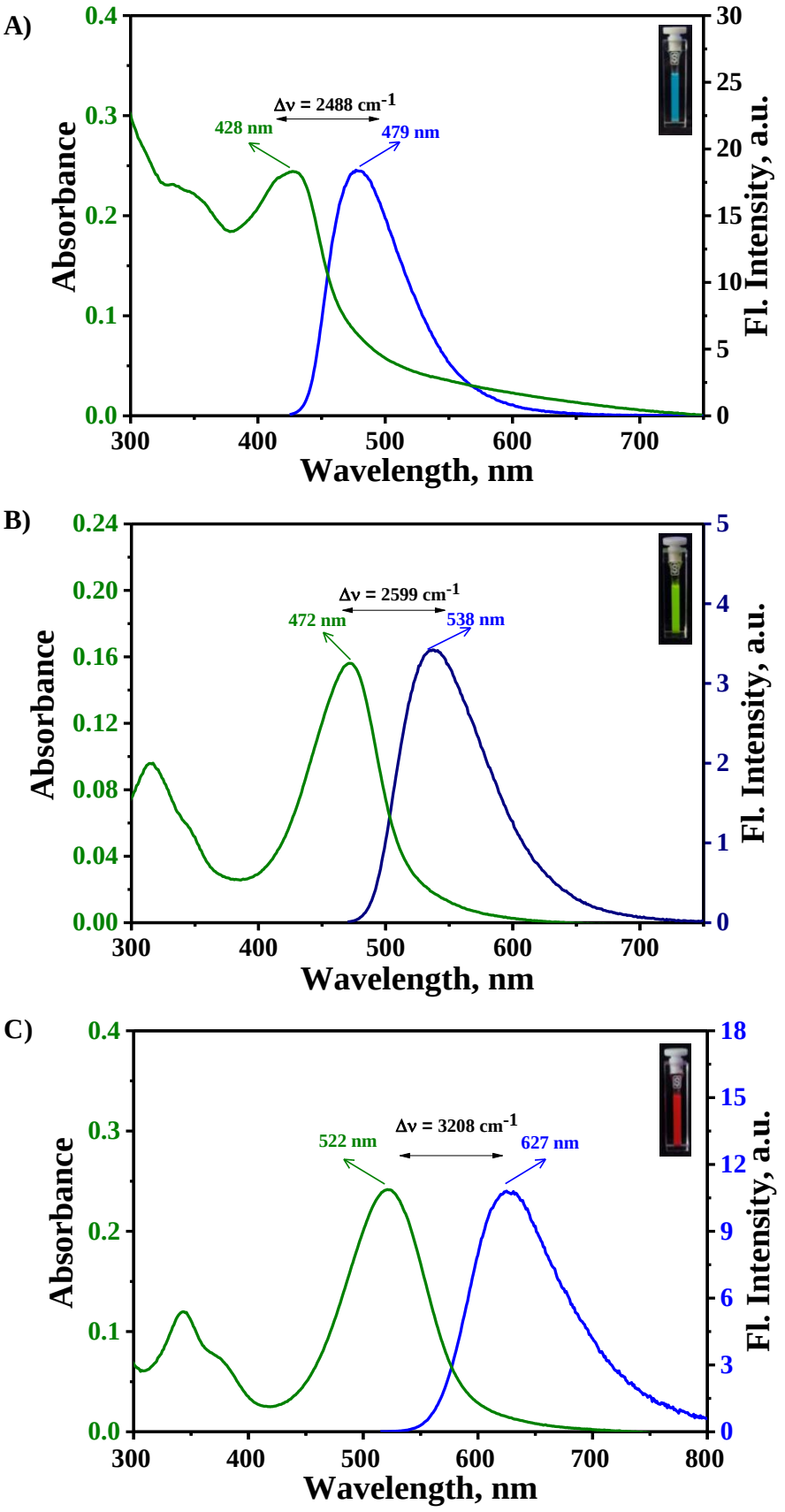

Figure 3.6. Absorption and emission spectra of (A) **AM-PYR**, (B) **AM-MPYR**, and (C) **AM-APYR** in phosphate buffer.

Table 3.1. Photophysical data of **AM-PYR**, **AM-MPYR** and **AM-APYR** in phosphate buffer (pH=7.4).

Compound	Ab. max (nm)	Em. Max (nm)	Stokes Shift (cm^{-1})	Molar extinction coefficient, ε ($M^{-1} cm^{-1}$)	Quantum Yield, ϕ (%)	Brightness ($M^{-1} cm^{-1}$)	Lifetime
AM-PYR (A)	428	479	2488	2610	54	1410	≤200 ps
AM-MPYR (B)	472	538	2599	11300	96	10850	4.74 ns
AM-APYR (C)	522	627	3208	20670	22	4550	379 ps

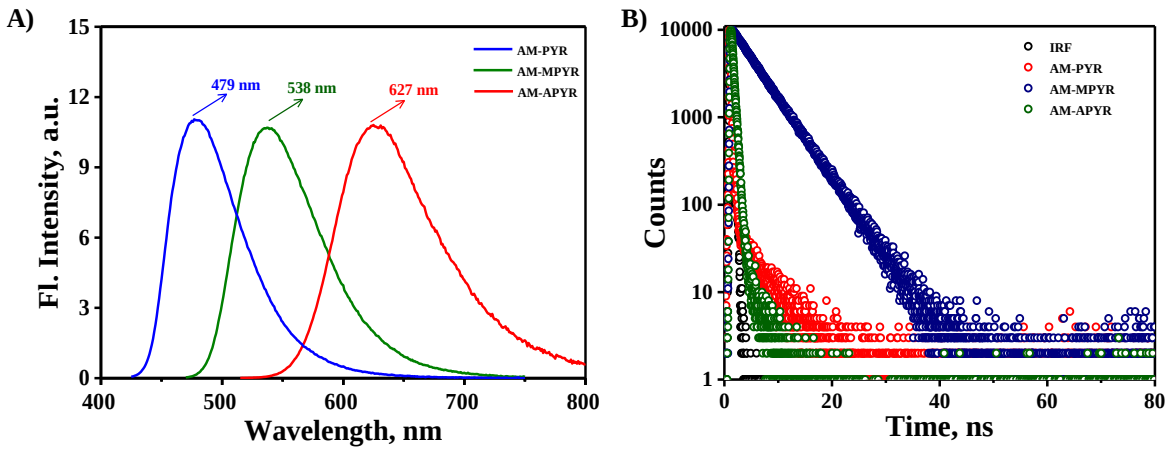

Figure 3.7. (A) Shift in emission spectra and (B) fluorescence lifetime spectra of **AM-PYR**, **AM-MPYR** and **AM-APYR** in phosphate buffer (pH=7.4).

Due to its higher fluorescence quantum yield, **AM-MPYR** core was selected for synthesizing styryl-pyrylium derivatives. The basic photophysical studies revealed that the absorption maxima of all the derivatives under study are around 500 nm, while the emission maxima varied from 550 - 615 nm, depending on the substitution. The relative quantum yields and lifetimes also vary significantly between these derivatives. For example, the absorption spectrum of **DB-MPYR** in ethanol shows an absorption maximum at 502 nm and an emission maximum at 565 nm, with a Stokes shift of 2221 cm^{-1} (**Figure 3.8A**). **DB-MPYR** exhibits the highest quantum yield value of 97% and an average lifetime of 3.67 ns. In contrast, **OM-MPYR** exhibited a relatively lower quantum yield of 48.5% and average lifetime of 1.43 ns. The absorption and emission maxima of **OM-MPYR** are at 497 and 607 nm, respectively, with a Stokes shift value of 3646 cm^{-1} (**Figure 3.8B**). The key photophysical data for all styryl-

pyrylium derivatives are summarized in **Table 3.2**, and their fluorescence lifetime spectra are depicted in **Figure 3.9**.

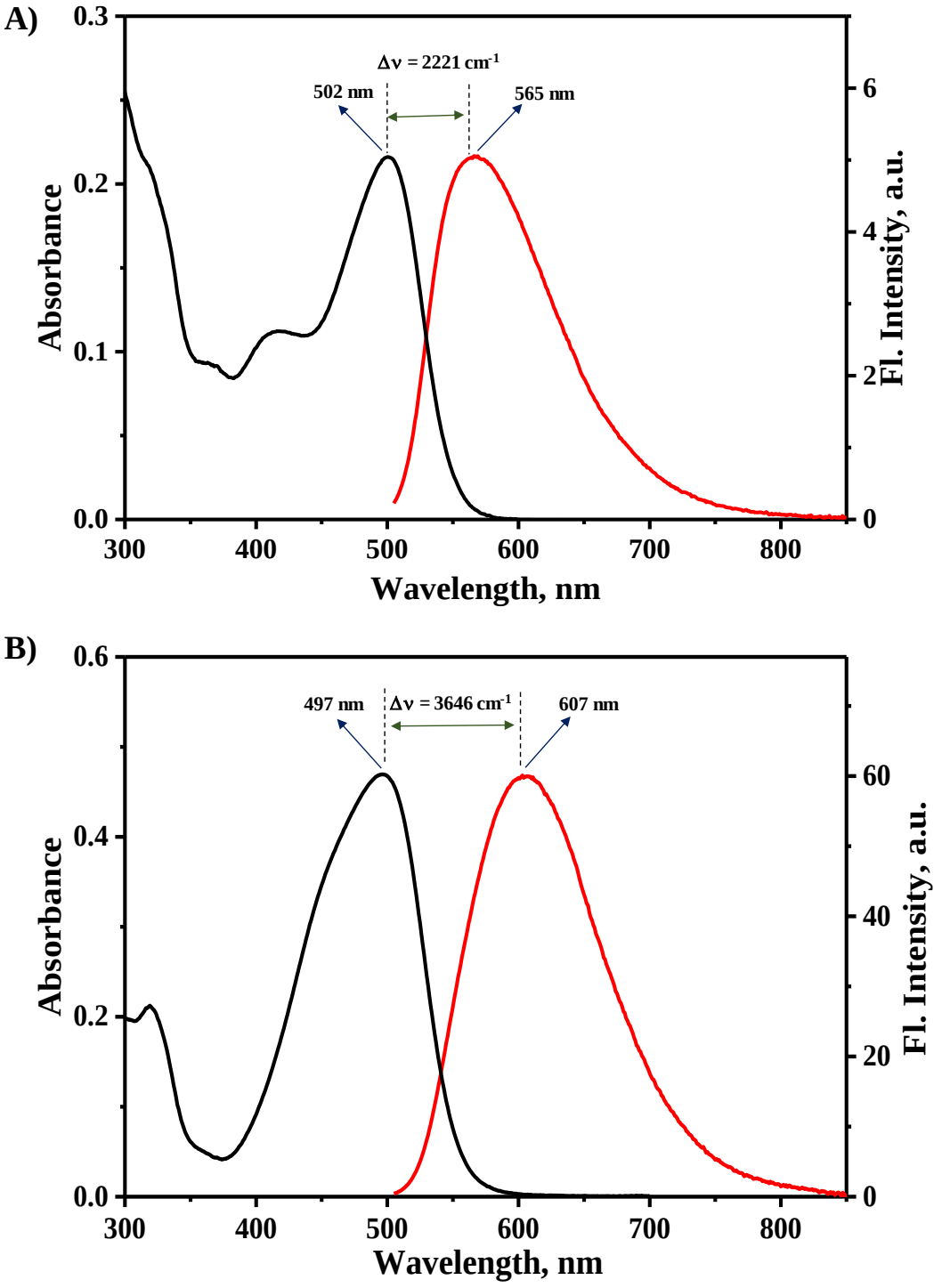

Figure 3.8. Normalized absorption and emission spectra of (A) **DB-MPYR** and (B) **OM-MPYR** in ethanol.

Table 3.2. Photophysical data of styryl pyrylium derivatives in ethanol.

Compound	Ab. max (nm)	Em. max (nm)	Stokes Shift (cm^{-1})	Quantum Yield (%)	Life time (ns)		
					τ_1 (%)	τ_2 (%)	τ_{av}
OM-MPYR (A)	497	607	3646	48.5	1.2 (78.4)	4.6 (21.6)	1.43
DB-MPYR (B)	502	565	2221	96.6	2.2 (29.3)	5.1 (70.7)	3.67
CF-MPYR (C)	506	562	1969	73.1	1.7 (16.9)	5.3 (83.1)	3.94
CN-MPYR (D)	512	615	3271	40.6	1.0 (81.5)	4.9 (18.5)	1.20
NO-MPYR (E)	513	552	1377	34.2	1.2 (10.0)	5.1 (90.0)	3.83
OH-MPYR (F)	500	602	3388	4.40	0.14 (81.7)	2.0 (18.3)	0.16

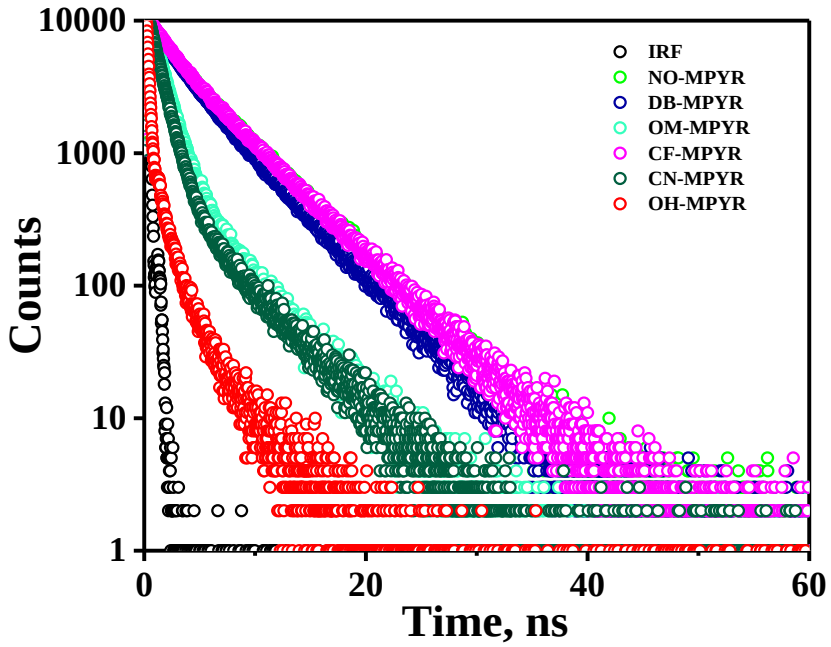

Figure 3.9. Fluorescence lifetime spectra of styryl-pyrylium derivatives in ethanol.

3.3.3. Viscosity sensing studies of styryl-pyrylium derivatives

Given that biocompatible molecules with molecular rotor structures are well suited for viscosity sensing applications, we explored the viscosity sensing ability of the styryl-pyrylium derivatives. Fluorescence spectra of each derivative were recorded in ethanol, 50% ethanol-glycerol mixture, and glycerol **(Figure 3.10)**, and the fluorescence intensities were compared. Among the different molecules, only the styryl-pyrylium derivative with hydroxyl functionality, **OH-MPYR**, showed a gradual and significant fluorescence enhancement with increasing glycerol concentration, indicating its potential as an efficient viscosity sensor. Therefore, **OH-MPYR** was selected for further detailed studies.

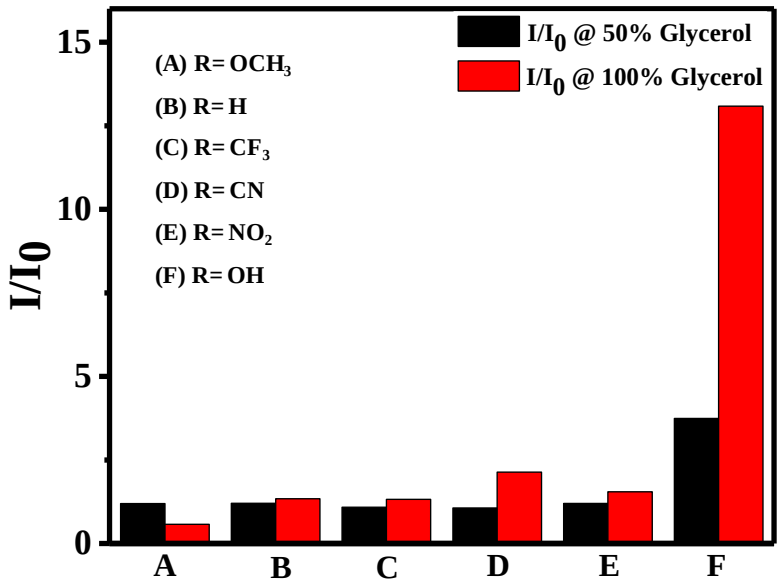

Figure 3.10. Change in I/I_0 values of the styryl-pyrylium derivatives at respective emission maxima in ethanol, 50% ethanol-glycerol, and glycerol.

3.3.4. Viscosity sensing studies of OH-MPYR

To investigate the effect of viscosity on the photophysical properties of **OH-MPYR**, absorption and emission spectra were recorded in viscosity-gradient mixtures of glycerol and ethanol at room temperature. The viscosity of the solutions was varied from 1.1 - 684 cP, by adjusting the volume fractions of glycerol. The absorption spectra of **OH-MPYR** showed no significant changes across different viscosity solutions, indicating negligible effect on the chromophore's ground state properties (**Figure 3.11A**). However, the fluorescence emission of **OH-MPYR** exhibited noticeable changes with increase in the viscosity of the solutions. The weakest fluorescence was observed in pure ethanol, while the emission intensity at 602 nm increased with a higher glycerol-to-ethanol ratio, indicating an enhancement in fluorescence intensity with increasing viscosity (**Figure 3.11B** and **3.12A**). This effect can be attributed to the inhibition of non-radiative decay process in viscous solutions, due to restricted molecular rotation.

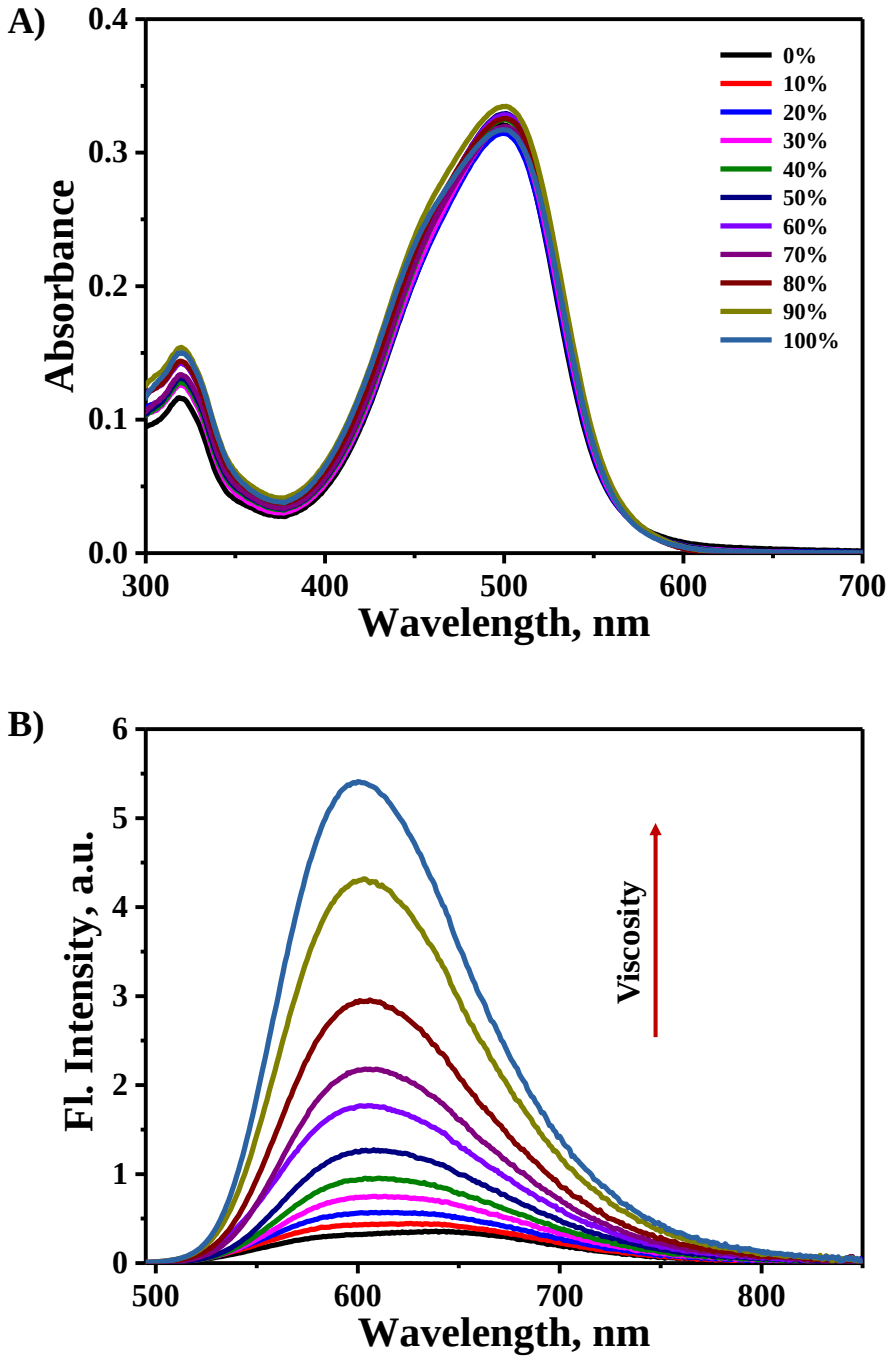

Figure 3.11. (A) Absorption and (B) emission spectra of **OH-MPYR** (10 μM) in different percentage of glycerol-ethanol mixtures (λ_{ex} = 495 nm).

In low-viscosity or non-viscous solutions, the intramolecular rotation occurs rapidly, causing the excited-state energy to dissipate through non-radiative pathways, resulting in weak fluorescence. In contrast, in viscous solutions, the intramolecular rotation is restricted, reducing non-radiative decay and enhancing the fluorescence of the probe. The probe demonstrated significant sensitivity, with an 18-fold increase in fluorescence intensity as viscosity increased

from 1.1 - 684 cP. Furthermore, a strong linear correlation between log I at 602 nm and log η (R^2 = 0.9823, x = 0.47) was observed (**Figure 3.12B**).

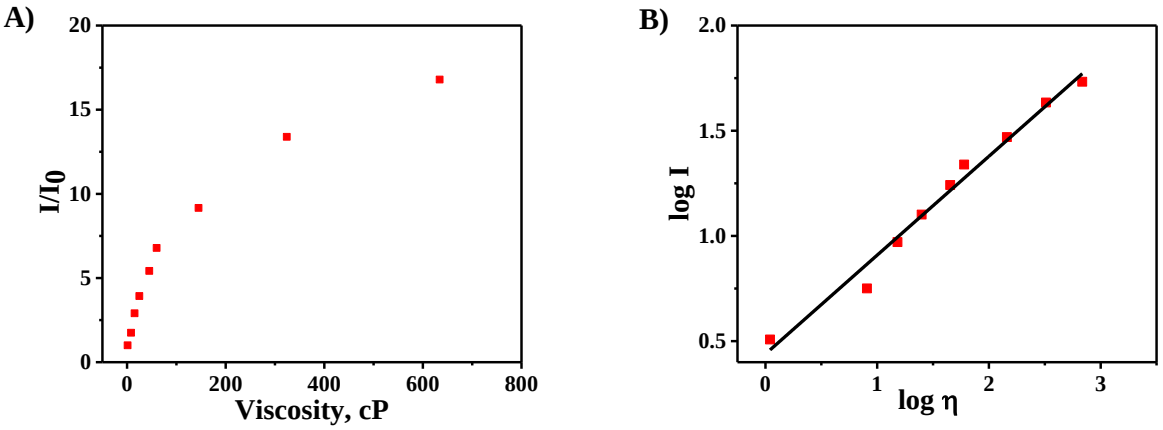

Figure 3.12. Secondary plot of (A) I/I_0 v/s viscosity(cP) and (B) log I (at 602 nm) v/s log η for **OH-MPYR** (10 μM).

3.3.5. Effect of viscosity on fluorescence properties of OH-MPYR

The relative fluorescence quantum yield values of **OH-MPYR** in glycerol-ethanol solutions with varying viscosities were measured using cresyl violet as the fluorescence standard. The probe showed a gradual increase in quantum yield as viscosity increased, showing a linear dependency **(Figure 3.13)**. For example, **OH-MPYR** exhibited a fluorescence quantum yield of 4% in ethanol, while in glycerol, the quantum yield increased to 28%.

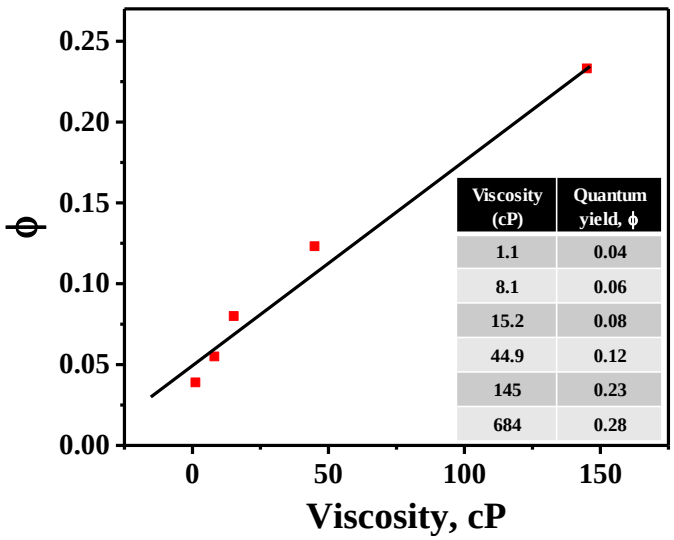

Viscosity (cP)	Quantum yield, ϕ
1.1	0.04
8.1	0.06
15.2	0.08
44.9	0.12
145	0.23
684	0.28

Figure 3.13. Fluorescence quantum yield as a function of viscosity.

To evaluate the effect of viscosity on fluorescence lifetime, the fluorescence intensity decay of **OH-MPYR** was studied in glycerol-ethanol mixtures with varying viscosities using TCSPC. In ethanol, the probe exhibited a biexponential decay, with the majority exhibiting a shorter lifetime (τ_1 = 0.13 ns; 87%), resulting in a low average lifetime of 0.15 ns. This short lifetime could be due to faster non-radiative processes and multiple possible conformations in the excited state. However, as the glycerol percentage increased, the probe showed a gradual increase in fluorescence lifetime, likely due to restricted molecular rotation, leading to a more stable conformation **(Figure 3.14 and Table 3.3)**. The average fluorescence lifetime increased from 0.15 ns in ethanol and 1.15 ns in glycerol, representing an approximately eight-fold enhancement as the solution viscosity increased from 1.1 - 684 cP. This viscosity-dependent increase in fluorescence lifetime demonstrates the potential of **OH-MPYR** for fluorescence lifetime imaging applications.

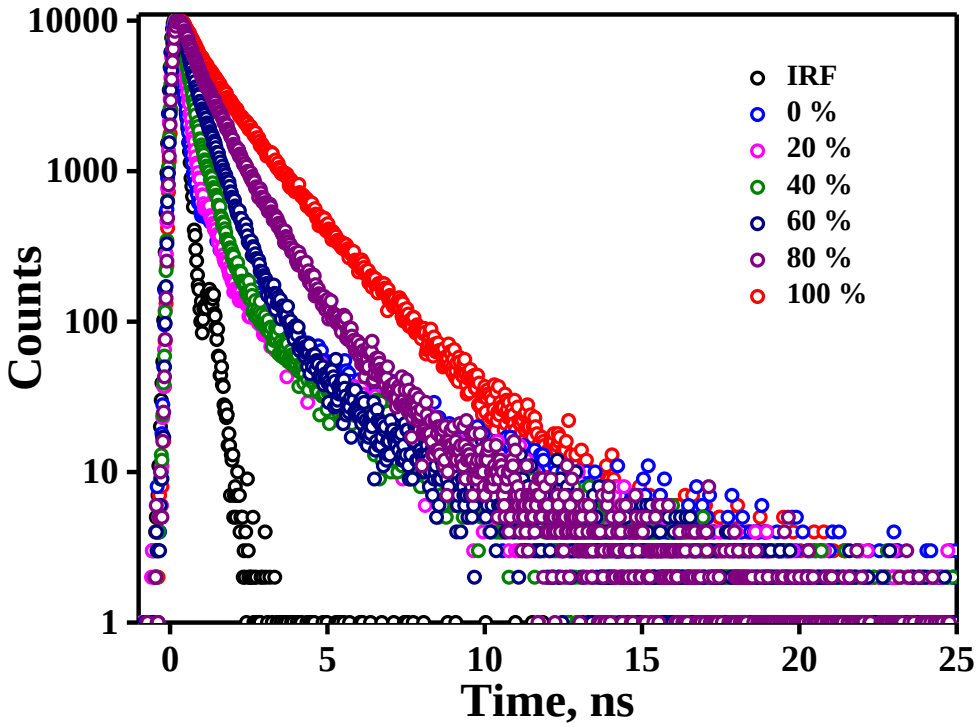

Figure 3.14. Fluorescence lifetime spectra of **OH-MPYR** in glycerol-ethanol mixtures with viscosity ranging from 1.1 - 684 cP.

Table 3.3. Fluorescence lifetime data of **OH-MPYR** in glycerol-ethanol mixtures within the viscosity range of 1.1 - 684 cP.

OH-MPYR	τ_1 (ns)	τ_1 (%)	τ_2 (ns)	τ_1 (%)	τ_a (ns)	χ^2
Gly 0% (1.1 cP)	0.13	86.8	2.49	13.2	0.15	1.09
Gly 20% (8.1 cP)	0.19	88.9	2.53	11.1	0.21	1.04
Gly 40% (15.2 cP)	0.31	90.7	2.32	9.3	0.34	1.07
Gly 60% (44.9 cP)	0.47	86.5	1.83	13.5	0.52	1.07
Gly 80% (145 cP)	0.59	60.8	1.55	39.2	0.79	1.02
Gly 100% (684 cP)	0.69	36.3	1.87	63.7	1.15	0.98

3.3.6. Förster -Hoffmann theory for molecular rotors

The viscosity-dependent photophysical properties of the probe is primarily caused by molecular twisting or rotation, which reduces the non-radiative decay rate. This leads to a significant increase in fluorescence quantum yield and lifetime as viscosity increases.[40] According to the Förster-Hoffmann theory for molecular rotors, the fluorescence quantum yield (ϕ_x) and lifetime (τ) are expected to vary linearly with viscosity:

$$\ln(\phi_x) = C + x \ln(\eta) \qquad \text{Equation (3.1)}$$

$$\ln(\tau) = C' + y \ln(\eta) \qquad \text{Equation (3.2)}$$

where η represents viscosity.[41] This theory predicts a linear relationship between log(quantum yield) vs. log(viscosity) and log(lifetime) vs. log(viscosity). The probe **OH-MPYR**, exhibited a strong linear correlation between its spectroscopic properties and viscosity, consistent with Förster-Hoffmann theory. Additionally, the linear dependence of log(ϕ) on log(τ) further confirmed the viscosity-dependent behaviour **(Figure 3.15A-C)**. The radiative and non-radiative rate constants, k_r and k_{nr}, respectively, were calculated from the experimentally measured quantum yields and the fluorescence lifetimes. While k_r remained relatively constant across varying viscosities, k_{nr} decreased sharply with increasing viscosity up to 684 cP **(Figure 3.15D)**. This observation confirmed that the increase in quantum yield with increasing viscosity is due to the suppression of non-radiative processes.

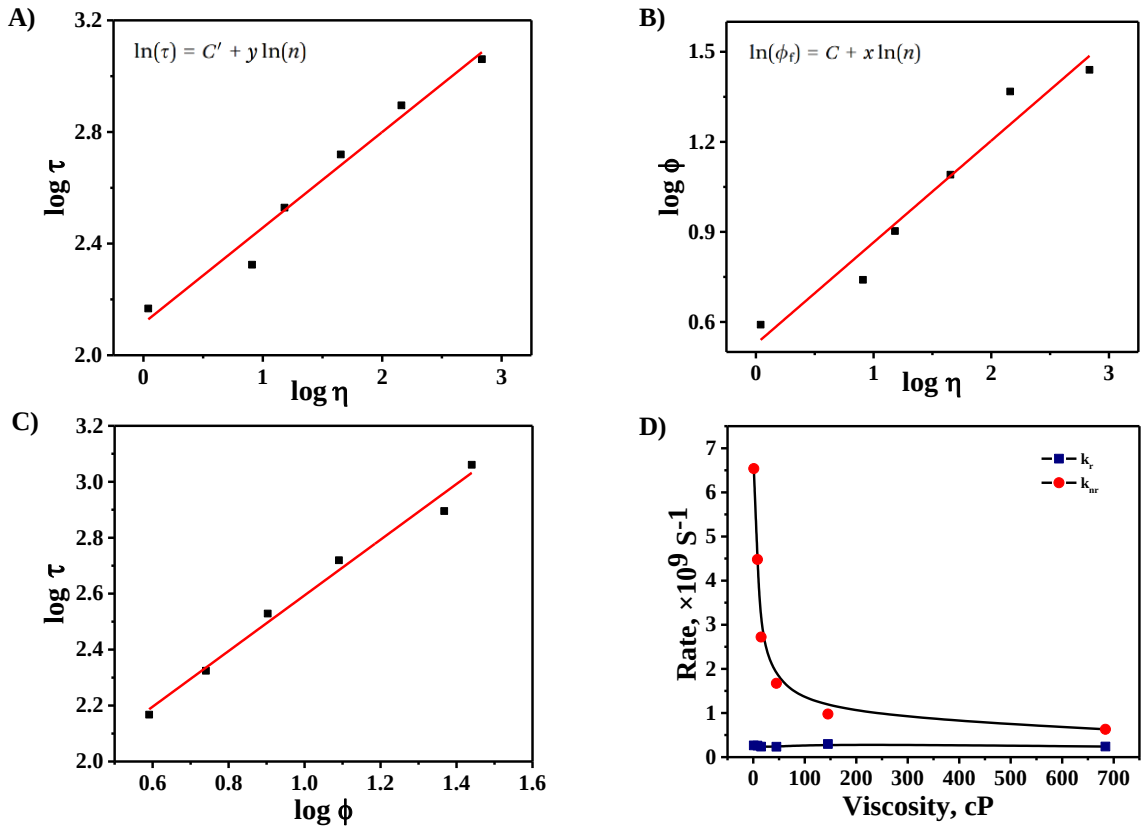

Figure 3.15. (A) The linear relationship between log η and log τ; (B) The linear relationship between log η and log ϕ; (C) A log-log plot of the average fluorescence lifetime and quantum yield of **OH-MPYR** obtained from different glycerol-ethanol mixtures; (D) Radiative and non-radiative rates of **OH-MPYR** in ethanol-glycerol mixtures as a function of viscosity.

3.3.7. Temperature dependent fluorescence measurements

Both solvent viscosity and non-radiative excited state decay processes are temperature dependent properties. To understand the effect of temperature, we recorded the absorption and emission spectra of the probe, **OH-MPYR** in glycerol, at various temperatures **(Figure 3.16)**. As the temperature increased, a notable decrease in fluorescence intensity was observed, which can be attributed to the reduction in the viscosity of glycerol and the subsequent enhancement in non-radiative decay pathways through facile molecular rotation. Interestingly, the absorption spectra remained unchanged across different temperatures, which suggests that the temperature-induced effects on molecular rotation are primarily limited to the excited state, while ground-state interactions and absorption processes remain unaffected.

These observations align with the general behaviour of molecular rotors, where excited-state dynamics, particularly rotational motions, are strongly influenced by viscosity. As temperature increases, the lowered viscosity allows for greater molecular freedom, thereby facilitating non-radiative processes and reducing the fluorescence quantum yield.[42, 43] This temperature-dependent behaviour further reinforces the probe's sensitivity to viscosity and highlights its potential application in environments where both viscosity and temperature fluctuate, such as in biological systems or complex fluidic environments.

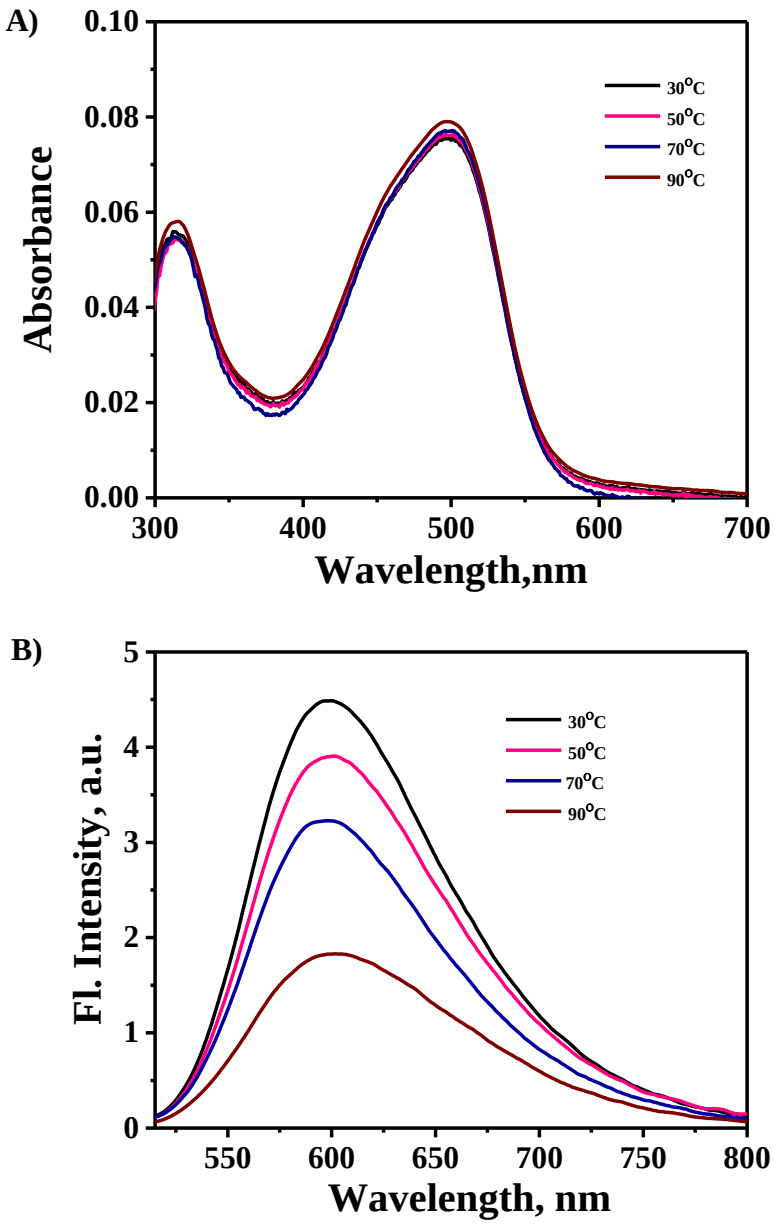

Figure 3.16. Temperature dependent (A) absorption and (B) emission spectra of **OH-MPYR** in glycerol.

3.3.8. Interference studies of OH-MPYR

In a cellular context, various biologically relevant analytes can also affect the fluorescence quantum yield. To evaluate the selectivity of **OH-MPYR** towards viscosity, the probe's fluorescence response was recorded in the presence of several biologically relevant species, including Zn^{2+}, Na^{+}, K^{+}, NH_4^{+}, ClO_4^{-}, OH^{-}, NO_2^{-}, CH_3COO^{-}, OCl^{-}, Cl^{-}, SO_3^{-} and GSH (**Figure 3.17A-B**). The fluorescence spectrum of **OH-MPYR** showed no significant change in emission intensity in the presence of these analytes, confirming its specificity for detecting viscosity changes in biological environments.

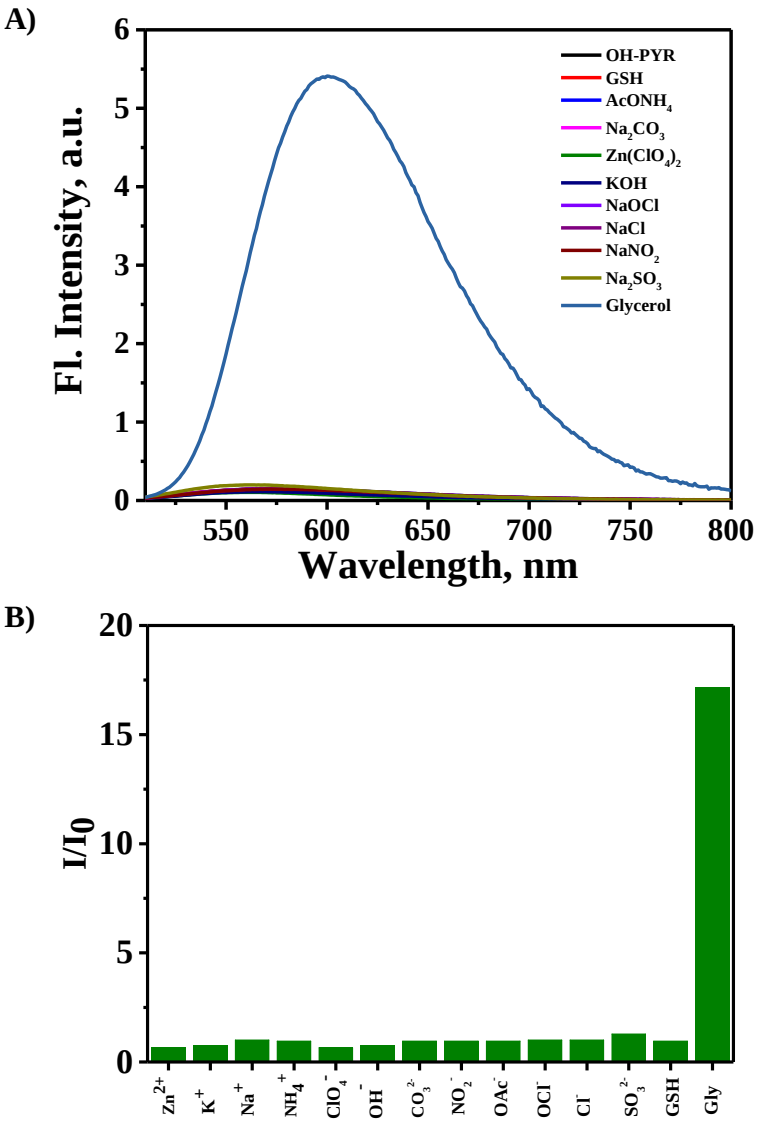

Figure 3.17. (A) Fluorescence Spectra of **OH-MPYR** (10 μM) in presence of various biologically relevant analytes (λ_{ex}= 495 nm); (B) The corresponding bar diagram representation of the I/I_0 values.

3.3.9. Photostability studies of OH-MPYR

Photostability studies of **OH-MPYR** were conducted in PBS buffer under a 200 W mercury lamp on an Oriel optical bench, with the sample positioned at a distance of 50 cm from the light source, using a 400 nm long-pass filter. The sample was irradiated for 60 minutes, and fluorescence spectra were recorded at regular intervals. The probe exhibited stable and reproducible emission profiles throughout the irradiation period, demonstrating excellent photostability **(Figure 3.18A-B)**.

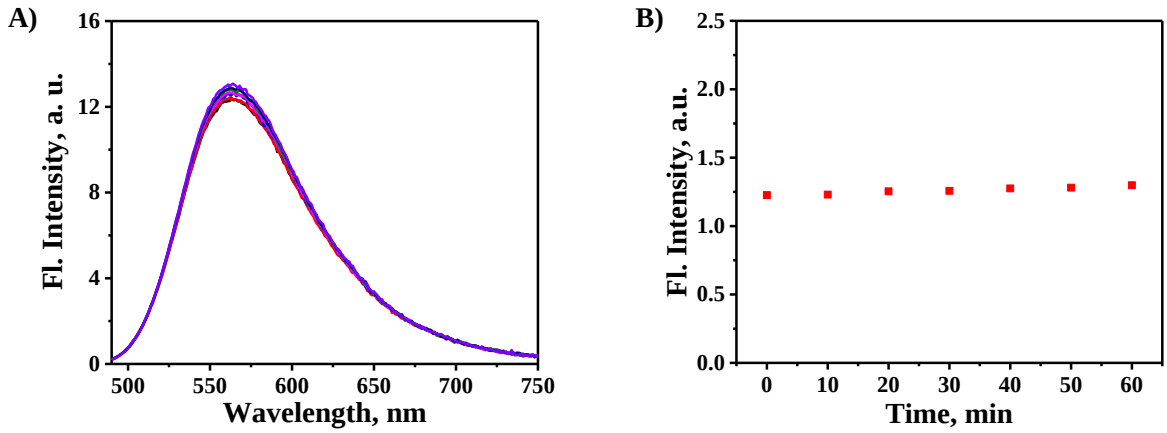

Figure 3.18. (A) Emission of **OH-MPYR** (10 µM) in phosphate buffer upon irradiation with a 200 W mercury lamp on an Oriel optical bench, with the sample positioned 50 cm from the light source, using a 400 nm long-pass filter for 60 minutes; (B) The secondary plot of fluorescence intensity at emission maximum of **OH-MPYR** with time of irradiation.

3.3.10. Aqueous Solubility of OH-MPYR

Many organic fluorophores suffer from poor aqueous solubility, which limits their use in biological systems. Further, aggregation can lead to fluorescence quenching and uneven distribution within cells, potentially resulting in inconsistent signals and errors in cellular imaging data. To assess the aqueous solubility of **OH-MPYR**, concentration dependent absorption spectra were measured in phosphate buffer at pH 7.4 **(Figure 3.19)**. The absorbance of **OH-MPYR** increased linearly with concentration, consistent with Beer-Lambert's law, ruling out aggregation possibilities. The gradual increase in absorbance indicates good

solubility, likely due to the positively charged pyrylium moiety, making **OH-MPYR** a promising candidate for biological applications.

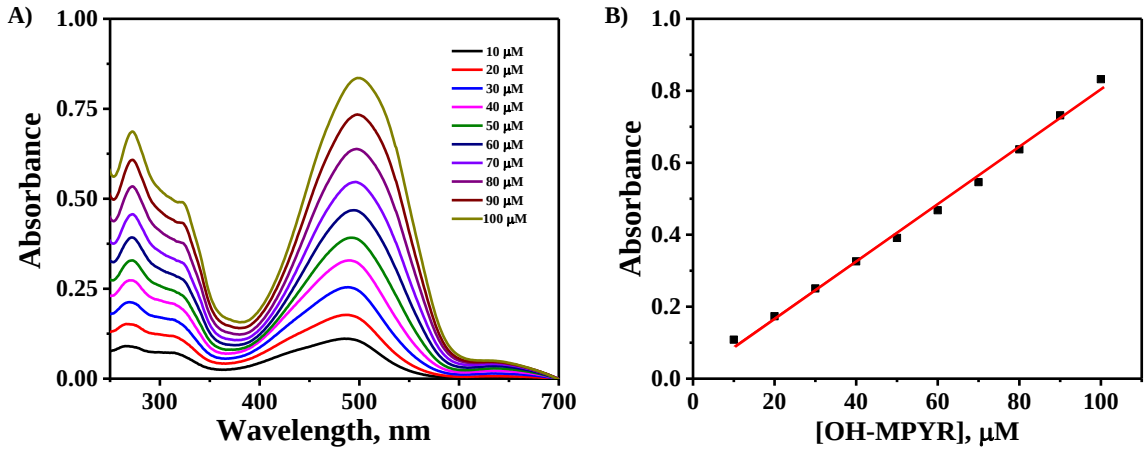

Figure 3.19. Absorption spectra of **OH-MPYR** at different concentrations (10-100 µM) in phosphate buffer (pH=7.4).

3.3.11. Cytotoxicity of OH-MPYR

The cytotoxicity of **OH-MPYR** was evaluated at various concentrations in HeLa cells using the MTT assay, as cytotoxicity is a key concern for cellular imaging probes. As shown in **Figure 3.20**, the probe showed over 90% cell viability, even at a concentration of 10 µM, indicating its non-toxic nature at the concentrations used for cellular imaging (typically <10 µM).

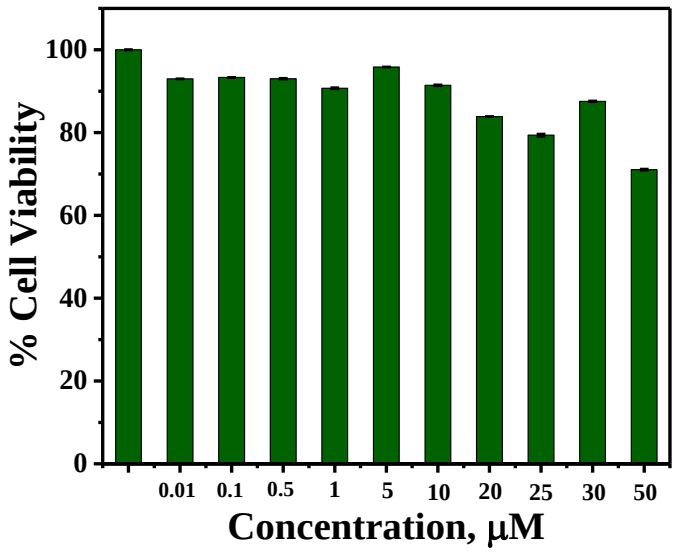

Figure 3.20. *In vitro* cytotoxicity profiling of **OH-MPYR** (10 nM - 50 µM) in HeLa cells using MTT assay**.**

3.3.12. Co-localization studies of OH-MPYR

The co-localization ability of the probe, **OH-MPYR** within cells was evaluated using confocal laser scanning microscopy imaging and co-staining assays. HeLa cells were first incubated with **OH-MPYR** (100 nM) for 30 min, followed by staining with Lyso-tracker deep red (100 nM) for 15 min. The probe **OH-MPYR** exhibited very weak fluorescence in the 514 nm channel under the same brightness and contrast settings (B&C) as the 638 nm channel. However, after adjusting the brightness and contrast, the fluorescence from **OH-MPYR** was visible, having significant overlap with Lyso-tracker deep red, with a co-localization coefficient of 0.84. This can be attributed to the higher viscosity of lysosomes compared to other cellular organelles.[44-46] As a "turn-on" viscosity sensor, **OH-MPYR** remains non-fluorescent in low viscosity regions, however, exhibits enhanced fluorescence in higher-viscosity environments, resulting in a stronger signal from the lysosome **(Figure 3.21A-B)**.

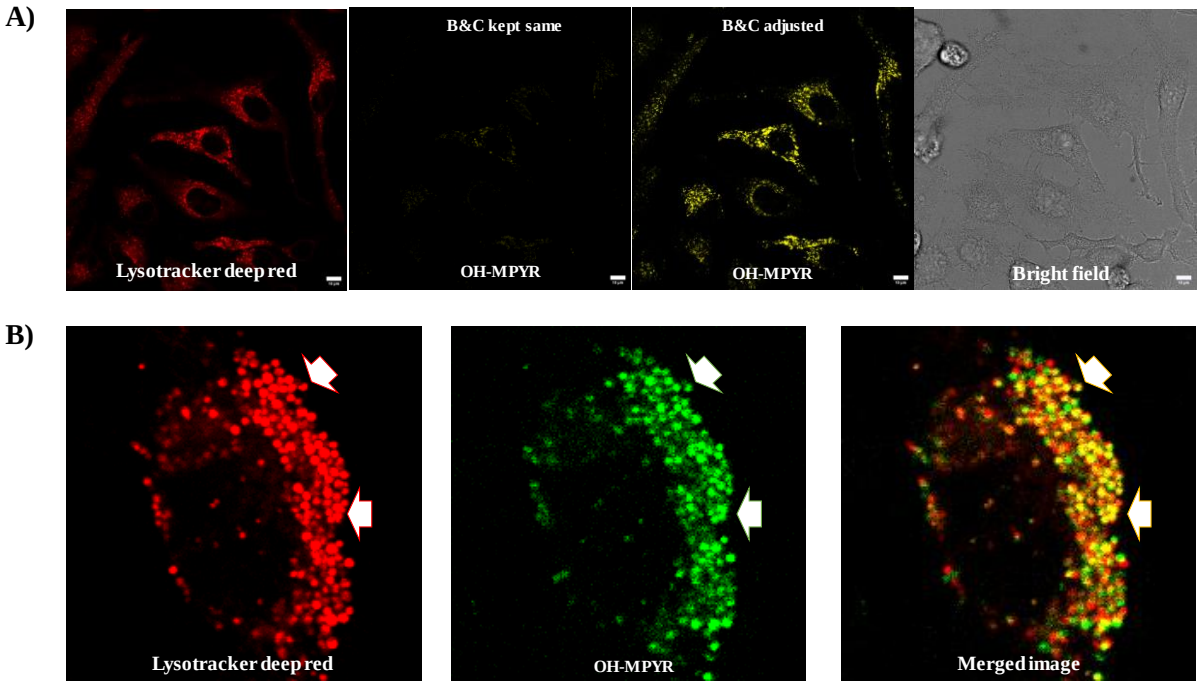

Figure 3.21. (A) Confocal laser scanning microscopy images of HeLa cells incubated with **OH-MPYR** (100 nM, λ_{ex} = 514 nm) for 30 min and subsequently with Lyso-tracker deep red (100 nM, λ_{ex} = 638 nm) for 15 min (Scale bar: 10 μm); (B) Single cell image showing co-localization of Lyso-tracker deep red and **OH-MPYR**.

3.3.13. Viscosity monitoring in live cells

To evaluate the ability of the probe, **OH-MPYR** to detect intracellular viscosity changes, cells were treated with Nystatin (10 μM) for 30 min. Nystatin is known to increase the cellular viscosity, by facilitating Na^+ transport into the cell, resulting in dehydration and inducing cellular abnormalities such as swelling or structural changes.[47, 48] The live HeLa cells incubated with **OH-MPYR** alone (100 nM) exhibited weak fluorescence. However, cells pre-treated with Nystatin showed a significant enhancement in fluorescence intensity due to the increase in intracellular viscosity **(Figure 3.22A-D)**. These results demonstrate that the **OH-MPYR** can accumulate in the lysosome and effectively monitor intracellular viscosity changes.

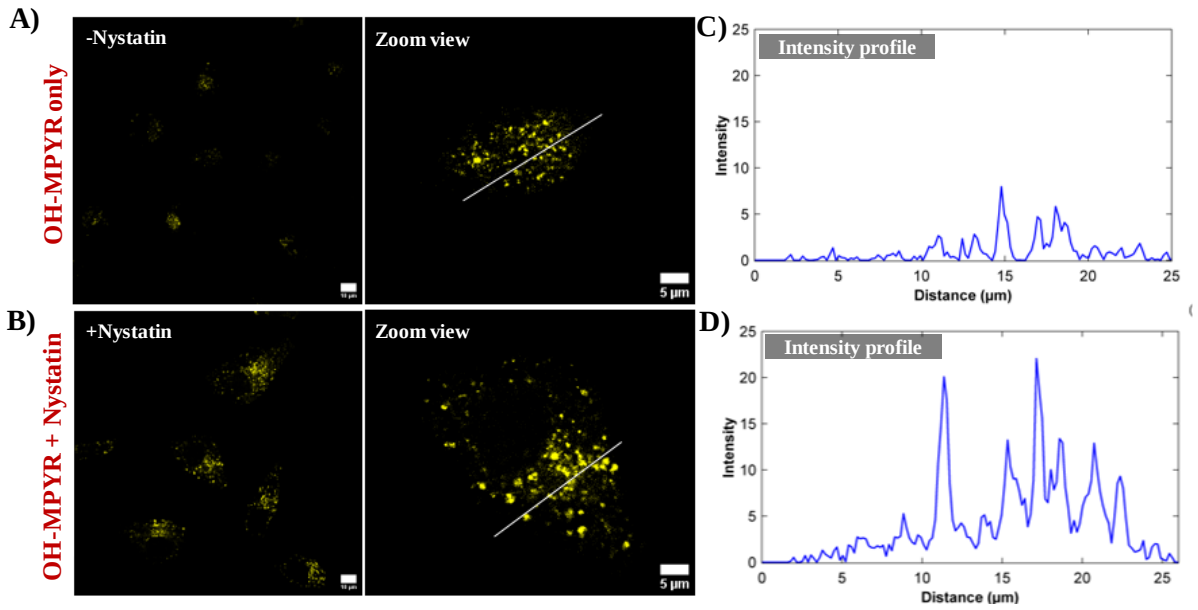

Figure 3.22. Confocal laser scanning microscopy images of HeLa cells: (A) incubated with 100 nM **OH-MPYR** and (B) incubated with 100 nM **OH-MPYR** + 10 μM Nystatin for 30 min (λ_{ex} = 514 nm); (C) and (D) are the corresponding fluorescence intensity profiles.

3.4. Conclusion

In conclusion, we have synthesised three new, rigid pentacyclic pyrylium compounds appended with an active methyl group (**AM-PYR**, **AM-MPYR** and **AM-APYR**), through a one-pot single step process. Varying the substitution on both sides of the rigid pyrylium ring from -H to $-OCH_3$ and $-NH_2$, resulted in a red shift of both the absorption and emission maxima,

to a wide spectral range. Further, **AM-MPYR** is utilized for synthesising a series of new styryl-pyrylium derivatives by Knoevenagel condensation reaction. Since biocompatible molecules with molecular rotor structures are known for monitoring intracellular viscosity, we conducted a comparative photophysical investigation of styryl-pyrylium derivatives in glycerol-ethanol solutions with varying concentrations. The hydroxyl-functionalized styryl-pyrylium derivative, **OH-MPYR** displayed an 18-fold enhancement in fluorescence intensity and an 8-fold increment in fluorescence lifetime with increasing glycerol percentage, highlighting its potential for monitoring intracellular viscosity. Additionally, the probe exhibited large Stokes shift, good water solubility, photostability, and low cytotoxicity. The demonstration of bioimaging in HeLa cell lines confirmed the "turn on" fluorescence of the probe in the higher-viscosity environment of lysosomes compared to other organelles. Furthermore, confocal laser scanning microscopy imaging experiments showed enhanced fluorescence of the probe in HeLa cells treated with Nystatin, confirming the intracellular viscosity sensing ability of the probe.

3.5. Experimental Section

3.5.1. Materials and Methods

All the starting materials and reagents used in this work were purchased from commercial suppliers (Sigma Aldrich and TCI chemicals) and used as received without further purification. Moisture sensitive reactions were carried out under argon atmosphere in dried solvents purchased from Sigma-Aldrich and Merck chemical suppliers. Thin layer chromatography (TLC) analysis was performed using aluminum plates coated with silica gel purchased from Merck. Silica gel (100-200 mesh) was used for column chromatography. ^{1}H NMR (500 MHz) and ^{13}C NMR (125 MHz) spectra were obtained on a Bruker Avance DPX spectrometer, with TMS as the internal standard. High-resolution mass spectra (HRMS) were recorded using Thermo Scientific Q Exactive Hybrid Quadrupole-Orbitrap Electrospray Ionization Mass Spectrometer (ESI-MS). The UV-Vis absorption spectra were measured using a Shimadzu UV-Vis spectrophotometer (UV-2600), and emission spectra were recorded using a SPEX Fluorolog spectrofluorimeter. The fluorescence lifetime measurements were done using picosecond single photon counting system (Horiba, DeltaFlex) with 510 nm laser as excitation source and picosecond photon detection module (PPD-850) as the detector. The fluorescence decay profile was deconvoluted using EzTime software and fitted with multi exponential decay of chi-square value 1±0.1. The photostability of **OH-MPYR** was studied by recording emission spectra with freshly prepared 10 μM solution in phosphate buffer in the presence and absence of light irradiation on an Oriel optical bench model 11200 fitted with a 200 W mercury lamp using a 400 nm long-pass filter at regular time intervals. *In vitro* studies were performed using the HeLa cell line (purchased from ATCC) and the images were captured with a Lyca confocal microscope.

3.5.2. *In Vitro* Studies

The MTT assay was conducted using the HeLa cell line, which was obtained from ATCC. The cells were placed in a 96-well plate at a density of 12,000 cells per well and incubated for 24 h in DMEM supplemented with 10% FBS. Subsequently, the cells were exposed to **OH-MPYR** at concentrations ranging from 10 nM to 50 μM for an additional 24 h. After incubation, MTT dissolved in DMEM (0.5 g/L) was added to each well and kept at 37 °C in a CO_2 incubator for 2- 4 h. 100 μL of DMSO was added to each well and the ability of the cells to reduce this substrate to the blue formazan product was determined colorimetrically (570 nm) after 20 min using a microplate reader. For Lysosomal co-localization studies, cells were first treated with **OH-MPYR** for 30 minutes. After washing, the cells were exposed to 100 nM Lyso-tracker deep red for 15 minutes and then washed twice with PBS. Co-localization of **OH-MPYR** with Lyso-tracker deep red was visualized using a confocal laser scanning microscope with 514 nm and 638 nm channels, respectively. To monitor the intracellular viscosity sensing ability of the probe, one set of HeLa cells was pre-treated with Nystatin (10 μM) for 30 minutes, followed by incubation with **OH-MPYR** (100 nM) for another 30 minutes. Another set of cells was incubated with the same concentration of probe without Nystatin treatment, and both sets were compared by visualizing the cells using confocal microscopy.

3.5.3. Synthesis and characterization

3.5.3.1. Synthesis of **AM-PYR**: To a solution of 1-tetralone derivative (0.5 mL, 2 eq.) in toluene (5 mL), acetaldehyde (0.1 mL, 1 eq.) and acetic anhydride (400 μL) were added, and the mixture was refluxed at 138 °C for 1.5 h. Then perchloric acid (350 μL) was added, and the mixture was stirred for another 3 h, and the reaction mixture was kept overnight at 90 ^{o}C. Completion of the reaction was monitored by TLC, toluene was decanted, and the product was precipitated by the addition of a minimum amount of acetone and excess ether. The precipitated product was purified further using silica gel column chromatography. We followed the same

procedure for the synthesis of **AM-MPYR** and **AM-APYR**, substituting 6-methoxy tetralone and 6-amino tetralone, respectively, in place of 1-tetralone.

AM-PYR - ^{1}H NMR (500 MHz, CD_3CN), δ(ppm): 8.25 (d, *J* = 5 Hz, 2H), 7.66 (t, *J* = 10 Hz, 2H), 7.55 (t, *J* = 10 Hz, 2H), 7.46 (d, *J* = 10 Hz, 2H), 3.4 (m, 8H), 2.6 (s, 3H).

^{13}C NMR (125 MHz, CD_3CN): 17.7, 23.4, 26.3, 126.1, 126.5, 128.7, 129.6, 131.4, 135.5, 142.2, 163.6, 168.4.

HRMS calculated = 299.1430, found = 299.1437.

AM-MPYR - ^{1}H NMR (500 MHz, Acetone-d_6), δ(ppm): 8.33 (d, *J* = 8.4 Hz, 2H), 7.13 (d, *J* = 9.3 Hz, 4H), 3.99 (s, 6H), 3.28-3.24 (m, 4H), 3.23-3.19 (m, 4H), 2.71 (s, 3H).

^{13}C NMR (125 MHz, Acetone-d_6): 22.8, 26.4, 55.6, 113.8, 114.7, 118.5, 128.2, 144.4, 165.2.

HRMS calculated = 359.1642, found = 359.1653.

AM-APYR - ^{1}H NMR (500 MHz, CD_3CN), δ(ppm): 7.91 (d, *J* = 10 Hz, 2H), 6.70 (m, 2H), 6.58 (s, 2H), 5.31 (s, 4H), 2.94 (m, 8H), 2.4 (s, 3H).

^{13}C NMR (125 MHz, CD_3CN): 21.3, 28.0, 31.8, 117.8, 118.8, 119.5, 129.6, 149.2, 159.7, 185.9, 187.0, 189.4.

HRMS calculated = 329.1648, found =329.1654.

3.5.3.2. Synthesis of **OH-MPYR:** To a solution of **AM-MPYR** (0.5g, 3.9 mmol) in glacial acetic acid, 4-Hydroxybenzaldehyde (1g, 8.2 mmol) was added and the mixture was refluxed at 138 ºC for 48 h. The solvent was removed under reduced pressure and the residue was precipitated using minimum amount of acetone and excess ether. The completion of the reaction was confirmed by TLC. The dried product was further purified by silica gel column chromatography with 3% methanol/chloroform to yield 40% of the product as a red solid.

^{1}H NMR (500 MHz, CD_3CN), δ(ppm): 8.18 (d, *J* = 10 Hz, 2H), 7.64 (t, *J* = 10 Hz, 2H), 7.29 (d, *J* = 15 Hz, 1H), 7.19 (d, *J* = 15 Hz, 1H), 7.09 (d, *J* = 5 Hz, 2H), 7.02 (s, 2H), 6.93 (d, *J* = 10 Hz, 2H), 3.93 (s, 6H), 3.23 (t, *J* = 5 Hz, 4H), 3.06 (t, *J* = 5 Hz, 4H).

^{13}C NMR (125 MHz, CD_3CN): 24.9, 27.2, 56.4, 114.5, 114.9, 116.7, 119.6, 126.3, 127.6, 128.6, 131.0, 144.6, 145.5, 160.6, 160.8, 163.1, 165.5.

HRMS calculated = 463.1904, found = 463.1914.

All the styryl-pyrylium derivatives under study were synthesized by following the above procedure using respective benzaldehyde derivatives. Pyrene carboxaldehyde and anthracene carboxaldehyde were used to synthesize **PYRN-PYR** and **ATCN-PYR**, respectively.

CF-MPYR: ^{1}H NMR (500 MHz, CD_3CN), δ(ppm): 8.20 (d, *J* = 10 Hz, 2H), 8.15 (d, *J* = 5 Hz, 1H), 7.89 (d, *J* = 10 Hz, 2H), 7.80 (d, *J* = 10 Hz, 3H), 7.41 (d, *J* = 20 Hz, 1H), 7.22 (d, *J* = 20 Hz, 1H), 7.09 (d, *J* = 10 Hz, 2H), 7.02 (s, 2H), 3.94 (s, 6H), 3.21 (t, *J* = 5 Hz, 4H), 3.06 (t, *J* = 5 Hz, 4H).

^{13}C NMR (125 MHz, CD_3CN): 24.6, 27.0, 56.4, 114.5, 115.1, 119.3, 123.7, 126.1, 126.5, 127.1, 128.9, 130.8, 130.9,141.5, 144.9,160.1, 163.9, 165.8.

HRMS calculated = 515.1829, found = 515.1839.

CN-MPYR: ^{1}H NMR (500 MHz, CD_3CN), δ(ppm): 8.20 (d, *J* = 10 Hz, 2H), 7.84 (t, *J* = 10 Hz, 4H), 7.41 (d, *J* = 20 Hz, 1H), 7.19 (d, *J* = 15 Hz, 1H), 7.09 (d, *J* = 5 Hz, 2H), 7.02 (s, 2H), 3.94 (s, 6H), 3.19 (t, *J* = 5 Hz, 4H), 3.06 (t, *J* = 5 Hz, 4H).

^{13}C NMR (125 MHz, CD_3CN): 24.6, 27.0, 29.9, 30.5, 56.4, 114.5, 115.1, 124.5, 127.5, 128.9, 129.0, 133.5, 139.9, 141.2, 145.0,163.9, 165.8, 207.8.

HRMS calculated = 472.1907, found =472.1912.

DB-MPYR: ^{1}H NMR (500 MHz, CD_3CN), δ(ppm): 8.20 (d, *J* = 10 Hz, 2H), 7.74 (d, *J* = 5 Hz, 2H), 7.50 (d, *J* = 5 Hz, 3H), 7.33 (d, *J* = 15 Hz, 1H), 7.23 (d, *J* = 15 Hz, 1H), 7.09 (d, *J* = 5 Hz, 2H), 7.03 (s, 2H), 3.94 (s, 6H), 3.23 (t, *J* = 5 Hz, 4H), 3.07 (t, *J* = 5 Hz, 4H).

^{13}C NMR (125 MHz, CD_3CN): 24.7, 27.0, 56.4, 113.0, 114.5, 115.0, 126.9, 128.6, 128.8, 129.8, 131.2, 137.8, 142.0, 144.8,149.7, 156.5, 157.9, 165.6.

HRMS calculated = 447.1956, found = 447.1979.

NO-MPYR: ^{1}H NMR (500 MHz, CD_3CN), δ(ppm): 8.66 (t, *J* = 5 Hz, 2H), 8.55 (d, *J* = 5 Hz, 1H), 8.39 (d, *J* = 10 Hz, 1H), 8.25 (d, *J* = 5 Hz, 1H), 7.97 (t, *J* = 10 Hz, 1H), 7.78 (d, *J* = 15 Hz, 1H), 7.55 (d, *J* = 20 Hz, 1H), 7.45 (m, 2H), 7.37 (s, 2H), 4.28 (s, 6H), 3.73 (t, *J* = 5 Hz, 1H), 3.55 (t, *J* = 5 Hz, 2H), 3.41 (m, 4H), 3.12 (t, *J* = 10 Hz, 1H).

HRMS calculated = 492.1805, found = 492.1814.

OM-MPYR: ^{1}H NMR (500 MHz, CD_3CN), δ(ppm): 8.18 (d, *J* = 10 Hz, 2H), 7.71 (d, *J* = 5 Hz, 2H), 7.27 (d, *J* = 15 Hz, 1H), 7.20 (d, *J* = 15 Hz, 1H), 7.08 (d, *J* = 5 Hz, 2H), 7.04 (d, *J* = 10 Hz, 2H), 7.02 (s, 2H), 3.93 (s, 6H), 3.87 (s, 3H), 3.23 (t, *J* = 5 Hz, 4H), 3.06 (t, *J* = 5 Hz, 4H).

^{13}C NMR (125 MHz, CD_3CN): 16.4, 23.4, 27.4, 40.0, 110.9, 111.9, 113,4, 124.2, 127.8, 140.7, 142.0, 143.6, 147.5, 154.8, 159.7, 161.9, 162.0, 167.5.

HRMS calculated = 477.2060, found = 477.2067.

3.5.4. Spectral Data

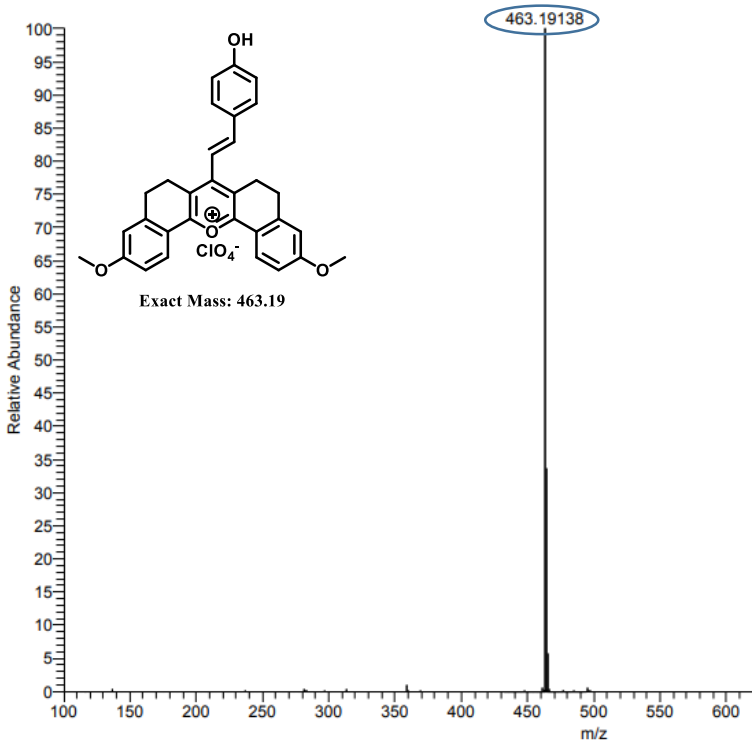

Figure 3.23. HRMS spectrum of **OH-MPYR**.

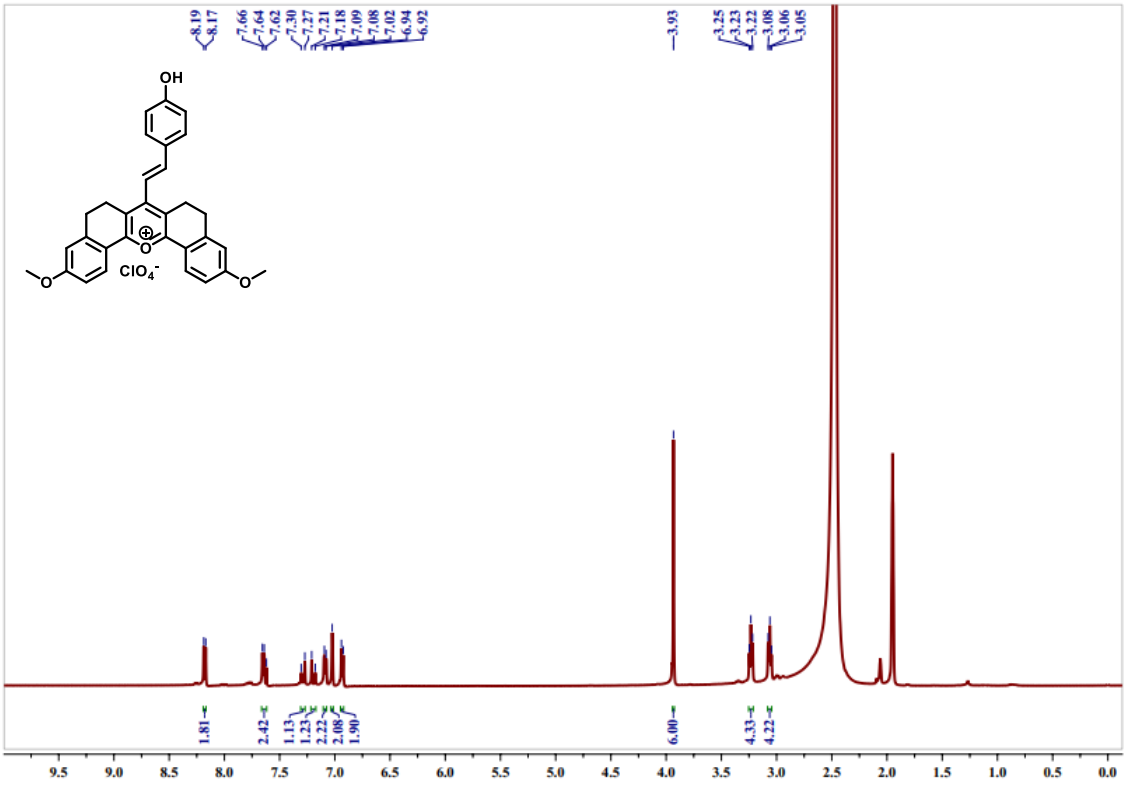

Figure 3.24. ^{1}H NMR spectrum of **OH-MPYR**.

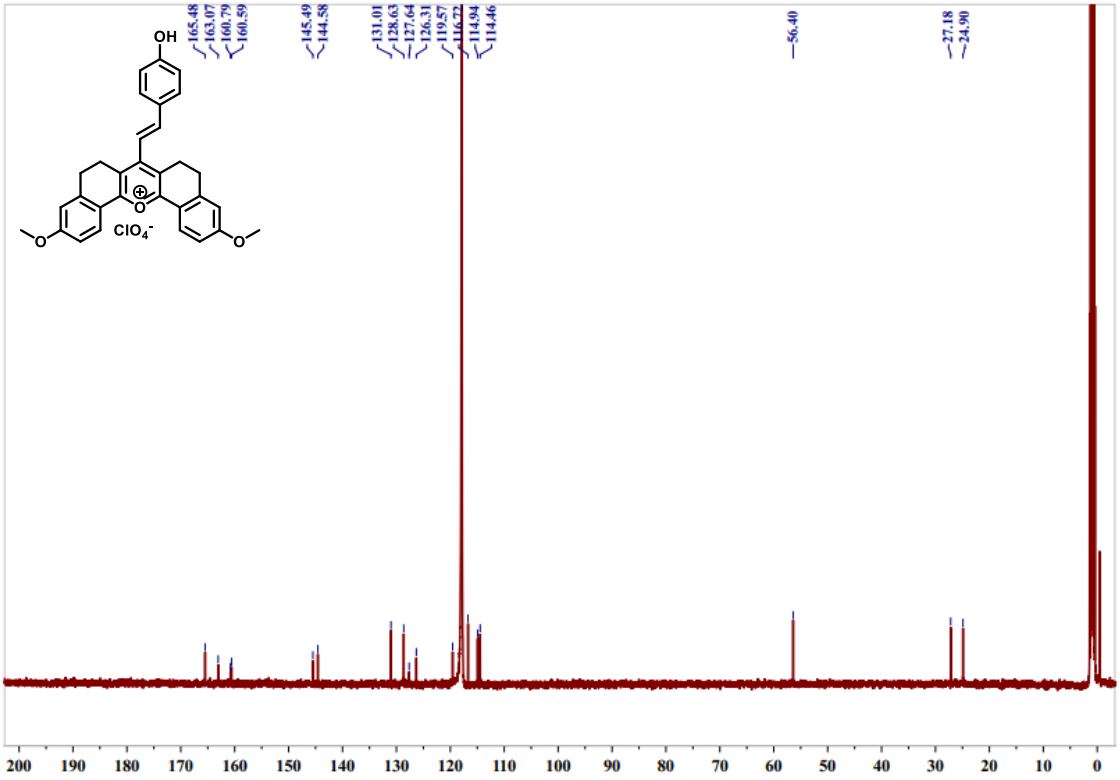

Figure 3.25. ^{13}C NMR spectrum of **OH-MPYR**

3.6. References

1. Ma, C.; Sun, W.; Xu, L.; Qian, Y.; Dai, J.; Zhong, G.; Hou, Y.; Liu, J.; Shen, B., A minireview of viscosity-sensitive fluorescent probes: design and biological applications. *Journal of Materials Chemistry B* **2020,** *8* (42), 9642-9651.

2. Yin, J.; Huang, L.; Wu, L.; Li, J.; James, T. D.; Lin, W., Small molecule based fluorescent chemosensors for imaging the microenvironment within specific cellular regions. *Chem. Soc. Rev.* **2021,** *50* (21), 12098-12150.

3. Gong, J.; Liu, C.; Jiao, X.; He, S.; Zhao, L.; Zeng, X., Novel mitochondria-targeted viscosity probe based on a fluorescent rotatable xanthene-hemicyanine dyad. *Microchem. J.* **2020,** *158*, 105191.

4. Yin, J.; Xu, Q.; Mo, X.; Dai, L.; Ren, M.; Wang, S.; Kong, F., Construction of a novel mitochondria-targeted near-infrared (NIR) probe for detection of viscosity changes in cancer cells ferroptosis process. *Dyes and Pigments* **2022,** *200*, 110184.

5. Lowe, G. D. O.; Lee, A. J.; Rumley, A.; Price, J. F.; Fowkes, F. G. R., Blood viscosity and risk of cardiovascular events: the Edinburgh Artery Study. *British journal of haematology* **1997,** *96* (1), 168-173.

6. Dou, K.; Huang, W.; Xiang, Y.; Li, S.; Liu, Z., Design of activatable NIR-II molecular probe for in vivo elucidation of disease-related viscosity variations. *Anal. Chem.* **2020,** *92* (6), 4177-4181.

7. Sreejaya, M. M.; Pillai, V. M.; Ayesha, A.; Baby, M.; Bera, M.; Gangopadhyay, M., Mechanistic analysis of viscosity-sensitive fluorescent probes for applications in diabetes detection. *Journal of Materials Chemistry B* **2024**.

8. Miao, W.; Yu, C.; Hao, E.; Jiao, L., Functionalized BODIPYs as fluorescent molecular rotors for viscosity detection. *Frontiers in chemistry* **2019,** *7*, 825.

9. Guo, Y.; Leng, H.; Wang, Y.; Shi, W.-J.; Zhang, L.; Yan, J., A novel H2O2-activated NIR fluorescent probe for imaging β-amyloid fibrils and mitochondrial viscosity. *Dyes and Pigments* **2022,** *206*, 110665.

10. Haidekker, M. A.; Theodorakis, E. A., Molecular rotors—fluorescent biosensors for viscosity and flow. *Organic & biomolecular chemistry* **2007,** *5* (11), 1669-1678.

11. Ning, P.; Dong, P.; Geng, Q.; Bai, L.; Ding, Y.; Tian, X.; Shao, R.; Li, L.; Meng, X., A two-photon fluorescent probe for viscosity imaging in vivo. *Journal of Materials Chemistry B* **2017,** *5* (15), 2743-2749.

12. Bahri, M. A.; Hoebeke, M.; Grammenos, A.; Delanaye, L.; Vandewalle, N.; Seret, A., Investigation of SDS, DTAB and CTAB micelle microviscosities by electron spin resonance. *Colloids and Surfaces A: Physicochemical and Engineering Aspects* **2006,** *290* (1-3), 206-212.

13. Markovic, S.; Bryan, J. L.; Ishimtsev, V.; Turakhanov, A.; Rezaee, R.; Cheremisin, A.; Kantzas, A.; Koroteev, D.; Mehta, S. A., Improved oil viscosity characterization by low-field NMR using feature engineering and supervised learning algorithms. *Energy & Fuels* **2020,** *34* (11), 13799-13813.

14. Fang, H.; Chen, Y.; Jiang, Z.; He, W.; Guo, Z., Fluorescent probes for biological species and microenvironments: from rational design to bioimaging applications. *Accounts of Chemical Research* **2023,** *56* (3), 258-269.

15. Yin, X.; Cai, Y.; Cai, S.; Jiao, X.; Liu, C.; He, S.; Zeng, X., A deep-red fluorescent molecular rotor based on donor-two-acceptor modular system for imaging mitochondrial viscosity. *RSC advances* **2020,** *10* (51), 30825-30831.

16. Liu, X.; Chi, W.; Qiao, Q.; Kokate, S. V.; Cabrera, E. P.; Xu, Z.; Liu, X.; Chang, Y.-T., Molecular mechanism of viscosity sensitivity in BODIPY rotors and application to motion-based fluorescent sensors. *Acs Sensors* **2020,** *5* (3), 731-739.

17. Bonam, S. R.; Wang, F.; Muller, S., Lysosomes as a therapeutic target. *Nature Reviews Drug Discovery* **2019,** *18* (12), 923-948.

18. Li, X.; Zhao, R.; Wang, Y.; Huang, C., A new GFP fluorophore-based probe for lysosome labelling and tracing lysosomal viscosity in live cells. *Journal of Materials Chemistry B* **2018,** *6* (41), 6592-6598.

19. Tang, T.; Yang, Z.-y.; Wang, D.; Yang, X.-y.; Wang, J.; Li, L.; Wen, Q.; Gao, L.; Bian, X.-w.; Yu, S.-c., The role of lysosomes in cancer development and progression. *Cell & bioscience* **2020,** *10* (1), 1-18.

20. Futerman, A. H.; Van Meer, G., The cell biology of lysosomal storage disorders. *Nature reviews Molecular cell biology* **2004,** *5* (7), 554-565.

21. Devany, J.; Chakraborty, K.; Krishnan, Y., Subcellular nanorheology reveals lysosomal viscosity as a reporter for lysosomal storage diseases. *Nano Lett.* **2018,** *18* (2), 1351-1359.

22. Wang, L.; Xiao, Y.; Tian, W.; Deng, L., Activatable rotor for quantifying lysosomal viscosity in living cells. *J. Am. Chem. Soc.* **2013,** *135* (8), 2903-2906.

23. Gupta, N.; Reja, S. I.; Bhalla, V.; Gupta, M.; Kaur, G.; Kumar, M., A bodipy based fluorescent probe for evaluating and identifying cancer, normal and apoptotic C6 cells on the basis of changes in intracellular viscosity. *Journal of Materials Chemistry B* **2016,** *4* (11), 1968-1977.

24. Song, Y.; Zhang, H.; Wang, X.; Geng, X.; Sun, Y.; Liu, J.; Li, Z., One stone, three birds: pH triggered transformation of aminopyronine and iminopyronine based lysosome targeting viscosity probe for cancer visualization. *Anal. Chem.* **2020,** *93* (3), 1786-1791.

25. Liu, C.; Ye, S.; Zhang, D.; Chen, J.; Xiao, H.; Qu, J.; Liu, R., Far-Red Fluorophore for Monitoring Viscosity In Vitro, In Vivo, and Ex Vivo and Dynamic Tracking of Lipid Droplets in Live Systems. *ACS Applied Optical Materials* **2023,** *1* (3), 795-801.

26. Abdel-Megid, M., Part—II: Utilities of active methylene compounds and heterocycles bearing active methyl or having an active methine in the formation of bioactive pyrazoles and pyrazolopyrimidines. *Synthetic Communications* **2020,** *50* (23), 3563-3591.

27. Massa, A., Recent advances in the chemistry of active methylene compounds. *Current Organic Chemistry* **2012,** *16*, 2159-2159.

28. Yin, W.; Wang, H.; Deng, B.; Ma, F.; Zhang, J.; Zhou, M.; Wang, H.; Lu, Y., A pyrylium salt-based fluorescent probe for the highly sensitive detection of methylamine vapour. *Analyst* **2022,** *147* (15), 3451-3455.

29. Resta, I. M.; Lucantoni, F.; Apostolova, N.; Galindo, F., Fluorescent styrylpyrylium probes for the imaging of mitochondria in live cells. *Organic & Biomolecular Chemistry* **2021,** *19* (41), 9043-9057.

30. Lou, W.; Zhang, Y.; Xiang, Y.; Cui, Z.; Li, B., A Symmetric Pyrylium Based Fluorescence Probe for Sensing H2s in Environmental Water Samples, Food Samples, and Living Cells. *Food Samples, and Living Cells*.

31. Chakraborty, S.; Joseph, M. M.; Varughese, S.; Ghosh, S.; Maiti, K. K.; Samanta, A.; Ajayaghosh, A., A new pentacyclic pyrylium fluorescent probe that responds to pH imbalance during apoptosis. *Chemical Science* **2020,** *11* (47), 12695-12700.

32. Basavaraja, D.; Dey, D.; Varsha, T. L.; Salfeena, C. T. F.; Panda, M. K.; Somappa, S. B., Rapid visual detection of amines by pyrylium salts for food spoilage taggant. *ACS Appl. Bio Mater* **2020,** *3*, 772-778.

33. Daus, K.; Tharamak, S.; Pluempanupat, W.; Galie, P. A.; Theodoraki, M. A.; Theodorakis, E. A.; Alpaugh, M. L., Fluorescent molecular rotors as versatile in situ sensors for protein quantitation. *Scientific Reports* **2023,** *13* (1), 20529.

34. Sasaki, S.; Drummen, G. P. C.; Konishi, G.-i., Recent advances in twisted intramolecular charge transfer (TICT) fluorescence and related phenomena in materials chemistry. *Journal of Materials Chemistry C* **2016,** *4* (14), 2731-2743.

35. Erdemir, S.; Malkondu, S.; Oguz, M.; Kocyigit, O., A novel pathway for ratiometric hydrazine sensing in environmental samples and the detection of intracellular viscosity by a mitochondria-targeted fluorescent sensor. *Talanta* **2024,** *267*, 125143.

36. Li, Y.; Zhang, M.; Chen, X.; Liang, J.; Chen, D.; Gao, M.; Ren, L., TICT based fluorescent probe with excellent photostability for real-time and long-term imaging of lipid droplets. *Tetrahedron Lett.* **2019,** *60* (29), 1880-1884.

37. Ma, Y.; Pang, Y.; Chabbra, S.; Reijerse, E. J.; Schnegg, A.; Niski, J.; Leutzsch, M.; Cornella, J., Radical C− N borylation of aromatic amines enabled by a pyrylium reagent. *Chemistry–A European Journal* **2020,** *26* (17), 3738-3743.

38. Narsaria, A. K.; Poater, J.; Fonseca Guerra, C.; Ehlers, A. W.; Lammertsma, K.; Bickelhaupt, F. M., Rational design of near-infrared absorbing organic dyes: Controlling the HOMO–LUMO gap using quantitative molecular orbital theory. *Journal of Computational Chemistry* **2018,** *39* (32), 2690-2696.

39. Mukherjee, S.; Torres, D. E.; Jakubikova, E., HOMO inversion as a strategy for improving the light-absorption properties of Fe (II) chromophores. *Chemical science* **2017,** *8* (12), 8115-8126.

40. Kuimova, M. K.; Yahioglu, G.; Levitt, J. A.; Suhling, K., Molecular rotor measures viscosity of live cells via fluorescence lifetime imaging. *J. Am. Chem. Soc.* **2008,** *130* (21), 6672-6673.

41. Raut, S.; Kimball, J.; Fudala, R.; Doan, H.; Maliwal, B.; Sabnis, N.; Lacko, A.; Gryczynski, I.; Dzyuba, S. V.; Gryczynski, Z., A homodimeric BODIPY rotor as a fluorescent viscosity sensor for membrane-mimicking and cellular environments. *PCCP* **2014,** *16* (48), 27037-27042.

42. Li, S.; Li, Y.; Zhang, S.; Fang, H.; Huang, Z.; Zhang, D.; Ding, A.; Uvdal, K.; Hu, Z.; Huang, K., Response strategies and biological applications of organic fluorescent thermometry: cell- and mitochondrion-level detection. *Analytical Methods* **2024,** *16* (14), 1968-1984.

43. Saha, S. K.; Purkayastha, P.; Das, A. B.; Dhara, S., Excited state isomerization and effect of viscosity-and temperature-dependent torsional relaxation on TICT fluorescence of trans-2-[4-(dimethylamino) styryl] benzothiazole. *Journal of Photochemistry and Photobiology A: Chemistry* **2008,** *199* (2-3), 179-187.

44. Liu, T.; Liu, X.; Spring, D. R.; Qian, X.; Cui, J.; Xu, Z., Quantitatively mapping cellular viscosity with detailed organelle information via a designed PET fluorescent probe. *Scientific reports* **2014,** *4* (1), 5418.

45. Adachi, J.; Oda, H.; Fukushima, T.; Lestari, B.; Kimura, H.; Sugai, H.; Shiraki, K.; Hamaguchi, R.; Sato, K.; Kinbara, K., Dense and Acidic Organelle-Targeted Visualization in Living Cells: Application of Viscosity-Responsive Fluorescence Utilizing Restricted Access to Minimum Energy Conical Intersection. *Analytical Chemistry* **2023,** *95* (12), 5196-5204.

46. Wei, Y.-F.; Weng, X.-F.; Sha, X.-L.; Sun, R.; Xu, Y.-J.; Ge, J.-F., Simultaneous imaging of lysosomal and mitochondrial viscosity under different conditions using a NIR probe. *Sensors and Actuators B: Chemical* **2021,** *326*, 128954.

47. Chen, H.; Zhao, J.; Lin, J.; Dong, B.; Li, H.; Geng, B.; Yan, M., Two-photon fluorescent probes for detecting the viscosity of lipid droplets and its application in living cells. *RSC advances* **2021,** *11* (14), 8250-8254.

48. Soltoff, S. P.; Mandel, L. J., Potassium transport in the rabbit renal proximal tubule: effects of barium, ouabain, valinomycin, and other ionophores. *The Journal of membrane biology* **1986,** *94*, 153-161.

A Light-Activated Pyridinium-Spiropyran Conjugate for Monitoring Cellular HOCl and SO_2

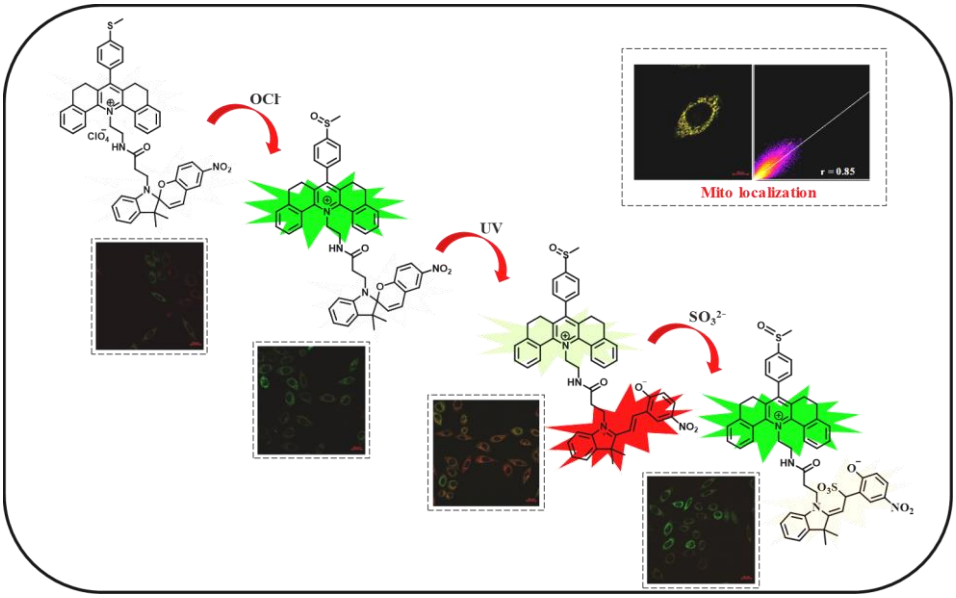

4.1. Abstract

Heat shock is a growing global health concern, characterized by a core body temperature exceeding 40.6 °C, which disrupts normal thermoregulatory homeostasis. The design and development of fluorescent probes that facilitate a better understanding of the heat shock process and sub-cellular defence mechanisms are of great importance. Intracellular redox homeostasis plays a pivotal role in the heat shock response. Hypochlorous acid (HOCl) and sulfur dioxide (SO_2), due to their respective oxidative and antioxidative properties, are closely associated with the oxidative stress involved in heat stroke, serving as key signalling molecules in the associated cellular response. Herein, we report a spiropyran-pyridinium conjugate, ***SPI-PYD****, for the dual sensing of HOCl and SO_2 within the cellular microenvironment.* ***SPI-PYD*** *functions as a ratiometric fluorescent sensor, wherein the*

pyridinium core having a thiomethyl group serves as the HOCl sensing unit, while the UV-activated spiropyran moiety responds to SO_2. Initially, the probe displays weak fluorescence in both the green and red channels. Upon addition of HOCl, the thiomethyl group undergoes oxidation, resulting in a 6-fold increase in fluorescence intensity in the green channel due to the suppression of photoinduced electron transfer (PET) from the thiomethyl group to the pyridinium chromophore. Further, upon UV irradiation, spiropyran part of the probe undergo ring opening to form merocyanine, which absorbs in the range of 550 nm, aligning with the emission of the pyridinium component. This overlap enables Förster Resonance Energy Transfer (FRET), resulting in a 3.3-fold increase in fluorescence intensity in the red channel and a corresponding decrease in the green channel. Furthermore, the addition of SO_2 causes a 4.2-fold decrease in the red channel fluorescence and a concomitant increase in fluorescence intensity in the green channel, due to disruption of the double bond in the merocyanin structure. Additionally, ***SPI-PYD*** *exhibits strong mitochondria targeting ability, with a Pearson coefficient of 0.85, along with excellent aqueous solubility and low cytotoxicity. Bioimaging experiments in SK-BR-3 breast cancer cells confirmed the intracellular ratiometric sensing capability of the probe for HOCl and SO_2, underscoring its potential as a valuable tool for studying oxidative stress and cellular responses during heat shock.*

4.2. Introduction

Heat Shock has emerged as a global health concern as it causes permanent damage to living cells and has a relatively high mortality rate. This condition represents a core body temperature greater than 40.6 °C and failure of the body's ability to maintain thermoregulatory homeostasis.[1] According to the U.S. National Weather Service, heat waves kill more people, on average, than any other extreme weather event. The global annual estimate for heat-related deaths is projected to rise by 92,207 (64,458-121,464) additional deaths in 2030, and 255,486 (191,816-364,002) additional deaths in 2050.[2-4] By the end of this century, it is expected that

there will be a 1.4 - 5.8 ^{o}C rise in global temperature, which can adversely affect human health and the ecosystem.[5,6] The rise in body temperature above 40.6 ^{o}C can spontaneously cause short term and long term side effects to people, which include dizziness, mental confusion, unconsciousness, serious injury to tissues and damage to the nervous system, leading to multiple organ failure and death.[7,8] So it is necessary to understand the action of heat shock on cells and the related defense mechanisms at the sub-cellular level.

The understanding of heat shock remains incomplete due to several factors, limiting a comprehensive examination of its causes and treatment strategies. As a result, the precise pathogenesis of heat shock is not fully understood, leading to a lack of effective diagnostic methods and therapies. Moreover, our knowledge of molecular and subcellular organelle behavior during heat stress in live cells is still limited. Over the past decade, research has shown that heat shock arises from thermoregulatory failure coupled with an exaggerated acute-phase response and an altered expression of heat shock proteins.[6,9] This condition induces hypoxia, which triggers the generation of highly reactive oxygen and nitrogen species, causing abnormalities in the cellular microenvironment. Consequently, HOCl, as a reactive oxygen species, and SO_2, as an antioxidant, can counterbalance each other and act as signalling molecules in the heat shock response.

Fluorescent probes are highly effective tools for real-time monitoring of sub-cellular activities due to their easy synthesis, low cost, high spatial and temporal resolution, and ability to track the process with minimal disruption to normal cellular functions.[10,11] Despite these advantages, only a few fluorescent probes have been reported for heat shock monitoring, most of which are based on detecting pH changes during thermoregulatory homeostasis.[12-16] More recently, studies have focussed on monitoring SO_2 levels and reduced mitochondrial viscosity in heat shock conditions.[17] In 2020, Yin *et al.* synthesized a naphthalimide-spiropyran conjugate, **Ly-NT-SP** for sulfur dioxide detection in lysosomes and used it for heat stroke

monitoring for the first time **(Figure 4.1)**.[18] The probe functions as a ratiometric fluorescent sensor, which upon UV irradiation, undergoes isomerization to produce the merocyanine (MR) derivative, **Ly-NT-MR**, displaying a red-shifted emission at 630 nm due to a Förster resonance energy transfer (FRET) process from the naphthalimide donor to the MR acceptor. The UV activated MR state contains a C-C double bond that serves as the recognition site for SO_2, where its disruption decreases red fluorescence intensity while increasing green fluorescence intensity. Confocal microscopy imaging in HeLa cells using **Ly-NT-SP** further enabled visualization of elevated lysosomal sulfur dioxide (SO_2) levels during heat shock.

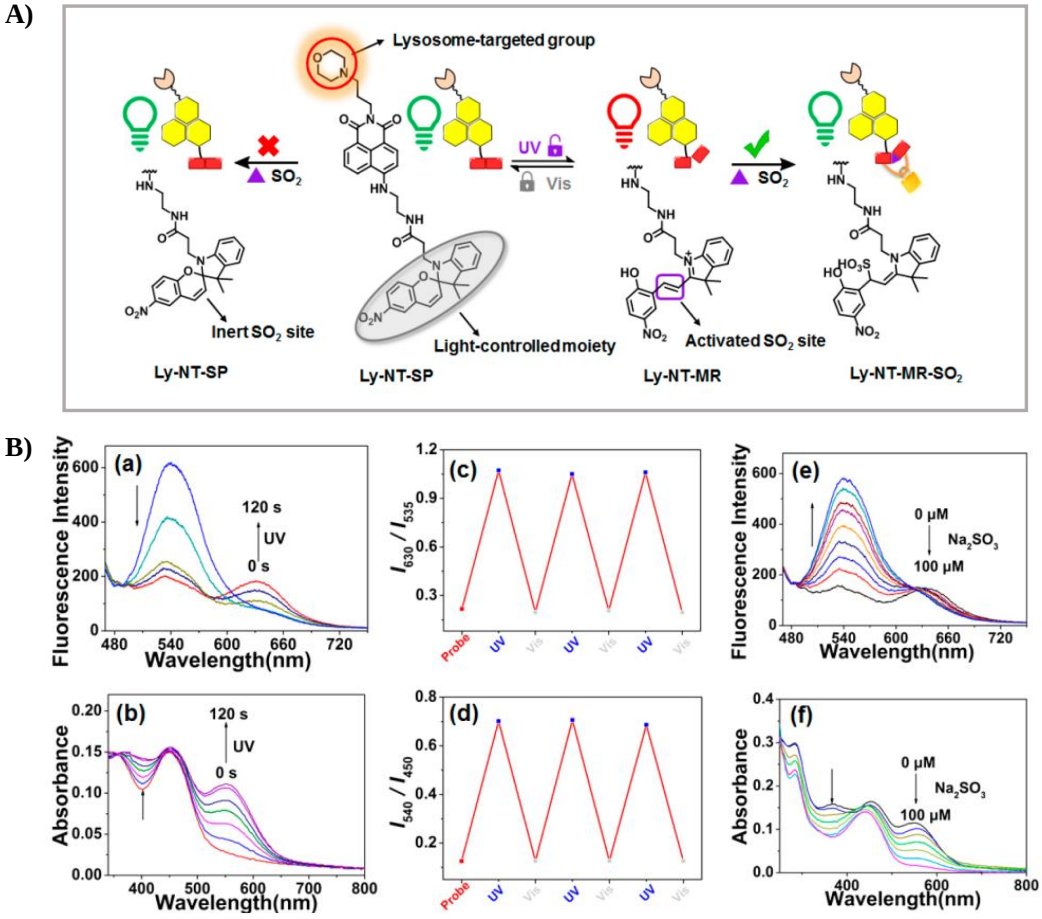

Figure 4.1. (A) Molecular design of **Ly-NT-SP** and proposed sensing mechanism toward SO_2; (B) (a) Fluorescence and (b) absorption spectral changes of probe **Ly-NT-SP** (10 μM) after irradiation with UV light for 120 s; (c) Fluorescence and (d) UV-Vis absorbance photoswitching of **Ly-NT-SP**; (e) Fluorescence and (f) absorption spectral changes of **Ly-NT-MR** (10 μM) upon addition of Na_2SO_3 (0-100 μM), (PBS buffer solution, pH = 5.0; λ_{ex} = 450 nm) (Figure adapted from reference 18).

As the SO_2 level increases during heat shock, HOCl level is also expected to rise since these two molecules counteract each other. Therefore, developing a dual sensor for HOCl and SO_2 could provide valuable insights into the underlying mechanisms of heat stroke. He and co-workers have utilized HOCl detection as a tool for heat shock monitoring and developed a NIR probe, **MB-HClO**, based on methylene blue for the rapid detection of HOCl levels **(Figure 4.2)**.[19] Bioimaging in RAW 264.7 cells at heat stroke temperatures revealed a gradual increase in red channel fluorescence intensity as the temperature rose from 37 - 45 ^{o}C. Thus, for the first time, the **MB-HClO** probe was successfully applied to monitor HOCl upregulation in lysosomes during heat shock.

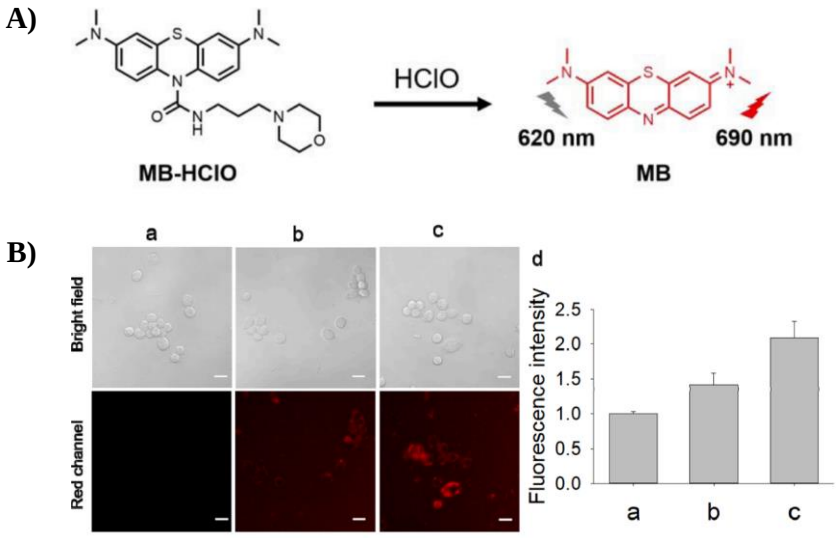

Figure 4.2. (A) Molecular design of **MB-HClO**; (B) Fluorescence images of **MB-HClO**-loaded RAW 264.7 cells under heat stroke at (a) 37 ^{o}C, (b) 41 ^{o}C, and (c) 45 ^{o}C for 20 min; λ_{ex} = 633 nm, λ_{em} = 638-755 nm, scale bar = 20 µm and (d) Quantified relative fluorescence intensity of (a-c) (Figure adapted from reference 19).

Yu et al. have developed a dual-response fluorescent probe, **HCy-SO$_2$-HClO**, for the simultaneous detection of hypochlorous acid (HClO) and sulfur dioxide (SO_2) during heat shock process **(Figure 4.3)**.[20] The probe consist of a *N*,*N*-dimethylthiocarbamate group as the response site for HClO, effectively suppressing the probe's intramolecular charge transfer, resulting in minimal fluorescence. Addition of HClO resulted in a significant enhancement in

fluorescence around 575 nm within 10 seconds. In contrast, exposure to SO_2 triggered a Michael addition reaction, disrupting the extended conjugation, resulting in enhanced fluorescence at 450 nm within 20 minutes. The distinct response times and emission wavelengths enabled the simultaneous detection of both species. Furthermore, the probe exhibited efficient mitochondrial accumulation and successfully enabled the concurrent detection of HClO and SO_2 in heat shock cells and mouse intestines.

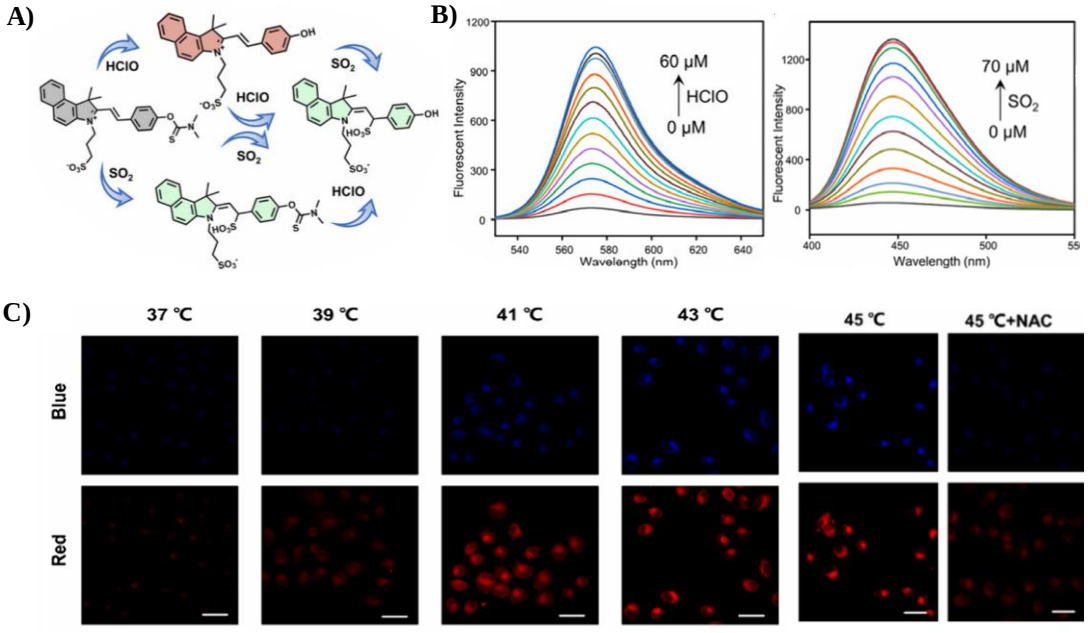

Figure 4.3. (A) Molecular design of **HCy-SO_2-HClO** and proposed mechanisms for HClO and SO_2 sensing; (B) The fluorescence emission spectra of **HCy-SO_2-HClO** in the presence of HClO (0-60 μM, λ_{ex}=480 nm) for 10 s and HSO_3^- (0-70 μM, λ_{ex}=370 nm) for 20 min in PBS buffer solution (10 mM, pH 7.4) and (C) Fluorescence images of HeLa cells co-cultured with the probe at different temperatures (Figure adapted from reference 20).

Spiropyran is a photochromic molecule that undergoes reversible isomerization between its ring-closed spiropyran (SP) form and the ring-opened merocyanine (MR) form when exposed to light of specific wavelengths, resulting in a change in color or optical properties.[21] In biological imaging, the ability to switch between two different colors of emitted light via Förster resonance energy transfer (FRET) is particularly advantageous, providing greater flexibility in optical output. In literature, spiropyran has been paired with various FRET

partners to achieve colour switching and fluorescent response. Some widely used FRET pairs for spiropyran include coumarin[22], tetraphenylethene[23] and naphthalimide.[24] Given that the emission of rigid pentacyclic pyridinium aligns with the absorption range of merocyanine, the pyridinium chromophore can serve as an efficient FRET pair for spiropyran.

Heat stroke is intricately linked to disruptions in intracellular redox homeostasis, where the interplay between reactive oxygen species (HOCl) and antioxidants (SO_2) plays a crucial role in understanding the mechanisms behind heat shock at both cellular and subcellular levels.[25,26] In this context, we designed a pyridinium spiropyran conjugate, **SPI-PYD**, for the dual sensing of HOCl and SO_2 within the cellular environment. The probe, **SPI-PYD**, initially exhibits weak fluorescence in both the green and red channels and provides a ratiometric response to the presence of HOCl and SO_2 in both channels. In the presence of HOCl, oxidation of the thiomethyl group in the pyridinium unit enhances fluorescence in the green channel, while UV activation of the spiropyran moiety triggers ring opening to form merocyanine, enabling the detection of SO_2 with a shift in fluorescence intensity from the red to green channel. Furthermore, the probe demonstrated excellent mitochondria targeting ability, low cytotoxicity, and a stable fluorescence response even under temperature fluctuations, making it a promising candidate for monitoring changes in the cellular microenvironment associated with heat shock. The dual-sensing capability of **SPI-PYD** thus provides valuable insights into the complex redox balance during heat stroke, offering a novel tool for studying the dynamic behaviour of signalling molecules under heat stress.

4.3. Results and Discussion

4.3.1. Design, synthesis and characterization of SPI-PYD

The probe **SPI-PYD** consists of two key components: a pyridinium moiety appended with thiomethyl benzaldehyde and a spiropyran unit. In buffered aqueous solutions, **SPI-PYD** exhibits quenched green fluorescence due to efficient, photoinduced electron transfer (PET) from the thiomethyl group to the pyridinium chromophore. Upon exposure to hypochlorous acid (HOCl), the thiomethyl group undergoes oxidation, disrupting the PET process and leading to a fluorescence enhancement. Spiropyran is a photochromic molecule that reversibly changes colour or optical properties through isomerization between its ring-closed spiropyran (SP) form and ring-opened merocyanine (MR) form when exposed to light of specific wavelengths. The pyridinium moiety emits in the 400-660 nm range, overlapping with the absorption spectrum of spiropyran (425-625 nm), making this conjugation an effective FRET pair. Upon UV irradiation, the SP form converts to the MR state, increasing fluorescence intensity in the red channel with a concomitant fluorescence decrease in the green channel, due to FRET from the pyridinium donor to the MR acceptor. Additionally, the C-C double bond in the UV-activated MR state serves as a recognition site for SO_2, which undergoes a Michael addition reaction, disrupting the double bond, which in turn reduces fluorescence in the red channel and restores emission in the green channel **(Figure 4.4)**.

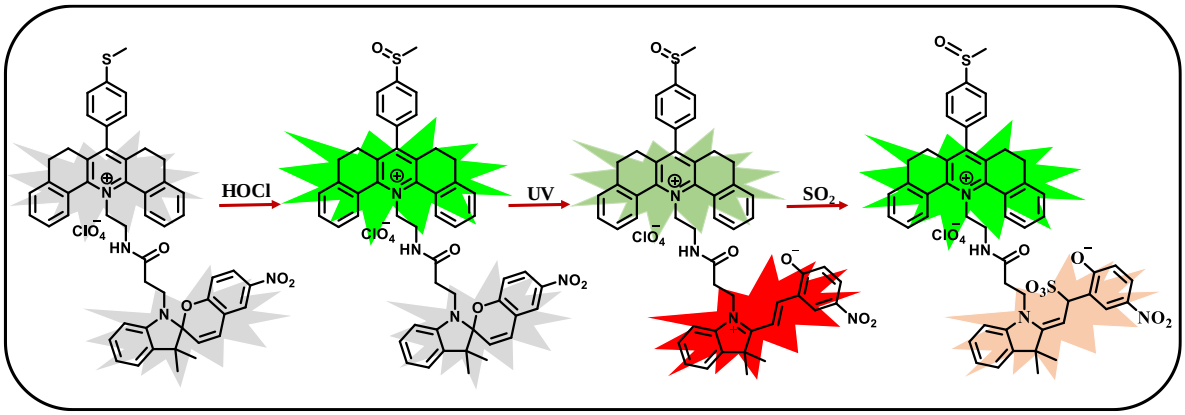

Figure 4.4. Design strategy of **SPI-PYD** and the mechanism of action.

The synthesis of **SPI-PYD** was carried out as outlined in **Scheme 4.1.** Pyrylium derivative (**1**) was synthesized via the cyclization of 4-thiomethylbenzaldehyde and 1-tetralone, followed by conversion to a pyridinium derivative (**2**) using *N-Boc*-ethylenediamine. Subsequent deprotection of the Boc group yielded the compound **3**, a pyridinium fluorophore with a free amino group (-NH_2). For the spiropyran unit, compound **4** was synthesized by reacting 2,3,3-trimethyl-3*H*-indole with 3-bromopropanoic acid. A subsequent reaction with 5-nitrosalicylaldehyde in the presence of trimethylamine yielded the compound **5**, a spiropyran unit containing a free carboxyl (-COOH) group. Finally, compound **3** was conjugated to the spiropyran unit (**5**) through EDC/NHS-mediated coupling, forming the final molecule **SPI-PYD (Scheme 4.1)**. All the intermediates and final products were characterized using ^{1}H NMR, ^{13}C NMR and HRMS, details of which are provided in the experimental section.

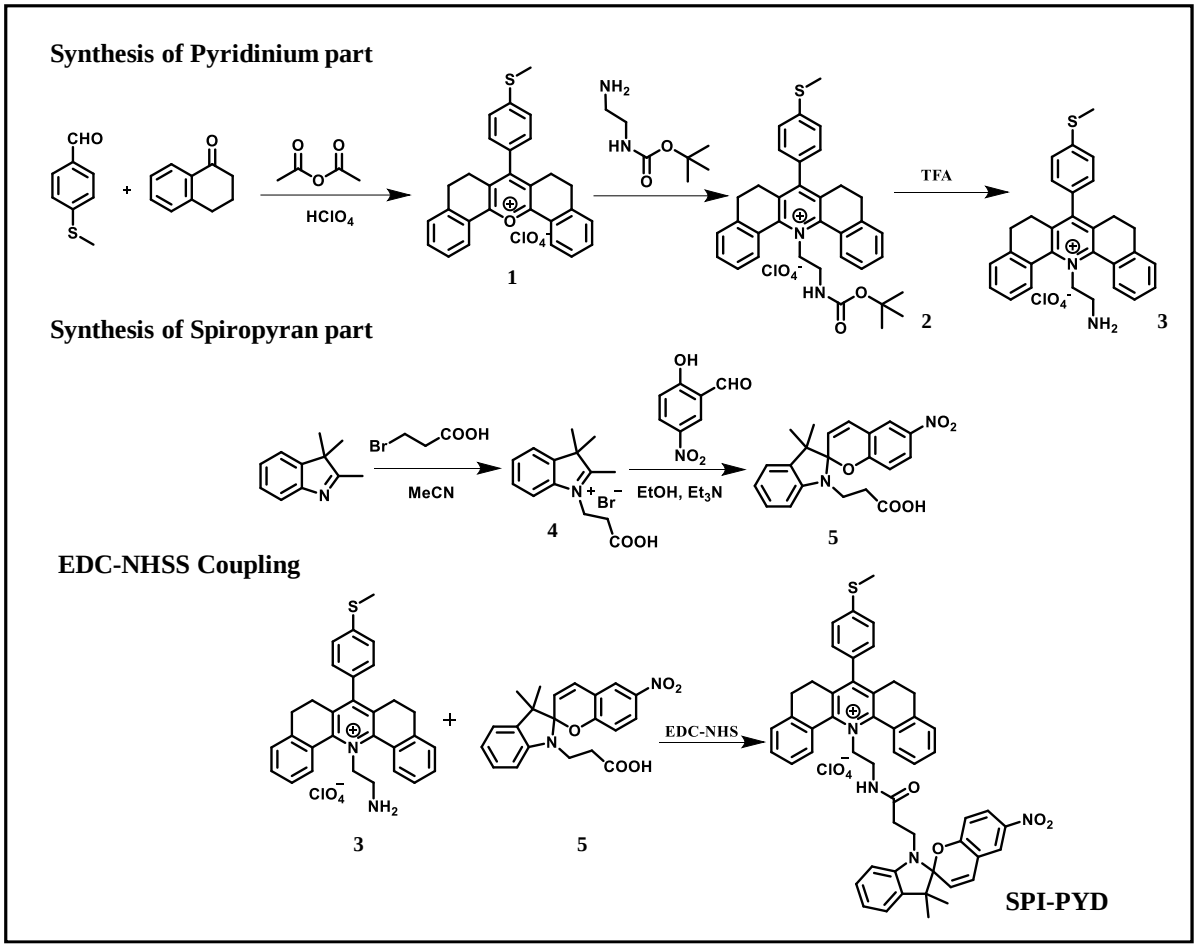

Scheme 4.1. Scheme for the synthesis of **SPI-PYD**.

4.3.2. Dual sensing studies of SPI-PYD

To validate our hypothesis for detecting HOCl (as OCl^-) and SO_2 (as SO_3^{2-}), we measured the absorption and fluorescence responses of the **SPI-PYD** probe in the presence of NaOCl and Na_2SO_3. Initially, **SPI-PYD** exhibited an absorption maximum of 394 nm and a fluorescence maximum of 506 nm, with a significant Stokes shift of 5618 cm^{-1}. Upon addition of NaOCl, the absorption maxima at 394 nm remained unchanged, while the fluorescence intensity at 506 nm increased significantly **(Figure 4.5A and 4.5B, Figure 4.8A)**. This fluorescence enhancement is attributed to the inhibition of the PET, as the thiomethyl group undergoes oxidation. Upon UV irradiation, the probe displayed a new absorption peak at 540 nm, accompanied by a decrease in the emission peak at 506 nm. Simultaneously, a new fluorescence band at 640 nm emerged, with its intensity gradually increasing over time, reaching a maximum after 100 seconds **(Figure 4.6A and B)**. These spectral changes indicate the conversion of **SPI-PYD** from its SP form to the MR form, activating the FRET process from the pyridinium donor to the MR acceptor. Upon addition of Na_2SO_3 (an SO_2 donor), the absorption band at 540 nm and the emission band at 640 nm gradually decreased, indicating the disruption of the **C=C** bond in the merocyanine unit and the formation of the Michael adduct with SO_2 **(Figure 4.7A and B, Figure 4.8B)**.

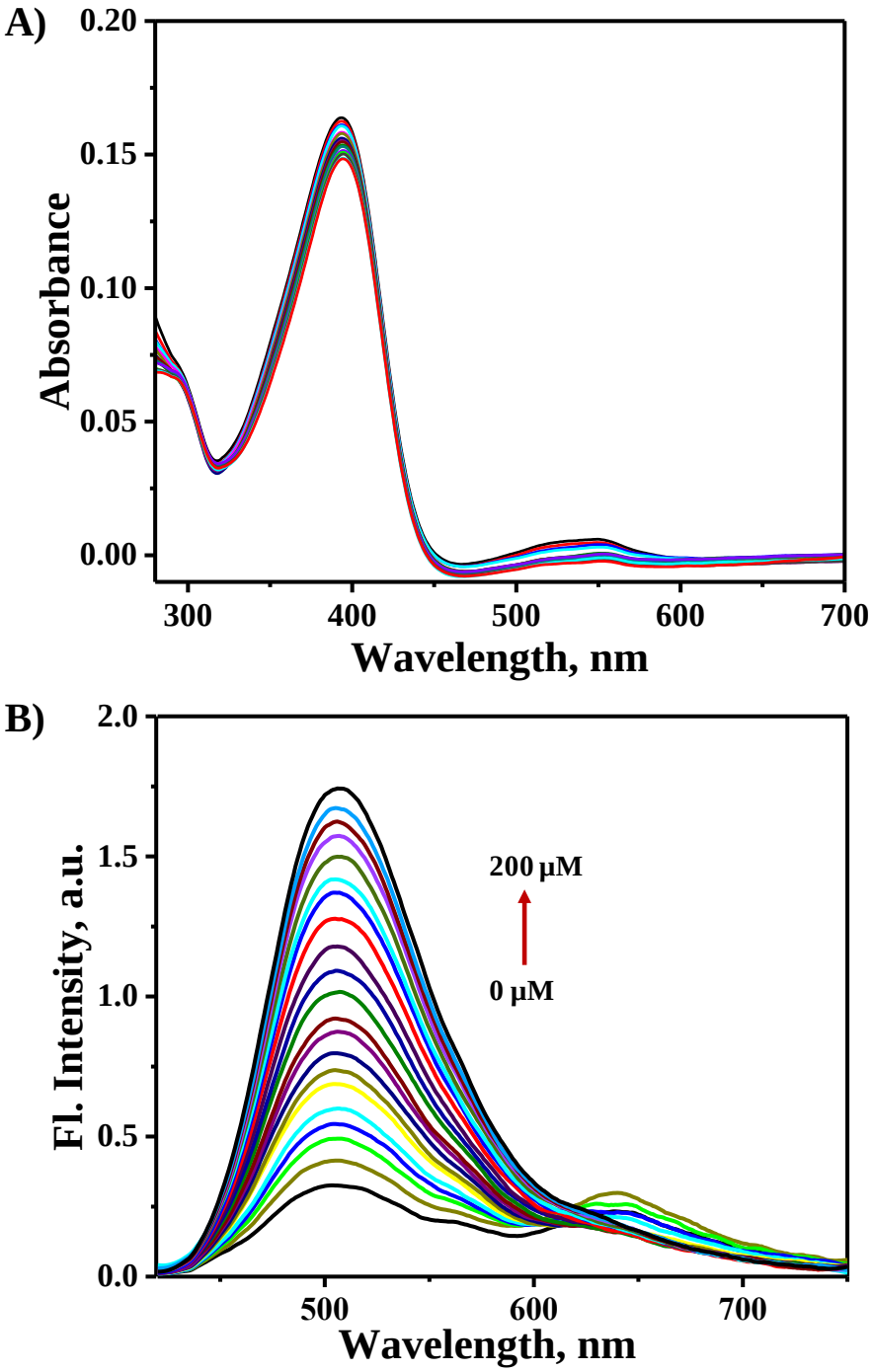

Figure 4.5. (A) Absorption and (B) fluorescence spectra of the probe **SPI-PYD** (10 µM) in presence of varying concentrations of NaOCl (0 - 200 µM) in phosphate buffer (0.1 M, pH = 7.4), λ_{ex} = 395 nm.

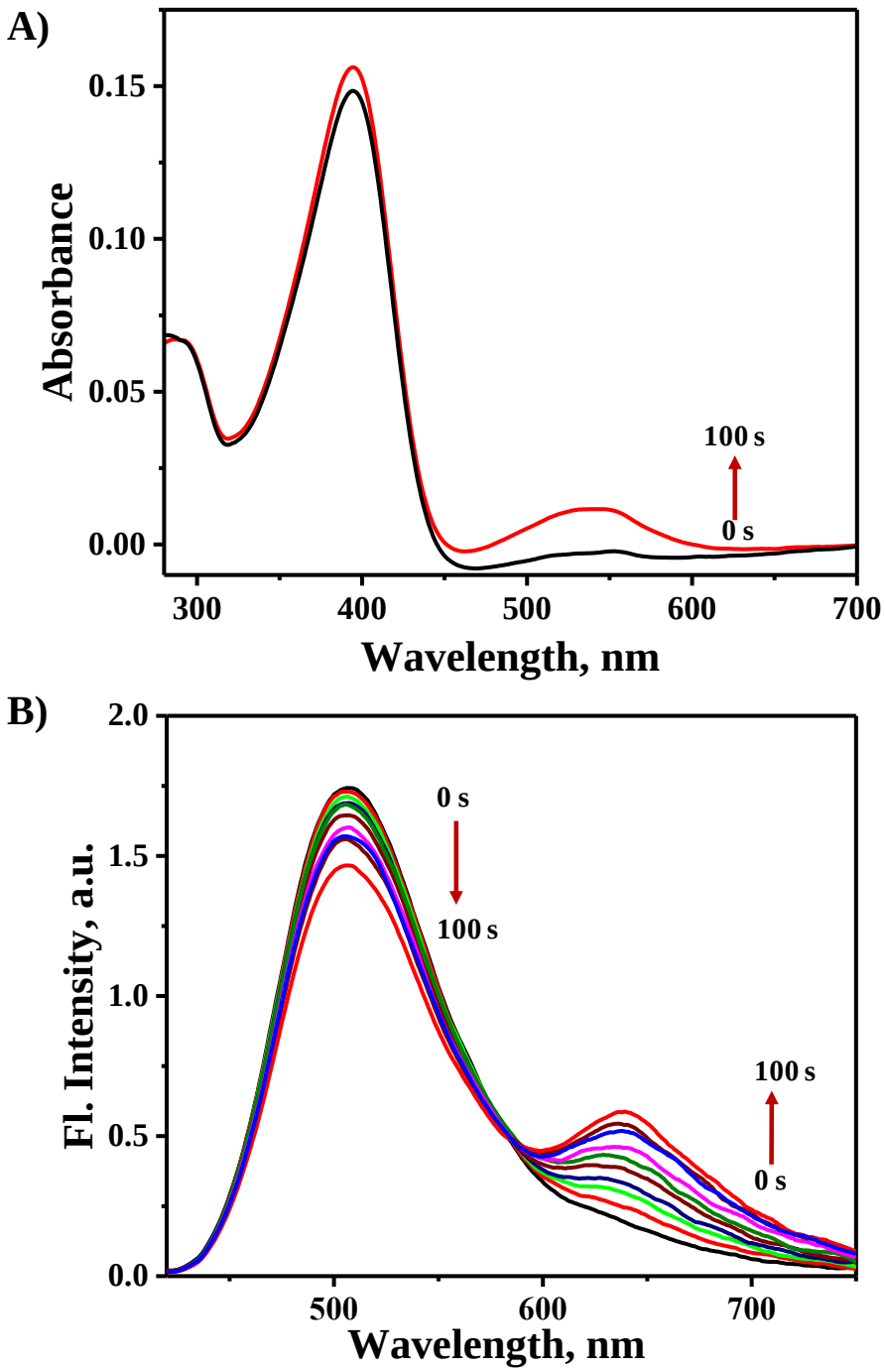

Figure 4.6. (A) Absorption and (B) fluorescence spectra of the probe **SPI-PYD** (10 μM) after the addition of NaOCl (200 μM), followed by UV lamp irradiation (0-100 s) in phosphate buffer (0.1 M, pH = 7.4), λ_{ex} = 395 nm.

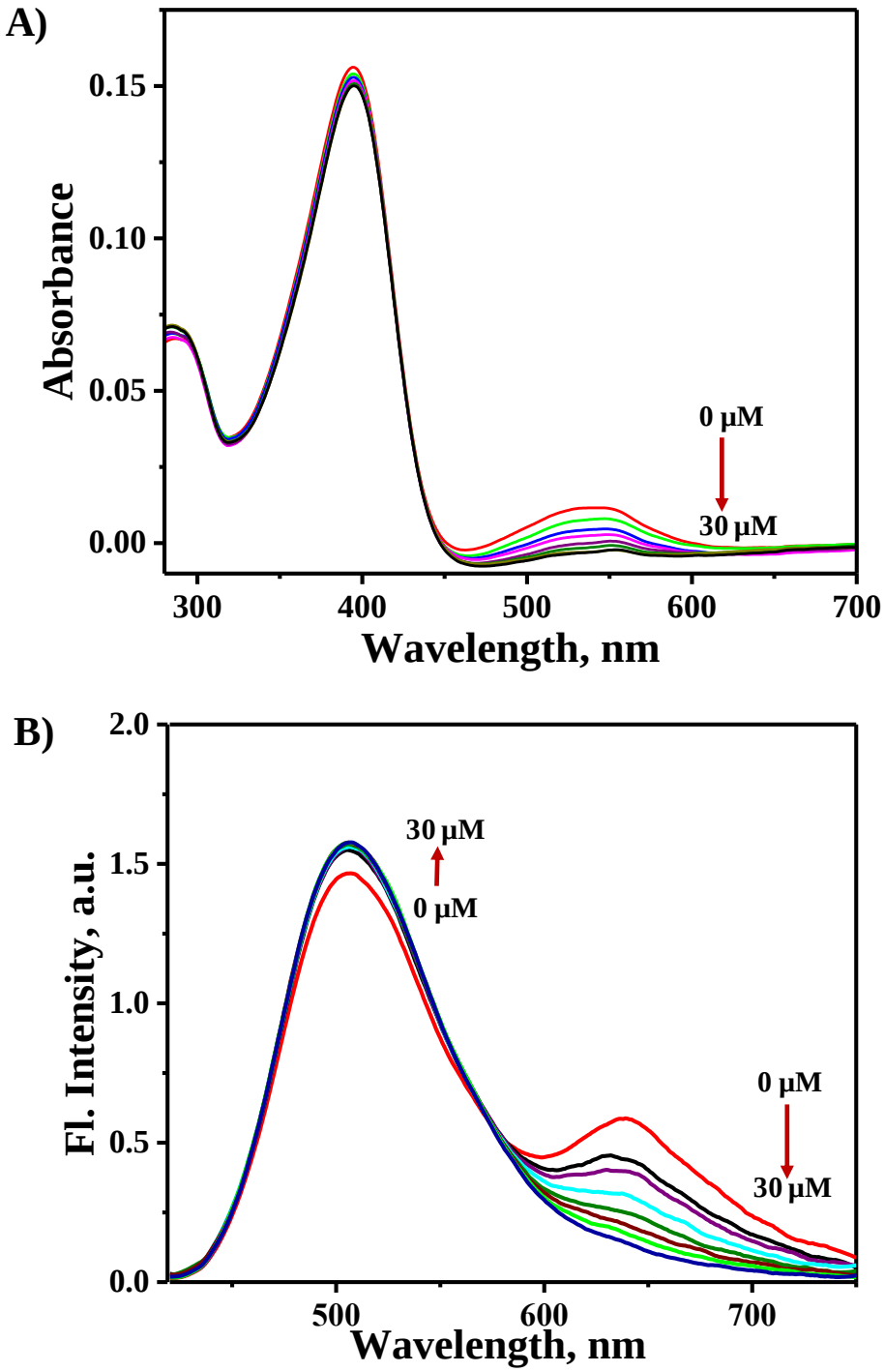

Figure 4.7. (A) Absorption and (B) fluorescence spectra of the UV irradiated probe **SPI-PYD** (10 µM) in presence of varying concentrations of Na_2SO_3 (0 - 30 µM) in phosphate buffer (0.1 M, pH = 7.4), λ_{ex} = 395 nm.

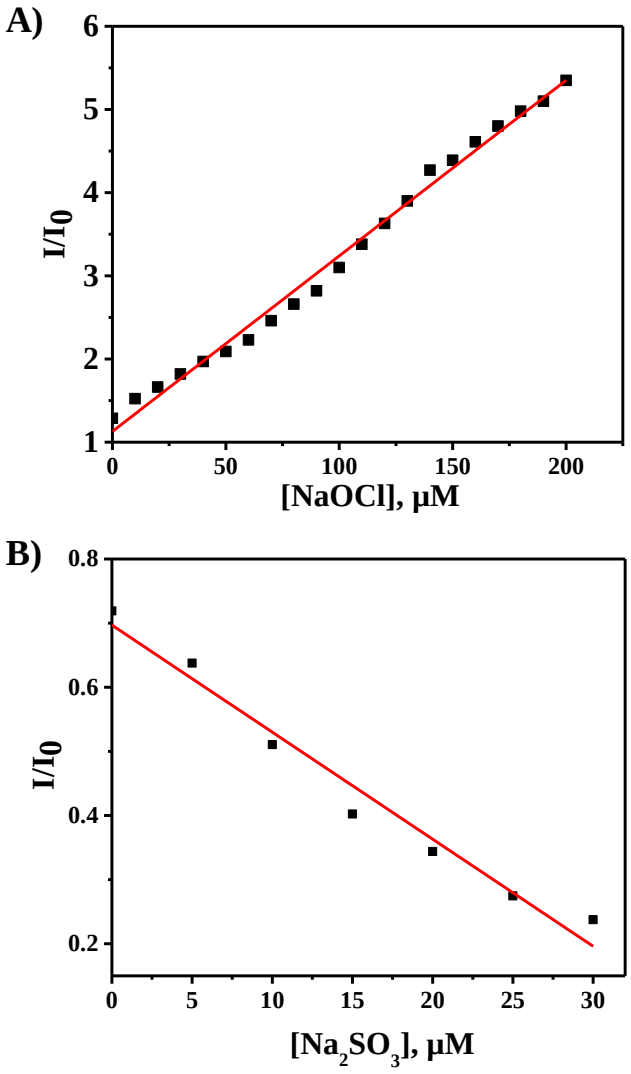

Figure 4.8. The linear curve obtained by the fluorescence intensity ratio of the probe **SPI-PYD** (10 µM) with (A) NaOCl (0-200 µM) and (B) Na_2SO_3 (0-30 µM).

4.3.3. Selectivity studies of SPI-PYD

In a cellular environment, various biologically important analytes can influence the fluorescence quantum yield of the probe. To assess the selectivity of **SPI-PYD** for HOCl and SO_2, its fluorescence response was evaluated in the presence of biologically relevant species, including thiols (Cys and GSH), metal ions (Na^+, K^+, Zn^{2+}, Cu^{2+}, etc.), and common biomolecules (F^-, Cl^-, AcO^-, NO_2^-, S^{2-}, CO_3^{2-}, etc.) **(Figure 4.9A and B)**. Both the probe and its UV activated form exhibited minimal fluorescence changes upon exposure to these biologically relevant species, highlighting its high selectivity and suitability for detecting HOCl and SO_2 levels in cells.

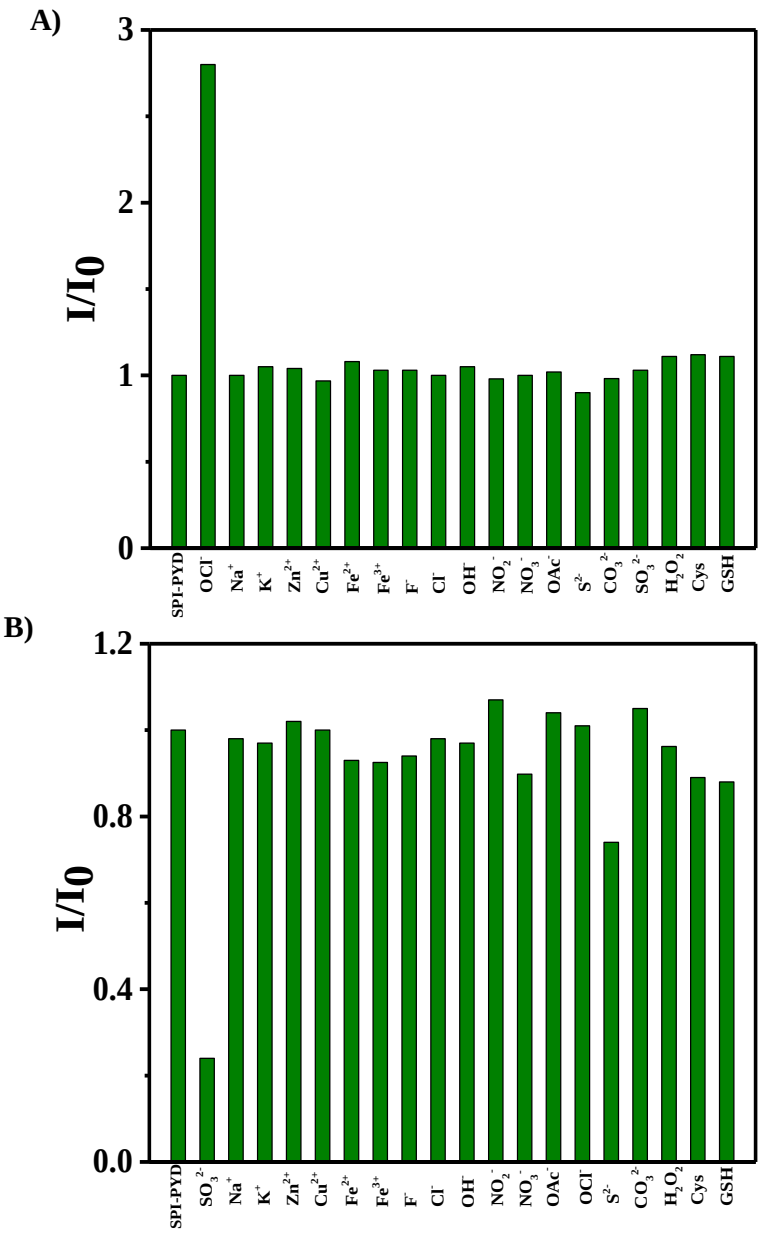

Figure 4.9. Fluorescence response of (A) **SPI-PYD** (10 μM) at 505 nm and (B) UV irradiated **SPI-PYD** at 640 nm, with various biologically relevant species (100 μM) in phosphate buffer (0.1 M, pH = 7.4).

4.3.4. Detection limit

The detection limit was calculated based on the fluorescence titration curve of **SPI-PYD** (1 μM) in the presence of NaOCl (0 to 6 μM) and UV activated **SPI-PYD** (1 μM) in the presence of Na_2SO_3 (0 - 0.3 μM). The fluorescence intensity of **SPI-PYD** and the standard deviation of the blank measurements were measured three times. The detection limit was calculated with the following equation,

Detection limit = 3σ/k Equation (4.1)

where, 'σ' is the standard deviation of the blank measurement, and 'k' is the slope between the fluorescence intensity and analyte concentrations. The detection limit of **SPI-PYD** for OCl^- was calculated to be 0.42 μM and that of UV-activated **SPI-PYD** for SO_3^{2-} was 0.08 μM **(Figure 4.10)**.

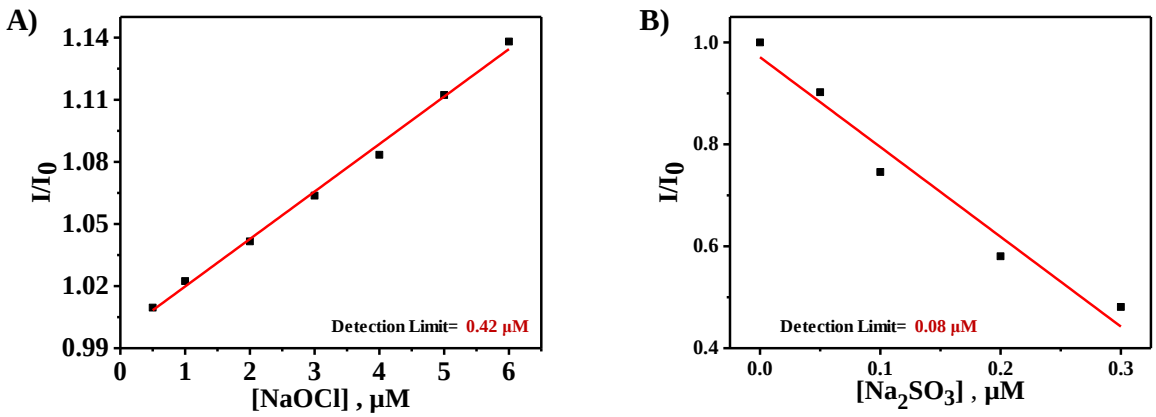

Figure 4.10. Fluorescence ratio (I/I_0) changes of **SPI-PYD** (10 μM) upon the titration of (A) NaOCl (0-6 μM) and (B) Na_2SO_3(0-0.3 μM) in phosphate buffer (0.1 M, pH = 7.4).

4.3.5. Quantum yield measurements

Quantum yield (QY) measurements of the probe **SPI-PYD** and its UV activated form before and after addition of the analytes, HOCl and SO_2 was carried out using the following equation,

$$\Phi_f^i = \frac{F^i f_s n_i^2}{F^s f_i n_s^2} \Phi_f^s \qquad \text{Equation (4.2)}$$

where, 'Φ^i_f' and 'Φ^s_f' are the photoluminescence QY of the sample and that of the standard, 'F^i' and 'F^s' are the integrated intensities (areas) of sample and standard emission spectra, 'f_i' and 'f_s' are the optical density of sample and standard at the excitation wavelength, 'n_i' and 'n_s' are the refractive indices of the sample and reference solution respectively.[27] Coumarin 153 and cresyl violet in ethanol were used as standard for **SPI-PYD** and its UV activated form respectively. The relative quantum yield of the probe increased from 2.4 - 6% in the presence

of HOCl (100 µM), while that of the UV-activated probe decreased from 3.6 - 1.3% in the presence of Na_2SO_3 (30 µM).

4.3.6. Temperature dependent fluorescence measurements

Since the probe is used under heat shock conditions, the effect of temperature (37 - 45 °C) on the fluorescence intensity of **SPI-PYD** was studied **(Figure 4.11)**. The results showed that the fluorescence intensity of the probe remained unchanged before and after irradiation, regardless of the temperature increase, confirming the probe's thermal robustness.

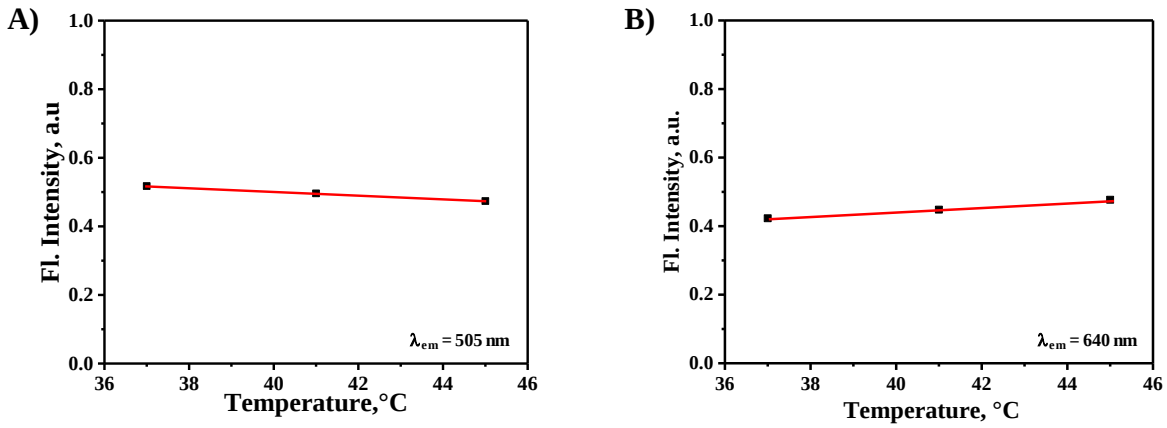

Figure 4.11. Fluorescence intensity changes under different temperatures, (A) **SPI-PYD**, λ_{em} = 505 nm and (B) **SPI-PYD** after UV irradiation, λ_{em} = 640 nm in phosphate buffer (0.1 M, pH = 7.4).

4.3.7. Aqueous solubility of SPI-PYD

Many organic fluorophores have poor aqueous solubility, which restricts their applicability in biological systems. Also, fluorophore aggregation can cause fluorescence quenching and uneven cellular distribution, leading to inconsistent signals and errors in cellular imaging data. The aqueous solubility of **SPI-PYD** was evaluated using concentration-dependent absorption spectra in 0.1 M phosphate buffer at pH 7.4 **(Figure 4.12)**. A gradual increase in absorbance confirmed good solubility, which can be attributed to the positively charged pyridinium moiety, making the probe well-suited for biological applications.

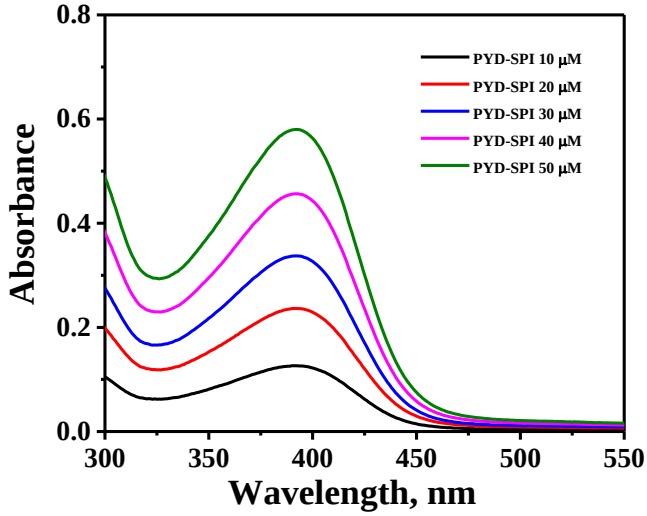

Figure 4.12. Absorption spectra of **SPI-PYD** at different concentrations (10-50 μM) in phosphate buffer (0.1 M, pH = 7.4)

4.3.8. Cytotoxicity of SPI-PYD

Cytotoxicity of the probe is a major concern in the development of cellular imaging probes, as it can adversely impact various bioassays.[28] To evaluate the cytotoxicity of **SPI-PYD**, MTT assay was performed on SK-BR-3 breast cancer cell lines at varying probe concentrations (1 - 50 μM). The probe exhibited minimal toxicity even at concentrations up to 50 μM, confirming its non-toxic nature under the experimental conditions **(Figure 4.13)**. We are using 10 μM concentration of **SPI-PYD** for bioimaging experiments.

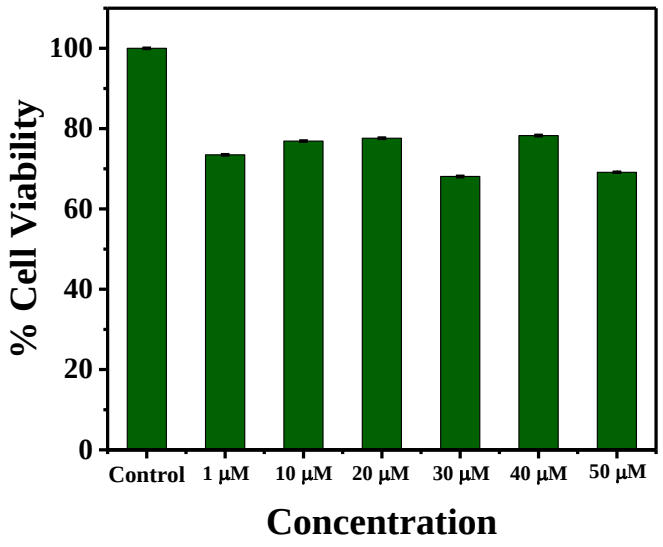

Figure 4.13. *In vitro* cytotoxicity profiling of **SPI-PYD** (1 μM - 50 μM) in SK-BR-3 cells using MTT assay.

4.3.9. Co-localization studies of SPI-PYD

Positively charged pyridinium dyes are known for their selective accumulation in mitochondria. To confirm the selective accumulation of **SPI-PYD** in mitochondria, we evaluated the co-localization ability of the probe within SK-BR-3 cells through confocal microscopy imaging, utilizing co-staining assays **(Figure 4.14 and 4.15)**. Cells pre-treated with NaOCl were subsequently co-stained with **SPI-PYD** (10 μM) along with Mito-tracker red (100 nM), Lyso-tracker red (100 nM), ER-tracker red (100 nM), and Hoechst 33342 (1 μM), a nucleus staining dye. The fluorescence of **SPI-PYD** from the green channel overlays well with that of Mito-tracker red, which was obtained from the red channel with a Pearson's Correlation Coefficient of ~0.85, indicating an excellent co-localization within the mitochondria. Further, **SPI-PYD** displayed relatively smaller co-localization with Lyso-tracker and ER-tracker and negligible co-localization with Hoechst 33342.

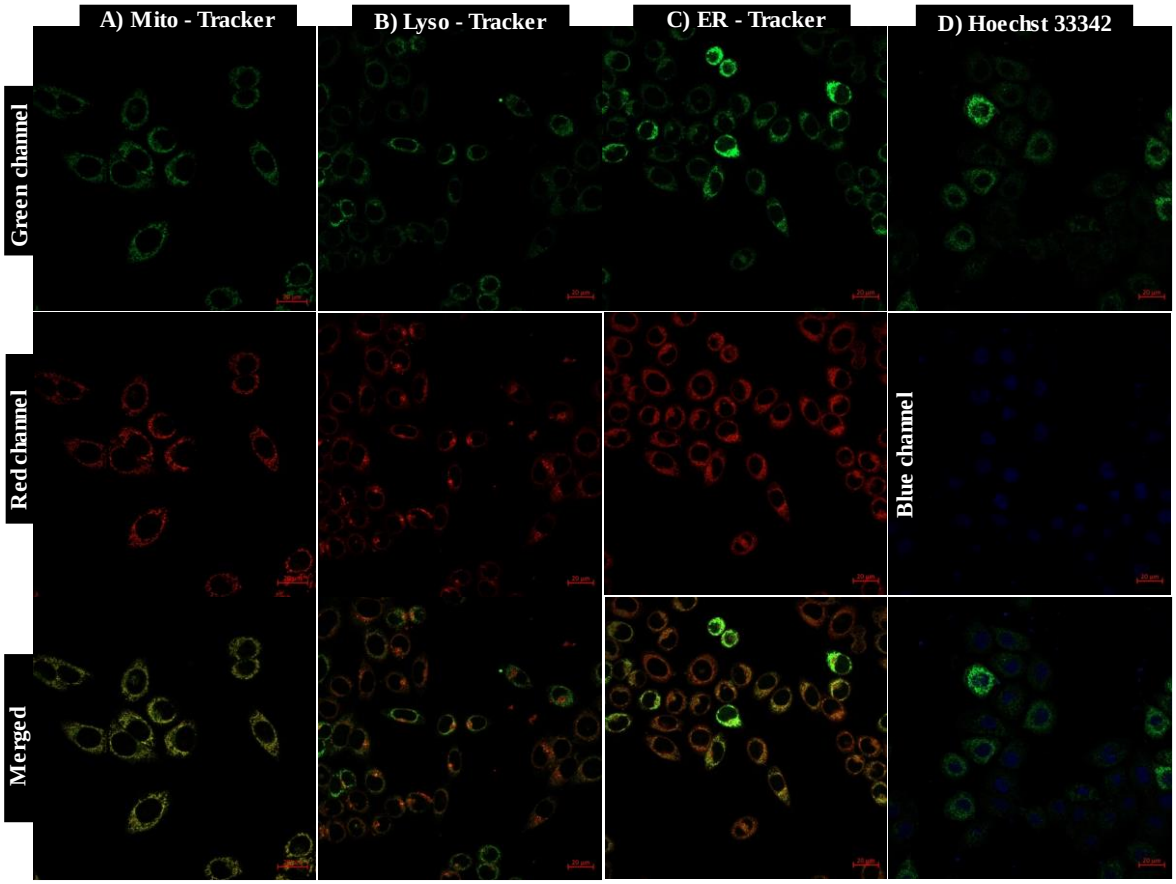

Figure 4.14. Confocal fluorescence microscopy images of intracellular localization of **SPI-PYD** (10 μM) in SK-BR-3 cells imaged after counter-staining with (A) Mito-tracker (100 nM);

(B) Lyso-tracker (100 nM); (C) ER-tracker (100 nM) and (D) Hoechst 33342 (1 μM). Scale bar is 20 μm.

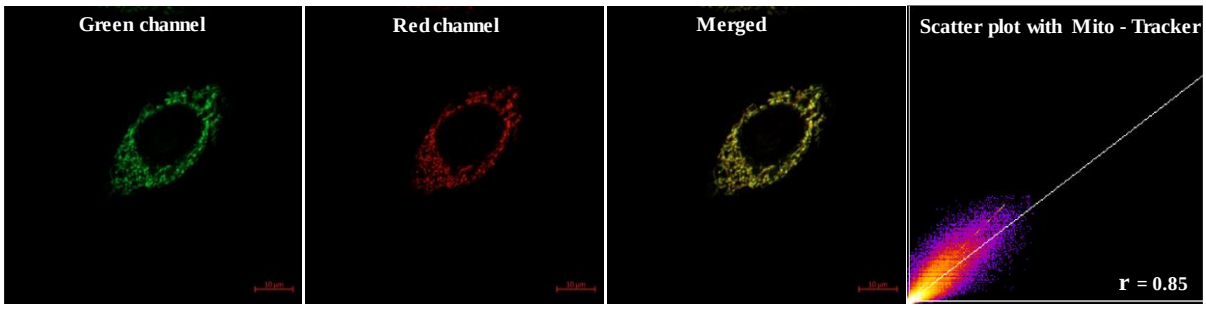

Figure 4.15. Single cell image of co-localization of **SPI-PYD** (10 μM) with Mito-tracker (100 nM) and the corresponding scatter plot. Scale bar is 10 μm.

4.3.10. Sensing studies of SPI-PYD

The sensing performance of **SPI-PYD** for detecting exogenous HOCl and SO_2 in living cells was evaluated in SK-BR-3 cells. Cells were first incubated with **SPI-PYD** (10 μM) for 15 minutes, followed by treatment with NaOCl (100 μM) for another 15 minutes. Fluorescence changes were then compared before and after the addition of NaOCl. As shown in **Figure 4.16A** and **4.16B**, cells treated with NaOCl displayed a considerable enhancement in emission intensity in the green channel, while control cells showed negligible fluorescence. These observations indicate the ability of the probe to detect elevated intracellular HOCl levels. Next, the cells were irradiated with blue laser (405 nm ± 10) for 2 minutes, leading to a strong fluorescence signal in the red channel and a corresponding decrease in the green channel **(Figure 4.16C)**, confirming the conversion of **SPI-PYD** to its merocyanine form. Subsequent treatment with Na_2SO_3 (100 μM) for 15 minutes resulted in a noticeable decrease in red channel fluorescence and a simultaneous increase in green channel fluorescence **(Figure 4.16D)**. These significant emission changes align with the isomerization of **SPI-PYD** to its MR form and its subsequent reaction with SO_2, confirming the probe's effectiveness for intracellular SO_2 detection.

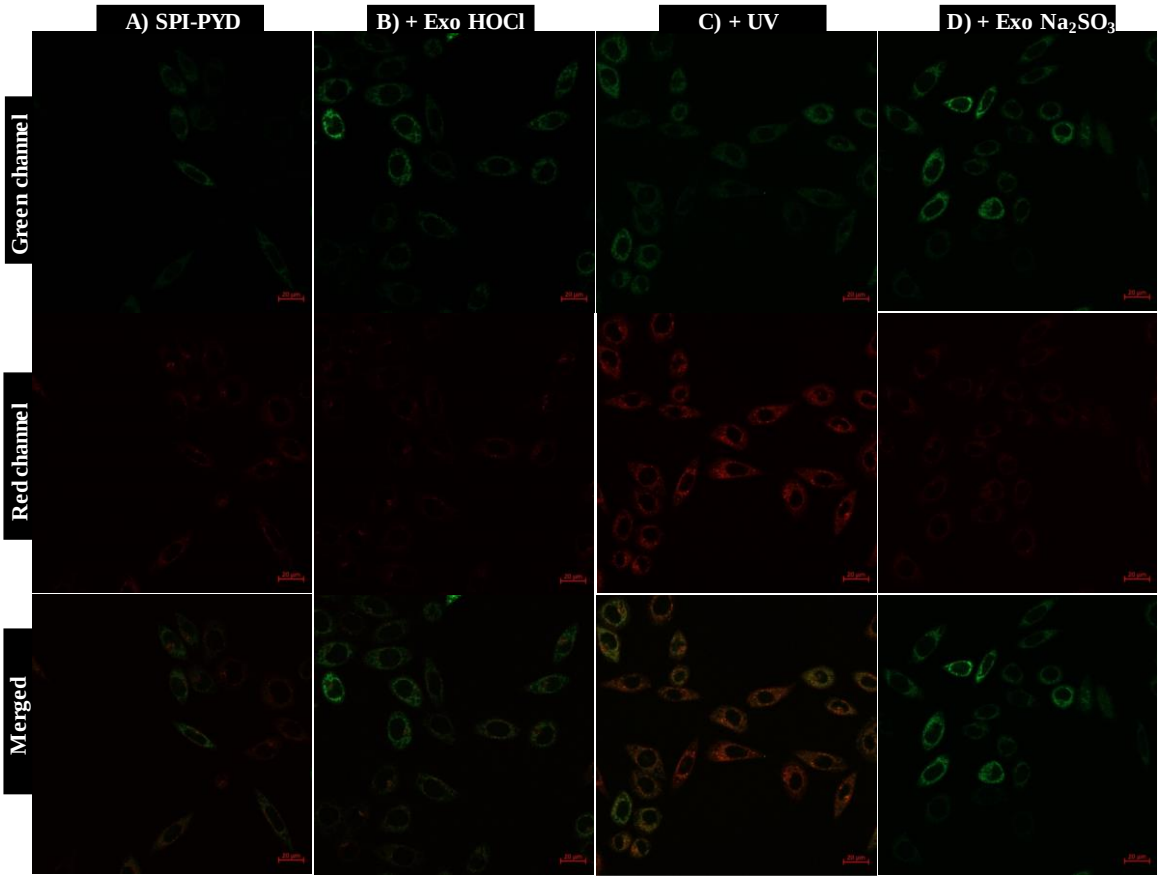

Figure 4.16. Confocal fluorescence microscopy images of SK-BR-3 cells incubated with (A) **SPI-PYD** (10 μM); (B) **SPI-PYD** (10 μM) with exogenous NaOCl (100 μM); (C) subsequent exposure to UV irradiation for 2 minutes and (D) further treatment with Na_2SO_3 (100 μM).

The oxidative and antioxidative properties of HOCl and SO_2, respectively, play crucial roles in regulating oxidative stress, a key factor in the progression of heat stroke.[29-33] HOCl acts as a strong oxidizing agent, contributing to cellular oxidative damage and signalling pathways associated with heat-induced stress. On the other hand, SO_2, with its reducing properties, functions as an antioxidant that counteracts oxidative stress by neutralizing reactive oxygen species (ROS) and other oxidants. Therefore, understanding the interplay between these two ions can provide valuable insights into how oxidative stress develops and resolves during heat stroke, potentially leading to new therapeutic strategies.

4.4. Conclusion

We developed a spiropyran-pyridinium conjugate, **SPI-PYD**, for the dual detection of HOCl and SO_2 ions in the cellular microenvironment. The pyridinium core, functionalized with a thiomethyl group, serves as a recognition site for HOCl, while the UV-activated open form of spiropyran detects SO_2. Initially, the probe exhibited a weak fluorescence in both the green and red channels. Upon exposure to HOCl, fluorescence intensity increased in the green channel due to the oxidation of the thiomethyl group. Subsequent UV irradiation triggered a remarkable fluorescence enhancement in the red channel, accompanied by a decrease in the green channel, attributed to the ring opening of spiropyran into merocyanine (MR). The MR form absorbing at ~550 nm, facilitates Förster Resonance Energy Transfer (FRET). Further exposure to SO_2 led to the disruption of the merocyanine double bond, causing a decrease in red channel fluorescence and a corresponding increase in green channel fluorescence. Additionally, **SPI-PYD** demonstrated excellent mitochondria-targeting ability, high aqueous solubility, strong selectivity, and low cytotoxicity. Bioimaging studies in SK-BR-3 breast cancer cells confirmed its intracellular ratiometric sensing capabilities for HOCl and SO_2. Since HOCl and SO_2 exhibit oxidative and antioxidative properties, respectively, both play crucial roles in heat stroke-induced oxidative stress. Therefore, the ability to dynamically monitor these two ions offers valuable insights into heat stroke pathophysiology and is potentially useful in developing future therapeutic strategies.

4.5. Experimental Section

4.5.1. Materials and methods

All the starting materials and reagents used in this work were purchased from commercial suppliers (Sigma Aldrich and TCI chemicals) and used as received without further purification. Moisture sensitive reactions were carried out under argon atmosphere in dried solvents purchased from Sigma-Aldrich and Merck chemical suppliers. Thin layer chromatography (TLC) analysis was performed using aluminum plates coated with silica gel purchased from Merck. Silica gel (100-200 mesh) was used for column chromatography. ^{1}H NMR (500 MHz) and ^{13}C NMR (125 MHz) analyses were achieved using a Bruker Avance DPX spectrometer, with TMS as the internal standard (δH = 0 ppm and δC = 0 ppm). High-resolution mass spectra (HRMS) were obtained from Thermo Scientific Q Exactive Hybrid Quadrupole-Orbitrap Electrospray Ionization Mass Spectrometer (ESI-MS). The UV-Vis absorption spectra were measured using a Shimadzu UV-vis spectrophotometer (UV-2600), and emission spectra were measured using a SPEX Fluorolog spectrofluorimeter. *In vitro* studies were performed using the SK-BR-3 breast cancer cell line (obtained from ATCC), and images were captured using a Zeiss LSM 980 confocal inverted microscope, equipped with Airyscan 2 detector, using 63x, 1.4 N.A. oil immersion objective under ambient conditions. 420, 488, and 568 nm lasers were used for imaging in the blue, green, and red channels, respectively.

4.5.2. *In vitro* studies

The MTT assay was conducted using the SK-BR-3 cell line, which was obtained from ATCC. The cells were plated in a 96-well plate at a density of 12,000 cells per well and incubated for 24 h in DMEM supplemented with 10% FBS. Subsequently, the cells were exposed to **SPI-PYD** at concentrations ranging from 1 - 50 μM for an additional 24 h. After incubation, MTT dissolved in DMEM (0.5 g/L) was added to each well and kept at 37°C in a

CO_2 incubator for 2- 4 h. DMSO (100 μL) was added to each well and the ability of the cells to reduce this substrate to the blue formazan product was determined colorimetrically (570 nm) after 20 min using a microplate reader. For mitochondrial co-localization studies, cells were first pretreated with NaOCl and then incubated with **SPI-PYD** (10 μM) for 20 minutes. For labeling of lysosomes, mitochondria, endoplasmic reticulum, and nuclei, SK-BR-3 cells were costained with Lyso-tracker red (100 nM) and Mito-tracker red (100 nM), ER-tracker red (100 nM), and Hoest 33342 (1 μM) respectively, and visualized using a confocal laser scanning microscope. To monitor the intracellular sensing ability of the probe towards exogenous HOCl and SO_2, SK-BR-3 cells were incubated with the probe, **SPI-PYD** (10 μM) for 15 minutes, followed by NaOCl (100 μM) treatment for another 15 minutes. The cells were then irradiated with a blue laser (405 nm ± 10) for 2 minutes, and subsequently treated with Na_2SO_3 (100 μM) for 15 minutes. The changes in fluorescence intensity in green and red channels were visualized using confocal microscopy.

4.5.3. Synthesis and characterization

Synthesis of compound-1: A solution of 1-tetralone (1 mL, 7.5 mmol) and 4-thiomethyl benzaldehyde (0.45 mL, 3.4 mmol) in a minimal amount of toluene was treated with acetic anhydride (0.35 mL) and refluxed at 120 °C for 2 h. Perchloric acid (0.25 mL) was then added, and the reaction was allowed to proceed under the same conditions for an additional 4 h. Upon completion, the toluene layer was decanted, and the resulting precipitate was collected and washed with diethyl ether. The product was purified by silica column chromatography using 3% methanol/chloroform as the eluent, yielding the desired compound (Yield: 79%).

^{1}H NMR ($CDCl_3$, 500 MHz) δ (ppm): 2.59 (s, 3H), 2.92 (t, J = 10 Hz, 4H), 3.06 (t, J = 10 Hz, 4H), 7.44 (d, J = 10Hz, 2H), 7.55 (d, J = 5Hz, 4H), 7.64 (t, J = 5Hz, 2H),7.75 (t, J = 5Hz, 2H), 8.41 (d, J = 10Hz, 2H).

^{13}CNMR ($CDCl_3$, 125 MHz): 24.6, 26.1, 126.1, 126.2, 126.6, 128.9, 129.5, 130.5, 135.6, 141.9.

HRMS calculated = 407.1464, found = 407.1467.

Synthesis of compound-2: A solution of compound 1 (1 g, 2.5 mmol) in a minimal amount of ethanol was treated dropwise with *N-Boc*-ethylenediamine (1 mL, 6 mmol). The reaction mixture was stirred at 90 °C for 4 h. Upon completion, ethanol was removed using a rotary evaporator, and the product was purified by silica column chromatography using chloroform as the eluent (Yield: 60%).

^{1}H NMR ($CDCl_3$, 500 MHz) δ (ppm): 1.23 (s, 9H), 2.32 (t, J = 10 Hz, 2H), 2.55 (s, 3H), 2.76 (d, J = 15 Hz, 2H), 2.93 (d, J = 15 Hz, 2H), 3.00 (s, 3H), 3.19 (t, J = 15 Hz, 2H), 3.48 (m, 2H), 5.58 (s, 2H), 6.92 (d, J = 5 Hz, 1H), 7.31 (d, J = 5 Hz, 1H), 7.40 (d, J = 5 Hz, 2H), 7.52 (m, 4H), 7.74 (d, J = 5 Hz, 1H), 8.00 (d, J = 10 Hz, 2H).

^{13}CNMR ($CDCl_3$, 125 MHz): 15.2, 26.7, 27.7, 28.4, 42.7, 42.8, 65.8, 127.8, 127.9, 128.5, 128.8, 129.0, 132.5, 138.0, 138.1, 140.8,142.1, 143.2, 153.2, 153.3.

HRMS calculated = 549.2570, found = 549.2594.

Synthesis of compound-3: A solution of compound 2 (0.8 g, 1.4 mmol) in chloroform was cooled in an ice bath, and trifluoroacetic acid (3 mL) was added dropwise. The reaction mixture was then stirred overnight at room temperature. Upon completion, the pH was adjusted to 8 using a NaOH solution, and the mixture was extracted with DCM. The organic layer was dried over Na_2SO_4, and the product was purified by precipitation using a DCM/ether system (Yield: 71%).

^{1}H NMR ($CDCl_3$, 500 MHz) δ (ppm): 0.88 (t, J = 5 Hz, 4H), 2.56 (s, 3H), 2.67 (t, J = 10 Hz, 4H), 2.83 (t, J = 10 Hz, 4H), 7.13 (d, J = 5 Hz, 2H), 7.20 (d, J = 5 Hz, 2H), 7.31 (t, J = 5 Hz, 2H), 7.39 (m, 4H), 8.57 (d, J = 10 Hz, 2H).

^{13}CNMR ($CDCl_3$, 125 MHz): 15.6, 25.8, 28.1, 40.9, 41.0, 125.3, 126.4, 127.0, 127.4, 128.6, 128.8, 129.2, 134.5, 135.3, 137.8, 138.1, 146.9, 150.1.

HRMS calculated = 449.2046, found = 449.2062.

Synthesis of compound-4: A mixture of 2,3,3-trimethyl-3H-indole (1.5 mL, 6 mmol) and 3-bromopropanoic acid (3 g, 3 eq.) was dissolved in dry acetonitrile and refluxed for 12 h. Upon completion, acetonitrile was removed under reduced pressure, yielding a dark purple residue. The residue was then washed three times with diethyl ether to remove any unreacted starting materials. Finally, the product was recrystallized from a DCM/acetone (1/5 v/v) mixture, giving a pale purple solid.

Synthesis of compound-5: A mixture of compound 4 (0.8 g, 3 mmol), 5-nitrosalicylaldehyde (0.5 g, 3 mmol), and trimethylamine (0.45 mL, 5 mmol) was refluxed in ethanol at 85 °C in the dark for 8 h. Upon completion, the reaction mixture was cooled to room temperature. The resulting precipitate was filtered and washed with cold ethanol, yielding the desired product. (Yield: 78%).

^{1}H NMR ($CDCl_3$, 500 MHz) δ (ppm): 1.18 (s, 3H), 1.29 (s, 3H), 2.62 (m, 2H), 3.53 (m, 1H), 3.68 (m, 1H), 6.09 (d, J = 10 Hz, 1 H), 6.74 (d, J = 10 Hz, 1 H), 6.86 (m, 2H), 7.18 (m, 3H), 8.06 (m, 1H), 8.15 (d, J = 5Hz, 1H).

^{13}CNMR ($CDCl_3$, 125 MHz): 19.1, 25.2, 32.9, 39.1, 52.7, 106.8, 106.9, 115.5, 119.2, 119.5, 121.7, 122.1, 122.7, 125.6, 127.7, 128.3, 136.1, 141.2, 146.6, 159.5, 172.3.

HRMS calculated = 380.1372, found = 381.4606

Synthesis of SPI-PYD: A mixture of compound 5, EDC, and NHS was dissolved in dry dichloromethane and stirred at room temperature for 10 minutes. Compound 3 was then added dropwise, and the reaction was allowed to proceed for 3 h. Upon completion, the mixture was

extracted with DCM, and the organic layer was dried over Na_2SO_4. The product was purified by alumina column chromatography using chloroform as the eluent (Yield: 20%).

^{1}H NMR ($CDCl_3$, 500 MHz) δ (ppm): 1.07 (s, 3H), 1.21 (s, 3H), 2.19 (t, J = 10 Hz, 2H), 2.27 (t, J = 10 Hz, 2H), 2.56 (s, 3H), 2.71 (t, J = 10 Hz, 2H), 2.90 (d, J = 15 Hz, 2H), 3.0 (m, 5H), 3.27 (t, J = 10Hz, 2H), 3.48 (m, 1H), 5.54 (m, 1H), 5.85 (d, J = 10 Hz, 1H), 6.47 (s, 1H), 6.51 (d, J = 5 Hz, 1H), 6.69 (d, J = 10 Hz, 1H), 6.85 (m, 3H), 7.02 (d, J = 5 Hz, 2H), 7.13 (t, J = 10 Hz, 1H), 7.30 (d, J = 5 Hz, 1H), 7.37 (m, 2H), 7.50 (s, 4H), 7.67 (d, J = 10Hz, 1H), 7.81 (s, 2H), 7.96 (m, 2H).

^{13}CNMR ($CDCl_3$, 125 MHz): 7.8, 9.4, 10.8, 13.7, 15.1, 15.3, 19.7, 25.8, 26.6, 27.6, 35.3, 39.8, 40.5, 41.2, 52.8, 62.9, 88.9, 106.7, 106.8, 115.4, 119.6, 121.7, 122.1, 122.7, 125.7, 127.8, 128.2, 128.4, 129,129.1,132.8, 156.7, 159.6, 172.1, 186.5, 188.4, 189, 204.

HRMS calculated = 811.3313, found = 811.3341.

4.5.4. Spectral data

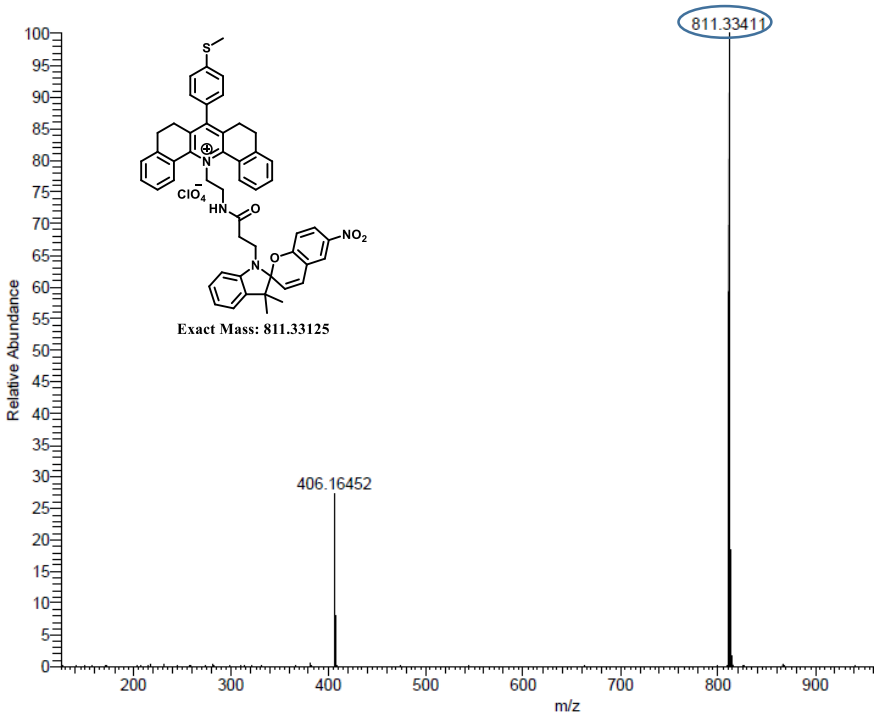

Figure 4.17. HRMS spectrum of **SPI-PYD**

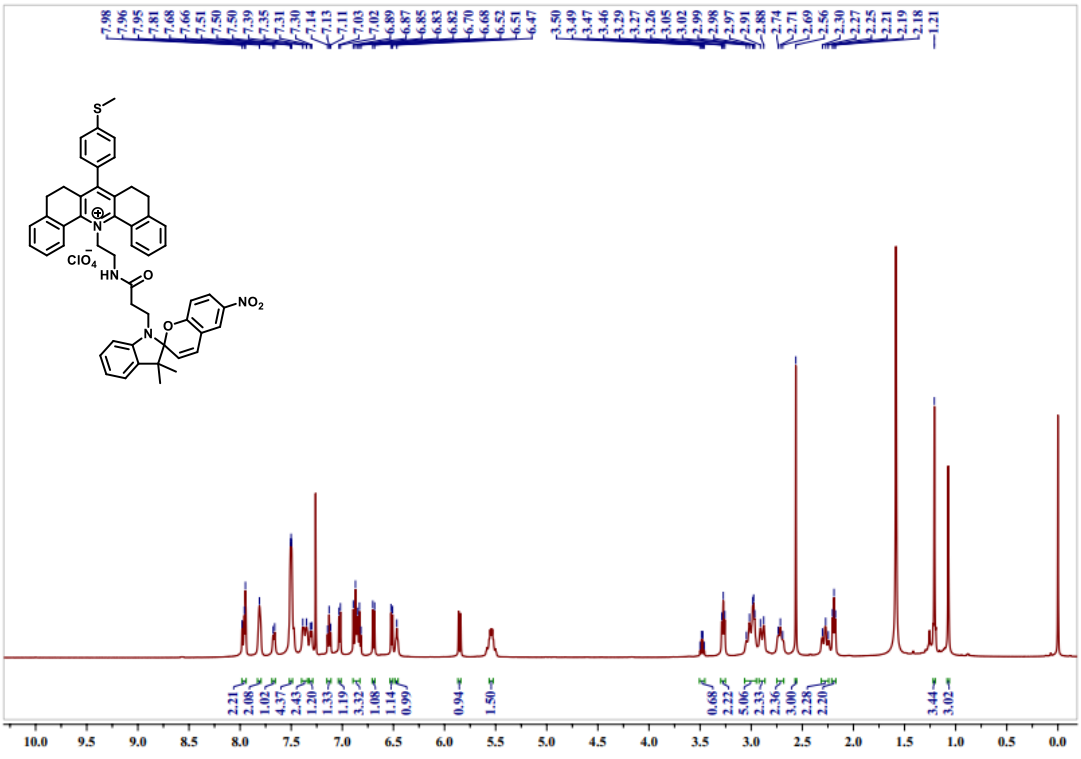

Figure 4.18. ^{1}H NMR spectrum of **SPI-PYD**.

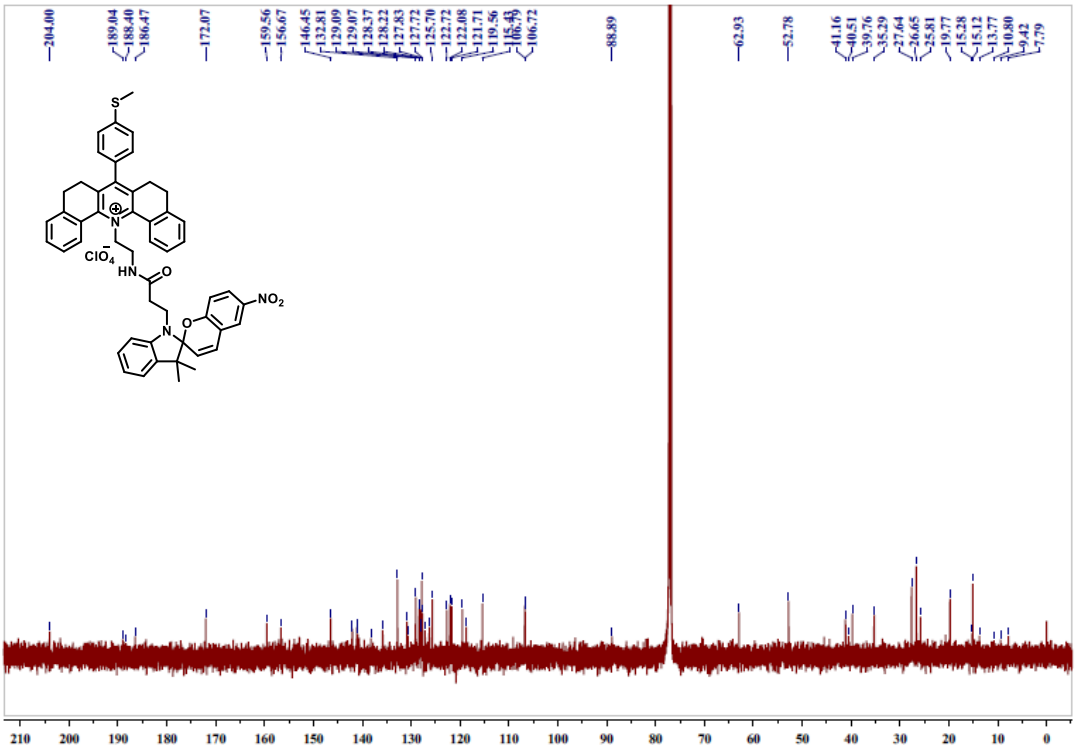

Figure 4.19. ^{13}C NMR spectrum of **SPI-PYD**.

4.6. References

(1) Yeo, T. P. Heat stroke: a comprehensive review. *AACN Advanced Critical Care* **2004**, *15*, 280-293.

(2) de Bont, J.; Nori-Sarma, A.; Stafoggia, M.; Banerjee, T.; Ingole, V.; Jaganathan, S.; Mandal, S.; Rajiva, A.; Krishna, B.; Kloog, I. Impact of heatwaves on all-cause mortality in India: A comprehensive multi-city study. *Environment international* **2024**, *184*, 108461.

(3) Hifumi, T.; Kondo, Y.; Shimizu, K.; Miyake, Y. Heat stroke. *Journal of intensive care* **2018**, *6*, 1-8.

(4) World Health, O.: Quantitative risk assessment of the effects of climate change on selected causes of death, 2030s and 2050s. In *Quantitative risk assessment of the effects of climate change on selected causes of death, 2030s and 2050s*, 2014.

(5) Hansen, J.; Sato, M.; Ruedy, R.; Lo, K.; Lea, D. W.; Medina-Elizade, M. Global temperature change. *Proceedings of the National Academy of Sciences* **2006**, *103*, 14288-14293.

(6) Bouchama, A.; Knochel, J. P. Heat stroke. *New England journal of medicine* **2002**, *346*, 1978-1988.

(7) Patz, J. A.; Campbell-Lendrum, D.; Holloway, T.; Foley, J. A. Impact of regional climate change on human health. *Nature* **2005**, *438*, 310-317.

(8) Argaud, L.; Ferry, T.; Le, Q.-H.; Marfisi, A.; Ciorba, D.; Achache, P.; Ducluzeau, R.; Robert, D. Short-and long-term outcomes of heatstroke following the 2003 heat wave in Lyon, France. *Archives of internal medicine* **2007**, *167*, 2177-2183.

(9) Shafie, H.; Wahab, M. A.; Masilamany, M.; Hassan, A. A. A. Exertional heat stroke: a lucky bunch of overly motivated policemen! *Hong Kong Journal of Emergency Medicine* **2007**, *14*, 37-44.

(10) Yin, J.; Huang, L.; Wu, L.; Li, J.; James, T. D.; Lin, W. Small molecule based fluorescent chemosensors for imaging the microenvironment within specific cellular regions. *Chemical Society Reviews* **2021**, *50*, 12098-12150.

(11) Chan, J.; Dodani, S. C.; Chang, C. J. Reaction-based small-molecule fluorescent probes for chemoselective bioimaging. *Nature chemistry* **2012**, *4*, 973-984.

(12) Mao, G.-J.; Liang, Z.-Z.; Gao, G.-Q.; Wang, Y.-Y.; Guo, X.-Y.; Su, L.; Zhang, H.; Ma, Q.-J.; Zhang, G. A photostable Si-rhodamine-based near-infrared fluorescent probe for monitoring lysosomal pH during heat stroke. *Analytica Chimica Acta* **2019**, *1092*, 117-125.

(13) Wen, Y.; Zhang, W.; Liu, T.; Huo, F.; Yin, C. Pinpoint diagnostic kit for heat stroke by monitoring lysosomal pH. *Analytical chemistry* **2017**, *89*, 11869-11874.

(14) Xia, Q.; Feng, S.; Hong, J.; Feng, G. Real-time tracking lysosomal pH changes under heatstroke and redox stress with a novel near-infrared emissive probe. *Talanta* **2021**, *228*, 122184.

(15) Wan, Q.; Chen, S.; Shi, W.; Li, L.; Ma, H. Lysosomal pH rise during heat shock monitored by a lysosome-targeting near-infrared ratiometric fluorescent probe. *Angewandte Chemie* **2014**, *126*, 11096-11100.

(16) Wu, L.; Wang, Y.; James, T. D.; Jia, N.; Huang, C. A hemicyanine based ratiometric fluorescence probe for mapping lysosomal pH during heat stroke in living cells. *Chemical Communications* **2018**, *54*, 5518-5521.

(17) Zhang, Y.; Wang, S.; Wang, X.; Zan, Q.; Yu, X.; Fan, L.; Dong, C. Monitoring of the decreased mitochondrial viscosity during heat stroke with a mitochondrial AIE probe. *Analytical and Bioanalytical Chemistry* **2021**, *413*, 3823-3831.

(18) Zhang, W.; Huo, F.; Yue, Y.; Zhang, Y.; Chao, J.; Cheng, F.; Yin, C. Heat stroke in cell tissues related to sulfur dioxide level is precisely monitored by light-controlled fluorescent probes. *Journal of the American Chemical Society* **2020**, *142*, 3262-3268.

(19) Li, S.; Yang, K.; Wang, P.; Liu, Y.; Cheng, D.; He, L. Monitoring heat stroke with a HClO-activatable near-infrared fluorescent probe. *Sensors and Actuators B: Chemical* **2023**, *385*, 133696.

(20) Cao, H.; Yu, F.; Dou, K.; Wang, R.; Xing, Y.; Luo, X.; Yu, F. Dual-Response Functionalized Mitochondrial Fluorescent Probe for a Double Whammy Monitoring of Hypochlorite and Sulfur Dioxide in Heat Shock via Time Scales. *Analytical Chemistry* **2024**, *96*, 18574-18583.

(21) Di Martino, M.; Sessa, L.; Diana, R.; Piotto, S.; Concilio, S. Recent progress in photoresponsive biomaterials. *Molecules* **2023**, *28*, 3712.

(22) He, X.; Xu, W.; Xu, C.; Ding, F.; Chen, H.; Shen, J. Reversible spiropyran-based chemosensor with pH-switches and application for bioimaging in living cells, Pseudomonas aeruginosa and zebrafish. *Dyes and Pigments* **2020**, *180*, 108497.

(23) Ho, F.-C.; Huang, K.-H.; Cheng, H.-W.; Huang, Y.-J.; Nhien, P. Q.; Wu, C.-H.; Wu, J. I.; Chen, S.-Y.; Lin, H.-C. FRET processes of bi-fluorophoric sensor material containing tetraphenylethylene donor and optical-switchable merocyanine acceptor for lead ion (Pb^{2+}) detection in semi-aqueous media. *Dyes and Pigments* **2021**, *189*, 109238.

(24) Zhang, W.; Huo, F.; Yin, C. Photocontrolled single-/dual-site alternative fluorescence probes distinguishing detection of H_2S/SO_2 in vivo. *Organic letters* **2019**, *21*, 5277-5280.

(25) Kalmar, B.; Greensmith, L. Induction of heat shock proteins for protection against oxidative stress. *Advanced drug delivery reviews* **2009**, *61*, 310-318.

(26) Belhadj Slimen, I.; Najar, T.; Ghram, A.; Dabbebi, H.; Ben Mrad, M.; Abdrabbah, M. Reactive oxygen species, heat stress and oxidative-induced mitochondrial damage. A review. *International journal of hyperthermia* **2014**, *30*, 513-523.

(27) Brouwer, A. M. Standards for photoluminescence quantum yield measurements in solution (IUPAC Technical Report). *Pure and Applied Chemistry* **2011**, *83*, 2213-2228.

(28) Tian, M.; Ma, Y.; Lin, W. Fluorescent probes for the visualization of cell viability. *Acc. Chem. Res.* **2019**, *52*, 2147-2157.

(29) Nagy, P.; Lemma, K.; Ashby, M. T. Reactive sulfur species: kinetics and mechanisms of the reaction of cysteine thiosulfinate ester with cysteine to give cysteine sulfenic acid. *The Journal of Organic Chemistry* **2007**, *72*, 8838-8846.

(30) Yap, Y. W.; Whiteman, M.; Cheung, N. S. Chlorinative stress: an under appreciated mediator of neurodegeneration? *Cellular signalling* **2007**, *19*, 219-228.

(31) Du, S. x.; Jin, H. f.; Bu, D. f.; Zhao, X.; Geng, B.; Tang, C. s.; Du, J. b. Endogenously generated sulfur dioxide and its vasorelaxant effect in rats 1. *Acta Pharmacologica Sinica* **2008**, *29*, 923-930.

(32) Zhang, W.; Huo, F.; Zhang, Y.; Chao, J.; Yin, C. Mitochondria-targeted NIR fluorescent probe for reversible imaging H_2O_2/SO_2 redox dynamics in vivo. *Sensors and Actuators B: Chemical* **2019**, *297*, 126747.

(33) Han, J.; Yang, S.; Wang, B.; Song, X. Tackling the selectivity dilemma of benzopyrylium–coumarin dyes in fluorescence sensing of HClO and SO_2. *Analytical Chemistry* **2021**, *93*, 5194-5200.

ABSTRACT

Name of the Student: **Ms. Anagha Thomas** Registration No.: 10CC19A39010
Faculty of Study: Chemical Sciences Year of Submission: 2025
AcSIR academic centre/CSIR Lab: CSIR-National Institute for Interdisciplinary Science and Technology (CSIR-NIIST)
Name of the Supervisor: Prof. A. Ajayaghosh
Name of the Co-supervisor: Dr. Joshy Joseph

Title of the thesis: **Design and development of small molecular fluorescent probes for monitoring cellular microenvironment**

Cells rely on a well-regulated microenvironment for normal function, and disruptions in factors such as pH, polarity, viscosity, temperature, and ion concentrations can signal disease development. For instance, cancer cells exhibit a more acidic environment than healthy cells, making pH a useful diagnostic and therapeutic target. Similarly, altered cellular viscosity is closely associated with diseases such as hypertension, diabetes, and Alzheimer's disease. Thus comprehensive characterization of fluctuations in the cellular microenvironment poses a significant challenge in the field of disease diagnostics and therapy. The design and development of new fluorescent probes with improved efficacy and selectivity is one viable alternative for achieving a better understanding of cellular homeostasis. In this thesis, we have chosen pyrylium and pyridinium as the central fluorescent cores and modified the scaffold for different bioimaging applications. **Chapter 1** provides an overview of small molecular fluorescent probes, highlighting the design principles and underlying mechanisms for sensing various analytes. It also delves into the detailed use of pyrylium and pyridinium chromophores as fluorescent cores in bioimaging applications.

In **Chapter 2A**, we have developed a new, pentacyclic pyridinium-based probe, **PYD-PA**, having a pendant *N*,*N*-di(pyridin-2-ylmethyl)amine (DPA) for Zn^{2+} detection in the cellular environment. The probe exhibited selective response to Zn^{2+} over other biologically relevant metal ions with excellent mitochondria targeting ability, moderate binding affinity, good photostability, aqueous solubility, pH insensitivity, and low cytotoxicity. Moreover, the probe was successfully applied for real-time monitoring of the fluctuation of intracellular free zinc ions during autophagy conditions. In **Chapter 2B**, we explored the differential binding properties of Zn^{2+} bound complex of PYD-PA, **PYD-PA-Zn^{2+}** towards nucleotides and DNA. The probe displayed a significant enhancement in both fluorescence intensity and lifetime upon binding to ctDNA and dsDNA over ssDNA, enabling the differential analysis of dsDNA, ssDNA, ADP, and ATP.

Chapter 3 focuses on the synthesis of a series of styryl-pyrylium derivatives and the investigation of a hydroxyl-functionalized analogue, **OH-MPYR**, as a potential viscosity sensor. The probe exhibited highly selective response to viscosity changes, excellent lysosome targeting ability, good water solubility, photostability, and low cytotoxicity, making it well-suited for monitoring intracellular viscosity in living cells. In **Chapter 4**, we developed a spiropyran-pyridinium conjugate, **SPI-PYD**, for the dual sensing of heat shock signalling molecules, HOCl and SO_2, in the cellular microenvironment. Bioimaging in SK-BR-3 cells revealed a ratiometric fluorescence response of the probe in the green and red channels to HOCl and SO_2, with efficient mitochondrial co-localization.

List of Publications Emanating from the Thesis

1. **Anagha Thomas**, Anaga Nair, Sandip Chakraborty, Roopasree O. Jayarajan, Joshy Joseph*, and Ayyappanpillai Ajayaghosh*, A Pyridinium fluorophore for the detection of zinc ions under autophagy conditions, *Journal of Photochemistry & Photobiology, B: Biology* 259 (2024) 113006. https://doi.org/10.1016/j.jphotobiol.2024.113006
2. **Anagha Thomas**, Sandip Chakraborty, Joshy Joseph* and Ayyappanpillai Ajayaghosh*, Differential binding interactions of a pyridinium dye integrated dipicolylamine-Zn^{2+} complex with nucleotides and nucleic acids *(Manuscript completed and to be submitted).*
3. **Anagha Thomas**, Sandip Chakraborty, Ritika Raghuvanshi, Sarit S. Agasti, Joshy Joseph* and Ayyappanpillai Ajayaghosh*, Design and development of viscosity-sensitive, pyrylium fluorophores for monitoring cellular microenvironment *(Manuscript completed and to be submitted).*
4. **Anagha Thomas**, Sandip Chakraborty, Roopasree O. Jayarajan, Joshy Joseph*, and Ayyappanpillai Ajayaghosh*, A light-activated pyridinium-spiropyran conjugate for monitoring cellular HOCl and SO_2 *(Manuscript under preparation).*

List of Publications Not Related to the Thesis

1. Sandip Chakraborty, Anivind Kaur Bindra, **Anagha Thomas**, Yanli Zhao* and Ayyappanpillai Ajayaghosh *. pH-Assisted multichannel heat shock monitoring in the endoplasmic reticulum with a pyridinium fluorophore. *Chem. Sci.*, 2024, 15, 10851-10857

List of Papers/Posters Presented in Conferences

1. *Development of a new pyrylium probe for pH monitoring during apoptosis*. **Anagha Thomas**, Sandip Chakraborty, Manu M. Joseph, Sunil Varughese, Samrat Ghosh, Kaustabh K. Maiti, Animesh Samanta and Ayyappanpillai Ajayaghosh; Indian Analytical Science Congress IASC 2022, Munnar, Kerala, March 10-12, 2022. (Poster presentation)

2. *Development of a new pyridinium probe for detection of zinc ions and monitoring autophagy.* **Anagha Thomas**, Anaga Nair, Sandip Chakraborty, Jayamurthy P., Joshy Joseph and Ayyappanpillai Ajayaghosh; National symposium on Radiation and Photochemistry, Organised by ISRAPS at BITS Pilani, Goa Campus, January 5-7, 2023. (Poster presentation)

3. *Development of a new pyridinium probe for monitoring autophagy through zinc ion detection.* **Anagha Thomas**, Anaga Nair, Sandip Chakraborty, Jayamurthy P., Joshy Joseph and Ayyappanpillai Ajayaghosh. Indian Analytical Science Congress 2023, Organised by ISAS, Kochi, Kerala, March 23-25, 2023. (Poster presentation)

4. *Design and development of pyrylium based fluorescent probes for monitoring cellular microenvironment.* **Anagha Thomas**, Ritika Raghuvanshi, Sandip Chakraborty, Sarit S. Agasti, Joshy Joseph and Ayyappanpillai Ajayaghosh. International Winter School and Recent Advances in Materials (RAM-90), Organised by JNCASR-Bengaluru, December 04-09, 2023. (Poster presentation)

5. *Development of a new pyridinium probe for the detection of zinc ions under autophagy conditions.* **AnaghaThomas**, Sandip Chakraborty, Anaga Nair, Roopasree O Jayarajan, Joshy Joseph and Ayyappanpillai Ajayaghosh; International Seminar on Advances in Applied and Chemical Science (AACS 2024), Organised by St. Paul's College, Kalamassery, October 24-25, 2024. (Oral presentation)

Abstracts for Conference Presentations

1. *Indian Analytical Science Congress IASC 2022, Munnar, Kerala, March 10-12, 2022.*

Development of a New Pyrylium Probe for pH Monitoring During Apoptosis

Anagha Thomas, Sandip Chakraborty, Manu M. Joseph, Sunil Varughese, Samrat Ghosh, Kaustabh K. Maiti, Animesh Samanta and Ayyappanpillai Ajayaghosh*

Photosciences and Photonics Section, Chemical Sciences and Technology Division, CSIR-National Institute for Interdisciplinary Science and Technology (CSIR-NIIST), Thiruvananthapuram 695 019, Kerala & Academy of Scientific and Innovative Research (AcSIR), Ghaziabad 201002, India
E-mail:ajayaghosh62@gmail.com, anaghathomas95@gmail.com

Development of molecular probes for imaging various analytes in biological tissues and cells has high importance in the modern disease diagnostics, therapy monitoring and patient management.Owing to the significant roles of pH in many physiological processes within intracellular organelles, enormous efforts have been made for the development of new pH imaging chemical probes with improved optical properties [1]. Accurate measurement of pH imbalance in cells is of paramount importance in clinical analysis and disease diagnostics. For example, the imbalance of pH in cancerous cells during apoptosis caused by chemotherapy needs to be monitored in real time for post treatment wellness of patients. Similarly, variations of the cytosolic pH are closely associated with cell migration, cellular proliferation and apoptosis. Herein, we report a new, rigid pentacyclic pyrylium based probe, **PS-OMe**, which was synthesized by a modified Vilsmeier-Haack reaction in single step [2]. Yield and reaction time of the product formation was improved significantly by mechanistic understanding of the reaction. **PS-OMe** upon demethylation resulted in a fluorescent "Turn ON" pH sensor, **PS-OH** which showed a sharp fluorescence change during minute cellular acidification. **PS-OH** exhibited excellent photophysical properties and is capable of monitoring and quantifying intracellular dynamic pH change during apoptosis, details of which are presented in this poster. This water soluble, pyrylium probe with its favourable photophysical properties and Turn ON fluorescence behaviour at lower pH conditions, could be a potential candidate for drug discovery, screening, and dose determination in anticancer therapeutic techniques.

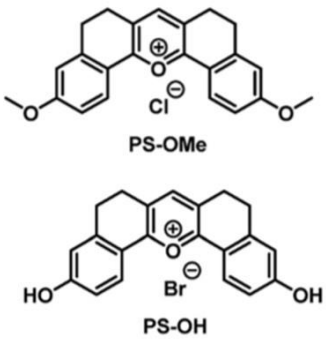

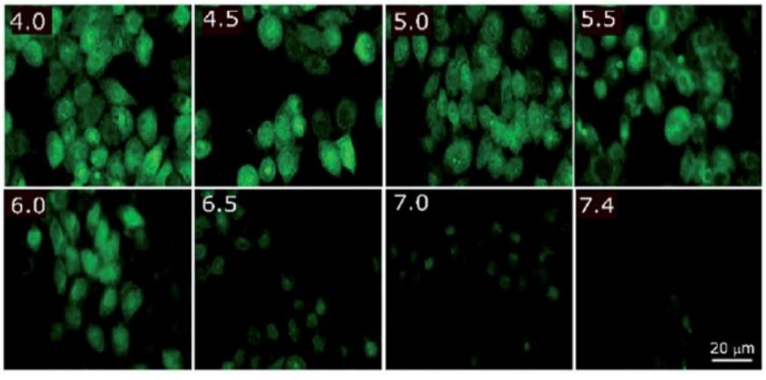

References

1. Hou, J.-T.; Ren, W. X.; Li, K.; Seo, J.; Sharma, A.; Yu, X.-Q.; Kim, J. S., *Chem. Soc. Rev.***2017,***46* (8), 2076-2090.
2. Chakraborty, S.; Joseph, M. M.; Varughese, S.; Ghosh, S.; Maiti, K. K.; Samanta, A.; Ajayaghosh, A., *Chem. Sci.***2020,***11* (47), 12695-12700.

2. *National symposium on Radiation and Photochemistry, Organised by ISRAPS at BITS Pilani, Goa Campus, January 5-7, 2023.*

Development of a New Pyridinium Probe for the Detection of Zinc Ions and Monitoring Autophagy

AnaghaThomas, Sandip Chakraborty, Anaga Nair, Jayamurthy P, Joshy Joseph and Ayyappanpillai Ajayaghosh*

[a]*Photosciences and Photonics Section, Chemical Sciences and Technology Division, CSIR-National Institute for Interdisciplinary Science and Technology (CSIR-NIIST), Thiruvananthapuram 695 019, Kerala*
[b]*Academy of Scientific and Innovative Research (AcSIR), Ghaziabad 201002, India*
anaghathomas95@gmail.com

Development of molecular probes for imaging various analytes in biological tissues and cells has high importance in the modern disease diagnostics, therapy monitoring and patient management. Zinc is one of the most abundant transition metals present in human body and evidence suggest that it plays crucial role in autophagy process. Herein, we report a new, rigid pentacyclic pyridinium based probe, **PYD-PA** having a pendant *N*,*N*-di(pyridin-2-ylmethyl)amine (DPA) for Zn^{2+} ion detection in cellular environment. The pyridinium moiety itself serves as mitochondria targeting unit and DPA act as the coordination site for Zn^{2+}.The probe exhibited highly selective response to Zn^{2+} over other biological metal ions, good water solubility, photostability, pH insensitivity, and low cytotoxicity. The demonstration of bioimaging in L6 cell lines of rat confirmed intracellular Zn sensing ability of the probe. Furthermore, the probe was successfully applied for sensitively monitoring the fluctuation of intracellular free zinc ions in real time during autophagy condition.

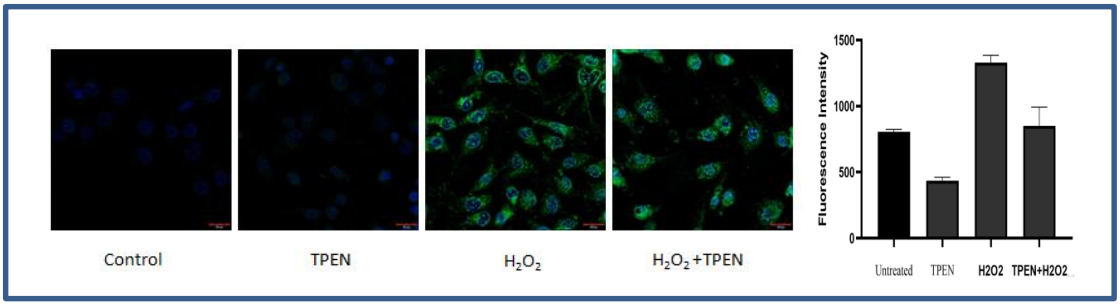

Figure 1. Imaging of Zn^{2+} using intracellular Zn^{2+} generators and chelators in L6 cells.

References

1. Sudheesh, K.V., et al., *Chemistryselect*, **2018**. 3(8): p. 2416-2422.

2. Chakraborty, S.; Joseph, M. M.; Varughese, S.; Ghosh, S.; Maiti, K. K.; Samanta, A.; Ajayaghosh, A., *Chem. Sci*.**2020,** 11 (47), 12695-12700.

3. *Indian Analytical Science Congress 2023, Organised by ISAS, Kochi, Kerala, March 23-25, 2023.*

Development of a New Pyridinium Probe for the Detection of Zinc Ions under Autophagy Conditions

AnaghaThomas, Sandip Chakraborty, Anaga Nair, Roopasree O Jayarajan,

Joshy Joseph* and Ayyappanpillai Ajayaghosh*

[a]Photosciences and Photonics Section, Chemical Sciences and Technology Division, CSIR-National Institute for Interdisciplinary Science and Technology (CSIR-NIIST), Thiruvananthapuram 695 019, Kerala

[b]Academy of Scientific and Innovative Research (AcSIR), Ghaziabad 201002, India

anaghathomas95@gmail.com

Development of molecular probes for imaging various analytes in biological tissues and cells has high importance in the modern disease diagnostics, therapy monitoring and patient management. Zinc is one of the most abundant transition metals present in human body and evidence suggest that it plays crucial role in autophagy process. Herein, we report a new, rigid pentacyclic pyridinium based probe, **PYD-PA** having a pendant *N*,*N*-di(pyridin-2-ylmethyl)amine (DPA) for Zn^{2+} ion detection in cellular environment. The pyridinium moiety itself serves as mitochondria targeting unit and DPA act as the coordination site for Zn^{2+}.The probe exhibited highly selective response to Zn^{2+} over other biological metal ions, good water solubility, moderate binding affinity, photostability, pH insensitivity, and low cytotoxicity. Further, the demonstration of bio imaging in SK-BR-3 breast cancer cell lines confirmed the intracellular zinc ion sensing ability of the probe during autophagy conditions.

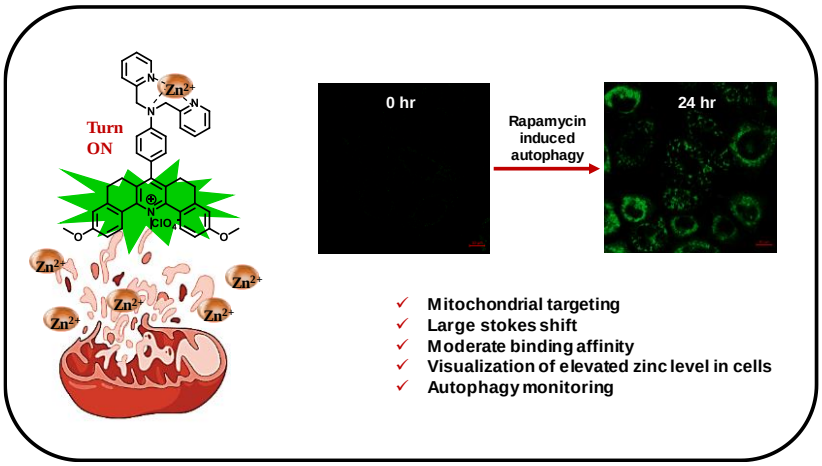

References

1. Sudheesh, K.V., et al., *Chemistryselect*, **2018**. 3(8): p. 2416-2422.

2. Chakraborty, S.; Joseph, M. M.; Varughese, S.; Ghosh, S.; Maiti, K. K.; Samanta, A.; Ajayaghosh, A., *Chem. Sci*., **2020,** 11 (47), 12695-12700.

4. International winter school and Recent Advances in Materials (RAM-90), Organised by JNCASR-Bengaluru, December 04-09, 2023.

Design and Development of Pyrylium Based Fluorescent Probes for Monitoring Cellular Microenvironment

Anagha Thomas*, Ritika Raghuvanshi, Sandip Chakraborty, Sarit S. Agasti, Joshy Joseph and Ayyappanpillai Ajayaghosh

Chemical Sciences and Technology Division, CSIR-National Institute for Interdisciplinary Science and Technology (CSIR-NIIST), Thiruvananthapuram 695 019, Kerala

Academy of Scientific and Innovative Research (AcSIR), Ghaziabad 201002, India

New Chemistry Unit, Chemistry & Physics of Materials Unit, and School of Advanced Materials (SAMat), Jawaharlal Nehru Centre for Advanced Scientific Research (JNCASR), Bangalore, Karnataka 560064, India

Email: anaghathomas95@gmail.com

Viscosity is a fundamental physical parameter that influences intracellular micro-environment when cells go through pathogenic changes. In recent years, molecular rotors are considered as suitable probes for imaging viscosity in living cells via fluorescence intensity and/or lifetime based responses. Herein, we report a series of new styryl pyrylium derivatives which could be used as "Turn ON" fluorescence probes for monitoring cellular microenvironment. Among these, styryl-pyrylium with hydroxyl functionality (**OH-PYR**) displayed a significant enhancement in fluorescence with increase in viscosity indicating the potential of this derivative for monitoring intracellular viscosity. The probe exhibited highly selective response to viscosity changes, good water solubility, photostability, pH insensitivity and low cytotoxicity. The demonstration of bioimaging in HeLa cell lines confirmed lysosome targeting ability of the probe. Furthermore, the enhancement in fluorescence intensity of the probe in HeLa cells upon treatment with nystatin confirmed its ability to monitor the fluctuation of intracellular viscosity in real time.

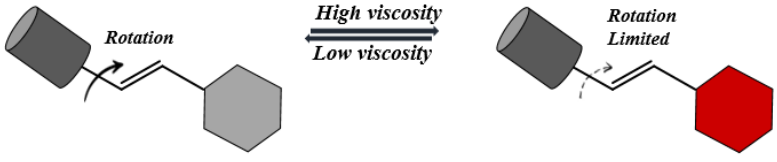

References

1. Zhang, Yuying, et al.; *Analytical chemistry*, **2019**, *91(15)*,10302-10309.
2. Resta IM, Lucantoni F, Apostolova N, Galindo F; *Organic & Biomolecular Chemistry*, **2021**,*19(41)*, 9043-57.
3. Ma, C., Sun, W., Xu, L., Qian, Y., Dai, J., Zhong, G., Hou, Y., Liu, J. and Shen, B; *Journal of Materials Chemistry B*, **2020**, *8(42)*,9642-9651.

5. International Seminar on Advances in Applied and Chemical Science (AACS 2024), Organised by St. Paul's College, Kalamassery, October 24-25, 2024.

Development of a New Pyridinium Probe for the Detection of Zinc Ions Under Autophagy Conditions

AnaghaThomas, Sandip Chakraborty, Anaga Nair, Roopasree O Jayarajan,

Joshy Joseph* and Ayyappanpillai Ajayaghosh*

[a]Photosciences and Photonics Section, Chemical Sciences and Technology Division, CSIR-National Institute for Interdisciplinary Science and Technology (CSIR-NIIST), Thiruvananthapuram 695 019, Kerala

[b]Academy of Scientific and Innovative Research (AcSIR), Ghaziabad 201002, India

anaghathomas95@gmail.com

Development of molecular probes for imaging various analytes in biological tissues and cells has high importance in the modern disease diagnostics, therapy monitoring and patient management. Zinc is one of the most abundant transition metals present in human body and evidence suggest that it plays crucial role in autophagy process. Herein, we report a new, rigid pentacyclic pyridinium based probe, **PYD-PA** having a pendant N,N-di(pyridin-2-ylmethyl)amine (DPA) for Zn^{2+} ion detection in cellular environment. The pyridinium moiety itself serves as mitochondria targeting unit and DPA act as the coordination site for Zn^{2+}.The probe exhibited highly selective response to Zn^{2+} over other biological metal ions, good water solubility, moderate binding affinity, photostability, pH insensitivity, and low cytotoxicity. Further, the demonstration of bio imaging in SK-BR-3 breast cancer cell lines confirmed the intracellular zinc ion sensing ability of the probe during autophagy conditions.

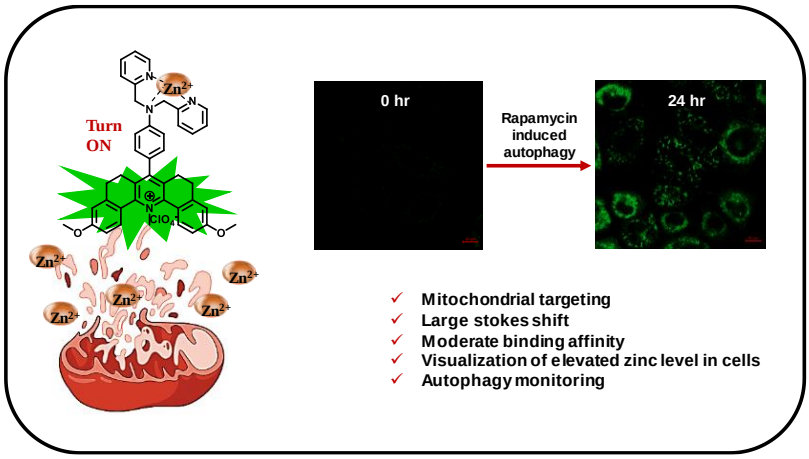

References

1. Sudheesh, K.V., et al., *Chemistryselect*, **2018**. 3(8): p. 2416-2422.

2. Chakraborty, S.; Joseph, M. M.; Varughese, S.; Ghosh, S.; Maiti, K. K.; Samanta, A.; Ajayaghosh, A., *Chem. Sci*., **2020,** 11 (47), 12695-12700.

Journal of Photochemistry & Photobiology, B: Biology 259 (2024) 113006

Contents lists available at ScienceDirect

Journal of Photochemistry & Photobiology, B: Biology

journal homepage: www.elsevier.com/locate/jphotobiol

A Pyridinium fluorophore for the detection of zinc ions under autophagy conditions

Anagha Thomas [a,b], Anaga Nair [a,b], Sandip Chakraborty [a,b], Roopasree O. Jayarajan [a,b], Joshy Joseph [a,b,*], Ayyappanpillai Ajayaghosh [a,b,1,*]

[a] Photosciences and Photonics Section, Chemical Sciences and Technology Division, CSIR-National Institute for Interdisciplinary Science and Technology, Thiruvananthapuram 695 019, India

[b] Academy of Scientific and Innovative Research (AcSIR), Ghaziabad 201002, India

ARTICLE INFO

Keywords:
Molecular probes
Cellular imaging
Zn^{2+} sensor
Pyridinium dye
Autophagy
Mitochondria targeting

ABSTRACT

Molecular probes for sensing and imaging of various analytes and biological specimens are of great importance in clinical diagnostics, therapy, and disease management. Since the cellular concentration of free Zn^{2+} varies from nanomolar to micromolar range during cellular processes and the high affinity Zn^{2+} imaging probes tend to saturate at lower concentrations of free Zn^{2+}, fluorescence based probes with moderate binding affinity are desirable in distinguishing the occurrence of higher zinc concentrations in the cells. Herein, we report a new, pentacyclic pyridinium based probe, **PYD-PA,** having a pendant *N,N*-di(pyridin-2-ylmethyl)amine (DPA) for Zn^{2+} detection in the cellular environment. The designed probe is soluble in water and serves as a mitochondria targeting unit, whereas the pendent DPA acts as the coordination site for Zn^{2+}. **PYD-PA** displayed a threefold enhancement in fluorescence intensity upon Zn^{2+} binding with a 1:1 binding stoichiometry. Further, the probe showed a selective response to Zn^{2+} over other biologically relevant metal ions with a moderate binding affinity ($K_a = 6.29 \times 10^4\ M^{-1}$), good photostability, pH insensitivity, and low cytotoxicity. The demonstration of bio-imaging in SK-BR-3 breast cancer cell lines confirmed the intracellular Zn ion sensing ability of the probe. The probe was successfully applied for real time monitoring of the fluctuation of intracellular free zinc ions during autophagy conditions, demonstrating its potential for cellular imaging of Zn^{2+} at higher intracellular concentrations.

1. Introduction

Mitochondria is the powerhouse of a cell, which plays a crucial role in maintaining cellular health [1]. Mitochondrial dysfunction is closely associated with various disease conditions such as cancer, cardiovascular diseases, and neurological disorders. [2] As a protective mechanism, cells undergo a process called mitophagy, which prevents the accumulation of dysfunctional mitochondria. [3] Several techniques have been used to understand this process which include western blot, fluorescence microscopy, transmission electron microscopy, and flow cytometry. Most of these techniques rely on the measurement of LC3-II proteins expressed on the autophagosomes. [4] Although these methods have achieved some success in monitoring the autophagy process, they are tedious and time consuming, expensive, and have difficulty in visualizing autophagosomes. In this context, small molecular fluorescent probes can be promising alternatives due to their easy synthesis, low cost, high spatial and temporal resolution, and ability to track the process with least disruption to normal cellular function. [5]

Several small molecular fluorescent probes have already been developed to track autophagy process by monitoring the changes in pH, polarity, viscosity, ROS, and RNS levels in cells. [6–10] Even though there are several reports on the close correlation between intracellular Zn^{2+} concentration and autophagy process, there have been very few attempts to develop a Zn^{2+} sensor to monitor the autophagy process. [11,12] Zn^{2+} is a biologically relevant transition metal ion that plays a crucial role in cell homeostasis, neurological functions, insulin secretion, immune function, signal transduction, and apoptosis. [13–15] Therefore, zinc probes have been used for different applications such as

* Corresponding authors at: Photosciences and Photonics Section, Chemical Sciences and Technology Division, CSIR-National Institute for Interdisciplinary Science and Technology, Thiruvananthapuram 695 019, India.

E-mail addresses: joshy@niist.res.in (J. Joseph), ajayagha@srmist.edu.in (A. Ajayaghosh).

[1] Current affiliation: Department of Chemistry, SRM Institute of Science and Technology, Kattankulathur, Chennai 603,203, India.

https://doi.org/10.1016/j.jphotobiol.2024.113006
Received 22 May 2024; Received in revised form 18 July 2024; Accepted 6 August 2024
Available online 8 August 2024

prostate cancer identification, apoptosis monitoring, controlled photodynamic therapy, etc. [16–19]

Hwang et al. have reported the activation of autophagy by tamoxifen induced accumulation of labile Zinc ions in autophagosomes and lysosomes in MCF-7 cells. [20] Further, Lee et al. found an increase of Zinc ions in autophagic vacuoles, including autolysosomes, as a prerequisite for lysosomal membrane permeabilization and cell death in cultured brain cells. [11] This increase in Zn^{2+} level can be attributed to its release under oxidative conditions from zinc-binding proteins such as metallothioneins. Investigation of the role of Zn^{2+} in autophagy in human hepatoma cells VL-17 A by Yoo et al. has found that Zn^{2+} depletion caused significant suppression of autophagy and, conversely, Zn^{2+} addition to the medium stimulated autophagy. [21] The report by Kim et al. revealed the role of Zn^{2+} as a positive regulator of autophagy by finding that the zinc ionophore PCI-5002 radiosensitizes lung cancer cells by inducing autophagic cell death. [22] The turn-on Zn^{2+} fluorescent probe reported by Diao et al. showed that the green fluorescence intensity of the mitophagic cells was ~2.0-fold higher than that in non-autophagic cells, confirming the increase in the average labile Zn^{2+} level. [23] All these reports indicate a strong connection between autophagy and intracellular Zn^{2+} levels and leave room for further exploration, preferably in real time.

Zinc is the second most abundant transition metal ion present in human body and intracellular zinc concentration is maintained in the range from 100 μM to 500 μM. [24–26] However, 99% of intracellular zinc is in the protein bound form and the concentration of labile zinc is barely perceptible, which estimates between 10^{-9} M to 10^{-12} M. [27] Numerous fluorescent probes with detection limits in the picomolar to nanomolar range have already been developed for zinc sensing. [28–33] Affinity of the probe towards the analyte is an important parameter in sensing applications. For example, a low affinity probe may not respond to a low Zinc ion concentration, while a high affinity probe may easily get saturated at a high Zinc ion concentration. [34] Therefore, an imaging probe with modest affinity can be a useful tool for tracking the elevated Zn^{2+} levels (in the micromolar range), especially during cellular processes like autophagy.

Herein, we report a mitochondria targeting, pyridinium based fluorescence imaging probe having a pendant *N,N*-di(pyridin-2-ylmethyl) amine (DPA) for Zn^{2+} detection in cellular environment (**PYD-PA**, Fig. 1). **PYD-PA**, shows an initial, weak green fluorescence emission due to photoinduced electron transfer (PET) from the amine moiety. Zn^{2+} binding results in an enhancement of fluorescence intensity by blocking the PET process. This probe exhibited moderate binding affinity (K_a = 6.29×10^4 M^{-1}) and good selectivity among biologically relevant metal ions. Due to the moderate binding affinity, the probe will remain non-fluorescent at normal, sub-nanomolar levels of cellular Zn^{2+}, and can specifically track elevated Zn^{2+} levels in cells by fluorescence enhancement upon binding (fluorescence Turn ON signaling). Further, we demonstrated the use of this new probe for mitochondria targeted imaging and real time monitoring of the labile Zn^{2+} during cellular autophagy conditions.

2. Results and Discussion

The probe, **PYD-PA** has a donor-acceptor (D-A) design with a rigid pentacyclic pyridinium based acceptor core and a pendant *N,N*-di(pyridin-2-ylmethyl)amine (DPA) donor. The pyridinium moiety, with its positive charge, serves also as an inherent mitochondria-targeting unit, [35] while the DPA acts as the coordination site for Zn^{2+}. [36] **PYD-PA** in buffered aqueous solutions shows a quenched, green fluorescence due to the efficient, photoinduced electron transfer from the DPA to the pyridinium chromophore. As per the design, Zn^{2+} binding to the DPA receptor will perturb the PET process, resulting in an enhancement of the fluorescence emission from the probe (Fig. 1A). The synthesis of the probe, **PYD-PA** has been achieved by cyclization reaction of 4-(bis (pyridin-2-ylmethyl)amino)benzaldehyde with 6-methoxytetralone followed by methylamine reaction for converting pyrylium to pyridinium fluorophore (Fig. 1B). [37] All the intermediates and final products were characterized by ^{1}H NMR, ^{13}C NMR, and HRMS, details of which are available in the Supporting Information (Figs. S1-S3).

PYD-PA in HEPES buffer exhibited an absorption maximum of 402 nm and a fluorescence maximum of 542 nm, displaying a significant Stokes shift of 6425 cm^{-1} (Fig. 2A). A Contour map of the three-dimensional fluorescence spectra at different excitation wavelengths is depicted in Fig. 2B, which confirms that fluorescence intensity approaches its maximum when the irradiation wavelength is at 400 nm. The absorption, fluorescence, and Stokes shift values are not influenced significantly by the solvent polarity (Fig. S4 & Table S1). Since the positively charged pyridinium moiety in **PYD-PA** facilitated solubility (Fig. S5) in aqueous solutions, aqueous HEPES buffer solutions were used for all the photophysical studies. The molar extinction coefficient is calculated as 22,840 M^{-1} cm^{-1} in HEPES buffer.

Absorption and fluorescence spectra of **PYD-PA** probe showed negligible changes in the pH range 5–8, whereas the protonation of the DPA amine at pH 4 resulted in an enhancement of the fluorescence emission, which further attests to the possible PET fluorescence quenching of the probe (Fig. S6). However, at the physiological pH range, **PYD-PA** remains unprotonated and hence, the pH response at lower pH conditions will not interfere with the cellular metal-probe interactions. Similarly, the photostability studies of **PYD-PA**

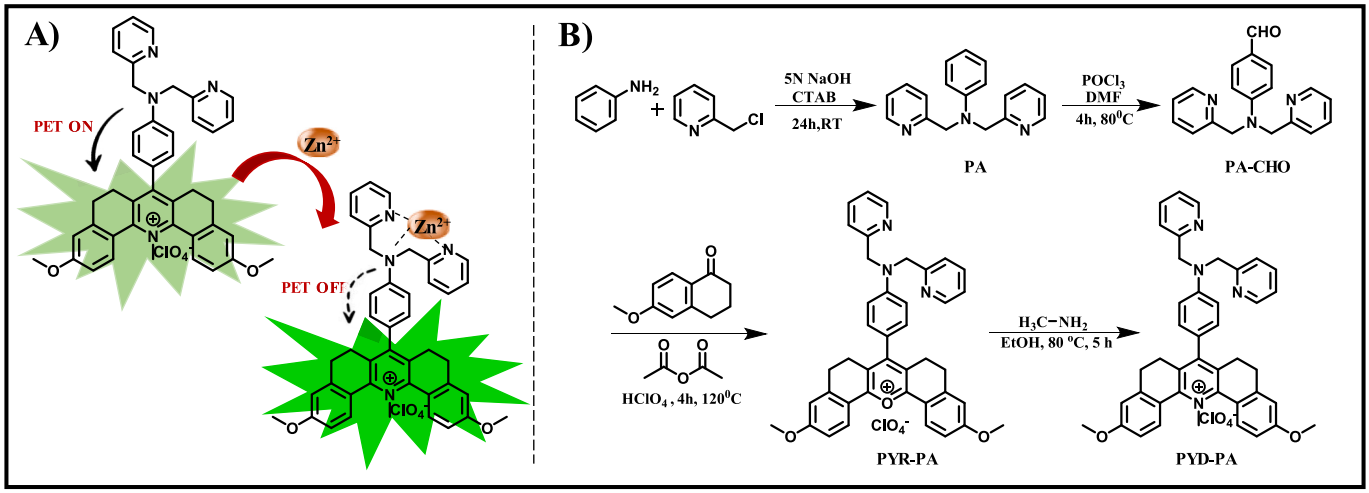

Fig. 1. (A) Probe design strategy and (B) scheme for the synthesis of **PYD-PA**.

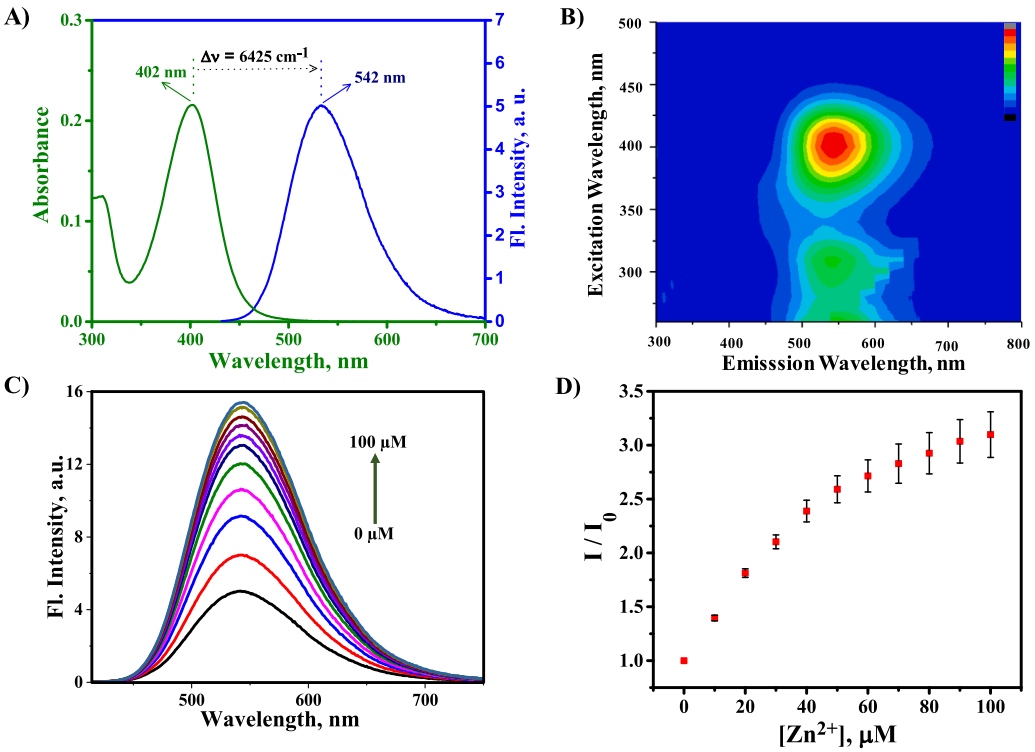

Fig. 2. (A) Absorption and emission spectra of **PYD-PA** (10 μM) in HEPES buffer. (B) A Contour map of the three-dimensional fluorescence excitation-emission spectra. (C) Changes in the fluorescence spectrum of **PYD-PA** (10 μM) against varying concentrations of Zn^{2+} (0–100 μM) in HEPES buffer; λ_{ex} = 400 nm. (D) corresponding changes in the ratio of integrated, fluorescence area.

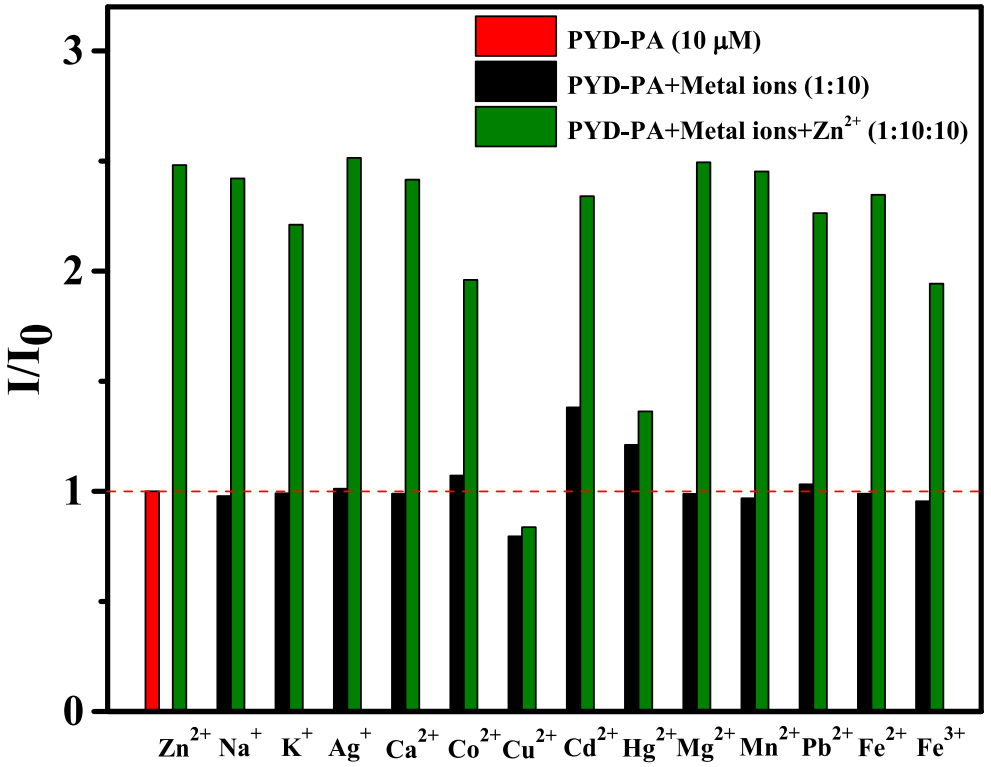

Fig. 3. Fluorescence response of **PYD-PA** (10 μM) at 542 nm (the red bar portion), with 100 μM of other metal ions (the black bar portion) and to the mixture of other metal ions (100 μM) with 100 μM of Zn^{2+} (the green bar portion). (For interpretation of the references to colour in this figure legend, the reader is referred to the web version of this article.)

conducted in HEPES buffer, under 200 W mercury lamp irradiation, using a 400 nm long pass filter for 60 min, and compared with Coumarin 153 and Rhodamine B, reflected negligible changes (Fig. S7).

The changes in the absorption and emission properties of **PYD-PA** in the presence of Zn^{2+} were evaluated by titration of a buffered solution of **PYD-PA** against 0–100 μM Zinc chloride. The results are shown in Fig. S8 A, Fig. 2C, and Fig. 2D. Absorption spectra in the presence of Zn^{2+} did not show significant changes, indicating that the Zn^{2+} binding to DPA unit has negligible effect on the chromophore ground state properties (Fig. S8 A). On the other hand, the fluorescence emission of **PYD-PA** with a maximum at 542 nm showed a gradual enhancement with added Zn^{2+} (Fig. 2C and D), without any shift in the emission maximum. This enhancement in emission could be attributed to the disruption of PET from the di-2-picolylamine moiety due to the binding with Zn^{2+}. The quantum yield of the probe in HEPES buffer before and after binding with Zn^{2+} was estimated as 0.44% and 1.1%, respectively, indicating a moderate (2.5 times) enhancement of the fluorescence emission in presence of Zn^{2+}. The binding stoichiometry of **PYD-PA** and Zn^{2+} was determined as 1:1, using Job's method of continuous variations (Fig. S9 A). [38] The binding constant (K_a), estimated from Benesi - Hildebrand Eq. [39], was found to be $6.3 \times 10^4\ M^{-1}$ (Fig. S9 B), while the limit of detection (LOD) calculated was 0.60 μM (Fig. S10), both indicating moderate affinity of the probe to Zn^{2+}, which could be useful for the monitoring of elevated Zn^{2+} concentrations during autophagy.

The suitability of **PYD-PA** as a Zn^{2+} cellular imaging probe was further tested by exploring the selectivity of the probe-metal ion interactions by monitoring the changes in the fluorescence response in the presence of various biologically relevant metal ions (Fig. 3 and Fig. S11). The probe showed negligible fluorescence changes in presence of biologically relevant and competing cations such as Na^+, K^+, Ag^+, Mg^{2+}, Fe^{2+}, Fe^{3+}, Mg^{2+}, Mn^{2+}, Pb^{2+} and Co^{2+} (Fig. 3; [**PYD-PA**]: [metal ion] = 1:10). Among other toxic metal cations of the same group, Cd^{2+} and Hg^{2+} showed slight fluorescence enhancement of the probe, however will not interfere with cellular imaging of Zn^{2+} due to the negligible presence of these cations in cells. [40,41] To study the influence of other metal ions on Zn^{2+} binding with the probe **PYD-PA**, competitive experiments were performed with different metal ions (100 μM) in the presence of Zn^{2+} (100 μM). Addition of Zn^{2+} in presence of these metal ions resulted in an enhancement of fluorescence, testifying to the competitive binding of Zn^{2+} even in the presence of these metal ions. On the other hand, the addition of Cu^{2+} resulted in a significant quenching of the fluorescence. Further addition of Zn^{2+} to this solution showed negligible fluorescence changes, revealing comparatively stronger interactions of Cu^{2+} with the DPA receptor moiety. [42]

In order to confirm the site of Zn^{2+} coordination, ^1H NMR measurements of **PYD-PA** and its corresponding 1:1 Zn^{2+} complex were performed in acetonitrile (Fig. 4 and Fig. S12). After the addition of Zn^{2+}, the ^1H NMR signals of the protons on carbon adjacent to the N atom (marked n), exhibited a downfield shift from 8.57 to 9.12 ppm, indicating significant deshielding upon Zn^{2+} coordination. Similarly, all the aromatic protons of the DPA units (marked l, k, j) and the two protons in the benzene ring near to the imino N atom (marked f) showed downfield shifts from 7.74 to 8.11, 7.35 to 7.65, 7.25 to 7.63 and 6.88 to 7.13, respectively. However, the protons of pyridinium moiety and the aliphatic protons remain unaffected in the presence of Zn^{2+}. These results indicate that the imino N atom and the two pyridine N atoms are the Zn^{2+} coordination sites in the Zn-complex. [43]

2.1. Cytotoxicity and Co-Localization Studies

Cytotoxicity of the probe is a major concern in the development of cellular imaging probes, which detrimentally affect various bioassays. [44] The cytotoxicity of the **PYD-PA** was evaluated on SK-BR-3, breast cancer cell lines using MTT assay, at different concentrations of the probe. The probe exhibited a proliferation of cells above 90% at a 10 μM concentration and minimal toxicity up to 50 μM concentration, confirming its non-toxic nature under the experimental conditions (Fig. S13).

Positively charged, pyridinium dyes are known to exhibit selective accumulation in the mitochondria. [35,45] Our Zn^{2+} probe design utilizes the mitochondria-targeted cellular accumulation of pyridinium derivatives, in monitoring elevated Zn^{2+} during autophagy. To confirm

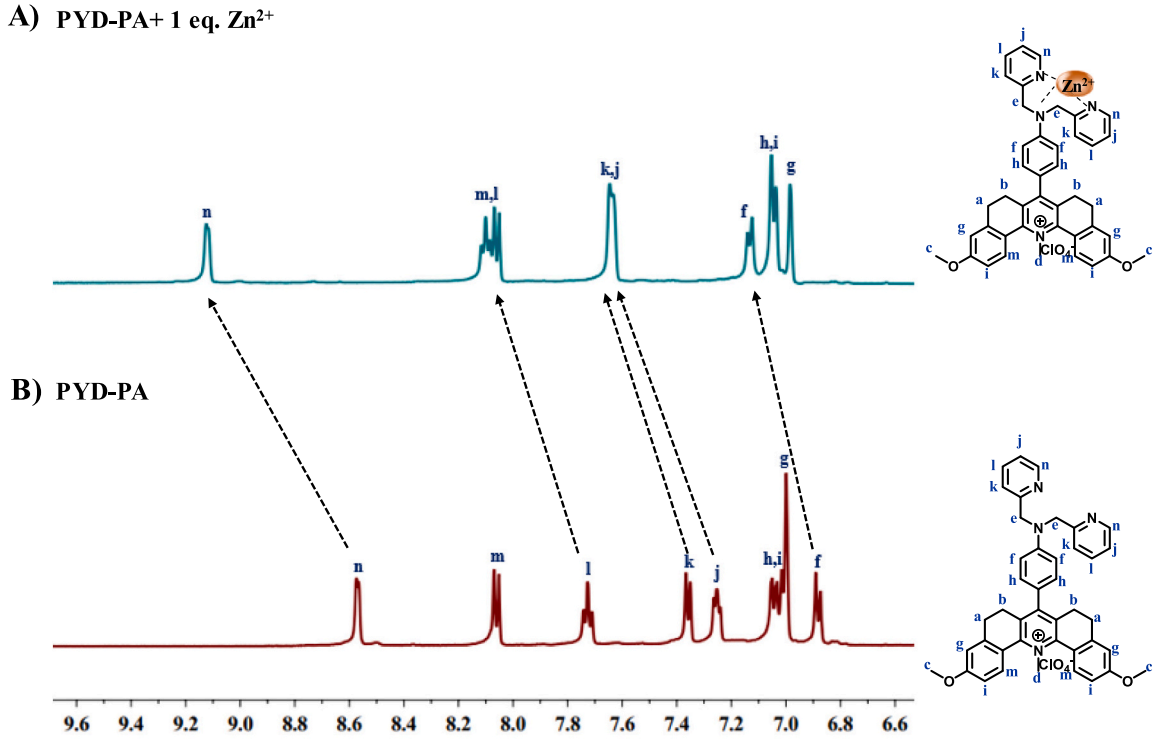

Fig. 4. ^1H NMR (in 500 MHz) spectra of (A) **PYD-PA** in the presence of 1 equivalent of Zn^{2+} and (B) **PYD-PA** alone.

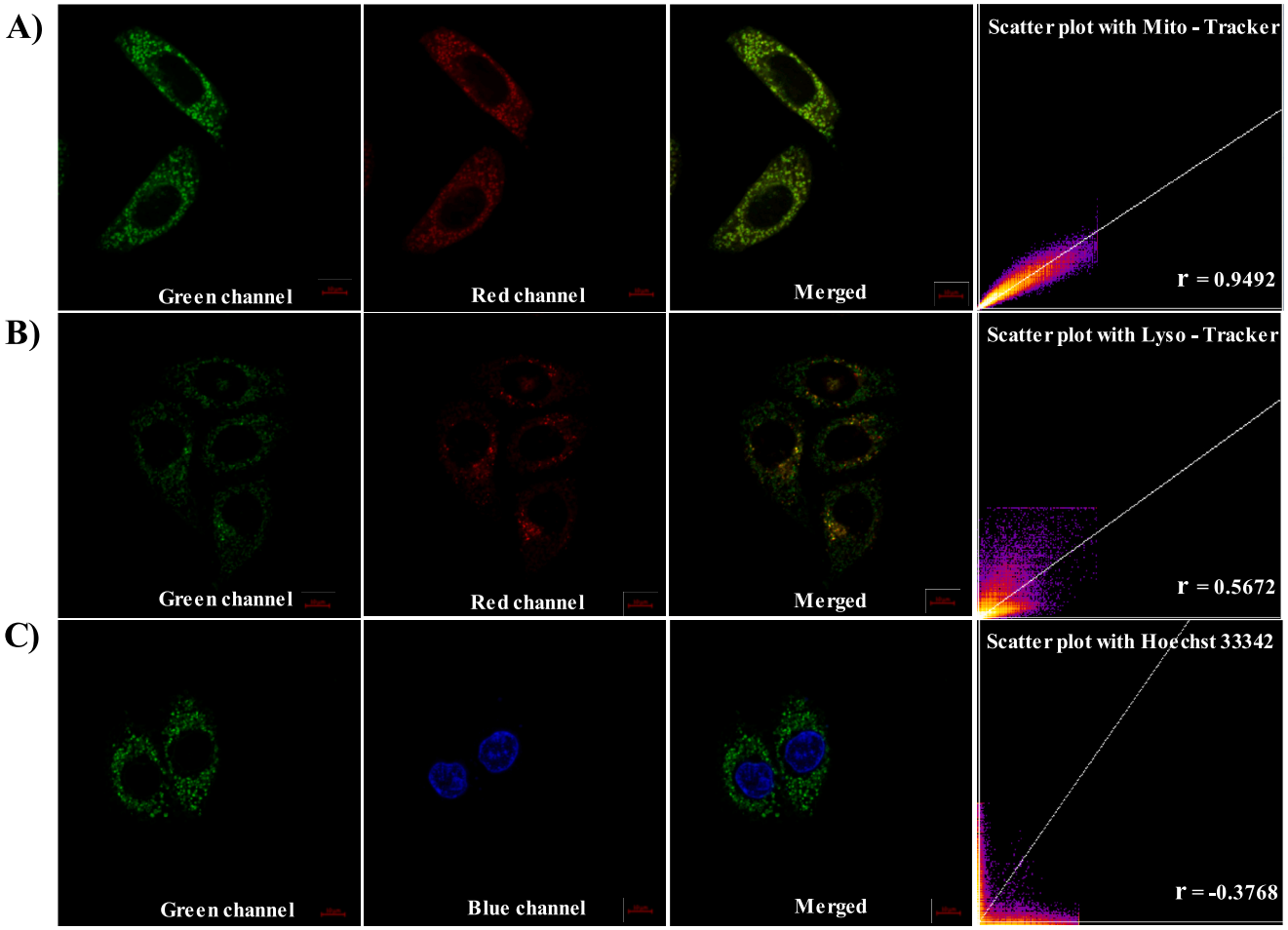

Fig. 5. Confocal fluorescent microscopy images and scatter plots for intracellular localization of **PYD-PA** (1 μM) in SK-BR-3 cells imaged after counter-staining with (A) Mito-Tracker (100 nM), (B) Lyso-Tracker (100 nM) or (c) Hoechst 33342 (1 μM). The co-localization was calculated using Pearson's Correlation Coefficient (r). Scale bar 10 μm.

the selective accumulation of the **PYD-PA** in mitochondria, we have assessed the co-localization ability of the probe within cells through confocal fluorescent microscopy imaging, utilizing co-staining assays (Fig. 5). Cells pretreated with $ZnCl_2$ were subsequently co-stained with **PYD-PA** (1 μM) along with mito-tracker red (100 nM), lyso-tracker red (100 nM), and Hoechst 33342 (1 μM), a nucleus staining dye. The fluorescence of **PYD-PA** from the green channel overlays well with that of Mito-tracker red, which was obtained from the red channel with a Pearson's Correlation Coefficient [46] of ~0.95, indicating an excellent co-localization within the mitochondria. Further, **PYD-PA** displayed relatively smaller co-localization with lyso-tracker and negligible co-localization with Hoechst 33342, with Pearson's correlation coefficient values of 0.5672 and − 0.3768, respectively.

2.2. Zn^{2+} Sensing in Cells under Oxidative Stress

After confirming the localization in mitochondria, the ability of **PYD-PA** to monitor dynamic changes in intracellular Zn^{2+} concentration in SK-BR-3 cells, before and after the pretreatment with $ZnCl_2$ was evaluated using Confocal Fluorescence Microscopy. $ZnCl_2$-pretreated cells displayed a considerable enhancement in emission intensity in the green channel, while the controls showed negligible fluorescence, indicating the ability of the probe to monitor elevated levels of intracellular Zn^{2+} (Fig. 6A-C). Further, the **PYD-PA** probe was used to monitor the release of Zn^{2+} during oxidative stress induced by H_2O_2. During oxidative stress within cells, a rapid influx of hydrogen peroxide takes place, which causes the oxidation of cysteine residues in the Zn-bound metallothioneins and the subsequent release of Zn^{2+}. [47] SK-BR-3 cells incubated with **PYD-PA** showed negligible, initial fluorescence (Fig. 6D), and subsequent treatment of these cells with H_2O_2 to induce oxidative stress resulted in a significant increase in fluorescence intensity, signaling the release of free Zn^{2+} (Fig. 6F). Pre-treatment of these cells with a competitive, Zn^{2+} chelator, *N,N,N′,N′*-tetrakis(2-pyridylmethyl)-ethylenediamine (TPEN), showed reduced cellular fluorescence (Fig. 6E, G), which confirms the role of free Zn^{2+} in the enhancement of fluorescence. Thus, these experiments demonstrate that the probe **PYD-PA** can efficiently monitor the elevated, intracellular Zn^{2+} levels during cellular events such as oxidative stress.

2.3. Zn^{2+} Sensing in Cells under Autophagy Conditions

Autophagy is a cellular degradative process in which cells remove dysfunctional components and recycle their constituents. During autophagy, the cellular microenvironments, including pH, viscosity, and polarity will change and these changes can be used to monitor the autophagy process. [48] Along with these microenvironmental fluctuations, elevated Zn^{2+} levels in the cells can also be an indication of autophagy. Since Rapamycin is a generally used chemical for inducing autophagy in cells during biological experiments, [49,50] we used SK-BR-3 cells incubated with Rapamycin as an autophagy model. Confocal fluorescence microscopy imaging in the green channel of SK-BR-3 cells treated with the probe, **PYD-PA,** without Rapamycin incubation did not show green fluorescence, while the fluorescence in the cells with Rapamycin exposure (10 μM) confirmed the autophagy

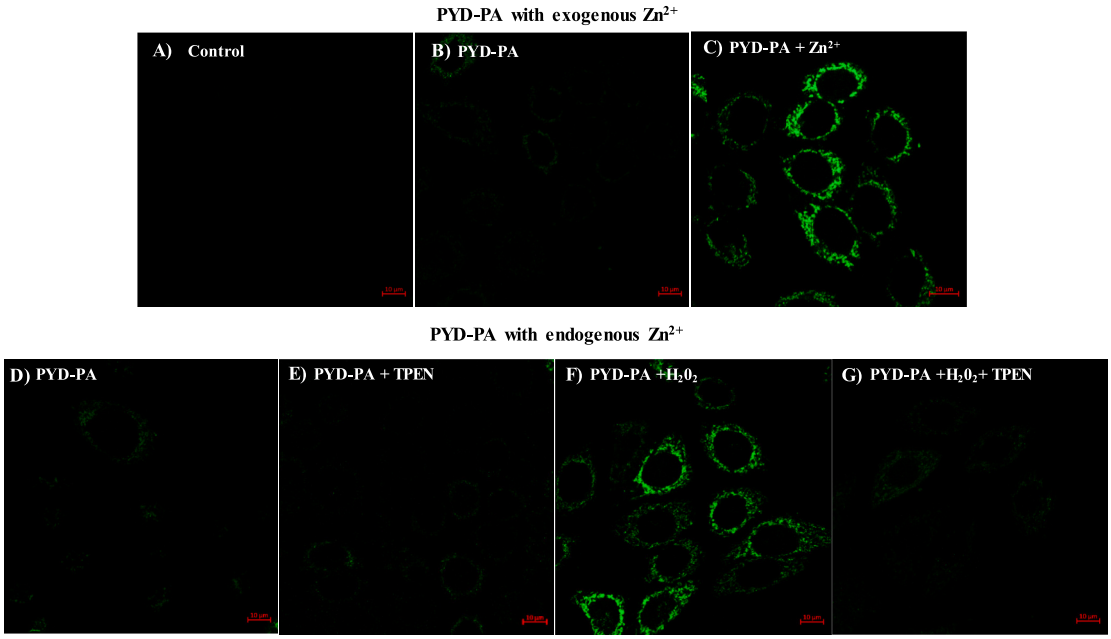

Fig. 6. Confocal microscopy images of **PYD-PA** in SK-BR-3 cells, with exogenous Zn^{2+}; (A) Control; (B) treated with **PYD-PA** (1 μM); (C) pretreated with $ZnCl_2$ (10 μM) followed by **PYD-PA** (1 μM) and with endogenous Zn^{2+} generators and chelators; (D) treated with **PYD-PA** (1 μM); (E) pretreated with TPEN (20 μM) followed by PYD-PA (1 μM); (F) pretreated with H_2O_2 (50 μM) followed by **PYD-PA** (1 μM) and (G) pretreated with TPEN (20 μM) and H_2O_2 (50 μM) followed by **PYD-PA** (1 μM). Scale bar 10 μm.

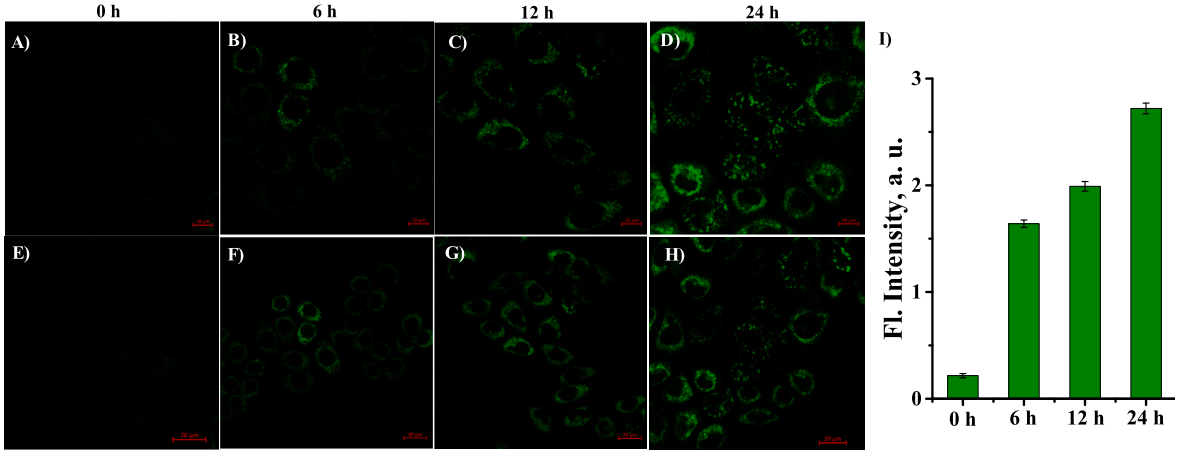

Fig. 7. Confocal microscopy images of **PYD-PA** in SK-BR-3 cells pretreated with Rapamycin (10 μM) for (A) & (E) 0 h (B) & (F) 6 h (C) & (G) 12 h (D) & (H) 24 h at two different maginifications. (I) A plot of the fluorescence intensity with time during autophagy. Scale bar is 10 μm for A-D and 20 μm for *E*-H.

induction. With time, we could clearly see a considerable fluorescence increment in the green channel, indicating an upregulation of mitochondrial Zn^{2+} concentration during autophagy (Fig. 7). For a longer time period of 24 h, the fluorescence increment was even higher. This is a clear indication that Zn^{2+} is a positive regulator of autophagy, and there is an increase in Zn^{2+} concentration associated with the process.

3. Conclusion

In conclusion, the pentacyclic pyridinium based fluorophore, **PYD-PA,** reported here is a novel 'Turn ON' fluorescent probe for the selective detection of Zn^{2+}. The probe displayed a three-fold increase in fluorescence intensity upon Zn^{2+} binding, demonstrating remarkable selectivity in the presence of other biologically relevant metal ions. Moreover, the probe exhibited good water solubility, photostability, pH insensitivity, and low cytotoxicity, ensuring its viability for cellular imaging applications. The probe's moderate binding affinity for Zn^{2+} ($K_a = 6.29 \times 10^4\ M^{-1}$) and its capability to target mitochondria, ensure the effective detection of elevated Zn^{2+} levels, particularly within mitochondria. Bioimaging experiments conducted in SK-BR-3 breast cancer cell lines confirms the ability of the probe to efficiently monitor intracellular dynamic changes in Zn^{2+} levels. Furthermore, the probe was successfully applied for monitoring the fluctuations in intracellular free zinc ions during autophagy conditions in real time.

CRediT authorship contribution statement

Anagha Thomas: Writing – original draft, Validation, Methodology, Investigation, Formal analysis, Data curation. **Anaga Nair:** Methodology, Investigation. **Sandip Chakraborty:** Methodology, Formal analysis. **Roopasree O. Jayarajan:** Methodology, Investigation, Formal analysis. **Joshy Joseph:** Writing – original draft, Supervision,

Methodology, Funding acquisition, Formal analysis, Conceptualization. **Ayyappanpillai Ajayaghosh:** Writing – review & editing, Supervision, Project administration, Funding acquisition, Formal analysis, Conceptualization.

Declaration of competing interest

There are no conflicts to declare.

Data availability

Data will be made available on request.

Acknowledgements

A.A. is thankful to the DST-SERB, Govt. of India for a J. C. Bose National Fellowship (SB/S2/JCB-11/2014). Financial support from the Council of Scientific and Industrial Research (MLP-0073) and DST-Nanomission (DST/NM/TUE/EE-02/2019) are gratefully acknowledged. A.T. acknowledges DST INSPIRE (DST-INSPIRE Fellowship/2018/IF1900030) for Research Fellowship.

Appendix A. Supplementary data

Supplementary data to this article can be found online at https://doi.org/10.1016/j.jphotobiol.2024.113006.

References

[1] S. Javadov, A.V. Kuznetsov, Mitochondria: the cell powerhouse and nexus of stress, Front. Physiol. 4 (2013) 207.
[2] D. Xie, W. Ma, C. Wang, W. Zhang, Z. Ding, Mitochondria-targeted fluorescent probe for imaging viscosity in hepatic ischemia–reperfusion injury cell model, Chem. Commun. 59 (2023) 1030–1033.
[3] W.-X. Ding, X.-M. Yin, Mitophagy: mechanisms, pathophysiological roles, and analysis, Biol. Chem. 393 (2012) 547–564.
[4] Z. Chen, J. Li, X. Chen, J. Cao, J. Zhang, Q. Min, J.-J. Zhu, Single gold@ silver nanoprobes for real-time tracing the entire autophagy process at single-cell level, J. Am. Chem. Soc. 137 (2015) 1903–1908.
[5] J. Chan, S.C. Dodani, C.J. Chang, Reaction-based small-molecule fluorescent probes for chemoselective bioimaging, Nat. Chem. 4 (2012) 973–984.
[6] Y. Liu, D. Zhang, Y. Qu, F. Tang, H. Wang, A. Ding, L. Li, Advances in small-molecule fluorescent pH probes for monitoring Mitophagy, Chem. Biomed. Imaging 2 (2024) 81–97.
[7] X. Li, X. Li, H. Ma, A near-infrared fluorescent probe reveals decreased mitochondrial polarity during mitophagy, Chem. Sci. 11 (2020) 1617–1622.
[8] S. Su, L. Chai, Q. An, W. Hu, L. Wang, X. Li, H. Zhang, C. Li, Tracking autophagy process with a TBET and AIE-based ratiometric two-photon viscosity probe, Anal. Chem. 94 (2022) 15146–15154.
[9] C. Guo, M. Yang, L.I. Jing, J. Wang, Y. Yu, Y. Li, J. Duan, X. Zhou, Y. Li, Z. Sun, Amorphous silica nanoparticles trigger vascular endothelial cell injury through apoptosis and autophagy via reactive oxygen species-mediated MAPK/Bcl-2 and PI3K/Akt/mTOR signaling, Int. J. Nanomedicine 11 (2016) 5257–5276.
[10] J. Feng, X. Chen, J. Shen, Reactive nitrogen species as therapeutic targets for autophagy: implication for ischemic stroke, Expert Opin. Ther. Targets 21 (2017) 305–317.
[11] S.-J. Lee, J.-Y. Koh, Roles of zinc and metallothionein-3 in oxidative stress-induced lysosomal dysfunction, cell death, and autophagy in neurons and astrocytes, Mol. Brain 3 (2010) 1–9.
[12] J.P. Liuzzi, R. Pazos, Interplay between autophagy and zinc, J. Trace Elem. Med. Biol. 62 (2020) 126636.
[13] Z. Mao, L. Hu, X. Dong, C. Zhong, B.-F. Liu, Z. Liu, Highly sensitive quinoline-based two-photon fluorescent probe for monitoring intracellular free zinc ions, Anal. Chem. 86 (2014) 6548–6554.
[14] H. Santhakumar, R.V. Nair, D.S. Philips, S.J. Shenoy, A. Thekkuveettil, A. Ajayaghosh, R.S. Jayasree, Real time imaging and dynamics of hippocampal Zn^{2+} under epileptic condition using a ratiometric fluorescent probe, Sci. Rep. 8 (2018) 9069.
[15] K.P. Divya, S. Sreejith, P. Ashokkumar, K. Yuzhan, Q. Peng, S.K. Maji, Y. Tong, H. Yu, Y. Zhao, P. Ramamurthy, A ratiometric fluorescent molecular probe with enhanced two-photon response upon Zn^{2+} binding for in vitro and in vivo bioimaging, Chem. Sci. 5 (2014) 3469–3474.
[16] C. Du, S. Fu, X. Wang, A.C. Sedgwick, W. Zhen, M. Li, X. Li, J. Zhou, Z. Wang, H. Wang, Diketopyrrolopyrrole-based fluorescence probes for the imaging of lysosomal Zn^{2+} and identification of prostate cancer in human tissue, Chem. Sci. 10 (2019) 5699–5704.
[17] J.M.K. Kwong, C. Hoang, R.T. Dukes, R.W. Yee, B.D. Gray, K.Y. Pak, J. Caprioli, Bis (zinc-Dipicolylamine), Zn-DPA, a new marker for apoptosis, Investig. Ophthalmol. Vis. Sci. 55 (2014) 4913–4921.
[18] P. Hu, R. Wang, L. Zhou, L. Chen, Q. Wu, M.-Y. Han, A.M. El-Toni, D. Zhao, F. Zhang, Near-infrared-activated upconversion nanoprobes for sensitive endogenous Zn^{2+} detection and selective on-demand photodynamic therapy, Anal. Chem. 89 (2017) 3492–3500.
[19] K.P. Divya, S. Sreejith, B. Balakrishna, P. Jayamurthy, P. Anees, A. Ajayaghosh, A Zn^{2+}-specific fluorescent molecular probe for the selective detection of endogenous cyanide in biorelevant samples, Chem. Commun. 46 (2010) 6069–6071.
[20] J.J. Hwang, H.N. Kim, J. Kim, D.-H. Cho, M.J. Kim, Y.-S. Kim, Y. Kim, S.-J. Park, J.-Y. Koh, Zinc (II) ion mediates tamoxifen-induced autophagy and cell death in MCF-7 breast cancer cell line, BioMetals 23 (2010) 997–1013.
[21] J.P. Liuzzi, C. Yoo, Role of zinc in the regulation of autophagy during ethanol exposure in human hepatoma cells, Biol. Trace Elem. Res. 156 (2013) 350–356.
[22] K.W. Kim, C.K. Speirs, D.K. Jung, B. Lu, The zinc ionophore PCI-5002 radiosensitizes non-small cell lung cancer cells by enhancing autophagic cell death, J. Thorac. Oncol. 6 (2011) 1542–1552.
[23] H. Fang, S. Geng, M. Hao, Q. Chen, M. Liu, C. Liu, Z. Tian, C. Wang, T. Takebe, J.-L. Guan, Simultaneous Zn^{2+} tracking in multiple organelles using super-resolution morphology-correlated organelle identification in living cells, Nat. Commun. 12 (2021) 109.
[24] P. Carol, S. Sreejith, A. Ajayaghosh, Ratiometric and near-infrared molecular probes for the detection and imaging of zinc ions, Chem. Asian J. 2 (2007) 338–348.
[25] K. Thambiayya, A.M. Kaynar, C.M.S. Croix, B.R. Pitt, Functional role of intracellular labile zinc in pulmonary endothelium, Pulm. Circ. 2 (2012) 443–451.
[26] S. Sreejith, K.P. Divya, A. Ajayaghosh, Detection of zinc ions under aqueous conditions using chirality assisted solid-state fluorescence of a bipyridyl based fluorophore, Chem. Commun. 2903-2905 (2008).
[27] E. Bafaro, Y. Liu, Y. Xu, R.E. Dempski, The emerging role of zinc transporters in cellular homeostasis and cancer, Signal Transduct. Target. Ther. 2 (2017) 1–12.
[28] K. Aich, S. Goswami, S. Das, C.D. Mukhopadhyay, A new ICT and CHEF based visible light excitable fluorescent probe easily detects in vivo Zn^{2+}, RSC Adv. 5 (2015) 31189–31194.
[29] A. Jayaraj, M.S. Gayathri, G. Sivaraman, A highly potential acyclic Schiff base fluorescent turn on sensor for Zn2+ ions and colorimetric chemosensor for Zn^{2+}, Cu^{2+} and Co^{2+} ions and its applicability in live cell imaging, J. Photochem. Photobiol. B 226 (2022) 112371.
[30] Y. Wang, C. Xia, Z. Han, Y. Jiao, X. Yao, Z. Lun, S. Fu, H. Zhang, P. Hou, D. Ning, Aminoantipyrine based efficient chemosensor for Zn (II) ions and its effectiveness in live cell imaging, J. Photochem. Photobiol. B 199 (2019) 111602.
[31] X. Zhang, G. Jin, Z. Chen, Y. Wu, Q. Li, P. Liu, G. Xi, An efficient turn-on fluorescence chemosensor system for Zn (II) ions detection and imaging in mitochondria, J. Photochem. Photobiol. B 234 (2022) 112485.
[32] P. Wang, J. Wu, A highly sensitive turn-on fluorescent chemosensor for recognition of Zn (II) ions and its application in live cells imaging, J. Photochem. Photobiol., A 386 (2020) 112111.
[33] D.S. Philips, S. Sreejith, T. He, N.V. Menon, P. Anees, J. Mathew, S. Sajikumar, Y. Kang, M.C. Stuparu, H. Sun, A three-photon active organic fluorophore for deep tissue Ratiometric imaging of intracellular divalent zinc, Chem. Asian J. 11 (2016) 1523–1527.
[34] M. Saleem, K.H. Lee, Optical sensor: a promising strategy for environmental and biomedical monitoring of ionic species, RSC Adv. 5 (2015) 72150–72287.
[35] Y. Huang, M. Li, Q. Zan, R. Wang, S. Shuang, C. Dong, Mitochondria-targeting multifunctional fluorescent probe toward polarity, viscosity, and ONOO–and cell imaging, Anal. Chem. 95 (2023) 10155–10162.
[36] S. Sumalekshmy, M.M. Henary, N. Siegel, P.V. Lawson, Y. Wu, K. Schmidt, J.-L. Brédas, J.W. Perry, C.J. Fahrni, Design of emission ratiometric metal-ion sensors with enhanced two-photon cross section and brightness, J. Am. Chem. Soc. 129 (2007) 11888–11889.
[37] S. Chakraborty, M.M. Joseph, S. Varughese, S. Ghosh, K.K. Maiti, A. Samanta, A. Ajayaghosh, A new pentacyclic pyrylium fluorescent probe that responds to pH imbalance during apoptosis, Chem. Sci. 11 (2020) 12695–12700.
[38] J.S. Renny, L.L. Tomasevich, E.H. Tallmadge, D.B. Collum, Method of continuous variations: applications of job plots to the study of molecular associations in organometallic chemistry, Angew. Chem. Int. Ed. 52 (2013) 11998–12013.
[39] I.D. Kuntz Jr., F.P. Gasparro, M.D. Johnston Jr., R.P. Taylor, Molecular interactions and the Benesi-Hildebrand equation, J. Am. Chem. Soc. 90 (1968) 4778–4781.
[40] K.V. Sudheesh, M.M. Joseph, D.S. Philips, A. Samanta, K. Kumar Maiti, A., Ajayaghosh, pH-Controlled Nanoparticles Formation and Tracking of Lysosomal Zinc Ions in Cancer Cells by Fluorescent Carbazole–Bipyridine Conjugates, ChemistrySelect 3 (2018) 2416–2422.
[41] H.-M. Liu, P. Venkatesan, S.-P. Wu, A sensitive and selective fluorescent sensor for zinc (II) and its application to living cell imaging, Sensors Actuators B Chem. 203 (2014) 719–725.
[42] L.J. Gomes, J.P. Carrilho, P.M. Pereira, A.J. Moro, A near InfraRed emissive Chemosensor for Zn^{2+} and phosphate derivatives based on a Di-(2-picolyl) amine-styrylflavylium push-pull fluorophore, Sensors 23 (2023) 471.
[43] L. Xue, H.-H. Wang, X.-J. Wang, H. Jiang, Modulating affinities of di-2-picolylamine (DPA)-substituted quinoline sensors for zinc ions by varying pendant ligands, Inorg. Chem. 47 (2008) 4310–4318.
[44] M. Tian, Y. Ma, W. Lin, Fluorescent probes for the visualization of cell viability, Acc. Chem. Res. 52 (2019) 2147–2157.

[45] S. Jiao, X. Dong, W. Zhao, Meso pyridinium BODIPY-based long wavelength infrared mitochondria-targeting fluorescent probe with high photostability, Anal. Methods 15 (2023) 3149–3155.
[46] I. Cohen, Y. Huang, J. Chen, J. Benesty, J. Benesty, J. Chen, Y. Huang, I. Cohen, Pearson correlation coefficient, Noise reduction in speech processing (2009) 1–4.
[47] M.C. McCord, E. Aizenman, The role of intracellular zinc release in aging, oxidative stress, and Alzheimer's disease, Front. Aging Neurosci. 6 (2014) 77.
[48] X. Li, X. Liang, J. Yin, W. Lin, Organic fluorescent probes for monitoring autophagy in living cells, Chem. Soc. Rev. 50 (2021) 102–119.
[49] H. Iwashita, H.T. Sakurai, N. Nagahora, M. Ishiyama, K. Shioji, K. Sasamoto, K. Okuma, S. Shimizu, Y. Ueno, Small fluorescent molecules for monitoring autophagic flux, FEBS Lett. 592 (2018) 559–567.
[50] F. Hu, X. Cai, P.N. Manghnani, W. Wu, B. Liu, Multicolor monitoring of cellular organelles by single wavelength excitation to visualize the mitophagy process, Chem. Sci. 9 (2018) 2756–2761.